Understanding forgeability in highly reinforced cast-and-wrought superalloys

Marcos Fernández-Álvarez

Queens' College

A dissertation submitted to the University of Cambridge for the degree of

Doctor of Philosophy

Department of Materials Science and Metallurgy

University of Cambridge

December 2022

DECLARATION

This dissertation is submitted for the degree of Doctor of Philosophy at the University of Cambridge. It describes the research carried out in the Department of Materials Science and Metallurgy from October 2017 to September 2020 and from March 2021 to May 2022 under the supervision of Dr Enrique Galindo-Nava. Except where reference is made to the work of others, the contents of this dissertation are original and have not been the result of collaboration. No part of the work described here has been submitted for the purpose of gaining academic qualification at this or any other institute of higher learning. This dissertation does not exceed 60,000 words in length and has fewer than 150 figures.

Parts of this dissertation have been presented at:

Appraising forgeability and surface cracking in new generation cast-and-wrought superalloys. M. Fernandez-Alvarez, A. Vaasudevan, E. Fischer, C. Rae, T. Witulski, E.I. Galindo Nava. EuroSuperalloys 2022, Bamberg, Germany, 18 – 22 September 2022.

Parts of this dissertation have been submitted for publication:

Appraising forgeability and surface cracking in new generation cast-and-wrought superalloys. M. Fernandez-Alvarez, A. Vaasudevan, E. Fischer, C. Rae, T. Witulski, E.I. Galindo Nava. Submitted to Metallurgical and Materials Transactions A.

Marcos Fernández-Álvarez

December 2022

Abstract

A physical mechanism is presented to describe the relationship between processing parameters, microstructural evolution, and the occurrence of surface cracking in the hot die forging of highly γ'-reinforced cast-and-wrought nickel-based superalloys. The theory postulates that surface cracking is controlled by the dissolution of the secondary γ' phase and its subsequent reprecipitation as very fine precipitates upon cooling. The commercial alloy Udimet 720 is used as a benchmark to explore this mechanism. A novel testing method is devised to assess forgeability and surface cracking through laboratory-scale tests on a Gleeble thermo-mechanical simulator. The method mimics the die chilling effect characteristic of hot die forging. FEM simulations are employed to obtain full-scale forging data to feed this method, and thermal analysis and electron microscopy observations are used to map the relevant solvus temperatures. Remarkably, samples heated up to higher initial temperatures prior to undergoing die chilling showed more extensive surface cracking than those heated up to lower temperatures. This challenges the notion commonly accepted in industry that these alloys ought to be forged at temperatures below but close to the γ' solvus. Post-deformation samples are examined via electron microscopy, energy dispersive X-ray microanalysis, and electron backscatter diffraction to confirm the hypothesis and explore deformation and fracture mechanisms. In addition, the investigation is extended by the said techniques to a second highly γ'-reinforced alloy – René 65 – for validation purposes. The results indicate that – along with the local mechanical conditions of the forging – die-chilling effects and forging temperatures are paramount in controlling surface cracking, as the key process variables governing the distribution of γ'. These findings and the novel forging simulation technique pave the way towards designing superalloys with improved processability and excellent performance.

ACKNOWLEDGEMENTS

I would like to express my sincere gratitude to my supervisor Dr Enrique Galindo-Nava for giving me the opportunity to undertake this research project under his guidance, for believing in my potential, and for his continuous support and advice. I am deeply grateful to my advisor Professor C.M.F. Rae for her invaluable advice and encouragement, particularly during the last stages of this project.

The funding and materials provided by Otto Fuchs KG are gratefully acknowledged. I would like to thank Dr Thomas Witulski, Dr.-Ing. Bernd Koch, and Enjuscha Fischer for sharing their expertise and helping me understand the industrial dimension of the project through many helpful discussions. I also gratefully acknowledge the financial support received from the Engineering and Physical Sciences Research Council (EPRSC).

I would like to thank the staff at the Department of Materials Science and Metallurgy, and in particular Dr Hon Tong Pang, Simon Griggs, and Dr Giorgio Divitini for training me on the various instruments required to conduct my research and diligently answering many queries throughout the years. A special thanks to Hans Hofman from Delft University of Technology for his crucial help conducting thermo-mechanical experiments – and replacing quite a few broken anvils.

I am thankful to my colleagues of the Rolls-Royce UTC for the good times together, interesting discussions, and support. In particular, I would like to thank Dr Kathy Christofidou, Dr Stella Pedrazzini, Dr Caspar Schwalbe, Max Bloomfield, Dr Dominik Dziedzic, and Mauro Velasco-Castro for helping with various aspects of the project.

I would like to extend my gratitude to my colleagues at the European Parliament for their warmness, curiosity, and encouragement; and for giving me the opportunity to explore alternative paths and make a contribution to the European project. I am also deeply grateful to my UK Civil Service colleagues for their kindness, understanding, and support during the last stretch of this journey.

I cannot begin to express my thanks to my friends in Cambridge for helping me through the ups and downs of this project, for the unforgettable times together, for encouraging me to embrace my true self, and for making Cambridge feel like home. I am extremely grateful to my friends beyond Cambridge for always being there for me, despite the distance, and helping me through every step of the way. I am also thankful to Peter for his support – and for reminding me with his unwavering cheerfulness of the beauty of nature, science, and research at the times when I needed it most.

Finally, I am deeply thankful to my family, without whom I could not have completed this project. Thank you for listening, encouraging, and supporting me in every possible way; for helping me navigate the challenging periods; and for being there to celebrate every accomplishment. Thank you for the education that you have given me, for your guidance throughout the years, for teaching me that where there is a will there is a way, and for encouraging me to pursue my ever-changing passions. I would like to dedicate this work to my grandfather, who was a lecturer in Materials Science, and who would have liked to see me following his footsteps and making my contribution to extend the knowledge of this subject.

TABLE OF CONTENTS

LIST OF FIGURES

LIST OF TABLES

NOMENCLATURE

Roman symbols and abbreviations

Ø	Diameter
$Ø_1$	Diameter at the base and top surface
$Ø_2$	Diameter at the equator
a	Lattice parameter
a_γ	Lattice parameter of the gamma phase
$a_{\gamma'}$	Lattice parameter of the gamma prime phase
a/o	Atomic percentage
at. pct.	Atomic percentage
aBSD	Annular backscatter detector
AGG	Abnormal grain growth
AOD	Argon oxygen decarburization
APB	Antiphase boundary
b	Magnitude of the Burgers vector
BCT	Body-centred tetragonal
BSE	Backscattered electron
C&W	Cast-and-wrought
CCD	Charge-coupled device
CNC	Computerised numerical control
CR	Crack
CRSS	Critical resolved shear stress
CSF	Complex stacking fault
DC	Double cone
DC	Dislocation cell
DG	Deformation glide
DMM	Dynamic material modelling
DRV	Dynamic recovery
DRX	Dynamic recrystallisation
DSC	Differential scanning calorimetry
DT	Deformation twin
DTA	Differential thermal analysis
EAF	Electric arc furnace
EBSD	Electron backscatter diffraction
ECCI	Electron channelling contrast imaging

ECT	Equicohesive temperature
EDM	Electro discharge machining
EDX	Energy-dispersive X-ray spectroscopy
EM	Electron microscopy
ESR	Electro-slag remelting
ETD	Everhart–Thornley detector
ETMT	Electro-thermal mechanical testing system
f	[Volume or area] fraction
$f_{\gamma'_p}$	Gamma prime fraction
$f_{\gamma'_p}$	Primary gamma prime fraction
$f_{\gamma'_s}$	Secondary gamma prime fraction
$f_{\gamma'_t}$	Tertiary gamma prime fraction
FCC	Face-centred cubic
FCP	Fatigue crack propagation
FEA	Finite element analysis
FEM	Finite element method
FSS	Fine structure superplasticity
G	Dissipator power content
GBS	Grain boundary sliding
GHG	Greenhouse gas
h	Height
HAGB	High-angle grain boundary
HCP	Hexagonal close-packed
HIP	Hot isostatic pressing
I/C	Investment casting
I/M	Ingot metallurgy
I–L SED	In-lens secondary electron detector
IAE	International Energy Association
IPF	Inverse pole figure
J	Dissipator power co-content
JMA	Johnson–Mehl–Avrami
LAGB	Low-angle grain boundary
LSW	Lifshitz–Slyozov–Wagner
m	Strain rate sensitivity
MRDV	Metadynamic recovery
MRDX	Metadynamic recrystallisation
NDE	Non-destructive evaluation
P	Power per unit volume entering the system
P/M	Powder metallurgy
PPB	Prior particle boundary

PSD	Precipitate size distribution
r	Radial coordinate
r	Radius
$\hat{r}$	Mean particle radius
$r_{\gamma' p}$	Radius of primary gamma prime particles
$r_{\gamma' s}$	Radius of secondary gamma prime particles
$r_{\gamma' t}$	Radius of tertiary gamma prime particles
RA	Reduction of area
SE	Secondary electron
SEM	Scanning electron microscopy/microscope
SESF	Superlattice extrinsic stacking fault
SFE	Stacking fault energy
SISF	Superlattice intrinsic stacking fault
SIT	Silicon intensifier target
SRV	Static recovery
SRX	Static recrystallisation
t	Time
t-EBSD	Transmission electron backscatter diffraction
T	Temperature
$T_{\gamma' \text{ solvus}}$	Solvus temperature of the gamma prime phase
$T_{\gamma' s \text{ solvus}}$	Solvus temperature of secondary gamma prime
T_0	Initial, forging, or furnace temperature
T_f	Final or deformation temperature
T_h	Homologous temperature
T_m	Melting temperature
$\widehat{T}$	Line tension
TCP	Topologically close packed [phases]
TEM	Transmission electron microscopy/microscope
TET	Turbine entry temperature
UTS	Ultimate tensile strength
VAR	Vacuum arc remelting
VD	Void
VIM	Vacuum induction melting
w	Dimensionless constant of order unity
wt.	Weight
wt. %	Weight percentage
z	Axial coordinate
Z	Atomic number

Greek symbols

γ	Gamma phase
γ	Interface energy
$\gamma_{\gamma/\gamma'}$	Interface energy γ / γ'
γ_{APB}	Antiphase boundary energy
γ'	Gamma prime phase
γ'_{p}	Primary gamma prime phase
γ'_{s}	Secondary gamma prime phase
γ'_{t}	Tertiary gamma prime phase
γ''	Gamma double-prime phase
δ	Delta phase
ε	Strain
ε_{r}	Radial strain
ε_{z}	Axial strain
ε_{θ}	Tangential strain
$\varepsilon_{\mathrm{rz}}$	Shear strain r – z
$\varepsilon_{\mathrm{r}\theta}$	Shear strain r – θ
$\varepsilon_{\theta\mathrm{z}}$	Shear strain θ – z
$\dot{\varepsilon}$	Strain rate
η	Eta phase
η	Power dissipation efficiency
Θ	Cooling rate
κ	Cracked area
μ	Shear modulus
ξ	Instability parameter
τ	Shear stress
τ_{wc}	CRSS due to weakly coupled dislocations
τ_{sc}	CRSS due to strongly coupled dislocations
τ_{rz}	Shear stress r – z
$\tau_{\mathrm{r}\theta}$	Shear stress r – θ
$\tau_{\theta\mathrm{z}}$	Shear stress θ – z
σ	Stress
σ_{r}	Radial stress
σ_{z}	Axial stress
σ_{θ}	Tangential stress
σ_{Y}	Yield stress
φ	Bowing angle

1

Introduction

Air transport is a key element of today's highly interconnected world. In 2019, the number of passengers carried reached an all-time high of 4.4 billion, up from 0.3 billion in 1970 [1]. In the same period, air freight grew from under 15 to 215 million ton-km [2]. Aviation not only allows people to interact globally; it also boosts trade and economic growth [3].

However, aviation is an important source of greenhouse gas (GHG) emissions, and global civil aviation currently accounts for 4–5% of total GHG emissions [4]. Under the Paris Agreement, nearly 200 countries pledged to keep global warming well below 2°C. But according to the International Energy Association (IAE), efforts to cut aviation emissions are not on track [5]. Technological advances are crucial to attain net zero GHG emissions, possibly coupled with modal shifts and demand curtailment. Current aircraft are approximately 85% more efficient than those of the 1960s, and fuel efficiency has continued to improve at 1.9% per year between 2010 and 2019 [5]. However, the notable maturity of these technologies makes it improbable that future efficiency gains will follow past trends, and fuel reductions are unlikely to be higher than 35% during the next four decades. Unless radical design changes are adopted, such as the introduction of the blended wing body aircraft, improvements in

airframe aerodynamics can only result in small fuel savings. Working under the current design paradigm, the most significant reductions in emissions are likely to come from the propulsion system [6].

In gas-turbine engines, efficiency is mainly determined by the combustion temperature, which in turn dictates the turbine entry temperature (TET). The turbine (see Figure 1.2) is the section of the engine where components are subject to the highest temperature and stress requirements. Consequently, the main constraint to increasing combustion temperatures is the development of materials with the necessary strength, oxidation resistance, and thermal stability to withstand the operating conditions in the turbine.

For over eight decades, superalloys have been the material of choice for aero engine turbines. The emergence of early superalloys in the 1940s was driven by the needs of gas turbine engines, and these have been a crucial driver for developing new alloys and adapting existing ones ever since [7,8]. Modern jet aircraft would not exist if it were not for the existence of superalloys [9]. Figure 1.1 shows that in the 1940 to 2010 period, the TET of Rolls-Royce's civil gas turbine engines rose by 700°C. Out of this, around 300°C – 400°C can be attributed to the increase in high temperature capability of superalloys themselves [9].

Despite being profoundly intertwined with gas turbine engines, superalloys have progressively found their way into many other applications, such as furnaces, heat-exchangers, oil equipment and biomedical implants [1, 3]. Recent research in superalloy metallurgy has continued to seek improvements in temperature capability, but significant efforts are being devoted to developing novel alloys for land-based turbines for power production, driven by the growing demand in developing countries [3]. Similarly, hydrogen-fuelled turbines are strong contenders in the race to decarbonise aviation and power-generation, posing new challenges for superalloy metallurgists. In essence, superalloys have never been as technologically and economically important as they are nowadays [1, 3].

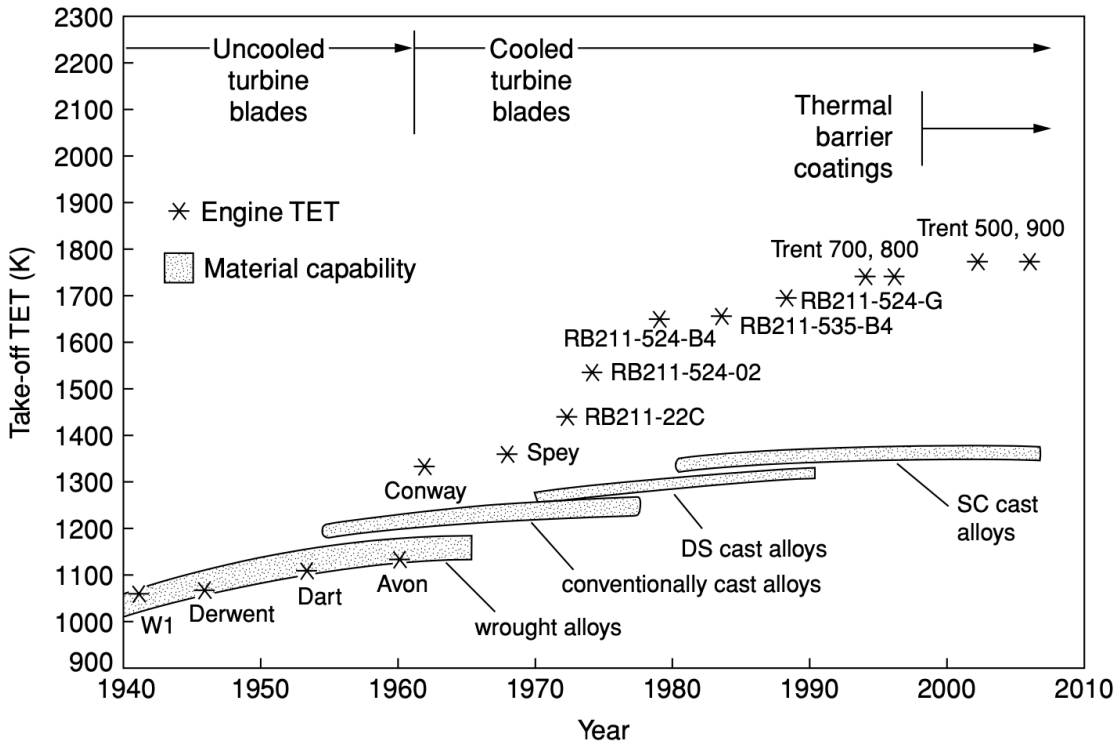

Figure 1.1. Evolution of material capability, processing innovation, and take-off turbine entry temperature (TET) of Rolls-Royce's civil gas-turbine engines [9].

1.1 The turbofan engine

Most modern commercial aircraft are powered by turbofan engines such as that shown schematically in Figure 1.2. A typical turbofan engine consists of a fan at the front of the engine and a core engine formed of several compressor stages, a combustor, and high- and low-pressure turbine stages. As with other jet engines, turbofans produce thrust by capturing ambient air, compressing it, mixing it with fuel, igniting it, and expanding the resulting hot gas through an exhaust nozzle [10].

The distinctive feature of turbofans is that part of the air captured by the fan passes through the engine without entering (bypassing) the core section. Since the velocity of the bypassed airflow increases as it goes through the fan, the fan is effectively acting as a propeller. The remaining air goes through the core engine and undergoes the flow process outlined above: first, the compressor squeezes the

air and increases its pressure and potential energy. Secondly, air is mixed with fuel in a combustor and ignited, producing hot expanding gases at up to 1700°C. The hot gases expand through a turbine, where they pass through several stages of blades making them rotate. The turbine is connected with the front fan and the compressor through a shaft; hence, the mechanical work extracted at the turbine serves to move these components. Finally, the resulting airflow is exhausted through a nozzle to produce thrust; often, the hot air is mixed with the cold bypassed air prior to exhaustion in order to reduce noise. By combining a high-velocity jet of hot exhaust gas and a propeller to generate thrust, turbofans have higher propulsive efficiency than conventional turbojets [11–14].

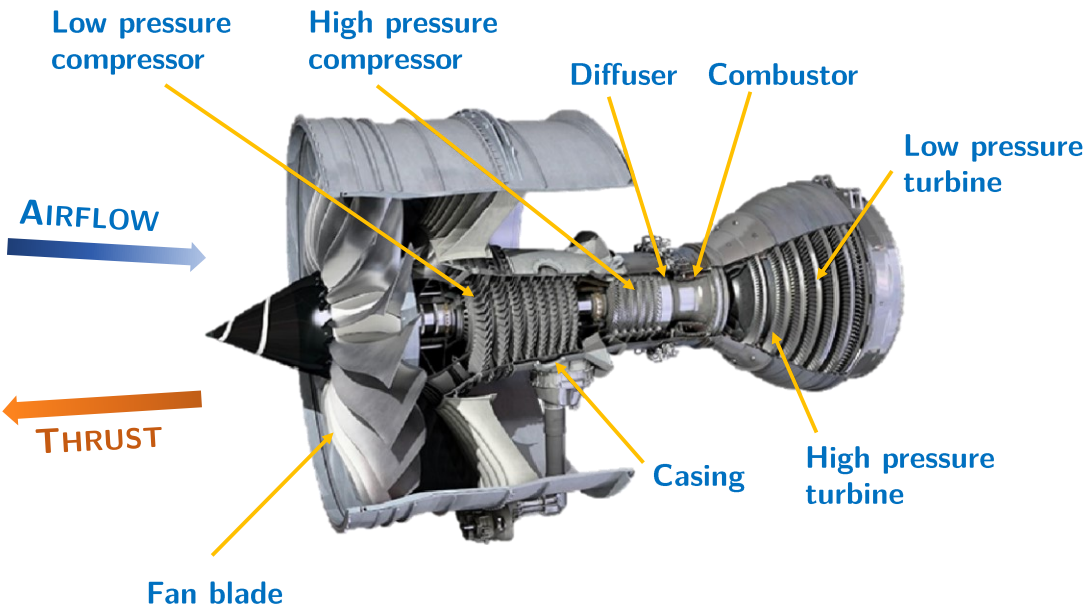

Figure 1.2. Impression of a Rolls-Royce Trent 1000 gas turbine engine. Adapted from [15].

1.1.1 Turbine discs

Turbine discs are the components that provide fixturing for the turbine blades and connect them to the engine shaft. Discs rotate at more than 10,000 revolutions per minute and are thus subject to very high rotational stresses. Stresses are maximum at the bore, where they are as high as 1000 MPa. But

unlike turbine blades, which are exposed to temperatures of up to 1800°C, discs operate in a relatively cool environment. The temperature at the rim of a high-pressure turbine disc is typically in excess of 650°C and decreases towards the inner diameter. To reduce heat conduction from the blades, both sides of the disc are exposed to a flow of cooling air [9,13].

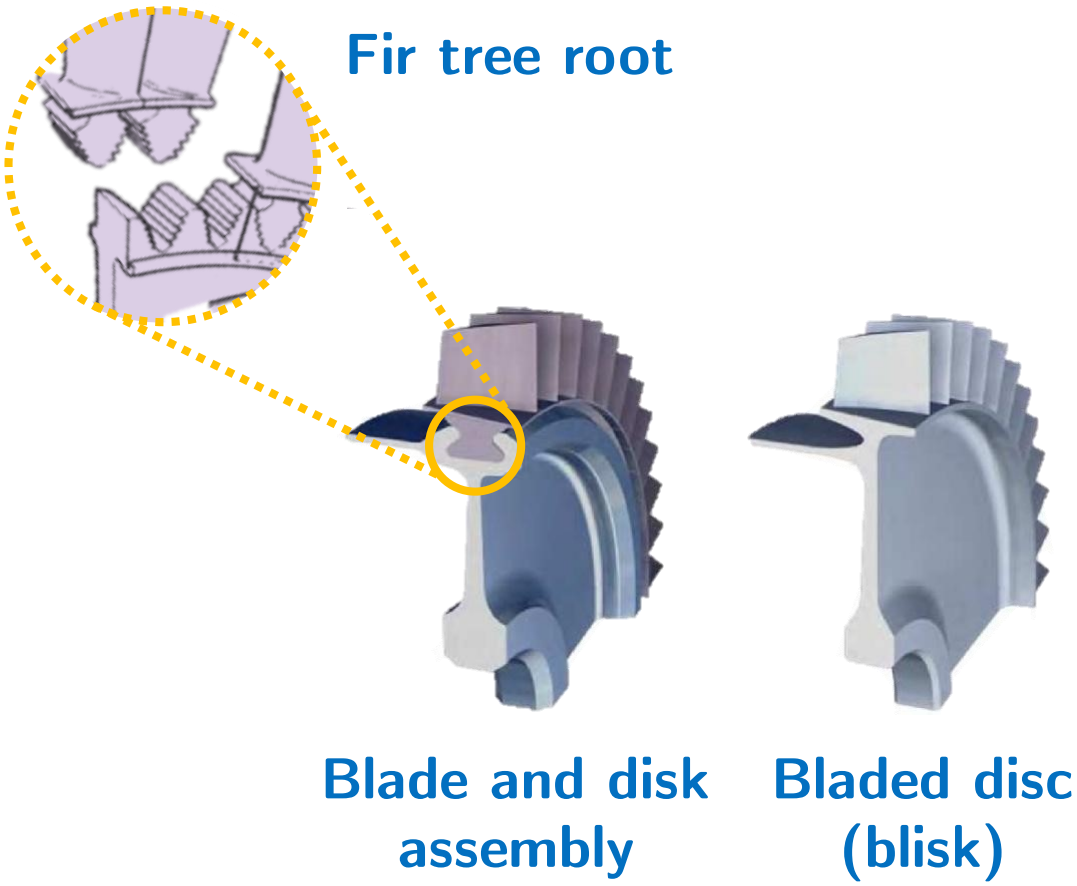

Figure 1.3. Impression of two methods of attaching blades to turbine discs. Adapted from [14,16].

Discs are commonly made of polycrystalline nickel-based superalloys. Ideally, their microstructure should account for the differences in thermal and mechanical loading along the radial direction. At the rim, where temperature is higher and stress lower, coarse grain microstructures are required for good creep and fatigue crack growth resistance. Conversely, fine grain microstructures are favourable at the bore, where temperature is relatively low and tensile stresses significant [9,17,18]. Discs are either manufactured as part of an integral shaft

assembly or joined with the shaft via a bolted flange. Similarly, the blades can be linked directly to the rim or attached with a 'fir-tree' fixing (Figure 1.3). Since the stress at the fixing and the blade root is relevant to the maximum rim speed, the method of fixing the blades is a critical design feature [13,19].

1.2 Problem description

The manufacturing of nickel-based superalloys turbine discs is complex, costly, and energy intensive. Whereas extensive efforts have been devoted to improving their temperature and mechanical in-service capabilities, many manufacturing hurdles remain unsolved. For example, a typical 5kg compressor disc processed conventionally via vacuum melting and cold forging requires an initial billet of approximately 95 kg; that is, 94% of the material is discarded along the process [7]. Although a comprehensive life-cycle assessment of gas turbine discs is lacking, an estimate can be readily obtained. In 2019, Rolls Royce delivered 510 large engines, and in 2020 it had a 12% share of the global commercial engines market [20,21]. Thus, manufacturers deliver ~ 4250 new engines per year for the civil aviation sector. A modern civil turbofan like Rolls-Royce's Trent 800 can have up to seven turbine stages accounting for ~ 20% of its total weight (6078 kg) [9,22]. The CO_2 footprint associated with primary production of typical nickel-based superalloy forging stock is 13 kg/kg – 18.3 kg/kg [23]. Assuming that the 94% figure quoted above applies to turbine discs, the CO_2 footprint attached to the discarded material totals ~ 1.5 Mt of CO_2 per year. This is equivalent to 0.15% of aviation's yearly CO_2 emissions [24], and it excludes the CO_2 footprint attached to reprocessing or disposing of the waste material. Since significant environmental and economic benefits can be gained from reducing energy consumption and waste, process optimisation is an urgent task.

Superalloys for turbine discs are processed via two distinct routes: ingot metallurgy (I/M) and powder metallurgy (P/M). The powder metallurgy route is

more complex and costly, so it is typically reserved for highly alloyed (i.e. highly γ' reinforced) grades where cracking and macro-segregation make conventional ingot metallurgy thermo-mechanical working unviable [7,9,25]. In exchange for higher costs, powder metallurgy alloys can increase the strength of discs by up to 10%; this allows increasing the rotational speed of the discs, hence boosting efficiency [13]. Alloys processed via ingot metallurgy are commonly referred to as cast-and-wrought (C&W) alloys.

Both ingot and powder metallurgy include forging steps. However, the forging of superalloys is particularly difficult, since they are designed to resist deformation up to very high temperatures [26]. Cast-and-wrought superalloys tend to have very narrow processing windows but can often be conventionally hot die forged [27]. Highly reinforced grades cannot normally be hot die forged and require isothermal forging. Isothermal forging significantly increases the processing costs, particularly when combined with powder metallurgy. Consequently, there is a continuing interest in researching if alloys that are currently isothermally forged can be hot die forged [28].

More recently, there has been a growing interest in high γ' content cast-and-wrought alloys, such as René 65, Udimet 720, and Udimet 720Li [29–33]. These alloys sit on the limit of the cast-and-wrought process capability [32] and bridge the gap between current ingot and powder metallurgy grades. They can be processed through conventional ingot metallurgy but can operate at temperatures higher than 650°C – the upper limit of the widely used Alloy 718 [29,30,33]. In this context, an ideal alloy is one which combines hot die forgeability with the highest γ' volume fraction possible. However, the forging of high γ' content cast-and-wrought alloys is not without hitches. Udimet 720Li is difficult and expensive to process due to its 45% γ' volume content [32]. Udimet 720 – a similarly composed alloy – has a rather limited forging window, even when forged isothermally [34].

The hot die forging of high γ' content cast-and-wrought alloys remains largely unexplored. So far, the efforts to optimise thermo-mechanical processing routes have been primarily empirical [35]. This may be due to the complexity of replicating industrial hot die forging in laboratory-scale testing. Accordingly, most research on the hot-workability of these alloys is focused on their isothermal forging, mostly using processing maps [28,34,36–40]. Similarly, several studies have analysed the microstructural evolution of Udimet 720, Udimet720Li and GH4720Li during forging, but not surface and internal cracking. This is despite the relevance of cracking in industrial practice, where it is a major cause for rejecting forged parts [41].

1.3 Thesis outline

The aim of this research project is to study the hot die forgeability of high γ' content cast-and-wrought polycrystalline nickel-based superalloys. The focus is on surface cracking, with the objective of elucidating the relationship between processing conditions, microstructural evolution, and the occurrence of surface cracking during hot die forging. The commercial alloy Udimet 720 is studied as a representative of this class of materials.

This thesis is structured as follows: the literature review in Chapter 2 introduces the physical metallurgy of superalloys, with particular emphasis on the relationship between microstructure and mechanical properties. The two main manufacturing routes of turbine discs are discussed, followed by a review of hot-temperature behaviour and forgeability in superalloys. The experimental methods and techniques used are described in Chapter 3. Chapter 4 explores the microstructural evolution of Udimet 720 within a prospective hot working window via thermal analysis, heat treatments, and electron microscopy examinations. In Chapter 5, the forging of a model full-scale turbine disc is studied via finite element analysis to understand and estimate the evolution of the relevant thermo-mechanical variables. Subsequently, in Chapter 6 a hypothesis is proposed on how

surface cracking is controlled by the dissolution and reprecipitation of the secondary γ' phase. A novel thermo-mechanical testing method is proposed to assess hot-forgeability under different processing conditions, and an experimental matrix is designed for Udimet 720 based on the FEA full-scale forging simulations. The results of these experiments are shown and discussed in Chapter 7. The thermo-mechanically tested specimens are analysed in Chapter 8 via fractography, electron microscopy, EDX microanalysis, and crystal orientation mapping. Possible deformation and fracture mechanisms at play are described and linked to the hypothesis. In Chapter 9, full-scale forging tests on Udimet 720 and laboratory-scale tests on another alloy – René 65 – are used to further validate the hypothesis. Finally, the conclusions of this study are presented in Chapter 10, followed by possible future work proposals.

2

Literature review

Superalloys are high temperature structural materials. They can be defined as metallic alloys which display excellent mechanical and environmental resistance at high homologous temperatures ($T_h = T/T_m$, where T_m is the melting point). They show significant resistance to creep, optimal static properties (yield stress, ultimate tensile strength, fracture toughness), good fatigue behaviour, and substantial oxidation resistance [7,9].

In gas-turbine engines, superalloys are the material of choice in sections where the temperature surpasses 700°C. Up to this temperature, titanium is an alternative on account of its lower weight. Below 540°C, less costly high-strength, creep-resistant ferritic steels can be used (Figure 2.1A). In turn, superalloys are iron-nickel-, cobalt-, and nickel-based. Iron-nickel alloys can withstand lower temperatures than nickel- and cobalt-based alloys, but they are less expensive and have lower thermal expansion coefficients. Cobalt-based superalloys are sometimes used in place of nickel-based superalloys depending on the strength and corrosion resistance requirements. Nickel-based superalloys are suitable for the hottest applications as they can be used at 800–1000 °C for long periods of time (Figure 2.1B) [7,9,42–44]. Against this backdrop, the question of why nickel makes an optimal solvent for superalloys arises naturally.

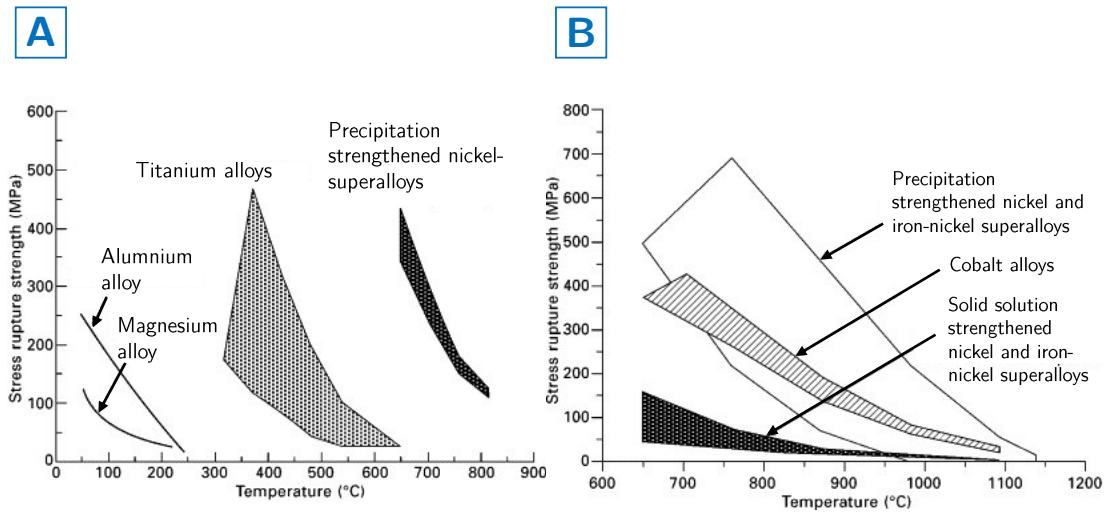

Figure 2.1. (A) Stress rupture strength curves (time not specified) for typical aerospace materials [42]. (B) Stress rupture strength (100h) for nickel-, cobalt-, and iron-nickel-based superalloys hardened by solid solution strengthening or precipitation strengthening [42,44].

2.1 Physical metallurgy of nickel-based superalloys

2.1.1 Alloying elements

Nickel is a transition metal with a face-centred cubic (FCC) structure. FCC crystals have four {111} non-parallel closed-packed planes with three ⟨110⟩ closed-packed directions each. These account for 12 slip systems and grant FCC crystals with high ductility. Nickel has a rather high melting point: $T_m = 1455°C$. It preserves its FCC structure from room temperature up until its melting point, precluding the undesirable expansions and contractions associated to phase transformations. Nickel also has considerable toughness thanks to the high cohesive force of its outer d-electrons bonds [9].

However, pure nickel cannot provide the outstanding properties required of superalloys. Nickel-based superalloys often contain as many as fourteen alloying elements – mostly transition metals and significant amounts of chromium and aluminium. Some alloying elements reside within the γ nickel phase in solid

solution, while others promote the formation of beneficial second phases. Alloying elements can be broadly classified as follows [7,9]:

I. **Cobalt**, **iron**, **chromium**, **rhenium**, **tungsten,** and **molybdenum** all have similar radii to nickel, so they tend to reside in the γ phase. They stabilise γ and serve one or several purposes, such as solid solution strengthening (Mo, W, Co, Fe, Cr, Re) or oxidation resistance (Cr) [7,45].

II. **Aluminium, titanium, niobium, and tantalum** have greater radii than nickel and promote the formation of ordered phases such as Ni_3(Al, Ta, Ti). This phase is known as γ' and is crucial to attain good mechanical properties, particularly at high temperatures. When in solid solution, aluminium provides oxidation resistance, and titanium enhances hot corrosion resistance [7].

III. **Carbon and boron** have very different radii from nickel and tend to segregate to the grain boundaries of the γ phase. In certain concentrations they are present as monolayers covering the grain boundary, but they often appear as distinct carbide and boride phases. They are called 'grain boundary strengtheners' since it is believed that they inhibit grain boundary sliding (GBS), enhancing creep performance [9,46,47]. However, the mechanism behind this beneficial effect remains highly contentious [48,49].

    (a) **Cr**, **Mo**, **W**, **Nb**, **Ta**, and **Ti** promote the formation of carbides.

    (b) **Cr** and **Mo** also promote the formation of borides.

IV. **Zirconium, and hafnium** are added due to their strengthening effects on grain boundaries, other than promoting the formation of carbides and borides [7].

Additionally, there might be several harmful tramp elements that have been associated to a reduction of properties – such as sulphur, phosphorus,

nitrogen, silicon, lead, tellurium, selenium, and especially bismuth. These cause damage through various mechanisms. Some (Pb, Bi, Te) migrate to grain boundaries promoting grain boundary decohesion and cause significant drops in ductility, creep, and stress rupture. Others (N) create micro-porosity. In the case of bismuth, concentrations as small as 0.2 ppm can cause a 20% loss of ductility [7,50,51].

Table 2.1 shows the composition of five common superalloys: the γ''-strengthened Alloy 718, its improved version ATI 718Plus®, the γ'-strengthened cast-and-wrought alloys René 65 and Udimet 720, and RR100. The latter is a powder metallurgy alloy used in gas turbine discs. It is observed that there are significant compositional differences in γ' promoting elements (Ti, Al, Nb) and those which favour its precipitation (Co).

Table 2.1. Compositional ranges of five commercial nickel-based superalloys (wt. %) [9,33,52–54].

Alloy	**Cr**	**Co**	**Mo**	**W**	**Nb**	**Al**	**Ti**
Inconel 718	19.0	-	3.0	-	5.1	0.5	0.9
ATI 718Plus®	18.0	9.0	2.75	1.0	5.45	1.45	0.7
René 65	16.0	13.0	4.0	4.0	0.7	2.1	3.7
Udimet 720	17.9	14.7	3.0	1.25	-	2.5	5.0
RR1000	15.0	18.5	5.0	-	1.1	3.0	3.6
Alloy	**Ta**	**Fe**	**Hf**	**C**	**B**	**Zr**	**Ni**
Inconel 718	-	18.5	-	0.04	-	-	Bal
ATI 718Plus®	-	10.0	-	0.020	0.006	-	Bal
René 65	-	1.0	-	-	0.016	0.05	Bal
Udimet 720	-	-	-	0.035	0.033	0.03	Bal
RR1000	2.0	-	0.5	0.027	0.015	0.06	Bal

The chemistry of superalloys strongly affects their properties [9,55–57]. For example, some studies indicate that the antiphase boundary (APB) energy in γ' – a crucial parameter for its strengthening effect – is very sensitive to alloy composition [58,59]. However, nickel-based superalloys are highly complex chemical systems, and there are no undisputed guidelines for chemistry selection. The classification above should therefore be understood as an outline of trends. Alloying elements interact in complex manners, making the outcome of adding or removing elements difficult to predict. Molybdenum partitions preferentially to the γ phase and strengthens the alloy by solid solution. But it also changes the lattice misfit and the coarsening kinetics of γ' precipitates, impacting the mechanical behaviour at high temperature [60]. Figure 2.2 shows that increasing concentrations of molybdenum elevate the solvus temperature of the γ' phase [61].

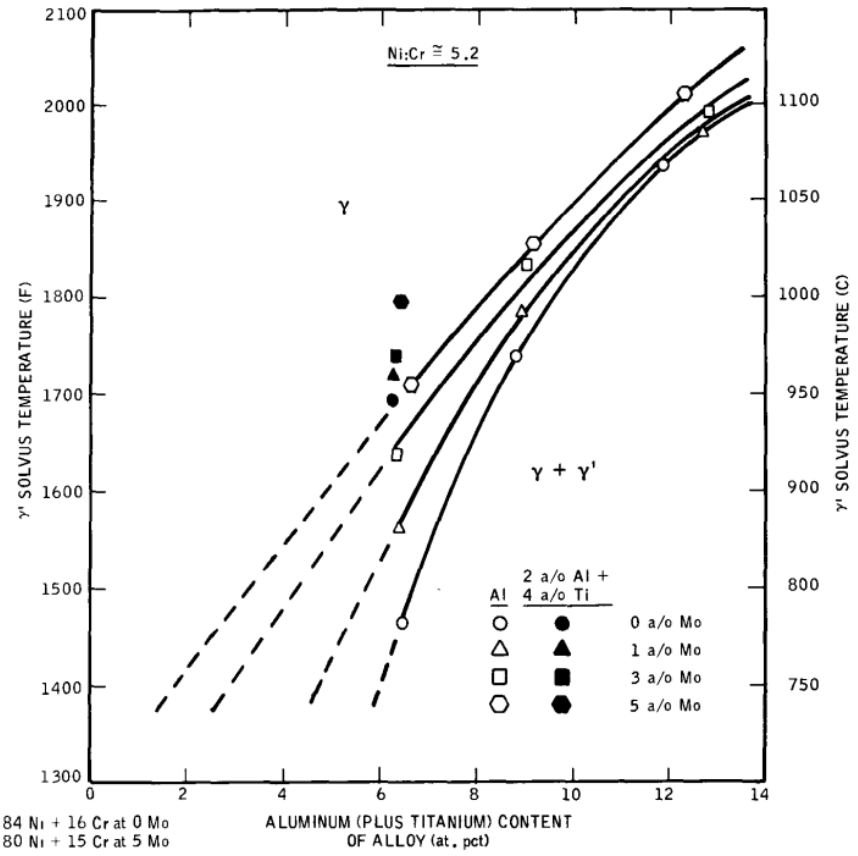

Figure 2.2. Influence of molybdenum, titanium, and aluminium (N.B. a/o stands for atomic percent) on the γ' solvus temperature of Ni-Cr-Al systems for alloys with a Ni:Cr ratio of approximately 5.2 [61].

2.1.2 Microstructure and phases

The mechanical behaviour of superalloys is controlled by the distribution, size, and morphology of its microstructural features. In turn, the microstructure is determined by the alloy's chemistry and processing path. Since the microstructure is key to attaining the highest properties, understanding the processing-microstructure-property relationship is of the utmost importance [7,62].

The microstructure of a typical nickel-based superalloy consists of up to four types of phases: a gamma phase (γ) matrix, gamma prime precipitates (γ'), carbides and borides, and topologically close-packed (TCP) intermetallic phases. What follows is a discussion of the structure and composition of these phases and how they govern the macroscopic behaviour of nickel-based superalloys. The defects present in each phase are discussed in Section 2.1.3, since they are crucial to explain the mechanical behaviour of superalloys [3].

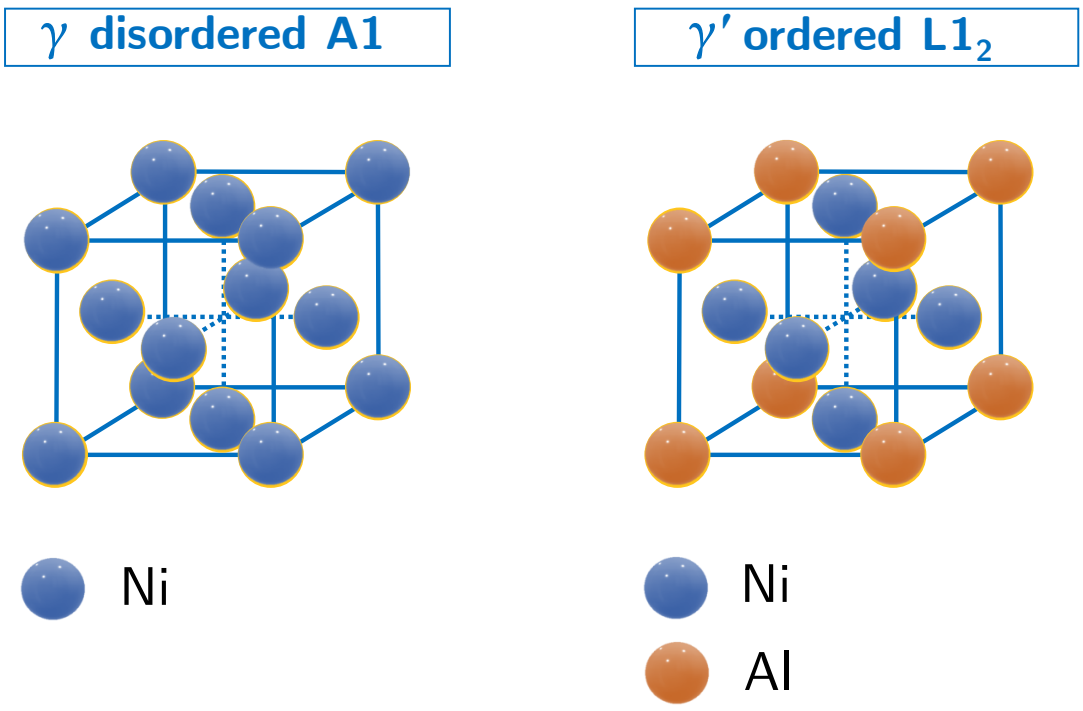

Figure 2.3. Diagram showing the unit cells of the FCC γ and $L1_2$ γ' phase.

I. The gamma phase (γ)

In most nickel-based superalloys, the γ-phase constitutes a continuous matrix where other phases reside. It consists of nickel atoms and typically a significant amount of alloying elements in a disordered FCC structure (Figure 2.3). Section 2.1.1 describes the properties that make γ an ideal matrix for superalloys. Alloying elements can significantly shift its melting (liquidus and solidus) temperatures: Re, W, Ru, and Co raise it; while Al, Mo, Ta, Ti, C, and B depress it [9,53,59].

II. The gamma prime phase (γ')

Nickel and aluminium have the same crystal structure, so mutual solid solubility could be expected. Conversely, the Ni-Al system shows non-FCC phases with significant chemical order – i.e. there is a significant degree of directional covalent bonding and precise stoichiometric relationships between the number of nickel and aluminium atoms in each unit cell. More precisely, crystal structures where lower energy Ni-Al rather than Ni-Ni or Al-Al bonds are preferred. Among these phases, the most relevant is the gamma prime (γ') phase (Ni_3Al), since it confers significant strength to nickel-based superalloys.

The γ'-phase displays a primitive cubic $L1_2$ (Strukturbericht designation) crystal structure with Al atoms at the cube corners and Ni at the centres of the faces. Each Ni atom has four Al atoms as closest neighbours, and each Al atom is coordinated by twelve Ni atoms. Other elements can be present in the gamma prime phase. Co and Pt substitute Ni, Ti and Ta substitute Al, and in rare cases – e.g. Cr, Fe, and Mn – a mixed behaviour is observed. This behaviour depends strongly on their size relative to Ni and Al [9]. It has been proved that γ' remains ordered up to approximately its melting point of $T_m = 1375°C$, although the stoichiometry and the presence of impurities can change these two temperatures [9,63,64].

Interface coherency and lattice misfit

The coherency of the γ/γ' interphase affects the properties of superalloys. The lattice parameters of γ and γ' are very similar: $a_{\gamma'} = 3.570$ Å and $a_{\gamma} = 3.517$ Å at room temperature. Consequently, γ' precipitates often remain coherent with the matrix and display a distinct cube-cube orientation with low energy interfaces ($\gamma_{\gamma/\gamma'} \sim 20$ mJ / m^2) along {100} planes [9,65,66].

There is an interplay between the lattice misfit (δ) and the size and morphology of γ' precipitates. A polydisperse γ/γ' mixture is not in its lowest energy state. In the absence of external stress, the system will reduce its interfacial area to reach equilibrium in a processed called Ostwald ripening. This normally happens by increasing the size of larger particles at the expense of dissolving smaller ones [67]. However, particle coarsening also depends on the γ/γ' lattice misfit. The total energy of a coherent particle is the sum of its interfacial energy, the elastic energy due to the γ/γ' misfit, and the elastic energy associated with interactions between particles. Precipitate coarsening implies a loss of coherency. Doi and Miyazaki [68] suggested that when the misfit is high, the coarsening rate decreases with time due to a change in the driving force from surface energy to elastic interaction energy. They confirmed this result by comparing large misfit Ni-Cu-Si alloys with low misfit Ni-Si-Al and Ni-Cr-Al alloys [9,68,69]. The shape of γ' precipitates is also affected by the lattice misfit. At sufficiently high temperatures, small spherical precipitates grow into cubes to minimise coherency strains. The rate at which this happens depends on the magnitude of δ. In high misfit alloys, the morphology changes occur at smaller precipitate sizes on account of their higher coherency strains. Low misfit precipitates retain their spherical shape until they reach larger sizes [65,69,70].

Morphology and size

The strengthening effect of γ' is also crucially dependent on the size and distribution of the precipitates – hereafter particle size distribution (PSD) – as

well as their chemical composition. Polycrystalline alloys for turbine discs normally contain a bimodal or trimodal distribution of precipitates. Large precipitates of 1 to 5 µm termed primary γ' (γ'_p) reside at the grain boundaries of the γ phase. They are generally incoherent with the γ matrix and serve for pinning the grain boundaries during thermo-mechanical processing (see Section 2.4.2). Smaller secondary ($\gamma'_s \sim 100$ nm – 500 nm) and tertiary ($\gamma'_t < 50$ nm) precipitates exist within the γ grains and are responsible for the bulk of the γ' strengthening [69,71–75]. Figure 2.4 shows a sample of Udimet 720 displaying all three populations of γ'.

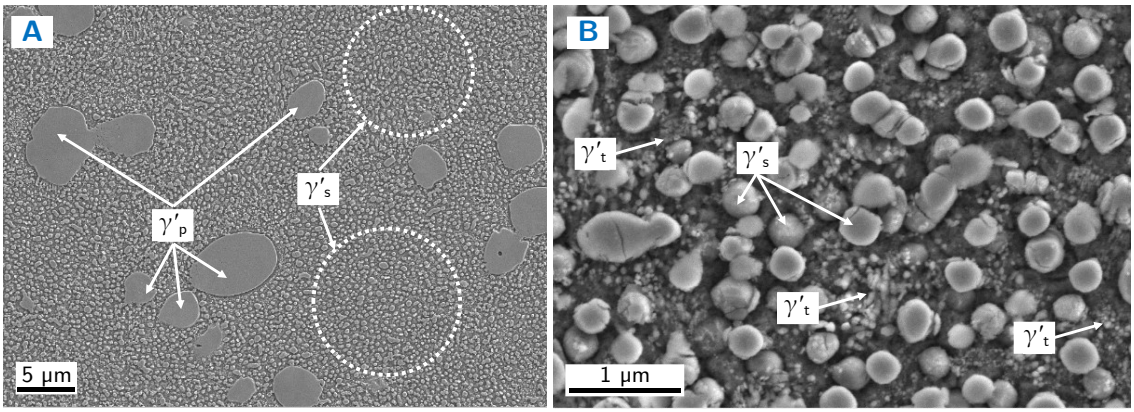

Figure 2.4. Scanning electron microscope (SEM) micrographs showing a trimodal distribution of γ' – primary (γ'_p), secondary (γ'_s), and tertiary (γ'_t) – in Udimet 720. (A) Low magnification; (B) high magnification.

The PSD and phase chemistry can be engineered with heat treatments and by controlling the temperatures and cooling rates during thermo-mechanical processing [76,77]. γ'_p forms at high temperature below the γ' solvus. Once present, γ'_p remains largely unaltered when alloys are heated below the solvus, as it is often the case in forging. By contrast, γ'_p is absent after annealing at super-solvus temperatures and cooling at sufficiently rapid rates (~ 10°C/min in Chen et al. [76]). γ'_s and γ'_t develop through multiple nucleation bursts at different temperatures upon cooling; they are the result of an interplay between nucleation, growth, and coarsening kinetics of γ'. The drop in temperature provides the driving force for new precipitates to nucleate from the supersaturated matrix. At

sufficiently slow cooling rates, γ' forming elements have enough time to diffuse into the newly formed γ'_s precipitates, and a bimodal ($\gamma'_p + \gamma'_s$) distribution results. But when the cooling rate is high, the diffusion time is cut short, and several supersaturation and nucleation events occur. This gives rise to a trimodal ($\gamma'_p + \gamma'_s + \gamma'_t$) precipitation structure, where intragranular precipitates are smaller and more narrowly size distributed. At even higher cooling rates, low γ' content alloys have been reported not to form intragranular precipitates. Since the relative amount of γ' forming elements in the matrix tends to change as cooling and reprecipitation develop, successive populations of γ' often have different chemical compositions [75,76,78].

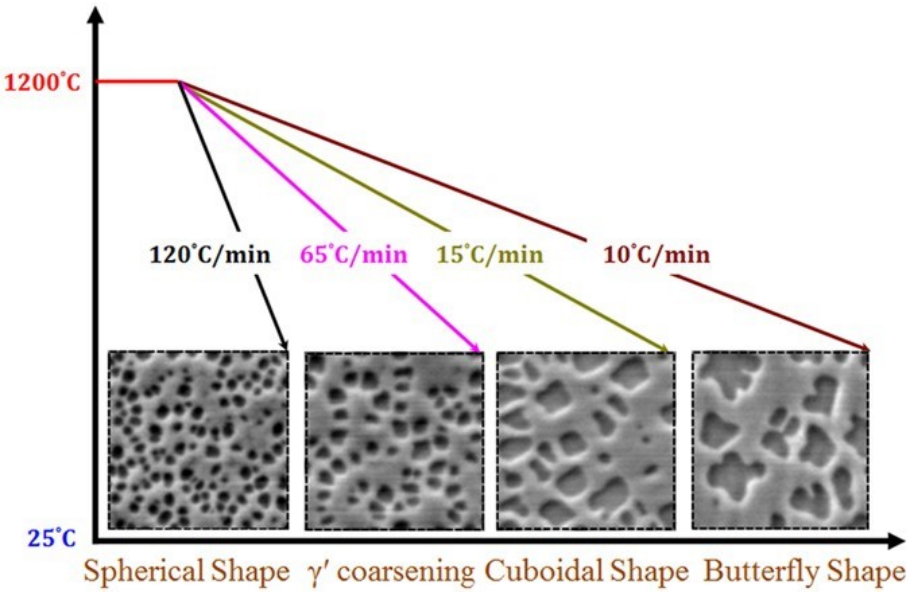

Figure 2.5. Diagram showing SEM micrographs of AD730™ samples heated above the γ' solvus and cooled down at different cooling rates [78].

The morphology of γ' precipitates also depends on the cooling rate. Masoumi et al. [78] studied the morphology of γ' upon cooling from super-solvus temperatures in AD730™ (Figure 2.5). Their results showed that high cooling rates of 120°C/min resulted in spherical precipitates, whereas coarser cuboidal and butterfly precipitates were observed at slower cooling rates (15°C/min and 10°C/min). This agrees with the findings of Ricks et al. [65] in a number of alloys during ageing. They noted that irrespective of the lattice misfit, precipitates

evolved upon coarsening in the sequence: sphere, cubes, arrays of cubes, and finally solid-state dendrites, as shown in Figure 2.6.

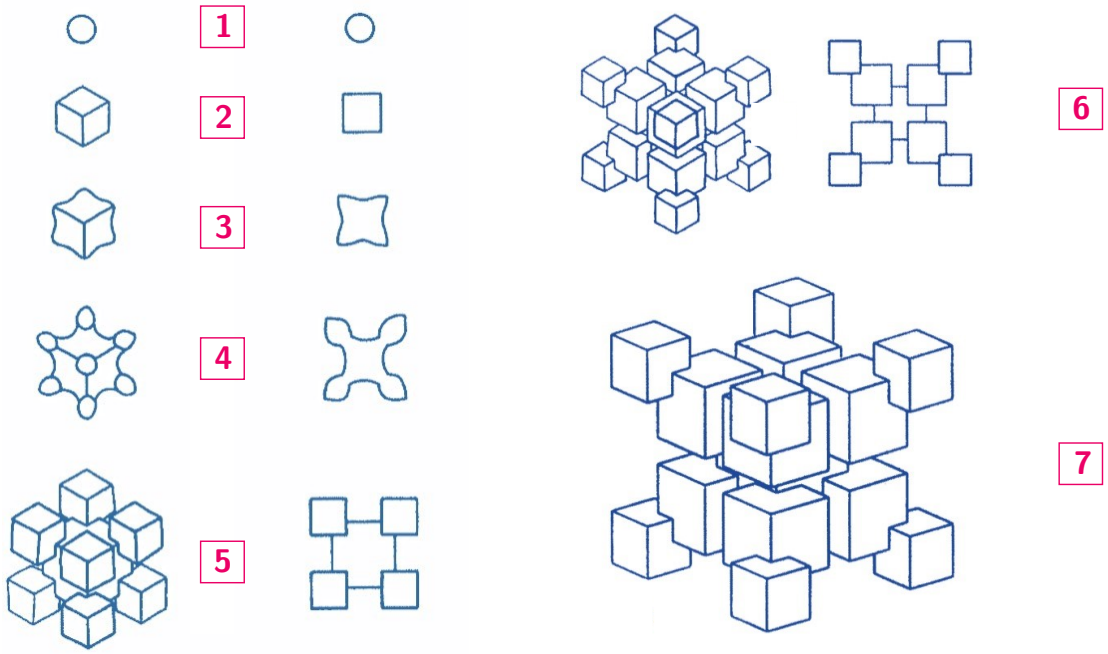

Figure 2.6. Schematic diagrams of the development from (1) to (7) of γ' precipitates during ageing. Left: projection along ⟨111⟩; right: projection along ⟨001⟩. Adapted from [65]

III. Other phases

Gamma double-prime phase (γ''): Certain nickel superalloys with significant amounts of niobium – such as Alloy 718 – are primarily strengthened by coherent precipitates of γ''. This phase displays a body-centred tetragonal (BCT) $D0_{22}$ crystal structure and a composition $Ni_3(Nb,Al,Ti)$ [7,9,79]. γ'' precipitates are disc shaped and are typically coherent with high coherency strains. The large lattice misfit makes the formation kinetics of γ'' much slower than γ'. The reinforcing effect of γ'' is a function of the coherency and the distortion introduced by its tetragonal axis (c-axis), where the matrix-precipitate misfit is concentrated.

Delta phase (δ): The transformation of γ'' into the brittle, thermodynamically stable δ phase imposes an upper limit on the use of γ''-strengthened alloys; for

Alloy 718, this limit is approximately 650°C [80,81]. δ shows an orthorhombic $D0_a$ crystal structure and a Ni_3Nb stoichiometry. It is always incoherent with the matrix and therefore does not strengthen the alloy, even when present in high quantities [9,52,81]. This phase can be beneficial for grain size refinement when present in small amounts at the grain boundaries [7,82].

Eta phase (η): η is a generally undesirable phase with a hexagonal close-packed (HCP) ordered $D0_{24}$ crystal structure. It is found in nickel-, iron-nickel-, and cobalt-based superalloys with high Ti/Al ratios after extended thermal exposures [83,84]. It exists in its stoichiometric composition, Ni_3Ti. η typically appears as large platelets in a Widmanstätten pattern or at the grain boundaries in a cellular form, and it is non-coherent with the matrix [83]. Accordingly, its presence is generally associated to a degradation of the mechanical performance. However, certain alloys like ATI 718Plus® rely on carefully precipitated distributions of η to control the grain size and strengthen the grain boundaries [85].

Carbides and borides: Small quantities of grain boundary elements such as C and B are present in the chemistry of polycrystalline superalloys on account of their grain-boundary strengthening properties. These additions significantly enhance their mechanical performance, namely their creep strength, ductility, and low-cycle fatigue behaviour [46,86]. The most relevant of these species are MC, M_6C, $M_{23}C_6$ (Figure 2.7), M_7C_3, and M_3B_2, where M denotes one of the aforementioned metals. Certain carbide phases or morphologies are undesirable. For example, $M_{23}C_6$ carbides in a continuous or discontinuous-cellular (zipperlike) morphology are detrimental for ductility and rupture life [7].

TCP phases: Topologically close packed (TCP) phases are undesirable phases that share several features. They have very high atomic packing density; large and complex crystallographic structures; and a degree of directional, non-metallic bonding. Precipitation of TCPs ensues when excessive amounts of beneficial elements (particularly refractory metals) such as Cr, Mo, W and Re are added in

excessive quantities. TCPs thereby form as extensive plates, highly coherent with {111} planes of γ and γ' [49]. TCPs are known to notably undermine the mechanical performance of nickel-based superalloys [7,9,87,88]. This is a consequence of their lack of ductility, which makes them sites for crack initiation [89], and their tendency to remove solid-solution strengthening elements from the matrix [88,89].

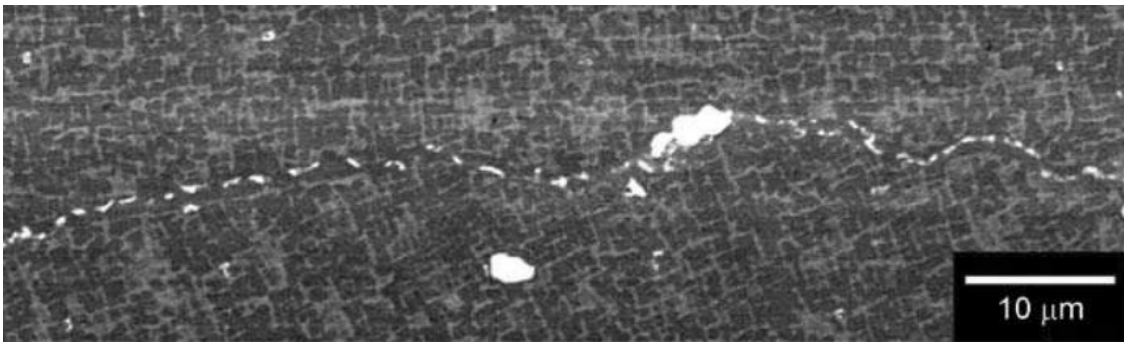

Figure 2.7. $M_{23}C_6$ carbides at the grain boundary of a second-generation single-crystal superalloy [9].

2.1.3 Deformation and strengthening mechanisms

Several deformation mechanisms have been identified in γ' strengthened nickel-based superalloys. These include dislocation glide in γ, dislocation shear (weakly and strongly coupled) in γ', Orowan looping, cross-slip of superdislocations in γ', climb-assisted glide within the γ matrix, and twinning [90–94]. Normally, time-independent athermal yielding occurs from ambient temperature to $\sim 700°C$ via dislocation shear or Orowan bypassing of γ' precipitates. Time-dependent creep deformation dominates at high temperatures ($\gtrsim 850°C$) or low strain rates and is associated with climb-assisted glide [95]. At intermediate temperatures of $\sim 650°C - 850°C$, a time-dependent, viscous deformation mode termed microtwinning is known to operate [93,96].

The deformation mechanisms in highly γ' reinforced single crystal nickel-based superalloys have attracted significant interest (Figure 2.8) [93,97–99].

Research on lower γ' content polycrystalline grades for discs is sparser, although several studies exist [35,97,100]. What follows is a brief review of these deformation mechanisms and their relationship with crystallographic defects and microstructural features.

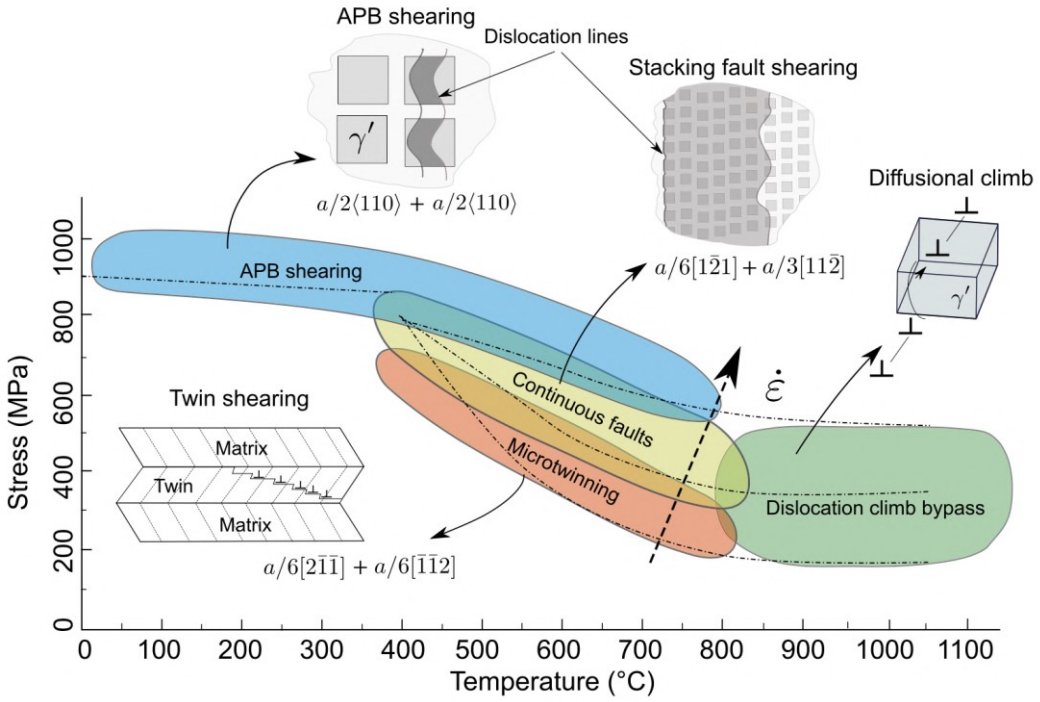

Figure 2.8. Deformation mechanism map for a single crystal nickel-based superalloy illustrating the dominant deformation mechanisms as a function of the stress, temperature, and strain rate [93].

I. Dislocation glide

Dislocation glide – or slip – is the movement of dislocations on their slip plane. It is the main method of deformation in the γ matrix of nickel-based superalloys [92,101]. Macroscopically, plastic deformation in FCC metals occurs by gliding of dislocations with Burgers vector $a/2\langle 1\bar{1}0\rangle$ on $\{111\}$ planes. But micromechanically, perfect dislocations dissociate as per Eq. 2.1 into two partial dislocations known as Shockley partials.

$$\frac{a}{2}\langle 110\rangle\ \{\bar{1}11\} \rightarrow \frac{a}{6}\langle 211\rangle\ \{\bar{1}11\} + \frac{a}{6}\langle 12\bar{1}\rangle\ \{\bar{1}11\} \qquad 2.1$$

Partial dislocations do not displace atoms by a lattice vector. Therefore, a passing Shockley partial does not leave behind a perfect crystal but a local stacking fault. A perfect FCC lattice is equivalent to a stack of close-packed planes with a periodicity of three (ABCABCABC...). Two consecutive planes are displaced by a/6, where a is the length of the side of a unit cell. A stacking fault arises when the stacking sequence is altered by either removing a plane (ABCA[ ]CABC) or inserting an extra plane (ABCACBCABC) – see Figure 2.9. The former is called intrinsic stacking fault and creates locally a hexagonal close-packed (HCP) structure (ABCACABC); the latter is called extrinsic stacking fault and generates two HCP planes (ABCACBCABC) separated by an FCC plane (ABCACBCABC) [9,102]. In the case of Shockley partials, a stacking fault is created by the passage of the first partial. The second partial annihilates it as it glides past it and restores the original crystal structure.

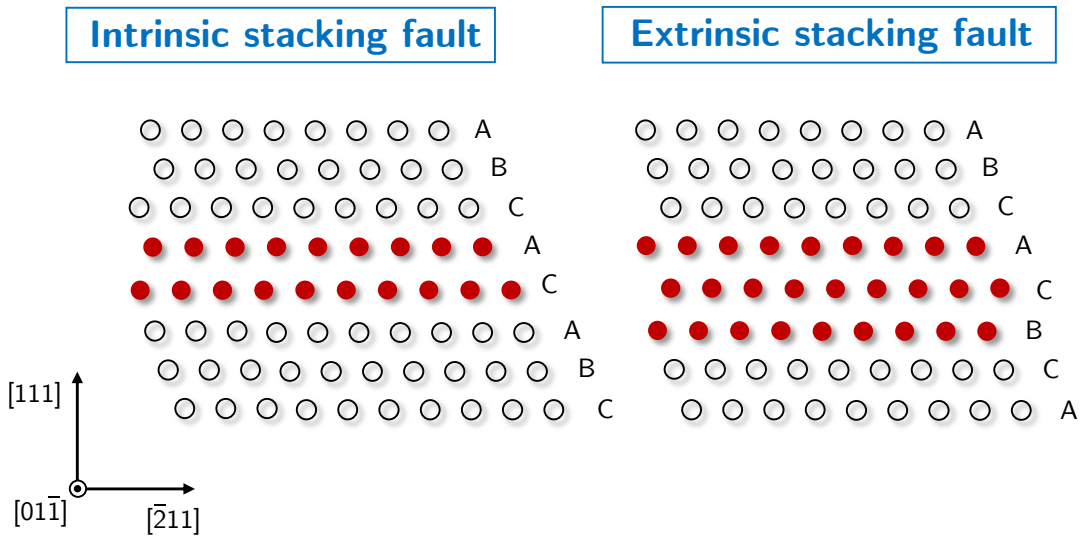

Figure 2.9. Illustration of an intrinsic and an extrinsic stacking fault in an FCC lattice. The planes shown are close packed {111}. Adapted from [103].

Dissociation has important implications in dislocation dynamics, particularly at high temperatures. The dissociation of a/2⟨1$\bar{1}$0⟩ dislocations into Shockley partials is energetically favourable on account of Frank's rule; this states that the elastic energy per unit length of a dislocation is directly proportional to the square of the magnitude of its Burgers vector [104]. The distance between two

Shockley partials is determined by the balance of energy between their elastic repulsion energy and the stacking fault energy (SFE) [105]. The repulsive elastic interaction energy decreases as partial spacing increases, while the SFE decreases with decreasing partial spacing. Thus, high stacking fault energies can reduce partial spacing. Nickel has an SFE of $\sim 240\ \mathrm{mJ/m^2}$, although it is highly dependent on the presence of alloying elements [9,106–109].

II. Dislocation shear

Dislocation glide in the γ' precipitates is termed particle shear. γ' deforms significantly differently from the γ matrix where it resides. In γ, the shortest lattice vectors $a/2\langle 1\bar{1}0\rangle$ reside in the closed-packed planes $\{111\}$. In the $L1_2$ lattice, the close-packed planes are the same, but the lattice vectors are $a\langle 100\rangle$ and do not lie in them. Thus, it is not immediately obvious what the preferred slip system is: $a\langle 110\rangle\{001\}$, $a/2\langle 1\bar{1}0\rangle\{001\}$, or $a\langle 1\bar{1}0\rangle\{111\}$, but it is clear that $a/2\langle 1\bar{1}0\rangle\{111\}$ dislocations are not perfect in γ' [9].

When $a/2\langle 1\bar{1}0\rangle\{111\}$ dislocations enter γ' precipitates, they create planar defects termed antiphase boundaries (APBs). APBs are generated by shearing one $\{111\}$ plane in a perfect $L1_2$ crystal by $a/2\ \langle\bar{1}01\rangle$ (i.e. the vector that links Ni and Al atoms), as shown in Figure 2.10A [97,110]. The number of Ni-Al bonds is considerably lower in the vicinity of the APB, since 'incorrect' Ni-Ni and Al-Al exist. Consequently, the creation of an APB is associated with a significant energy penalty ($\gamma_{\mathrm{APB}} \sim 250\ \mathrm{mJm^{-2}}$ – $350\ \mathrm{mJm^{-2}}$ [111]). APBs can also lie on $\{110\}$ or $\{001\}$ planes, but these are associated with different γ_{APB} [112–114].

The closure vector required to restore the γ' lattice to its perfect state is twice the Burgers vector of a single $a/2\langle 1\bar{1}0\rangle$ dislocation. Consequently, these dislocations travel in pairs in γ': the leading dislocation creates an APB, and the trailing dislocation restores order (Figure 2.10B,C). Each of these dislocations is called superpartial, and a pair of superpartials separated by an APB constitute a superdislocation. Superdislocations typically reside in the same precipitate on

account of the high value of γ_{APB}. This arrangement is called strong coupling and is observed especially when the γ' precipitates are large. When the γ' precipitates are small, superdislocations can be spaced by several faulted particles and are said to be weakly coupled [35,115].

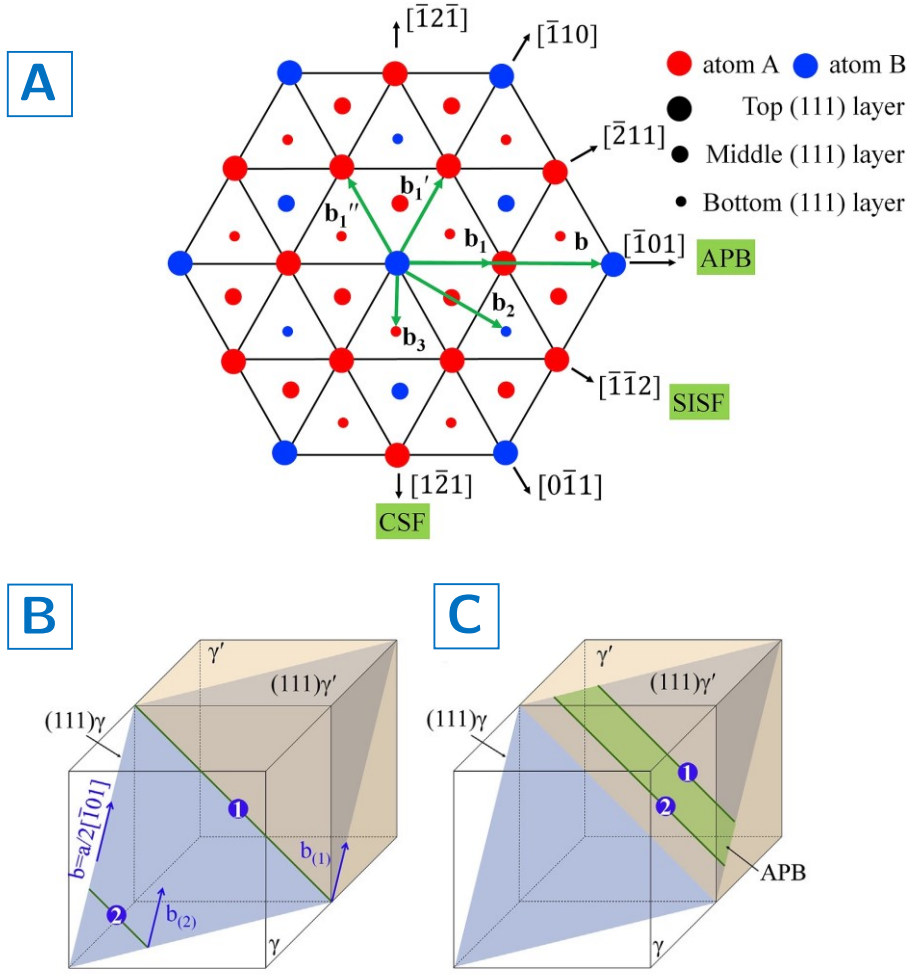

Figure 2.10. (A) Schematic of the [111] projection of {111} planes in the $L1_2$ γ' phase structure, showing the formation of different types of planar defects in the γ'-phase. (B) Schematic diagram of the formation of APBs by a/2⟨1$\bar{1}$0⟩{111} dislocations gliding on γ and γ'. Adapted from [110].

Dislocations in the γ'-phase $L1_2$ superlattice dissociate into partial dislocations in the same way as a/2⟨1$\bar{1}$0⟩{111} dislocations do in γ. Besides, APBs are one of four planar defects identified in the γ' phase – together with complex stacking faults (CSF), superlattice intrinsic stacking faults (SISF), and superlattice extrinsic stacking faults (SESFs). CSFs, SISFs, and SESFs are formed

by shearing {111} planes by a/6⟨$\overline{1}\overline{1}$2⟩, a/3⟨$\bar{2}$11⟩, and a/3⟨$\overline{2}\overline{1}$1⟩ respectively (Figure 2.10A). Since various planar faults exist in the $L1_2$ structure, complex dislocation dissociations are possible; the interested reader is referred to [9,112] for further information on these reactions. CSFs, SISFs, and SESFs have been noticed to arise upon γ' shearing by various dislocation systems in the intermediate temperature range ($\sim$ 650°C to $\sim$ 815°C) [97]. As these faults are also associated with significant energies, they impart resistance to γ' shearing and contribute to strengthening the alloy.

Precipitation strengthening

Biphasic γ/γ' alloys show considerably higher yield strengths than γ or γ' systems alone, both at room and high temperature. While solid solution strengthening is partially responsible for it, the γ/γ' synergy causes most of this strengthening [7,91,115–117]. Precipitation strengthening is mainly ascribed to the formation of high energy planar defects by gliding dislocations (order strengthening), the coherency strain induced γ' by precipitates (coherency strengthening), and a particular mechanism linked to cross-slip (Kear-Wilsdorf).

The strengthening effect of the γ' phase depends on its volume fraction (f) and PSD. Classic γ' strengthening models are limited to unimodal distributions of γ' precipitates. They are based on the well-established fact that dislocations glide in pairs to cut through γ' particles and consider two cases: weak coupling and strong coupling. Weak coupling occurs when the volume fraction and particle size of γ' is low and is normally observed in underaged samples. It denotes the configuration where the spacing of the two superpartials is large compared to the precipitates; so, fully faulted particles exist in the space between superpartials. In strong coupling, the spacing of superpartials is comparable to the size of γ' particles, meaning that superdislocations can reside within any given particle. Strong coupling occurs when precipitates are large, for example in over-aged condition [9,115,118,119].

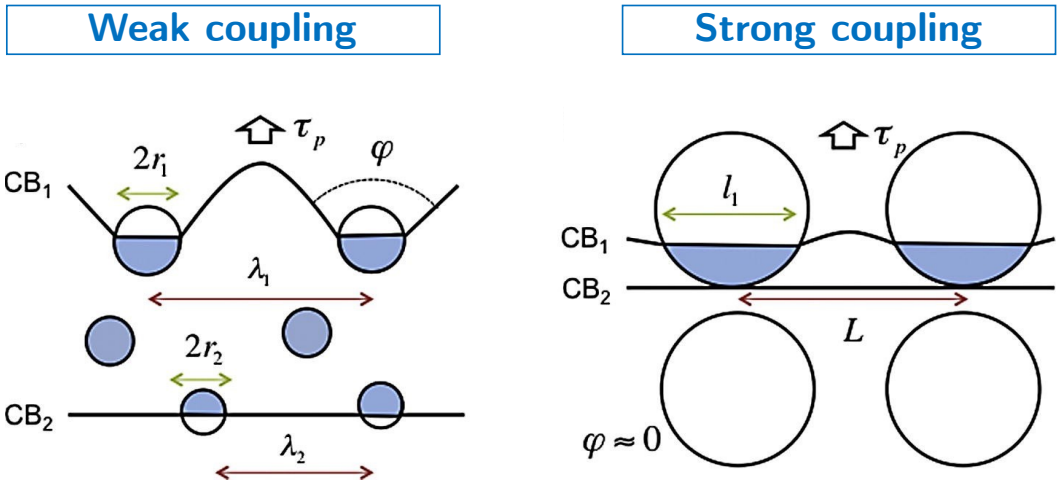

Figure 2.11. Weak and strong coupling in the classical precipitation hardening model for γ/γ' alloys. Adapted from [91].

The main difference between both situations lies in the length of the bowing dislocations, which determines the force a precipitate of a given size can resist. In turn, this is controlled by the bowing angle φ. In weak coupling, the leading dislocation controls the start of γ' shearing. The dislocation is pinned by γ' particles and must bow ($\varphi < 180°$) to develop a component of line tension in the gliding direction. Conversely, the controlling stress in strong coupling happens when the trailing superpartial reaches the precipitate, and φ for the leading dislocation is $\sim 180°$. The critical resolved shear stress (CRSS) due to weakly paired dislocations (τ_{wc}) and strongly coupled dislocations (τ_{sc}) are given by Eq. 2.2 and 2.3, where b is the magnitude of the Burgers vector, $\hat{r}$ is the mean particle radius, $\hat{T}$ is the line tension ($\sim$ ½ μ b^2), w is a dimensionless constant of order of unity, and μ is the shear modulus. The reader is referred to [9] for a detailed derivation of these equations.

$$\tau_{wc} = \frac{\gamma_{APB}}{2\,b}\left(\frac{6\,f\,\hat{r}\,\gamma_{APB}}{\pi\,\hat{T}}\right)^{1/2} - f \qquad 2.2$$

$$\tau_{sc} = \sqrt{\frac{3}{2}}\left(\frac{\mu\,b}{\hat{r}}\right) f^{1/2}\,\frac{w}{\pi^{3/2}}\left(\frac{2\,\pi\,\hat{r}\,\gamma_{APB}}{w\,\mu\,b^2} - 1\right)^{1/2} \qquad 2.3$$

The classical precipitation hardening model proves to a first approximation that in unimodal size distributions, optimum hardening lies at the transition

between weak and strong coupling. This has been confirmed by experimental observations. It must be noted that the precipitate size corresponding to optimum hardening depends on both f and γ_{APB}. Reppich et al. [120,121] studied the behaviour of alloys PE16 ($\gamma_{APB} = 0.125$ J/m^2) and Nimonic 105 ($\gamma_{APB} = 0.110$ J/m^2) following different heat treatments (Figure 2.12). The optimum precipitate size was 26 nm – 30 nm for PE16 and 55 nm – 85 nm for Nimonic 105. For Udimet 720Li, Jackson and Reed [122] found that the maximum theoretical critical resolved shear stress occurred at ~ 40 nm. Collins and Stone [119] predicted that for RR100 in the range 600°C – 700°C, maximum yield strength corresponded to precipitates of 34 nm – 57 nm.

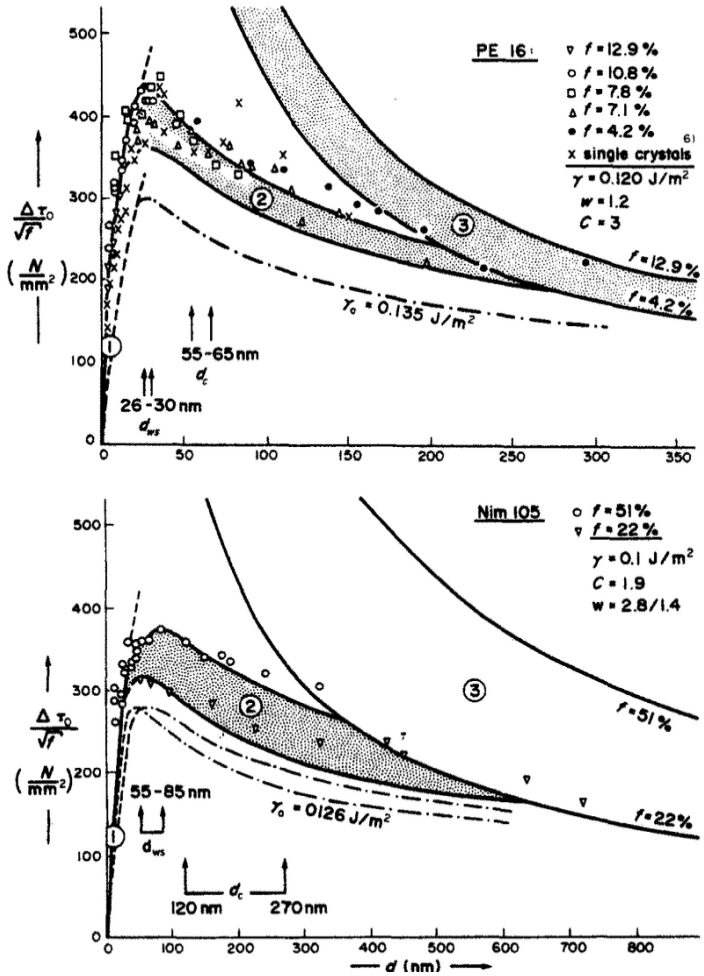

Figure 2.12. Critical resolved shear stress (divided by the square root of the volume fraction of the particles) versus mean particle diameter for Nimonic PE16 and Nimonic 105. Regime 1 corresponds to weak coupling, regime 2 to strong coupling, and regime 3 to the Orowan mechanism. The peak strength occurs at the transition from weak to strong coupling [9,91].

However, the actual behaviour is more complex than this simplified model. Galindo-Nava et al. [91] noted inaccuracies of this model for both weak and strong coupling, as well as the incompatibility of the weak and strong pair models in the transition regime, where both models should converge. They developed a new model for the yield stress in P/M superalloys. This model accounts for multimodal distributions of γ' and reconciles the incompatible weak and strong models using an intermediate dislocation pair-coupling configuration. Using this model, they determined that tertiary γ' size and volume fraction are the crucial parameters which define the yield stress (σ_Y). It was suggested that maximum strength in multimodal distributions corresponds to r_t = 10 nm – 15 nm and $f_t \geq 10\%$, where r_t is the radius and f_t is the volume fraction of tertiary γ' precipitates. Additionally, it was found that yield stress is only marginally higher for alloys with unimodal and fine γ' sizes.

Achieving high static yield strength via γ' precipitation strengthening needs to go together with appropriate creep and fatigue strength. There is strong evidence linking the volume fraction of tertiary γ' and creep behaviour [29,123,124]. Locq et al. [125] studied the creep behaviour of the P/M alloy NR3 at 700°C. They concluded that fine tertiary γ' distributions impede dislocation motion and confer the alloy strong resistance against creep deformation. Smaller γ' precipitates are also known to result in higher dwell-time fatigue crack propagation (FCP) [126]. Thus, Galindo-Nava et al. suggested that besides having a certain amount of primary γ' to prevent grain growth, a secondary and tertiary γ' structure is desirable since it improves ductility, fatigue, and creep behaviour at the expense of small yield stress decrements.

III. Orowan looping

The Orowan mechanism (also referred to as Orowan looping or bowing) describes a process by which dislocations bypass rather than shear gamma prime particles. Orowan looping is believed not to be a prevalent deformation mode in nickel-based superalloys. This is attributed to the generally small size and high

volume fraction of the γ' precipitates, the low γ/γ' misfit, and the complex multimodal precipitation structures [35,115]. However, this contradicts the findings of other authors [127,128]. Preuss [35] reported that Orowan loops have rarely been observed in polycrystalline nickel-base superalloys, and it is widely thought that cutting of strongly coupled dislocations is the predominant deformation mechanism in coarse (< 400 nm) γ' precipitates.

IV. Twinning

Deformation twinning entails the homogeneous movement of atoms in a crystal structure to generate a band where atoms are oriented as a mirror image with respect to the parent lattice [129,130]. Traditionally, deformation twins were assumed to arise by highly coordinated atom displacements resulting in the simple shear of the original lattice. This orderly mechanism is unlike the seemingly chaotic dynamics of dislocation glide. However, some authors [129] have questioned this hypothesis: it has been proposed that twins thicken by coalescence of embryonic twins that nucleate on twin boundaries, within grain boundaries, and within slip bands. This idea implies that deformation twins contain many stacking faults and is consistent with the fact that FCC materials with high SFE (like aluminium) do not normally twin [129].

Twinning and dislocation glide are considered the main deformation mechanism at low homologous temperatures, when diffusion effects are not significant. Many researchers believe that twinning is necessarily accompanied by glide [129]. In particular, twinning in FCC metals only happens after substantial deformation by glide. Deformation twins have also been frequently observed at high strain rates, following the general equivalence of high strain rates and low temperatures in thermally activated processes [129,131,132].

In nickel-based superalloys, it is well established that microtwinning occurs in the $\sim$ 650 to 850°C temperature range [93,96]. However, there is very

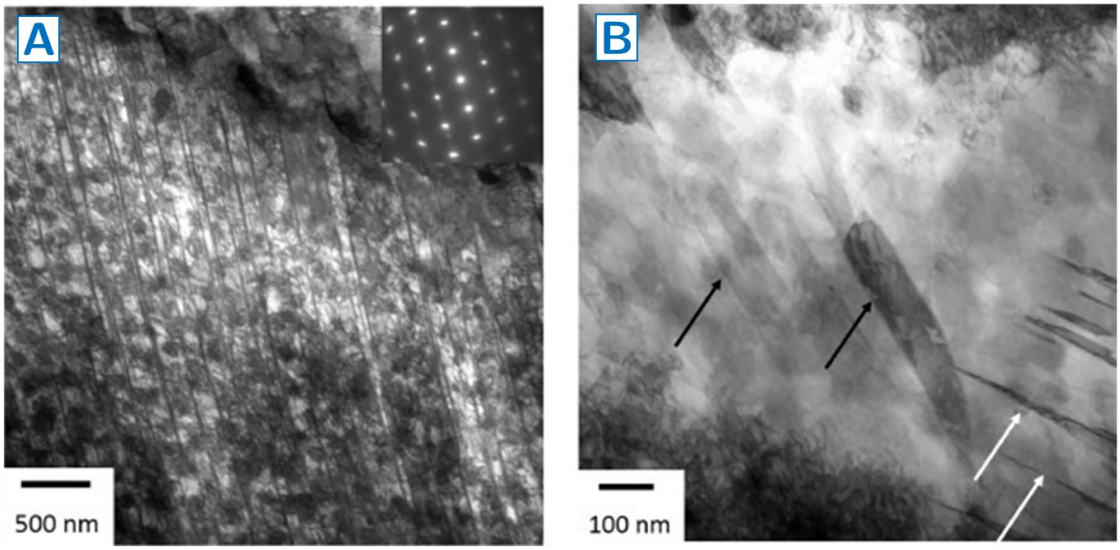

Figure 2.13. ATI 718Plus® samples deformed at 850°C with a strain rate of 1.0 s^{-1} showing: (A) deformation twinning and high dislocation density; (B) deformation twins on two different slip systems [94].

limited research on deformation twinning of high temperature alloys at typical hot die forging temperatures (> 800°C) and strain rates ($\dot{\varepsilon} \sim 0.1\ s^{-1}$) [94]. Pu et al. [133] conducted high temperature compression tests on the UNS10276 alloy; they found deformation twins in specimens deformed at 950°C and 1100°C at a strain rate of 10 s^{-1}. Fahrmann and Suzuki [134] studied the forgeability of Udimet 720 via Gleeble tension tests. They annealed polycrystalline samples at 1100°C and cooled them down at rates of 0.03°C/s ('slow cooling') or 30°C/s ('fast cooling') to testing temperatures of 950°C – 1100°C, prior to deformation at $\dot{\varepsilon} \sim 1\ s^{-1}$. The fast-cooled samples deformed at 1010°C showed twin bands of thickness 10 nm – 30 nm that seemed to penetrate the γ' precipitates. Since little sign of dislocation glide was observed, it was assumed that twinning was the main deformation mechanism in this condition. This was attributed to the presence of very fine γ' precipitates (~ 40 nm) that hindered dislocation motion and triggered microtwinning. The most comprehensive study of deformation twinning in hot die forging conditions is by Kienl et al. [94] on ATI 718Plus®. Deformation twins were found in all samples compression tested at temperatures of 850°C – 1025°C (below and above the γ' solvus) and strain rates 0.01 s^{-1} – 1 s^{-1}, as shown in Figure 2.13. They concluded that this was due to the low SFE of the alloy.

Importantly, no difference was detected in twinning at super-solvus temperatures, but samples deformed below the solvus showed more propensity to twinning. This is consistent with Fahrmann and Suzuki's hypothesis on the role of γ' in controlling twinning in these conditions.

V. Other mechanisms

Dislocation cross-slip: Dislocation cross-slip in FCC metals is the process by which screw dislocations switch from a {111} plane to another one that contains the direction of their Burgers vector. Cross-slip is possible since pure screw dislocations, unlike edge and mixed dislocations, do not have a unique slip plane [135]. Cross-slip activates when dislocation pile-ups impede the motion of the cross-slipping dislocation on its slip plane [136,137].

Dislocation climb: Dislocation climb refers to the non-conservative movement of dislocations out of their slip plane along the γ/γ' interfaces. It is considered a key mechanism in creep deformation of superalloys [138–141]. Climb involves the diffusion of atoms and vacancies to and away from the dislocation site to create small steps called jogs. Climb then develops by the generation and motion of these jogs along the dislocation line. As all diffusion processes, climb is highly dependent on the temperature and is enhanced at high temperatures [142–144].

Grain boundary sliding: Grain boundary sliding (GBS) describes the motion of grains relative to each other in a polycrystalline metal. This happens at high homologous temperatures by plastic flow at the grain boundaries. GBS is one of two main deformation mechanisms controlling creep in nickel-based superalloys, together with dislocation glide and climb. But whereas the latter mechanism dominates at high temperatures and stresses, GBS is preeminent at lower stresses and temperatures [42].

2.2 Turbine disc manufacturing

Superalloys are typically processed by three different methods: investment casting (I/C), ingot metallurgy (I/M), or powder metallurgy (P/M). Both I/M and P/M involve forging steps. I/C is used in very highly alloyed compositions to avoid excessive cracking during forging, and to produce directionally solidified and single crystal parts. Turbine discs are normally manufactured via I/M or P/M, whereas I/C is used to produce turbine blades [9,25,145].

The first step of both I/M and P/M is the production of large ingots of material, normally via vacuum induction melting (VIM) [146]. VIM is a more costly route than conventional (EAF/AOD) melting, but it provides better control of alloying elements and significantly enhances the micro-cleanliness of the alloy by reducing the presence of oxides, nitrides, and tramp elements such as lead and bismuth [9,146].

VIM starts by charging raw materials into a refractory crucible kept under vacuum. The raw materials typically include virgin, scrap, and reactive materials. Scrap comes from both melting and component manufacturing, while reactive materials include strong oxide and nitride formers (like aluminium and titanium) that can only be added to the melt after degassing the virgin portion. Then, carefully selected currents are passed through water-cooled copper coils that surround the crucible. This allows heating and electromagnetic stirring without eroding the inner surface of the crucible. Once all portions are charged and the appropriate chemical adjustments are made, the melt is poured into a mould under a partial pressure of argon. More than thirty elements can be removed or refined through VIM [9,146].

As-cast VIM ingots do not yet possess suitable properties and need to go through several melting and thermo-mechanical working processes before they are ready to be forged or machined into their final shape. Once that an appropriately

solidified ingot is obtained, the processing route that ensues is dictated mainly by the chemistry of the alloy [9,25].

2.2.1 Ingot metallurgy

Ingot metallurgy is employed on lean alloys – like Alloy 718 and Waspaloy – with low levels of strengthening elements. These are commonly referred to as cast-and-wrought (C&W) alloys [25,32,146]. In this route (see Figure 2.14), secondary and tertiary meltings are carried out by vacuum arc remelting (VAR) and electro-slag remelting (ESR). This pursues three objectives. First, reducing the significant levels of macro-segregation found in as-cast VIM ingots. Secondly, refining the population of refractory ceramic particles originated from the refractory lining. Finally, suppressing the solidification pipe, cracks, and porosity [9].

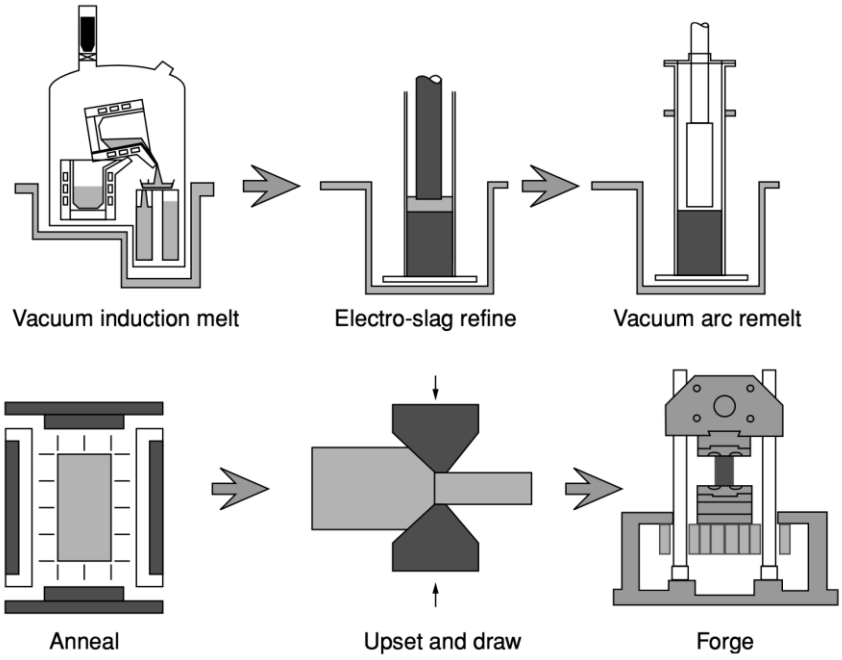

Figure 2.14. Schematic diagram showing the processing steps for producing turbine discs via ingot metallurgy [9].

In vacuum arc remelting (VAR), direct current is passed through a consumable electrode – a VIM/ESR casting – to the bottom of a water-cooled

crucible kept under vacuum. The heat generated by the arc between the electrode (cathode) and the pool of molten metal on top of the solidifying ingot melts the surface of the electrode, transferring material as droplets onto the crucible. VAR processing results in ingots with improved micro-cleanliness (especially tramp elements, oxygen, and nitrogen), and reduced macro-segregation and defects [9,147]. However, VAR can introduce inclusions, freckling, and white spots [147].

Electro-slag remelting (ESR) is similar to VAR, except that here molten droplets pass through a molten slag pool rather than vacuum. Additionally, an alternating current is used instead of direct current, and the heat source for melting the electrode comes from the slag. The molten material is exposed to the slag to allow certain chemical reactions which refine the material and reduce oxides and sulphur contents [7,148]. While a secondary (VAR) melting following VIM is enough for certain chemistries and applications, triple-melts (VIM + VAR + VAR or VIM + ESR + VAR) are used for attaining the highest levels of micro-cleanliness. In this case VAR always follows ESR, since ESR induces more defects in large ingots and results in greater chemical heterogeneity than VAR [9].

Once the material has gone through secondary and tertiary meltings, a sound, clean billet is obtained. These billets are still not suitable as an end of the line material, and thermal-mechanical working is required to break-down their microstructure, refine the grains, and reduce the still excessive levels of segregation [9]. Some alloys require homogenization heat treatments before hot working, while in others the heat cycle during hot working is sufficient to reduce compositional gradients [7].

Among the main hot working operations are cogging, extrusion, and rolling; these are schematised in Figure 2.15. Rolling is used to produce bars, sheets, and shapes, and it is remarkably challenging for superalloys. Extrusion is mainly used for powder consolidation in P/M alloys [7]. Cogging is a forging operation that entails reducing (typically halving) the diameter and increasing

the length of an ingot. The result of the cogging operation is a forged billet, and thus the whole process is called 'ingot to billet conversion'.

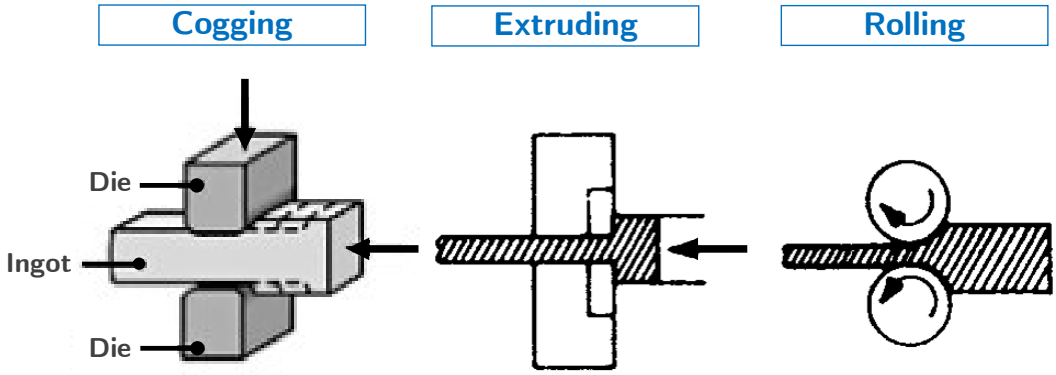

Figure 2.15. Schematic diagrams showing the three major thermal-mechanical working processes used to break-down an as-cast ingot. Adapted from [7,149].

The manufacture of gas-turbine discs normally involves cogging steps. Conversion by cogging consists of heating the ingot in a furnace and subsequently pressing it between two hydraulically driven dies. The combination of high deformation and high temperature triggers substantial dynamic and metadynamic recrystallisation, and results in a more refined microstructure. The process is then re-started in a series of cycles or 'heats' – as many as seven. They allow reducing the initially coarse ($\geq$ 10 mm) and often columnar grains to smaller and equiaxed $\sim$ 5 µm – 60 µm grains. The last heats are performed at temperatures below the solvus of the relevant grain-pinning phase to avoid grain growth [9,146,150].

Finally, the material is processed into its final shape via forging or ring rolling (see Section 2.4.2), followed by machining, a heat treatment to attain an appropriate distribution of reinforcing precipitates, and non-destructive evaluation (NDE) via ultrasonics.

2.2.2 Powder metallurgy

Not all nickel-based superalloys can be processed by the C&W route. Highly alloyed grades such as Astroloy, IN100, RR1000, and René 95 are prone

to cracking during melt and thermal-mechanical working. This is due to their greater levels of segregation in ingot form of elements such as W, Mo, Nb, Ti, and Ta; and their higher flow stress – and thereby lower ductility – at high temperatures [9,146,151]. The P/M route was developed to overcome these difficulties and is extensively used in superalloy production [7,152,153].

The P/M process (Figure 2.16) starts by remelting a VIM-produced stock ingot. This is followed by atomisation in an inert-gas atmosphere or vacuum, which effectively eliminates macro-segregation by cooling rapidly (10^2 K/s – 10^3 K/s) the molten material into small particles (30 μm to 300 μm). These particles are sieved to remove large, undesired inclusions and thereby improve the micro-cleanliness of the alloy. Next, the powder is loaded into a can, degassed, sealed, and consolidated into a billet or preform via hot isostatic pressing (HIP), extrusion, or a combination of both.

HIP entails heating the powders below or above the γ' solvus and keeping them under a hydrostatic pressure. These conditions trigger diffusion bonding and yield a fully dense product (typically a billet) after several hours, in a process termed sintering. If sintering is performed above the γ' solvus temperature, significant grain coarsening ensues [7,9,146]. One key aspect of sintering is avoiding pernicious prior particle boundary (PPB) precipitation [154–156]. Pollock and Tin [146] claimed that consolidation via hot extrusion is preferred on account of lessened PPB effects and the possibility of obtaining finer grains. This is disputed by Donachie and Donachie [7], who suggested that HIP is more advantageous because it allows obtaining products free of PPBs.

The remaining steps are analogous to the I/M route: forging (except in direct HIP), machining, and ultrasonic inspection. Hot or hot die forging are not normally suitable for these highly alloyed compositions with limited ductility, so isothermal forging often becomes a necessity. Isothermal forging involves maintaining both the workpiece and dies at identical temperatures along the

entire forging process. The combination of high temperature, very fine grains (thanks to P/M processing), and slow strain rates results in certain cases in superplastic flow. Superplasticity allows attaining near-net shape parts while controlling recrystallisation and grain growth [7,9,146,157].

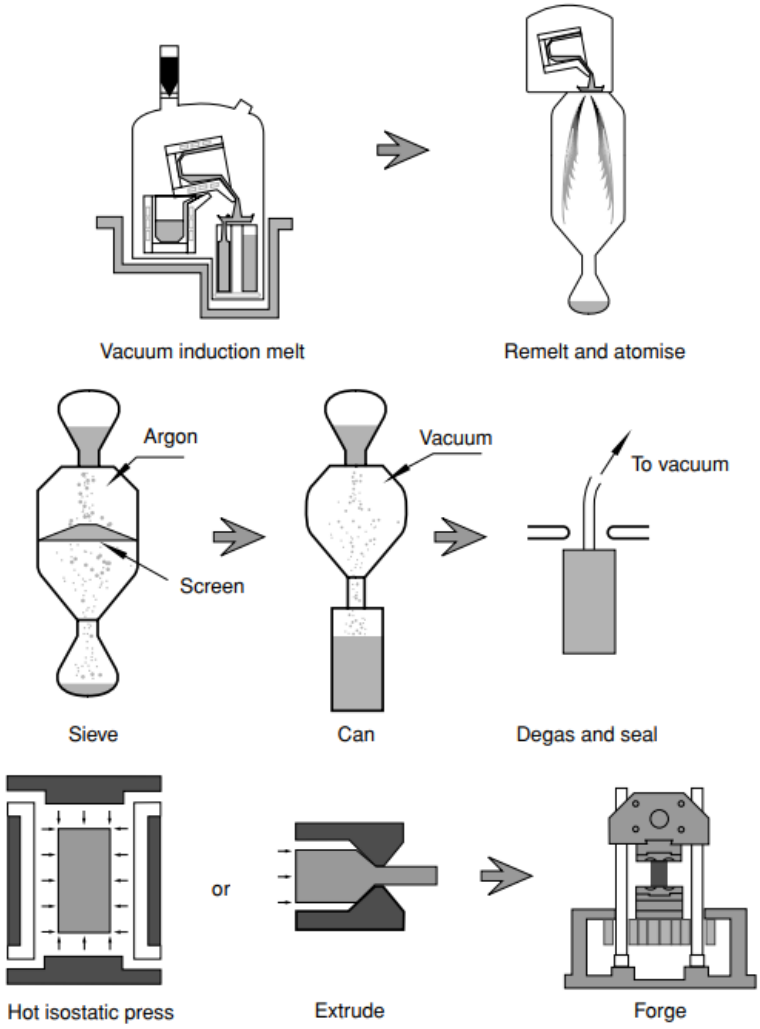

Figure 2.16. Schematic diagram showing the processing steps for producing turbine discs via powder metallurgy [9].

Overall, powder metallurgy has evolved into a well-established technique. It has proved to be advantageous in terms of input of raw materials and reduced number of forging and machining operations. However, it is a complex route and the costs associated to P/M nearly always exceed those of conventional C&W processing [151,158].

2.2.3 Bridging the gap: high γ' cast-and-wrought alloys

In addition to the well-established I/M and P/M grades, a new class of 'hybrid' alloys has attracted considerable attention recently. These are high γ' content cast-and-wrought alloys, such as Udimet 720, Udimet 720Li, René 65, and AD730™ [29–33].

Nearly 60 years after being patented, the cast-and-wrought Alloy 718 is still the most widely used nickel-based superalloy. It is extensively employed in turbine and compressor discs thanks to its ease and cost of manufacture, versatility, and remarkable properties [159–161]. However, Alloy 718 cannot operate at temperatures higher than 600°C – 650°C due to the coarsening of the γ' and γ'' strengthening precipitates and the formation of the deleterious δ phase [29,30,33]. There is hence a gap in temperature design space between Alloy 718 and P/M grades. High γ' content cast-and-wrought alloys aim to bridge this gap [29]. An ideal high γ' content cast-and-wrought alloy combines hot die forgeability with the highest γ' volume fraction possible.

In the quest for replacing Alloy 718, two main alloys were considered: Waspaloy and Udimet 720. Waspaloy has a higher temperature capability but a low $f_{\gamma'} \sim 26\%$ and lower yield strength than Alloy 718. By contrast, Udimet 720 and its derivative Udimet720Li have a high $f_{\gamma'} \sim 44\%$, and they have been successfully used for three decades now.

Efforts have also been devoted to developing new 718-type alloys. Such alloys would benefit from sluggish precipitation kinetics and a non-strengthening high-temperature phase (δ) for ease of hot working and grain refinement [162]. These efforts yielded positive results with ATI 718Plus®, an alloy mainly strengthened by γ' precipitation. It is claimed that this alloy increases the temperature capability of Alloy 718 by ~ 55°C with minimal losses in terms of yield strength, hot workability, weldability, and cost [163,164]. Yet Devaux et al. [30] argued that 718Plus cannot match the combination of cost and mechanical

properties combination of Udimet 720Li. 718Plus is less costly, but it behaves worse in creep at 700°C compared to Udimet 720Li. Another 718-type alloy is the newly developed VDM Alloy 780, which is claimed to increase by 100°C the temperature capability of Alloy 718 [162,165,166]. However, the limited number of studies for VDM Alloy 780 make difficult drawing a comparison between this grade and the aforementioned alloys.

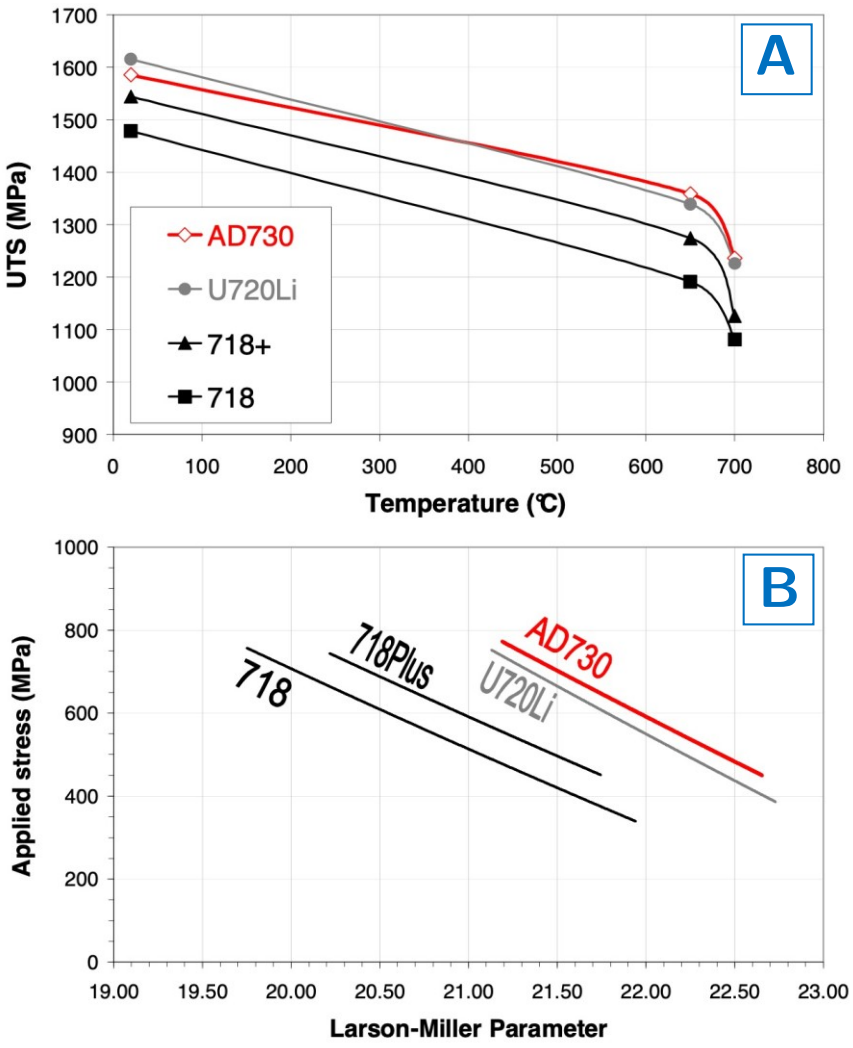

Figure 2.17. For various C&W superalloys: (A) Ultimate tensile strength versus temperature. (B) Creep behaviour characterised by the Larson-Miller Parameter [30].

Udimet 720 is a high strength alloy reinforced by γ' precipitation and solid solution of Mo, W, Cr, and Co [31]. It was originally intended for land-based turbine blades but was later used for turbine discs and second and third row

blades. Udimet 720 is corrosion resistant and shows outstanding stress corrosion resistance at intermediate temperatures in sulphate/chloride environments. It is also a versatile grade that shows a range of properties depending on thermo-mechanical processing, microstructural control, and grain size [31,34,167,168]. In fine grain form it possesses competitive strength levels and a temperature capability of 650°C – 700°C [29,167,169]. Although it is difficult to forge, it can be successfully forged via ring rolling, hot die forging, and superplastic isothermal forging [29,34,170].

A low interstitial version of Udimet 720 was developed to minimise its propensity to form the detrimental σ phase [122,171]. This grade – termed Udimet 720Li – also shows less tendency to TiN and TiCN inclusions [29,169]. Udimet 720Li can be processed via the I/M and P/M routes. Some authors [172,173] have extended the temperature capability of Udimet720Li up to ~ 730°C.

René 65 is a cast-and-wrought grade for turbine disc applications that derives from the successful P/M alloy René 88DT. It was developed by General Electric and ATI Specialty Materials with the stated aim of bridging the gap between Alloy 718 and P/M alloys. With this in mind, they started with René 88DT and adapted its chemistry to enable cast-and-wrought processing. The result was René 65: an alloy with a $f_{\gamma'} \sim 40\%$ and forgeable via hot die forging and ring-rolling [54,174]. According to Heaney et al. [33], the temperature capability of René 65 is ~ 90°C higher than that of Alloy 718. René 65 is currently used in several General Electric engine applications [33].

Similarly, AD730™ is a cast-and-wrought turbine disc superalloy developed recently by Aubert & Duval. In this case, alloy developers were aiming for a more cost-effective version of Udimet 720 for aeroengine turbine discs and land-based turbines. Its chemistry derives from alloys Ni 30 and Ni 33 [32]. AD730™ has a $f_{\gamma'} \sim 37$ % at 700°C, and a temperature capability that lies in the 700°C – 750°C range [30,78,175]. Because of the novelty of this alloy, much

independent data are still lacking on its properties, microstructural characteristics, and processing route. According to Aubert & Duval, AD730™ shows a tensile strength, fatigue resistance, and creep strength comparable to Udimet 720 [175,176]. Devaux et al. [30] reported that AD730™ can be successfully forged via conventional ring-rolling and closed-die forging. Moreover, they found that the alloy can be forged both above and below its γ' solvus, contrary to Waspaloy and Udimet 720. They suggested that this is advantageous since super-solvus forging can be used to break up the as-cast structure, followed by sub-solvus forging for grain refinement. However, recent work on hot-forging of AD730™ by Konkova et al. [176] and Pérez et al. [177] found bimodal distributions of recrystallised grains and large non-recrystallised grains, particularly at lower strains. These duplex microstructures are avoided in forging because they have been linked to a decrease in fatigue life [178–180].

2.3 Hot deformation behaviour of metallic materials

Hot working is ubiquitous in metal processing. It refers to operations where metallic workpieces are deformed at high homologous temperatures (typically $T_h \sim 0.7 - 0.8$) to change their shape, microstructure, or properties. It is sometimes referred to as 'hot forming' [181–183]. Hot working normally offers several advantages over cold working: higher ductility, lower flow stress, reduced chemical heterogeneity, and a positive effect in closing internal voids. However, this is only a broad principle, and many materials require a careful selection of optimal deformation temperatures and strain rates [184]. Superalloys cannot normally be cold forged, so they are formed at high temperatures [7].

The coupled micro- and macro-mechanisms that govern hot working are highly complex. At a microstructural level, hot working entails changes in dislocation structures, phase transformations, and annealing phenomena (recovery, recrystallisation, and grain growth). In turn, these affect the mechanical properties of the material [185]. What follows is a concise review of

the metallurgical phenomena relevant to hot working. Hot working operations as such are discussed in Section 2.4.

2.3.1 Deformation and fracture mechanisms

High temperature deformation can progress through different mechanisms to those dominant at low temperatures. Dislocation glide often remains a primary deformation mode, but it can be accompanied by thermally activated creep modes such as diffusional flow, dislocation climb and glide, and grain-boundary sliding (GBS). Among these, Dieter et al. [184] sustained that GBS plays a preeminent role at hot working temperatures, especially at slow strain rates. An analysis of the main high temperature deformation mechanisms for nickel-based superalloys is presented in Section 2.1.3.

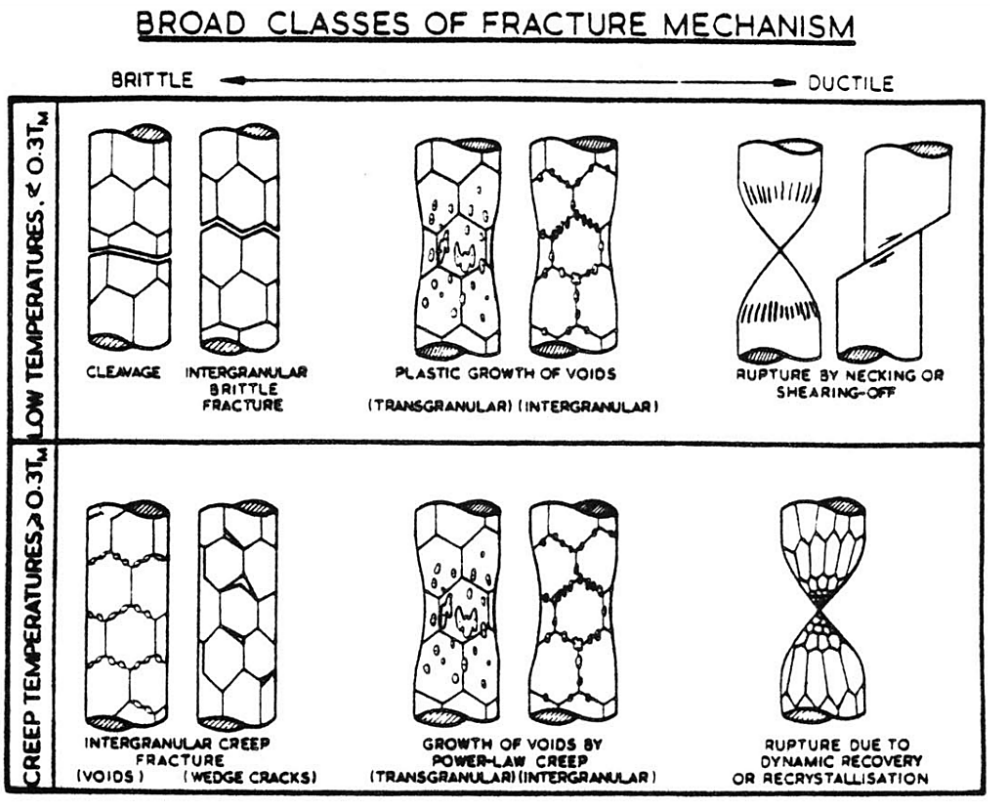

Figure 2.18. Classification of fracture mechanisms according to temperature and brittle – ductile nature. Upper row: low temperature modes where plastic flow does not depend strongly on temperature or time. Lower row: high temperature ($T \geq 0.3\ T_m$) modes [186].

Similarly, specific fracture mechanisms arise at high temperatures. Ductile fracture at low temperatures is frequently transgranular and associated to nucleation, growth, and coalescence of voids (see Figure 2.18). Nucleation occurs due to stress concentrations that result from the interaction between the yielding matrix and non-deformable second-phase particles [187–189]. These voids grow in regions with large triaxial stresses, and their eventual coalescence results in transgranular fracture [189]. Conversely, fracture at high temperature is often intergranular. This is attributed to the higher atomic mobility at grain boundaries outweighing the dislocation-barrier strengthening effect that dominates at low temperatures. Thus, once a crack nucleates it readily propagates through the weakened grain boundary [190]. The concept of 'equicohesive temperature' (ECT) was coined to differentiate both modes of fracture. The ECT is defined as the temperature at which grains and grain boundaries have equal strengths [191].

In addition, at high temperature there exists an extra mechanism for nucleating voids. It occurs when the temperature and strain regime are such that GBS is active but not accompanied by other stress-relieving or strain accommodation mechanisms. Then, wedge-shape cracks nucleate at grain boundaries causing a low-ductility fracture mode (see Figure 2.18) [187,192,193].

2.3.2 Annealing phenomena

Annealing phenomena refer to processes by which metallic materials rebuild their microstructure following deformation. Deformation creates defects that raise the free energy of the material and destabilise its thermodynamic equilibrium. Given sufficient thermal activation, the material will restore equilibrium via three main mechanisms: recrystallisation, recovery, and grain growth [194,195].

Recrystallisation involves the nucleation and growth of new, strain-free grains in a deformed microstructure. It is triggered by the combination of high

temperature and elevated dislocation density in strained grains [184]. Hot working is so closely linked to recrystallisation that some authors have defined it as 'plastic deformation operations conducted above the recrystallisation temperature' [196,197].

Dieter et al. [184] claimed that dynamic recrystallisation (DRX) is common at industrial metal-forming strain rates ($\geq 1\ s^{-1}$). This agrees with recent studies by Buckingham et al. [198] on the newly developed P/M alloy V207M, Wang et al. [199] on Alloy 718 , and Kienl et al. [200] on ATI 718Plus®. In addition, it is believed that dynamic recrystallisation acts as an accommodation mechanism in superplastic deformation. If that is the case, recrystallisation happens at strain rates as low as $10^{-3}\ s^{-1} - 10^{-5}\ s^{-1}$, on the boundary of creep conditions [201]. Recent research by Medeiros et al. [202] on Alloy 718 provided evidence that supports this assumption. Although DRX is normally recognised as a main restoration mechanism, it often competes with dynamic recovery (DRV). The question of which mechanism dominates in hot working conditions for nickel-based superalloys remains open, with data pointing in both directions [203,204]. It is thought that the strain, strain rate, and deformation temperature determine the dominant mechanism [198].

By contrast, Hosford [193] suggested that while typical hot working temperatures are above the recrystallisation temperature, hot working is often performed at too high a strain rate to allow for recrystallisation to occur during deformation. Consequently, recrystallisation ensues after deformation while the material is still at high temperature. A distinction is then made between dynamic (DRX), metadynamic (MDRX) and static (SRX) recrystallisation, on account of its occurrence simultaneously with, following, or without deformation [7].

Recovery implies a reduction of grain-stored energy by removal or rearrangement of crystallographic defects – particularly dislocations. This includes the annihilation of dislocations because of favoured dislocation climb, cross-slip,

and unpinning; and the formation of dislocation sub-cell structures (sub-grains) that act as sinks of mobile dislocations. Equivalently to recrystallisation, recovery is further classified as dynamic (DRV), metadynamic (MDRV), and static-recovery (SRV) [184,205].

Grain growth refers to the growth of strain-free grains following recrystallisation. In this case, the driving force is reducing the total grain boundary area. The kinetics of grain growth are dependent on the temperature and the presence of second phase particles. Grain growth advances more rapidly as the temperature increases. Conversely, second phase particles act as obstacles that retard the movement of grain boundaries – a phenomenon termed Zener pinning [206,207]. For nickel-based superalloys, intergranular primary γ' precipitates are known to have a grain pinning effect that prevents γ grain growth at sub-solvus temperatures [9,208].

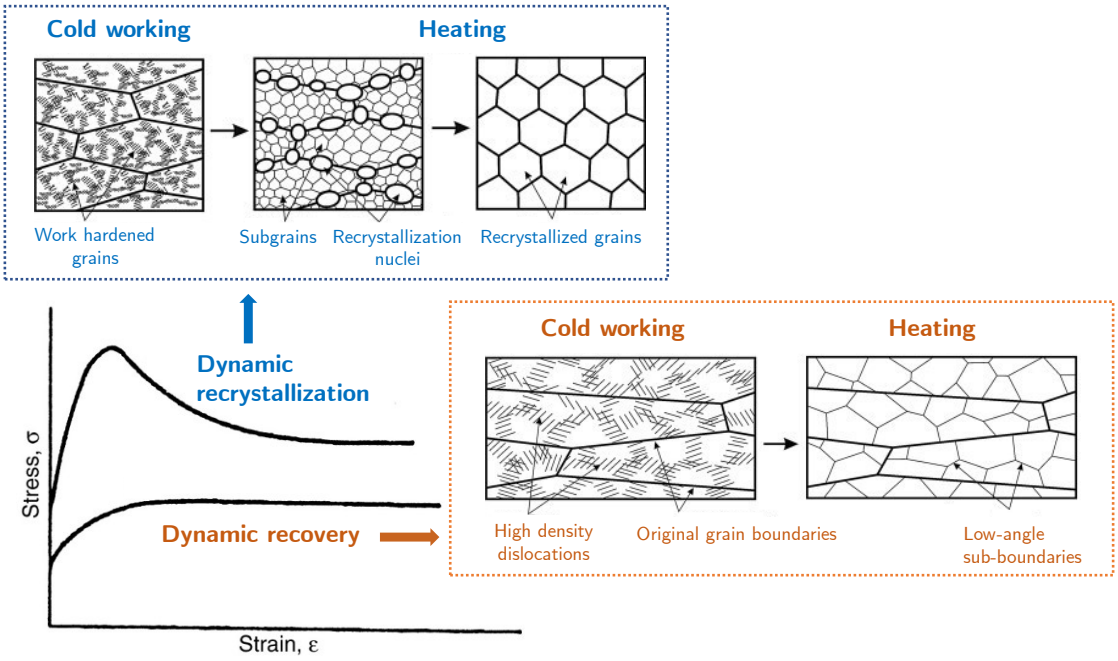

Figure 2.19. Model stress-strain curves for a metal undergoing dynamic recrystallisation (DRX) and dynamic recovery (DRV). Adapted from [184,209].

Both recovery and recrystallisation oppose the rise in dislocation density upon deformation (strain hardening). Yet the stress relaxation associated to each

process manifests in a different manner. This is shown in Figure 2.19: the flow stress in a metal undergoing DRV increases until a steady state is reached, whereas DRX is associated to a peak in flow stress and a subsequent steep drop once recrystallisation starts.

Recovery and especially recrystallisation also play a crucial role in facture. DRV increases ductility by reducing the flow stress and delaying cavity nucleation and growth. DRX is associated to various favourable processes. First, it prevents void nucleation thereby making possible fracture by rupture (see Figure 2.18). Gandhi and Ashby [210] defined rupture as a mode defined by such great ductility (reduction in area $> 90\%$) that the specimen necks to zero cross-section. DRX is also beneficial for GBS wedge-cracking because grain boundary migration hinders void coalescence. This sometimes happens in synergy with diffusional void-shrinkage, which has been detected under certain stress states [211].

2.4 Forgeability of metallic materials

Forming operations can be divided in two categories: bulk working and sheet forming. Sheet forming entails large changes in the shape of a workpiece while preserving its thickness. Bulk forming processes cause significant changes in the cross-sectional area of a workpiece and, optionally, in its shape. In turn, bulk forming processes are divided in primary and secondary operations. Primary operations refer to fabricating mill products – like sheets, tubes, or bars. Secondary operations turn mill products into final products and include cold and hot forging, rolling, extrusion, and others. So, forging is only one of numerous forming processes – although arguably the most relevant one. The analysis that follows is focused on forging, but most concepts and considerations can be readily applied to other wrought processes.

In a broad sense, workability refers to the ease with which a material can be plastically deformed into various shapes. When the stock material is deformed

via localised compressive forces, this property is called forgeability [184]. Nevertheless, forming operations should not be designed in isolation but as part of a multi-step thermal-mechanical processing route. Nielsen et al. then defined workability as the extent to which a material can be deformed in a specific metal working process without creating undesirable defects [212]. A more comprehensive definition was provided by Scallan [213]: "formability refers the ease with which a material can be formed while satisfying quality requirements". In this sense, forging aims to attain not only a prescribed shape but also a certain microstructure that provides desirable properties [7].

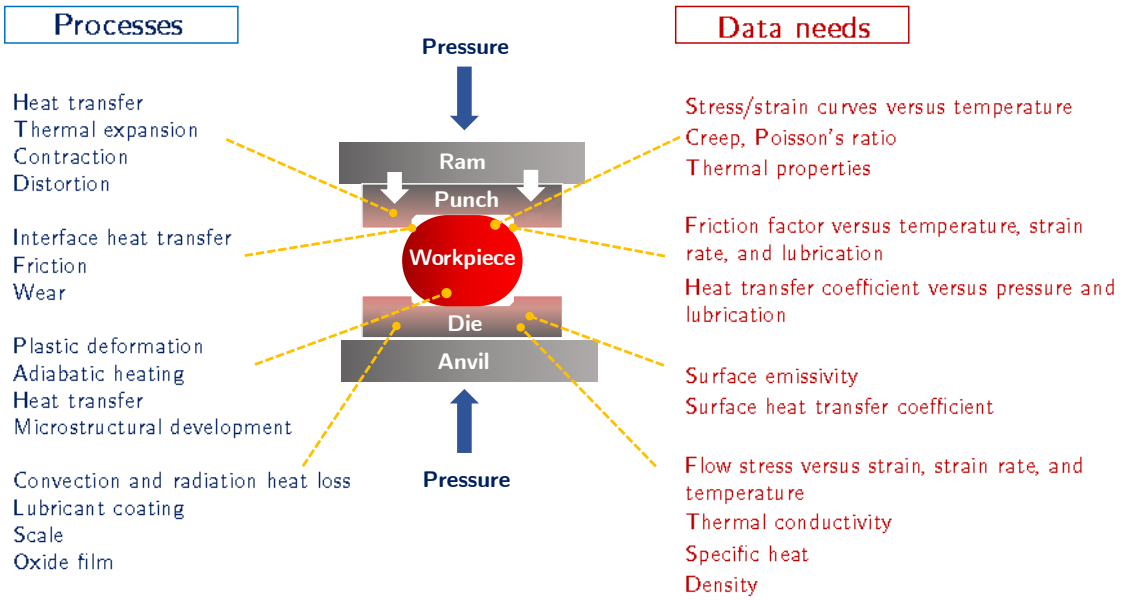

Figure 2.20. Summary of the physical phenomena relevant to hot working operations in metallic materials. Adapted from [184].

Workability (hereafter forgeability) is a complex property that depends on both the material's properties and the process parameters. Typical forging parameters include the initial temperature of the billet; the ram speed; and the initial temperature, geometry, and material of the dies. The forging parameters and the microstructural state determine the deformation variables (temperatures, strains, and strain rates) on the billet. To add complexity, the microstructure evolves dynamically depending on the deformation variables. Other aspects like lubrication, friction, wear, thermal expansion, and the effect of the oxide film also

play a key role [184]. Figure 2.20 provides an overview of the main variables relevant to hot working.

All things considered, forgeability can be expressed as Eq. 2.4, where the ductility of the material depends on the initial microstructure, local temperature, and local strain rates. Similarly, the local state of stresses and strains are dictated by the geometry of the dies and the friction between these and the workpiece.

$$\begin{aligned}\text{Forgeability} &= f_1\ (\text{material ductility}) \cdot f_2\ (\text{stress–strain states}) = \\ &= f_1\ (T,\ \dot{\varepsilon},\ \text{material conditions}) \cdot f_2\ (\text{die geometry, friction})\end{aligned} \tag{2.4}$$

Although several forgeability ratings for materials have been developed with a view to objectivity, these remain somehow subjective [7]. Even so, it is clear that the flow stress and plastic strain until failure (ductility) of a material are strong indicators of its forgeability.

2.4.1 Processing maps

Maps based on the dominant deformation mechanisms and fracture modes at different temperatures and strain rates are commonly used for studying forgeability [214–217]. Figure 2.21 shows a processing map for Udimet 720Li at $\varepsilon = 0.8$ developed by Wan et al. [217]. In this map, two safe forging domains (domain A) are identified. The first one exists at temperatures and strain rates of 1080°C – 1100°C and 0.01 s^{-1} – 0.3 s^{-1}; the second one at 1140°C – 1160°C and 0.01 s^{-1} – 0.1 s^{-1}. These correspond to homogeneous, fully recrystallised microstructures without defect. Domain B is an instability domain in the temperature range of 1140°C – 1180°C and strain rate range of 1 s^{-1} – 10 s^{-1} linked to intergranular cracking and incomplete recrystallisation. Domain C is unstable due to the formation of adiabatic shear bands and occurs at temperatures of 1060°C – 1100 °C and strain rates of 1 s^{-1} – 10 s^{-1}.

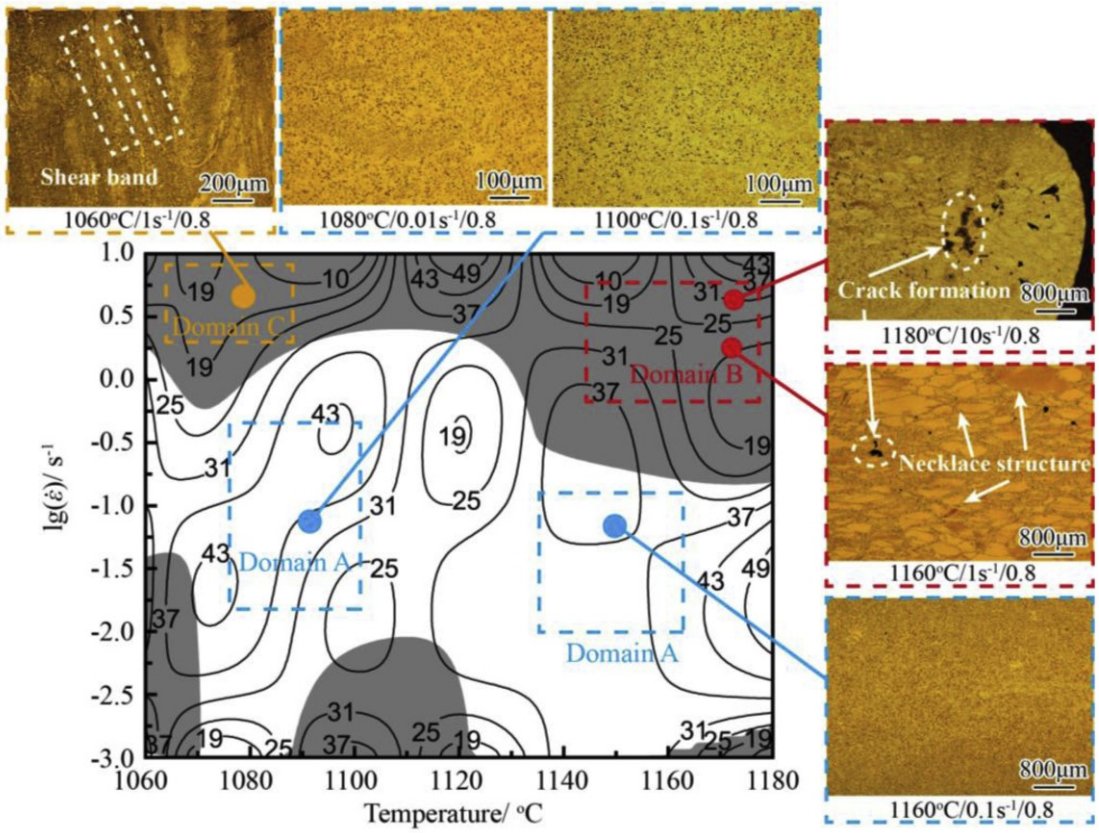

Figure 2.21. Processing map for alloy Udimet 720Li at $\varepsilon = 0.8$ and micrographs corresponding to the different deformation domains [217]. The black lines are isoefficiency (η) contours, while the shaded areas are regions of unstable flow.

A model termed dynamic material modelling (DMM) is frequently used to obtain processing maps [218–220]. In this model, the material is assumed to act as a power dissipator that follows the dynamic constitutive equation 2.5. In Eq. 2.5, σ is the stress and $\dot{\varepsilon}$ is the strain rate. The efficiency is given by Eq. 2.7, where m is the strain rate sensitivity that partitions power per unit volume entering the system (P) into two terms: G and J (Eq. 2.7). The G-term comprises power dissipated by plastic work – mostly as heat but also as lattice defects. The J-term is associated to several dynamic metallurgical processes such as dynamic recrystallisation, dynamic recovery, internal fracture, or deformation-induced phase transformations.

$$\sigma = \dot{\varepsilon}^{m} \qquad 2.5$$

$$P = G + J \tag{2.6}$$

$$\eta = J / J_{max} = 2\ m/\ (m + 1) \tag{2.7}$$

Since the material flow is maximum where most power is dissipated via safe dynamic metallurgical processes (such as. DRV and DRX), optimal forging conditions are those with the highest J [184,219,221]. Therefore, optimal strain rates and temperatures can be determined by plotting $\eta(T,\dot{\varepsilon})$ contour maps and identifying the dominant mechanism for each domain (peak) via microstructural examination [221].

Instability domains are associated to undesirable plastic instabilities such as fracture, grain boundary cavitation, flow localisation, and flow instabilities. Flow localisation describes the process whereby deformation is confined to narrow areas of the workpiece. This creates inhomogeneity that can lead to failure in service. If flow localisation is severe, it can even cause cracking during hot working [184]. There are two main modes of flow localisation. The first mode is due to poor lubrication or cooling at the tool-workpiece interface; it manifests as dead zones with little or no deformations along with bands of intense shearing [184].

The second flow localisation mode is termed flow instability; it is more severe and often leads to fracture. Flow instabilities result from negative strain hardening due to microstructural phenomena (flow softening). Such microstructural phenomena include DRV, DRX, grain coarsening, texture softening, deformation heating, and others [222]. Adiabatic shear bands are especially strong flow localisations associated to deformation heating. They arise at high strain rates due to high conversions of power into heat ($\sim 90\%$). If not dissipated at a sufficient rate, this heat causes flow softening – which in turn triggers further deformation. This way, deformation and adiabatic heating grow in an unstable manner [184,222]. An instability parameter called ξ similar to the power dissipation efficiency (η) is derived from irreversible thermodynamics and used to identify flow instability regions (Eq. 2.8).

$$\xi = \frac{\partial \ln [m/(m+1)]}{\partial \ln \dot{\varepsilon}} \tag{2.8}$$

The identification of unstable domains is then straightforward: a temperature and strain rate dyad is unstable if and only if $\xi < 0$. This allows plotting flow instability maps similar to the power dissipation contour maps. Flow instability and power dissipation maps are typically presented superimposed in a single processing map, as in Figure 2.21. This way, restricted domains can be found within the safe (stable) area where material flow is maximum. These domains constitute the optimum forging conditions [217,220,223].

Despite their popularity, processing maps are based in models made for pure metals and simple alloys and have limited application for more intricate microstructures. Besides, the domains distribution is quite sensitive to the microstructural state and the thermo-mechanical history of the alloy [184]. Hence, processing maps have been used extensively to study isothermal deformation [214–216,223,224]; yet they are not readily adaptable to processes like hot forging where the workpiece undergoes complex thermal cycles. For example, processing maps cannot account for thermal transfer (die chilling) effects, or the dynamic evolution of γ' precipitates in nickel-based superalloys – both of which have been shown to be relevant to the hot forging of these alloys [27,134,225].

2.4.2 Forgeability of nickel-based superalloys

Superalloys are designed to resist deformation up to very high temperatures, so they are intrinsically difficult to hot work [26]. Early iron-nickel based superalloys were not excessively difficult to forge, but the advent of nickel-based precipitation strengthened alloys brought new challenges. This is due of the hardening effect of γ', but also to the shrinking hot working window. Increasing the amount of alloying elements elevates the recrystallisation temperature and reduces the incipient melting temperature, thereby reducing forgeability [7].

Due to their narrow hot working window, the forging of superalloys requires a tight control of the processing parameters, especially temperature and strain rate. When the hot working window is particularly limited (e.g. Astroloy, U-500, René 41) cracking constitutes a major problem. The microstructure of the material – particularly its micro-cleanliness and chemical homogeneity – is also crucial [7]. Powder-metallurgy alloys in ingot form are a prime example of hard-to-work alloys due to segregation [9]. The hot working window of nickel superalloys may lie below, above, or contain the γ' solvus temperature.

Ingot metallurgy (C&W) alloys are often hot die forged in a variety of open and closed die operations, depending on the shape and tolerance required. These include die forging, upsetting, ring rolling, extrusion, forge rolling and swaging [1]. The typical forging process of a turbine disc includes two forging steps, as shown in Figure 2.22.

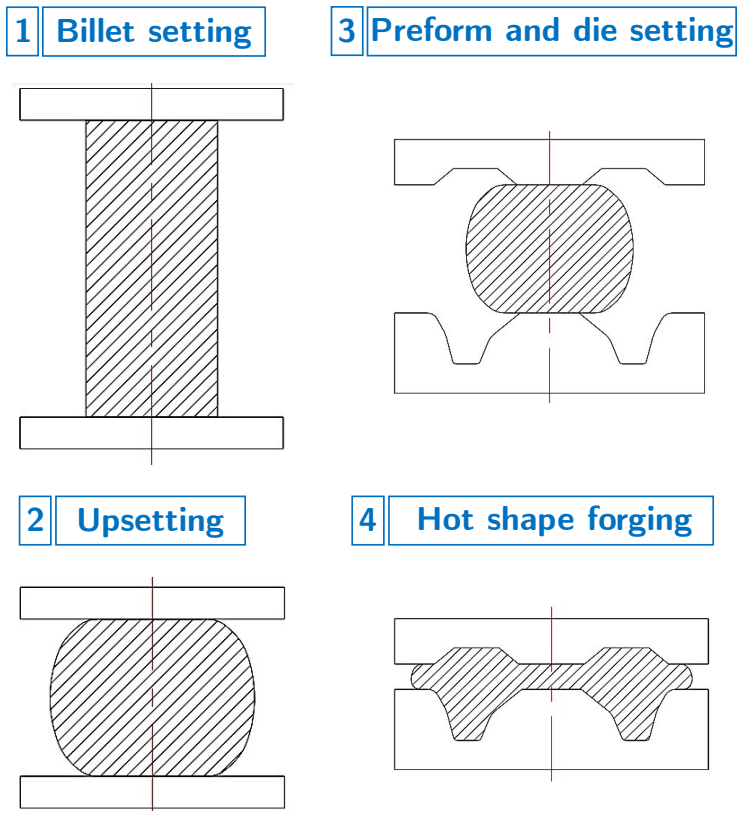

Figure 2.22. Schematic diagram of the typical two-step hot forging process of turbine discs. Adapted from [226].

I/M grades are typically forged below their γ' solvus temperature. This prevents undesirable grain-growth, since primary γ' particles inhibit grain boundary motion through Zener pinning [9,28,227]. Carbides, borides, and oxides have been reported to act in a similar manner, particularly when forging at super-solvus temperatures [208,228]. However, not all cast-and-wrought alloys are forged below the γ' solvus. Waspaloy is a difficult to work alloy normally forged over the narrow window of 1000°C – 1100°C. Below 1000°C, the flow stress increases significantly, and deformation tends to be inhomogeneous, often resulting in cracking. Above 1100°C, it becomes prone to cracking and hot shortness [150]. Its γ' solvus temperature is $\sim$ 1040°C – 1050°C, and its $M_{23}C_6$ carbide solvus temperature is $\sim$ 1060°C – 1080°C [150,229]. Therefore, Waspaloy does not really have a fine-grain hot working window [30,230].

Highly reinforced grades cannot normally be hot die forged [7,9]. Instead, they require isothermal forging (not necessarily superplastic) to avoid die chilling and adiabatic heating [27,231,232]. Die chilling lowers the temperature of the forging below the relevant solvus, and the precipitation of reinforcing phases that follows reduces workability and favours cracking. Similarly, adiabatic heating can cause melting at the grain boundaries, where low-melting-point phases are sometimes present [27].

The isothermal forging of finely grained materials at slow strain rates and elevated temperatures can result in superplastic behaviour. Superplastic flow is defined as the ability of a (polycrystalline) material to exhibit extraordinarily large elongations – commonly up to 200% – 500% and in some cases up to 5500% – before failure. The best understood mechanism of superplasticity is fine structure superplasticity (FSS), where deformation takes place by grain boundary sliding. FSS is assumed to occur by the motion of extrinsic dislocations along the grain boundary. Wedge-cracking is avoided thanks to accommodation mechanisms like grain boundary migration, DRX, dislocation movement, or diffusional flow. These relieve the stress associated to dislocation pile-ups and

prevent extensive cavity growth [201]. Superplastic flow allows attaining large strains without cracking or (ideally) substantial generation of dislocations [28]. It also provides a better control of recrystallisation and grain growth, preventing the undesirable microstructural differences that sometimes arise in cold die forging [9,181]. Finally, isothermal superplastic forging allows obtaining parts with a geometry very close to the 'sonic shape' required by ultrasonic testing, creating significant material savings [9].

According to Blankenship et al. [28], P/M grades for gas turbine applications are isothermally forged at temperatures slightly below their γ' solvus. This agrees with Higashi and Kanno's [233] study of Udimet 720Li in P/M form, where significant grain growth was observed at 1180°C (above the γ' solvus) and optimum isothermal hot workability at ~ 1100°C (sub-solvus). They concluded that hot workability was optimum at 1100°C due to the occurrence of superplastic flow, whereas the coarse grains at 1180°C prevented it. Similarly, Hardy et al. [29] noted that extremely fine grains are required for superplasticity. Following forging, super-solvus heat treatments are used to increase the grain size to 20 μm – 40 μm and thus optimise high-temperature properties [29]. The lower forging temperature limit is normally related to flow localisation [34,234], the onset of cracking due to concentration of dislocations [28,41], or prior particle boundary (PPB) cracking [234].

Isothermal forging significantly increases the processing costs, particularly when combined with powder metallurgy. Consequently, there has been a continuous interest in researching if alloys that are currently isothermally forged can be hot die forged. In hot die forging, the temperature of the die is lower than that of the workpiece (540°C – 830°C [181], ~ 600°C [28]) but still much higher than the temperatures used in conventional forging (205°C – 425°C [235], ~ 315°C [181]). Blankenship et al. [28] investigated the hot die forging of René 88DT, a P/M alloy. They achieved acceptable grain structures under certain conditions, but die filling issues and cracking persisted. To date, published research on hot

die forging of P/M is very sparse. Furthermore, the optimisation of thermo-mechanical processing routes and the resulting material properties still relies heavily on empirical trial and error approaches [35,236].

2.4.3 Forgeability of high γ' cast-and-wrought alloys

The forgeability of high γ' cast-and-wrought alloys has received little attention. Some research has been conducted on the isothermal deformation of Udimet 720 [31,34,237] and its variant Udimet 720Li [36,217,238,239], both of which can be processed via the P/M route [240]. Similar studies exist for René 65 [54], AD730™ [30], VDM Alloy 780 [165], and GH4720Li [37,241,242] – a newly developed grade derived from Udimet 720. Research work on their hot die forgeability is even more sparse [54,134,176,177].

Monajati et al. [34] studied the isothermal deformation of Udimet 720 in the temperature range 1000°C – 1175°C, to strains of $\varepsilon = 0.8$, and at strain rates of 10^{-3} s^{-1} – 1 s^{-1}. They reported limited DRX below 1150°C, with a recrystallised fraction below 10% at 1125°C that increased to more than 90% at 1150°C (see Figure 2.23). It was suggested that recrystallisation was inhibited by γ' at temperatures below 1125°C. This was supported by the observation of recrystallisation in regions free from precipitation. In addition, recrystallised grains were observed in heavily deformed areas of the specimens deformed at 1000°C and 1050°C. These existed at the grain boundaries of elongated grains and were attributed to the dissolution of γ' locally due to adiabatic heating. Homogeneous deformation happened at 1150°C, whereas shear bands were observed below 1150°C and grain boundary separation above 1150°C. They thus concluded that the hot working window for Udimet 720 lies in the 1100°C – 1150°C temperature range. This agrees with the results of Sczerzenie and Maurer [31] who found the most ideal superplastic behaviour at 1121°C linked to the presence of γ' only as primaries. For Udimet 720 in P/M form, Hyzak et al. [237] reported cracking at PPBs when deforming isothermally at low

temperatures and high strain rates (1050°C and 3.0 min^{-1}) and at large grain boundaries at high temperatures and slow strain rates (1140°C and 0.006 min^{-1}).

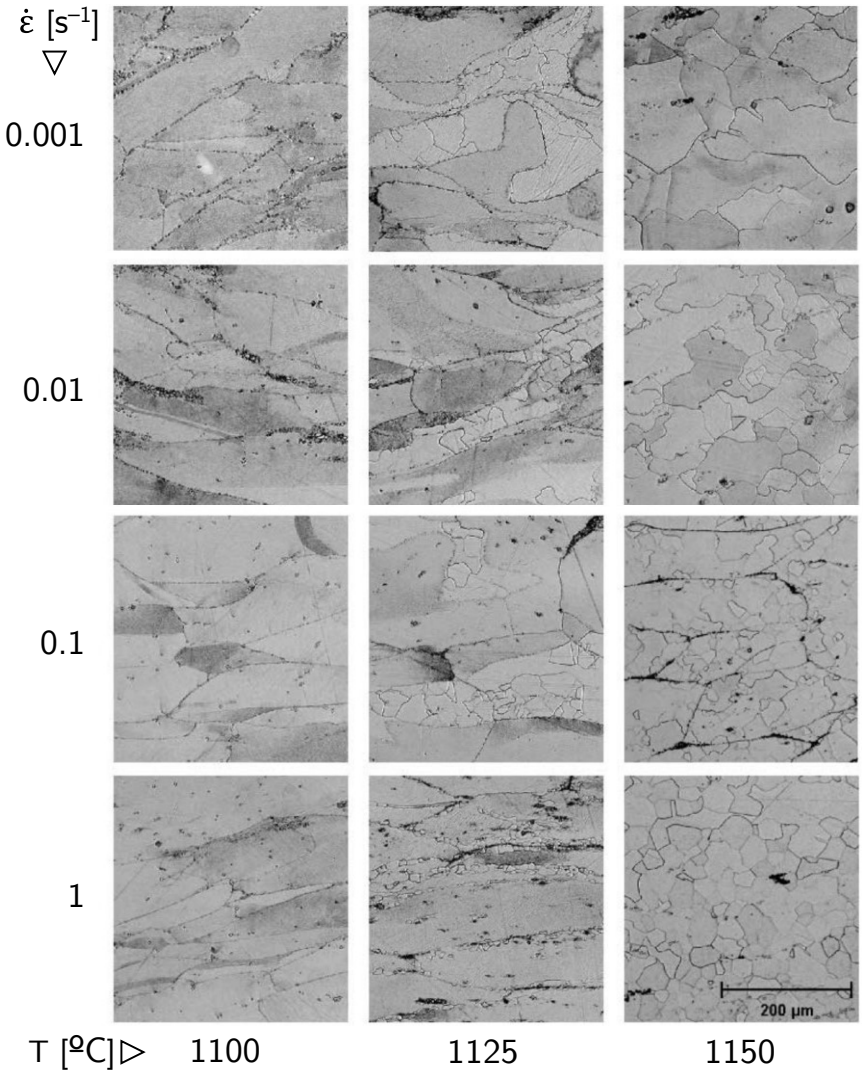

Figure 2.23. Micrographs of Udimet 720 deformed isothermally at 1100°C, 1125°C, or 1150°C and strain rates of 0.001 s^{-1}, 0.01 s^{-1}, 0.1 s^{-1} , or 1 s^{-1} to a strain of $\varepsilon = 0.8$ [34].

The findings of Wan et al. [217] on the isothermal forging of Udimet 720Li (see Figure 2.21) are discussed in Section 2.4.1. Similarly, Wang et al. [36] studied this alloy using processing maps and isothermal uniaxial compression tests at temperatures of 1060°C – 1160°C, strain rates of 10^{-3} s^{-1} – 20 s^{-1}, and to strains of 0.1 – 0.7. They noted the existence of two instability domains at $\varepsilon = 0.5$ (domains I and II) and three at $\varepsilon = 0.7$ (domains I, II, and III). Domain I corresponded to

strain rates of 0.007 s^{-1} – 0.7 s^{-1} and temperatures of 1060°C – 1075°C; shear bands were detected in this domain. Domain II existed at strain rates of 1.34 – 20 s^{-1} and temperatures of 1105°C – 1160°C and was characterised by incomplete and heterogeneous DRX. Domain III corresponded to strain rates of 1 s^{-1} – 20 s^{-1} and temperatures of 1060°C – 1095°C and was linked to the development of shear bands. In Domain I and III, they found incomplete DRX at the grain boundaries in heavily deformed shear band regions. This is in agreement with Monajati et al. [34] and was attributed to the dissolution of primary γ' due to adiabatic heating. Additionally, two full recrystallisation regions were identified: one at temperatures of 1080°C – 1120°C and strain rates of 0.001 s^{-1} – 1 s^{-1}, and the second one in the temperature range 1120°C – 1160°C and strain rate range 0.01 s^{-1} – 1 s^{-1}. These are similar to the optimum hot working conditions reported by Wan et al. [217]. By contrast, the similarly composed alloy GH4720Li showed significantly different regions in the studies of Qu et al. [241] and Yu et al. [37].

For René 65, Bond et al. [54] conducted isothermal rapid strain rate tensile tests and noted that the reduction of area (RA) increased in the ~ 900°C – 1025°C temperature range. The RA then plateaued at 100% until 1150°C, but grain coarsening to a duplex structure was detected at temperatures above 1085°C. Therefore, its optimum isothermal forging temperature lies in the 1025°C – 1085°C range. The forging of AD730™ and VDM Alloy 780 is not reviewed here, since these alloys are not considered in this research project. The interested reader is referred to [30,165,176,177] for data on these grades.

Fahrmann and Suzuki [134] conducted an insightful study on the hot die forgeability of Udimet 720 billet stock. They measured the tensile RA at temperatures in the range of 950°C – 1110°C. To simulate ingot to billet press forging, they prior to deformation annealed the specimens for 5 minutes at 1110°C and cooled them at 30°C/s (fast cooling) or 0.03°C/s (slow cooling) to the deformation temperature. Their results revealed a steep loss of ductility on the rapidly cooled specimens below 1050°C, whereas slowly cooled specimens

preserved significant ductility (Figure 2.24). Microstructural examinations revealed that high cooling rates from annealing temperatures resulted in the precipitation of copious amounts of very fine γ' (~ 40 nm). It was rationalised that this changed the dominant deformation mechanism from <110> {111} dislocation gliding to microtwinning, dramatically decreasing the tensile ductility.

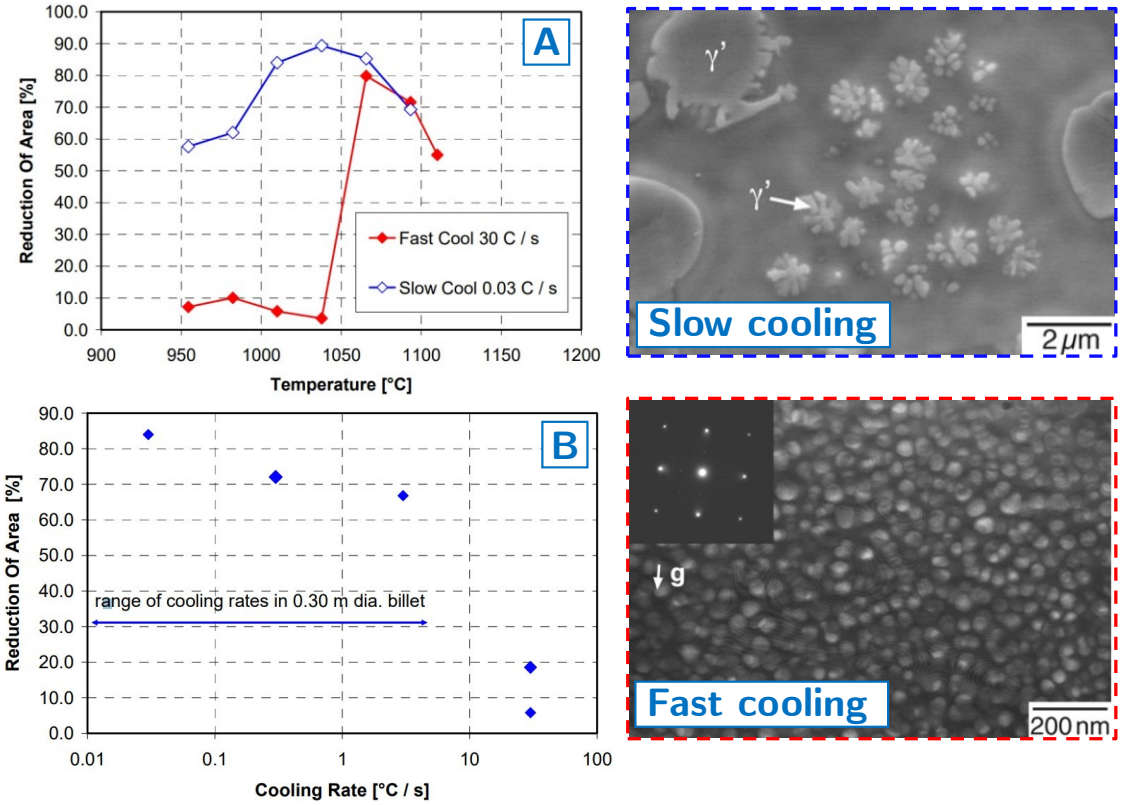

Figure 2.24. For Udimet 720: (A) RA as a function of the test temperature for samples annealed at 1110°C and cooled at 30°C/s or 0.03°C/s to the test temperature. (B) RA as a function of the cooling rate from 1110°C to the deformation temperature of 1010°C. Also shown are SEM and transmission electron microscopy (TEM) micrographs of specimens in the slow and fast cooling conditions showing differently sized γ' populations. Adapted from [134].

Sczerzenie and Maurer [31] researched the hot die forgeability of Udimet 720 by similar means (Figure 2.25). They preheated specimens to temperatures ~ 975°C – 1150°C for 10 minutes and cooled them to 982°C followed by tensile testing at a strain rate of 5 cm/s. They found that ductility decreased monotonically in the 1050°C – 1150°C range, with superior forgeability

(RA = 80%) at 1050°C and poor ductility (RA < 30%) at temperatures of 1100°C and above [31,184]. Conversely, yield strength increased at higher preheating temperature. The authors postulated that this was due to the solution of greater amounts of γ' at higher preheating temperatures. This caused grain coarsening and the precipitation of fine γ' on cooling, decreasing ductility and increasing strength.

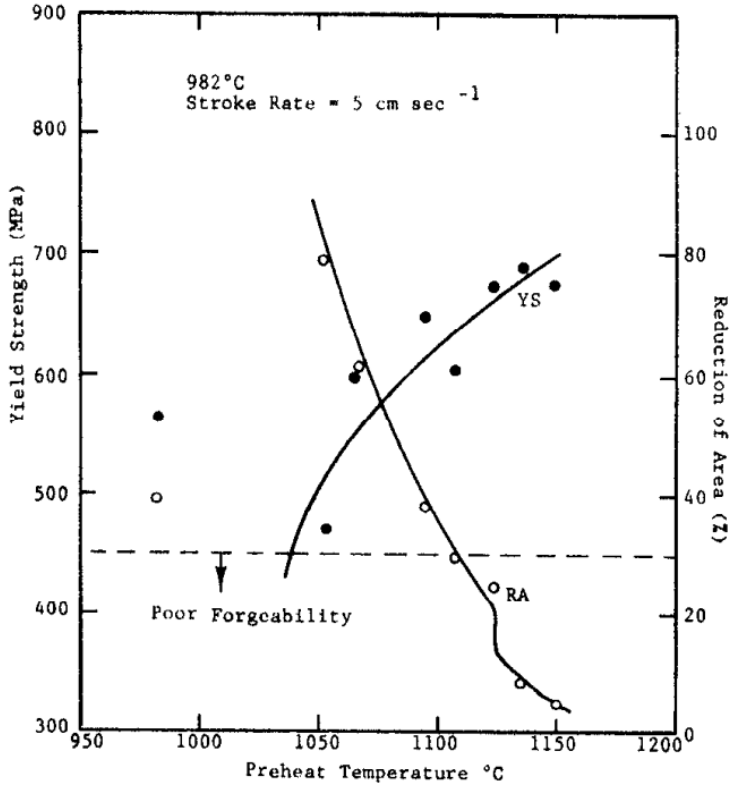

Figure 2.25. For Udimet 720 samples preheated at the x-axis temperature for 10 minutes, cooled to 982°C, then pulled at 5 cm/s: yield strength (left axis, black dots) and RA (right axis, white dots) versus preheat temperature [31].

Bond et al. [54] reported similar results on René 65. They obtained the rapid deformation RA for 254 mm billets at temperatures of 900°C – 1150°C. To simulate cooling from furnace temperature, the specimens were preheated to 1093°C, 1066°C, or 1038°C and cooled down to room temperature, prior to reheating to the test temperature and deformation. The ductility of specimens decreased as the preheating temperature increased. The authors attributed this to the dissolution of γ' and its subsequent reprecipitation as fine particles.

The results of Fahrmann and Suzuki [134], Sczerzenie and Maurer [31], and Bond et al. [54] indicate that the ductility of these alloys is substantially affected when specimens are annealed and subsequently cooled down to a lower testing temperature. This has important implications for their hot forgeability and hints that die chilling effects could be significant. Yet many questions remain open. Only Fahrmann and Suzuki related their mechanical testing results with electron microscopy (EM) micrographs. A comprehensive study of the interplay between processing conditions, microstructural evolution, and forgeability is still lacking. Besides, simulating forging through laboratory-scale tests requires careful experimental design. Fahrmann and Suzuki [134] and Sczerzenie and Maurer [31] used short annealing times and relatively high deformation temperatures. Bond et al. [54] used air cooling to room temperature followed by reheating and deformation. It remains unknown if these parameters are good representatives of full-scale forgings. This research project aims to answer some of these questions.

2.4.4 Surface cracking

The appearance of surface cracks in the working of metallic materials is acknowledged as a problem of technological and scientific significance [184,243,244]. This extends to the hot forging of nickel-based superalloys [7,41,150]. Hard to work alloys often present fracture-related problems. Fracture in bulk metal working can occur on free surfaces, on die contact surfaces, or internally. Internal fracture can develop by the mechanisms described in Section 2.3.1. Free surface cracking refers to fracture on surfaces that are expanding freely due to compressive loads. Surface cracking on exposed surfaces during upsetting falls into this category. It is caused by tensile stresses termed secondary because they are not applied directly by the die [184,245]. By contrast, die contact surface cracking happens on surfaces directly in contact with the dies. It is a common defect that often appears near the corner of the dies, where there is a combination of shear deformation and tensile stress or low hydrostatic

pressure. Die contact surface cracks do not normally extend inside the workpiece, yet they can result in excessive machining depths [184].

Surface cracking in nickel-based superalloys remains largely unexplored. Recently, G. He et al. [41] investigated forging cracking in a bespoke P/M hot-extrusion nickel-based superalloy. They conducted isothermal compression tests at temperatures of 1000°C – 1100°C, strain rates of 10^{-3} s^{-1} – 1 s^{-1}, and to strains of 0.1 – 0.7. They successfully replicated surface cracking in laboratory-scale tests (Figure 2.26). The severity of cracking decreased with increasing temperatures, which was ascribed to intensified dislocation annihilation and the concomitant decrease in flow stress. It was found that a critical strain existed for each temperature and strain rate dyad, such that cracks emerged only when the strain exceeded it. However, this critical strain was lower than 0.4 for all conditions – a fairly low value. Indeed, all samples deformed at $\varepsilon = 0.7$ (Figure 2.26) showed significant cracking.

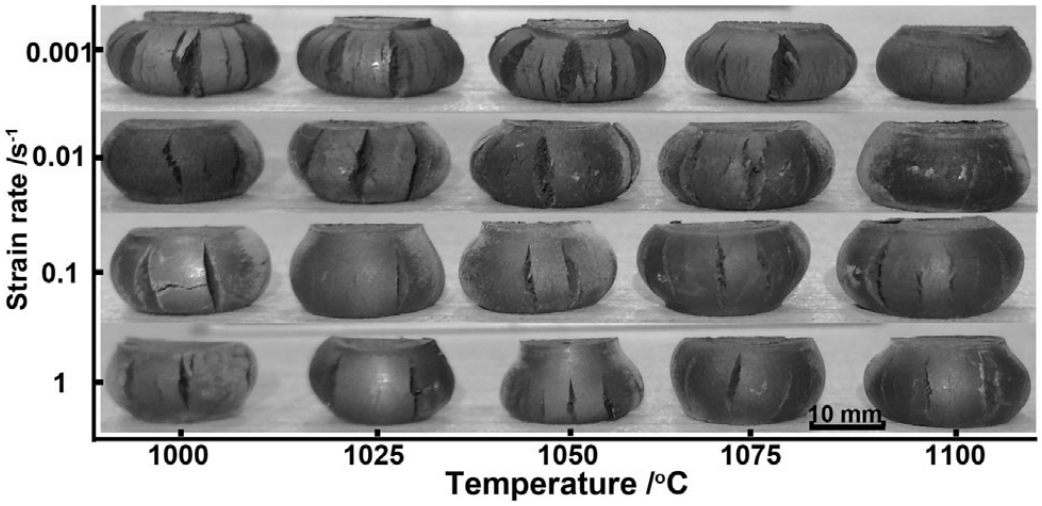

Figure 2.26. Specimens of the bespoke P/M alloy in G. He et al. [41] deformed isothermally to a true strain of 0.7 at various deformation temperatures and strain rates. All specimens show significant free surface cracking.

To the knowledge of the author, no published work on surface cracking of high γ' cast-and-wrought alloys exists to date. However, there exists limited evidence from Otto Fuchs KG – a collaborator to this project – that the hot die

forging of Udimet 720 pancakes can result in surface cracking. This research project aims to elucidate this phenomenon.

3

Experimental methods

3.1 Materials

The main alloy used in this research project was Udimet 720; all investigations in Chapters 4 – 8 pertain to this material. The chemical composition of Udimet 720 is provided in Table 3.1.

Table 3.1. Nominal composition of Udimet 720 (wt. %).

Cr	Co	Mo	W	Al	Ti	C	B	Zr	Ni
17.9	14.7	3.0	1.25	2.5	5.0	0.035	0.033	0.03	Bal

Udimet 720 material was made available by Otto Fuchs KG in the form of three as-forged pancakes. A round billet of diameter ~ 120 mm and height ~ 95 mm was upset (3:1) to produce a first pancake of height ~ 32 mm. Samples were cut from this pancake for thermal analysis, heat treatments, and microstructural analysis via electron microscopy (EM). The outermost and innermost regions were avoided as macroetching revealed that inhomogeneous deformation occurred in these areas. Two other pancakes were processed in the same manner to obtain thermo-mechanical testing samples. 33 double cone specimens were machined out of the second pancake and 33 circular cylinders out

of the third pancake. The double cones measured $Ø_1 = 10$ mm, $Ø_2 = 15$ mm, and $h = 15$ mm – where $Ø_1$ is the diameter at the base and top surface, $Ø_2$ is the maximum diameter at the middle of the specimen ('equator'), and h is the height. The circular cylinders measured $Ø = 10$ mm and $h = 15$ mm. The rationale behind the selection and design of the specimen geometries is presented in Section 6.3. Udimet 720 billet material was employed for the full-scale forging trials of Section 9.1.

Alloy René 65 was used for the supplementary tests of Section 9.2. The chemical composition of this alloy is provided in Table 3.2. A section of a René 65 disc forging was provided by Otto Fuchs KG. Samples were cut from the disc-forging section for thermal analysis, heat treatments, and EM examinations. In addition, 38 double cones and 32 circular cylinders with identical dimensions to the Udimet 720 samples were machined out of this material for thermo-mechanical testing.

Table 3.2. Nominal composition of René 65 (wt. %).

Cr	Co	Mo	W	Nb	Al	Ti	Fe	B	Zr	Ni
16.0	13.0	4.0	4.0	0.7	2.1	3.7	1.0	0.016	0.05	Bal

3.2 Thermal analysis

Differential scanning calorimetry (DSC) was employed to investigate phase transformations and phase transition temperatures in Udimet 720 and René 65. In DSC, samples of known mass are heated to a prescribed temperature at a fixed rate, and the heat flow is measured as a function of time and temperature.

DSC samples were prepared by cutting slices of ~ 1 mm of thickness using a Struers Accutom-5 precision cutting machine. This was followed by electro-discharge machining (EDM) into round discs of diameter ~ 3 mm. The discs were

manually finished to 2500-grit silicon carbide grinding paper to remove EDM marks.

DSC was conducted with a Netzsch DSC 404 high temperature differential scanning calorimeter. This instrument uses S-type thermocouples (Pt-Pt 10% Rh) on both the sample and the reference, calibrated against the T_m of pure nickel and pure gold. In order to minimise oxidation, tests were conducted using high-purity Al_2O_3 crucibles in a dynamic high-purity argon environment with an argon flow rate of 50 mL/min.

Samples were heated up to 1250°C to ensure the full dissolution of the γ' phase. Since the hot die forging window necessarily lies below T_m, complete melting was not required. The thermal cycle started with a 10-minute isothermal segment at 50°C, followed by heating to 1250°C at 10°C/min, a 3-minute dwell at 1250°C, and cooling to 80°C at a rate of $-$ 10°C/min.

3.3 Heat treatments

The Udimet 720 as-forged pancake was cut into smaller (~ 30 x 30 x 10 mm) sections with a Birkett Cutmaster Ltd. Aquacut power saw and a computerised numerical control (CNC) EDM machine. In turn, these sections were cut into 10 mm cubes using a Struers Accutom-5 precision cutting machine. The heat treatment of samples was performed in argon-backfilled quartz ampoules for 20 minutes or 4 hours at 1030°C, 1060°C, 1100°C, or 1150°C. All samples were swiftly water-quenched to preserve most microstructural features for SEM examination.

René 65 heat treatment specimens were obtained from the disc-forging section using the same equipment and procedure described above. They were subsequently heat treated for 20 minutes or 4 hours at 1000°C, 1030°C, and 1070°C, followed by swift water quenching.

Following SEM analyses, Udimet 720 and René 65 micrographs were processed with ImageJ to quantify the total area fraction of γ' ($f_{\gamma'}$), the area fraction of primary, secondary, and tertiary γ' ($f_{\gamma'p}$, $f_{\gamma's}$, $f_{\gamma't}$); as well as the average size of each population ($r_{\gamma'p}$, $r_{\gamma's}$, $r_{\gamma't}$). The results were compared with equilibrium phase predictions computed using the Thermo-Calc software package with the TCNI8 database.

3.4 Finite element analysis

The hot die forging of a model Udimet 720 turbine disc and of laboratory-scale thermo-mechanical testing specimens were simulated by finite element analysis (FEA). The simulations were conducted by Otto Fuchs KG with the commercial package FORGE®. The raw data were subsequently curated, analysed, and visualised with MATLAB R2018a and Microsoft Excel.

The hot die forging of the turbine disc was modelled as a two-step process. In the first operation ('pre-forging'), forging stock was deformed into an intermediate shape. The second closed-die forging operation ('forging') turned the workpiece into its final shape. The cooling step following deformation was also simulated for 3,600 s. Adiabatic heating and die chilling (heat transfer) effects were incorporated to the model. The heat transfer coefficient between the workpiece and the die was 10 000 W m^{-2} K^{-1} for all conditions; the heat transfer coefficient between the workpiece and the air was 50 W m^{-2} K^{-1}. For forging, a sliding friction (Coulomb) coefficient of $\mu = 0.15$ and a friction factor of $m = 0.3$ were used. Based on technical expertise, these were doubled for pre-forging ($\mu = 0.30$, $m = 0.6$) to account for lower lubrication. The temperature of the workpiece at the start of pre-forging and forging was 1030°C, 1060°C, or 1100°C. To simulate the transfer of the workpiece from the furnace to the dies, a time lag of 15 seconds was introduced where heat transfer occurred without deformation. The ram speed was kept constant at 15 mm/s.

The thermo-mechanical testing of laboratory-scale Udimet 720 specimens was simulated for three geometries (Figure 3.1): a truncated double cone ('double cone'), a truncated double cone with a central cylindrical section, ('cylindrical double cone'), and a cylinder (see Section 6.3). They were compressed to a strain of 0.8, at a strain rate of 0.1 s^{-1}, and at temperatures of 1030°C, 1060°C, or 1100°C. These simulations used tungsten carbide anvils at a temperature of 550°C as recommended by Otto Fuchs KG.

Stress, strain, and temperature maps were produced with FORGE®. Tracer points were located at different locations of the simulated parts, for each of which data series with temperature, stress, strain, strain rate, and time were generated. Cooling rates were obtained by linear regression. The results of the FEA simulations were used to design the laboratory-scale thermo-mechanical tests aimed at mimicking full-scale hot die forging.

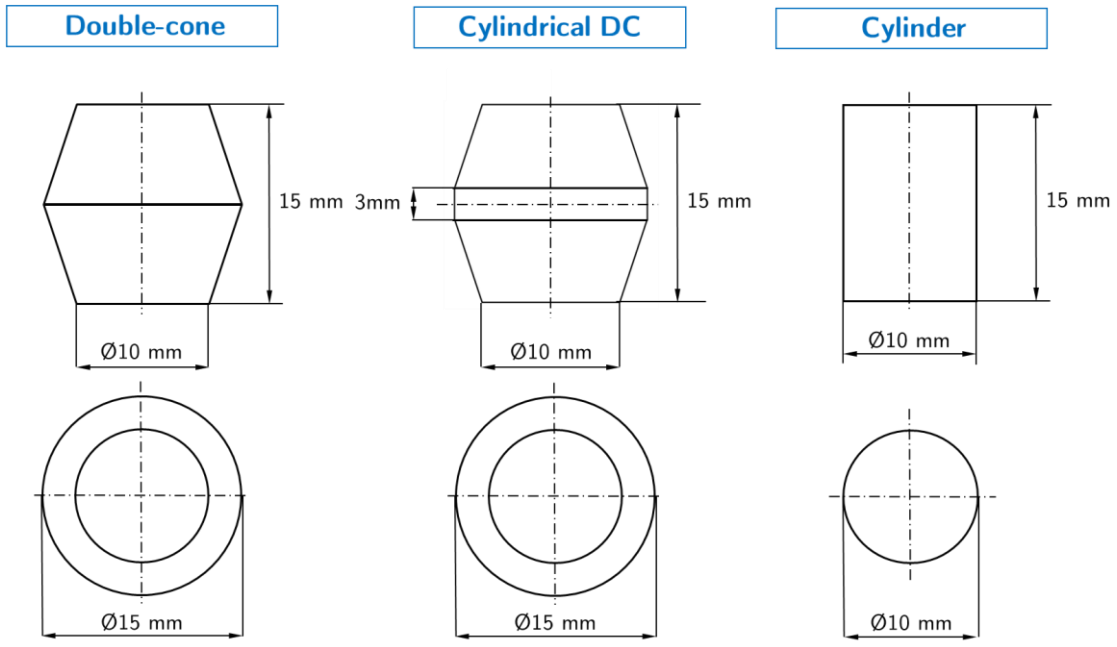

Figure 3.1. Candidate geometries for producing laboratory-scale thermo-mechanical testing specimens, which were studied by FEA.

3.5 Thermo-mechanical testing

High temperature compression tests were performed with a Gleeble 3800-GTC thermal-mechanical simulation system at Delft University of Technology. Figure 3.2A shows a schematic of the testing system. For Udimet 720, 14 cylinders and 26 double cone specimens were tested. For the validation experiments with René 65, 23 cylinders and 8 double cone specimens were tested.

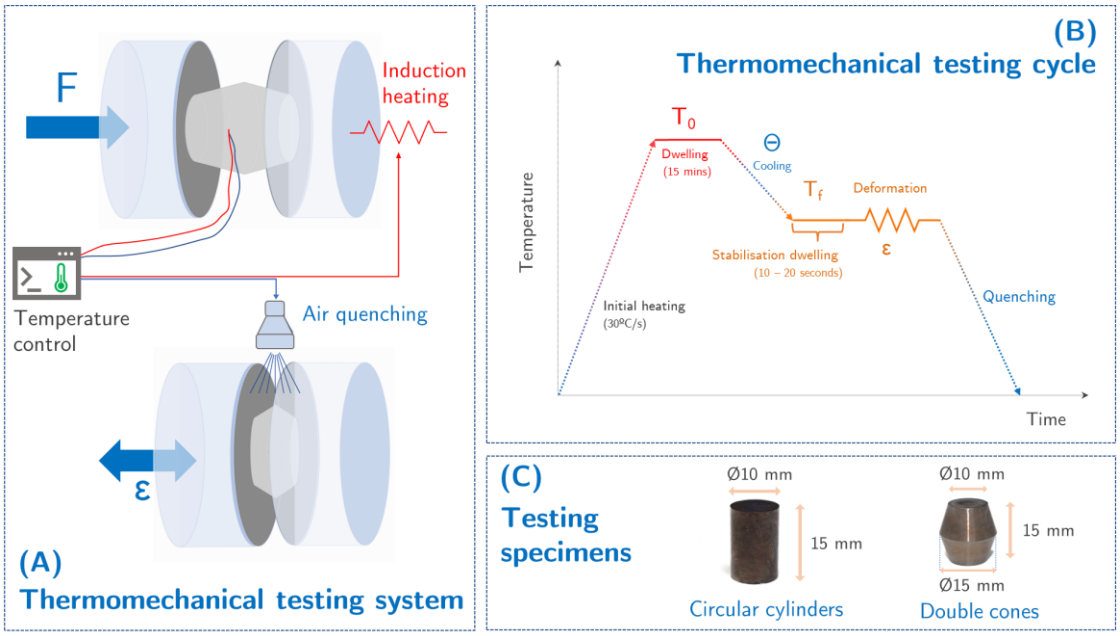

Figure 3.2. (A) Schematic of the Gleeble 3800-GTC thermal-mechanical simulation system. (B) Thermo-mechanical testing cycle. (C) Circular cylindrical and double cone specimens used for the forging simulation thermo-mechanical tests.

The Udimet 720 testing specimens were subject to the thermo-mechanical cycle shown in Figure 3.2B, which was designed to mimic full-scale hot die forging. The rationale behind this cycle is developed in Section 6.2. First, they were rapidly heat up to a 'forging temperature' (T_0) of 1030°C, 1060°C, or 1100°C. This was followed by a dwell step of 15 minutes to obtain microstructures representative of full-scale processing and ensure temperature homogeneity across the sample. Subsequently, the samples were cooled down at rates of 1°C/s, 10°C/s

or 30°C/s to a final temperature (T_f) of 880°C. Cooling at rates of 1°C/s, 10°C/s were achieved through natural cooling – reducing the heating input – whereas cooling at 30°C/s necessitated air quenching. After a stabilisation dwelling of 10 to 20 seconds to reach temperature homogeneity, samples were deformed to strains of $\sim 0.60 - 0.85$ at a strain rate of 0.1 s^{-1}. Finally, the specimens were air quenched to room temperature to freeze their microstructures for EM analysis. To minimise oxidation, all tests were conducted in vacuum.

To ensure appropriate induction heating, the oxide layer was removed by polishing the surface of the specimens with 2500-grit silicon carbide grinding paper. Before each test, an R-type thermocouple was welded to the centre of the specimen to measure the surface temperature. To reduce friction, anti-seizure nickel paste and graphite foil were applied between the specimen and the ISO-T tungsten carbide anvils. Prior to thermo-mechanical testing, all samples were heat treated for 4-hours at their respective T_0, followed by swift water quenching; this allowed obtaining microstructures representative of hot die forging using a dwell time of only 15 minutes (see Section 6.2).

Following thermo-mechanical testing, specimens were visually inspected and classified qualitatively according to their level of surface cracking. Their final dimensions were measured with callipers; with this, a strain measurement was obtained which was compared to the strain figure provided by the Gleeble. Data series of temperature, force, stress, ram displacement, strain, strain rate, and time were obtained. The raw data were processed and visualised with OriginPro and Microsoft Excel.

3.6 Full-scale forging

To validate the findings of Chapters 4 – 8, Udimet 720 forging stock was hot die forged into a turbine disc. The forging trial was completed by Otto Fuchs KG in Meinerzhagen, Germany. The workpiece was furnace heated at 1100°C

until thermal and microstructural homogeneity were achieved. Next, it was deformed through the two-step process (forging, reheating, forging) previously simulated by FEA. After forging, the workpiece was inspected for cracks. The sections where cracks were detected were imaged, cut, and provided by Otto Fuchs KG. They were cut into smaller sections by EDM and subsequently into SEM compliant samples (~ 10 x 10 mm) with a Struers Accutom-5 precision cutting machine.

3.7 Metallographic sample preparation

The heat treated specimens were prepared into SEM samples using standard metallographic preparation techniques. They were mounted in conductive resin, ground with successively finer grades of SiC paper, and polished down to 1 µm diamond paste using a semi-automatic grinder/polisher Saphir 560. The samples were later electrolytically etched using a 10% phosphoric acid solution at ~ 3 V.

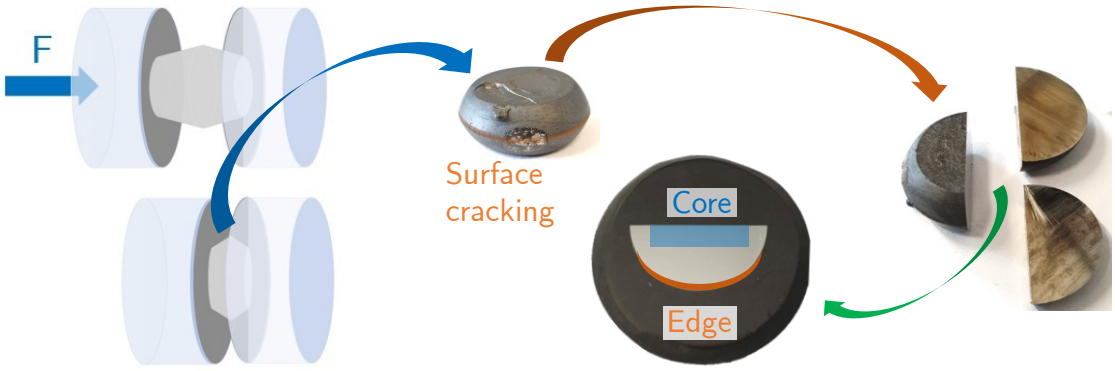

Figure 3.3. Schematic of the cutting and mounting process for Udimet 720 thermo-mechanically tested specimens.

Selected Udimet 720 thermo-mechanically tested specimens were examined fractographically and subsequently prepared into SEM samples. Figure 3.3 shows a schematic of the sample preparation process. Specimens were cut in parallel and perpendicularly to their vertical axis using a Struers Accutom-5 precision cutting

machine. The resulting semi-circular sections were prepared into EM samples using standard metallographic preparation techniques. Final chemical mechanical polishing was performed for 20 min – 30 min with non-crystallising 0.04 μm colloidal silica to obtain samples for backscattered electron (BSE) imaging, energy dispersive X-ray (EDX) microanalysis, and electron backscatter diffraction (EBSD). Later, the thermo-mechanically tested samples were electrolytically etched using a 10% phosphoric acid solution at ~ 3 V for secondary electron (SE) imaging.

Full-scale forging samples were prepared into SEM-BSE samples through the same procedure as Udimet 720 thermo-mechanically tested specimens.

3.8 Microstructural analyses

3.8.1 Scanning electron microscopy imaging

The microstructures of the heat treated, thermo-mechanically tested, and full-scale forging specimens were examined using a field emission gun scanning electron microscope Zeiss GeminiSEM 300. The heat treated specimens were imaged solely with SEs, whereas the rest were imaged with both SEs and BSEs.

SE imaging was performed with an acceleration voltage of 5 kV using an in-lens SE detector (I-L SED) and an Everhart Thornley detector (ETD). SEs result from inelastic interactions between the electron beam and atoms in the sample. They originate at the surface or near-surface of the sample, and their emission depends strongly on the topography of the sample. Therefore, collecting SEs allows using this contrast to create images of the topography of the sample. I-L SEDs provide better spatial resolution than ETDs [246], so the I-L SED was used to observe the smallest features – such as tertiary γ'. The ETD was used for lower magnifications as it displayed lower sensitivity to surface contamination and charging effects.

An annular backscatter detector (aBSD) was used for BSE imaging at 20 kV and working distances (WDs) of 4 – 6 mm. BSEs are incident beam electrons that upon hitting the sample are elastically scattered back out of it. BSEs have high energy and originate from a much larger region within the sample (interaction volume) than SEs. High atomic number (Z) elements increase the scattering frequency and thereby the yield of BSEs. This is used for imaging in the SEM by creating maps where the brightness of the pixels is a function of the BSE signal intensity. Since the intensity depends on Z, compositional contrast occurs whereby high-Z phases appear brighter than low-Z phases.

BSE imaging can also provide topographic and crystallographic information. Annular BSE detectors are normally divided in two or four segments. Subtracting the signal of alternating segments cancels the compositional contrast and allows recovering topographic information. For this reason, BSE imaging at 20 kV and WD ~ 4 mm – 6 mm was used for imaging a number of Udimet 720 and René 65 etched samples where charging and carbon contamination weakened SE topographic contrast.

3.8.2 EDX/EBSD

Energy-dispersive X-ray spectroscopy (EDX) and electron backscatter diffraction (EBSD) were performed on the Udimet 720 thermo-mechanically tested specimens using a Zeiss GeminiSEM 300 equipped with an Oxford Instruments X-Max EDX detector and an Oxford Instruments Symmetry EBSD detector.

EDX analysis was performed using an acceleration voltage of 20 kV, and a working distance of 10 mm. EDX provides information about the elemental composition of materials. It entails bombarding a sample with a focused electron beam and measuring the resulting X-ray emission spectrum. Incident electrons can excite inner shell electrons into higher energy states, creating vacancies in the

inner shell. As electrons from the outer shell fall to lower energy states to fill these vacancies, they emit element-specific X-ray photons. EDX detectors measure the intensity and energy of these X-rays. This allows identifying the elements present in the sample and their proportions – typically to an accuracy of ± 1 at. %.

Electron backscatter diffraction (EBSD) is an SEM based technique to study the crystallographic structure of materials. It provides information on the grain size distribution, grain boundary types, crystallographic orientation, misorientation, texture, and phase structure on a scale of millimetres to nanometres. In EBSD, samples are inclined to ~ 70° and hit by an electron beam. Primary beam electrons can be diffracted by the atomic planes of the crystal, and a phosphor screen is used to produce visible light diffraction patterns. These patterns – termed Kikuchi bands – are specific to the crystal structure and orientation of the material. The light produced by electrons hitting the phosphor screen is then detected by a CCD/SIT camera, converted to an image, and indexed digitally to obtain the structure and orientation of the crystal.

EBSD maps were acquired using an acceleration voltage of 25 kV, working distances of 10 – 15 mm, and step sizes of 0.1 – 0.2 μm. The EBSD maps were post-processed with Oxford Instruments HKL Channel 5 and AZtec software. Wide spikes and zero solutions were replaced with extrapolations from neighbouring pixels. For zero solutions, a minimum of five indexed neighbouring pixels were required. Separate grains were defined by a minimum of 100 pixels and a misorientation angle of 15°. Grain boundaries were divided in low-angle grain boundaries (LAGB) with misorientations lower than 15°, and high-angle grain boundaries (HAGB) with misorientations greater than 15°. Twin boundaries were defined by a misorientation of 60° about the ⟨111⟩ axis with a tolerance of 8.66°, according to Brandon's criterion for FCC crystals [247].

3.8.3 Panoramic imaging

A Zeiss GeminiSEM 300 was used to obtain SE panoramic images of the processed Udimet 720 thermo-mechanically tested samples. For each sample, ~ 10 x 30 individual SE images of magnification 100 X and a resolution of 4096 x 3072 pixels were acquired. These were stitched with Carl Zeiss SmartStitch software to high accuracy. The resulting panoramic images were split in two and post processed with ImageJ as described in Section 3.8.4. Splitting the images was required since ImageJ did not support images as large as ~ 40 K x 92 K pixels.

3.8.4 Image analysis

Image analysis was conducted using the ImageJ 1.50b software. For the Udimet 720 and René 65 heat treated samples and the Udimet 720 thermo-mechanically tested specimens, the PSD (area fraction and average size) of γ' precipitates was measured following the operations outlined in Figure 3.4.

First, as-acquired SE images were converted to 8-bit grayscale. A median filter with a radius of 2 pixels was applied, followed by thresholding and noise reduction. Noise reduction consisted of removing bright and dark outliers with a radius of 5 pixels, as well as despeckling. Subsequently, the 'close', 'fill holes', and 'watershed' binary operations were employed. Closing particles is equivalent to a dilation and erosion operation, while watershed serves for cutting apart incorrectly connected particles into separate ones. Finally, the particle analysis tool was used for measuring the area fraction and average size of γ' particles. Particles were filtered by area to separate γ'_{p}, γ'_{s}, and γ'_{t}. The Feret diameter was used to quantify the average particle size. A minimum of 100 particles of each population of γ' in each condition were averaged to obtain the average size.

Similarly, ImageJ was used to obtain the fraction of surface cracks of the panoramic images of Section 3.8.3. The stitched images were converted to 8-bit grayscale, and the black background surrounding the sample was made into RGB

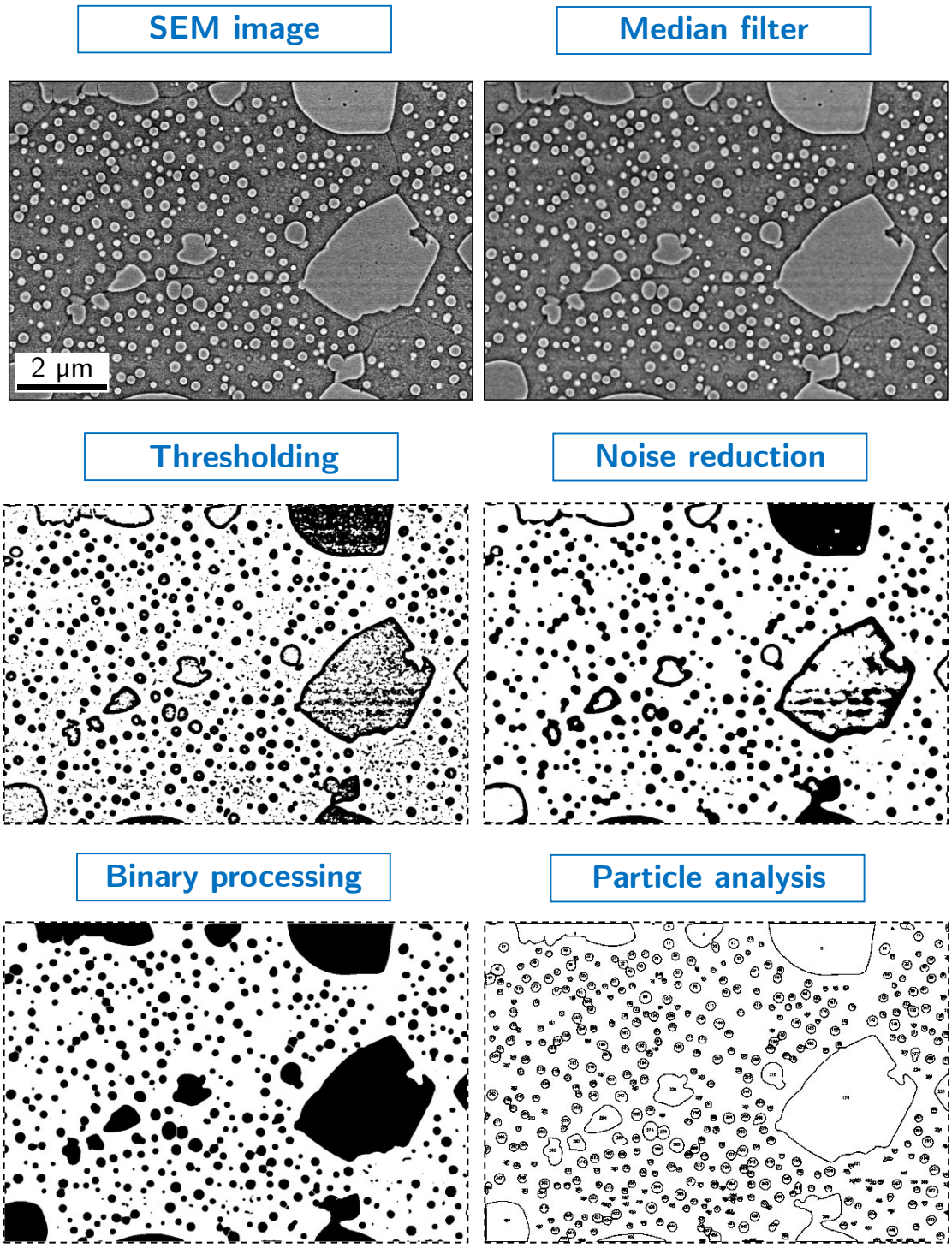

Figure 3.4. Image processing sequence used for measuring the γ' PSD on the Udimet 720 and René 65 heat treated material and the Udimet 720 thermo-mechanically tested specimens.

(255, 255, 255) white. The contour of the semi-circular samples was traced manually, and the area outside of it converted to RGB (0,0,0) black. After that, the thresholding tool was used to measure the area fraction of RGB (255, 255, 255), corresponding to the surface cracks. Finally, a multiple linear regression model was fitted with MATLAB to describe the relationship between forging temperature, cooling rate, and fraction of surface cracks.

4

Microstructural evolution

In this chapter, the microstructural evolution of Udimet 720 is studied within an exploratory hot working window. Research by Monajati et al. [34] on Udimet 720, and Wan et al. [217] and Wang et al. [36] on Udimet 720Li indicates that the isothermal forging window of Udimet 720 lies in the 1080°C – 1160°C temperature range. For hot die forging, the studies of Fahrmann and Suzuki [134] and Sczerzenie and Maurer [31] suggest that ductility is highest at ~ 1000°C – 1100°C. Therefore, this analysis considers the entire 1000°C – 1160°C range as a starting point.

The chapter is structured as follows: first, thermal analysis is employed to investigate phase transitions and track γ' evolution in the preliminary hot die forging window. Then, the initial (as received) material is characterised by EM. Heat treatments and SEM examinations are used to comprehensively study the microstructural evolution of the material. The volume fraction and mean size of γ' particles are quantified and compared to Thermo-Calc equilibrium predictions. Finally, the evolution of γ' with temperature is discussed in relation to hot die forgeability, and an upper limit is established for the forging window.

4.1 Thermal analysis

Figure 4.1 shows the DSC thermogram of Udimet 720 from initial (as forged) state. The dissolution of γ' occurs between ~ 760°C and ~ 1240°C, and melting starts slightly above the γ' solvus. The dissolution of the different populations of γ' is discussed below. No other phase transformations are identified.

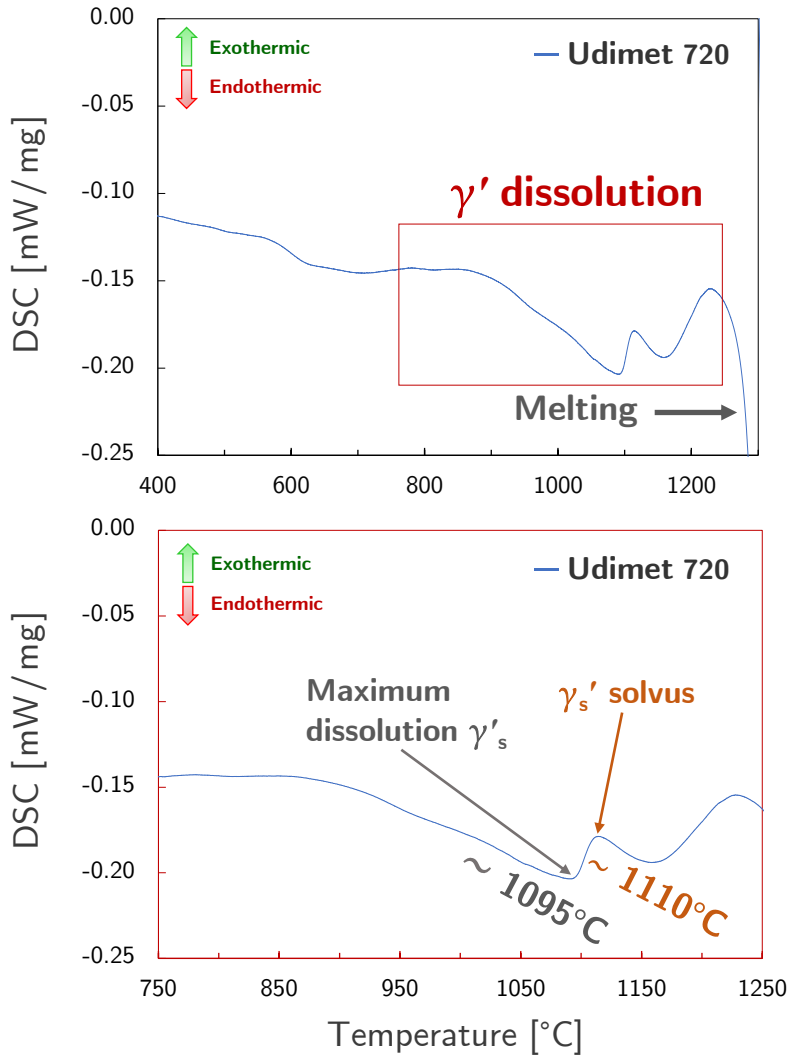

Figure 4.1. DSC thermogram of as-forged Udimet 720 material. The bottom figure is a close-up version of the γ' dissolution window shown at the top.

A small endothermic peak is detected at ~ 760°C – 840°C. Although γ'_t is not observed via SEM in the as-received condition (see Section 4.2), this event could be linked to the dissolution of γ'_t precipitates below the SEM resolution limit. The larger endothermic peak at ~ 860°C – 1110°C corresponds to the

dissolution of γ'_s. Here, the heat flow markedly decreases until 1095°C before starting to return to the baseline. This shows that the γ'_s dissolution rate accelerates until it peaks at ~ 1095°C. By ~ 1110°C all the γ'_s is dissolved.

A final endothermic event overlaps with the dissolution of γ'_s. The peak starts at 1110°C, extends until 1230°C, and is attributed to the dissolution of intergranular γ'_p. This event occurs considerably above the solvus temperature ~ 1143°C – 1157°C commonly reported in the literature [31,34,248]. Heat treatments and EM examinations (see Section 4.3) confirm that the material contains substantial amounts of γ'_p following 4 hours heat treatments at 1150°C. This suggests that equilibrium is not achieved when the material is heated at a rate of 10°C/min, so higher temperatures are required to completely dissolve γ'_p.

Although the splitting of γ'-dissolution in distinct γ'_p, γ'_s, and γ'_t events during DSC/DTA has been reported by some authors [249–251], it is not immediately obvious that this approach can be used effectively for Udimet 720. Moreover, no data on the γ'_s and γ'_t solvi of Udimet 720 are found in the literature. These results demonstrate that DSC can be successfully used for this purpose. The γ'_s and γ'_t solvi are determined to be ~ 1110°C and ~ 840°C, respectively.

4.2 EM analysis of as-received material

The SEM and EBSD characterisation of the material in as-forged condition are shown in Figure 4.2 and Figure 4.3, respectively. The microstructure consists of γ' precipitates of various sizes in a γ matrix. γ'_p precipitates of ~ 1 µm are present at the grain boundaries (Figure 4.2A–C). The interior of the grains is filled with fine γ'_s precipitates of ~ 100 nm. Cuboidal geometries and precipitate splitting are observed for γ'_s, indicating partial ageing. No other phases are observed. Image analysis reveals that γ'_p precipitates occupy an area fraction of 17% and have a mean size of 3 µm ± 3 µm, while γ'_s precipitates occupy an

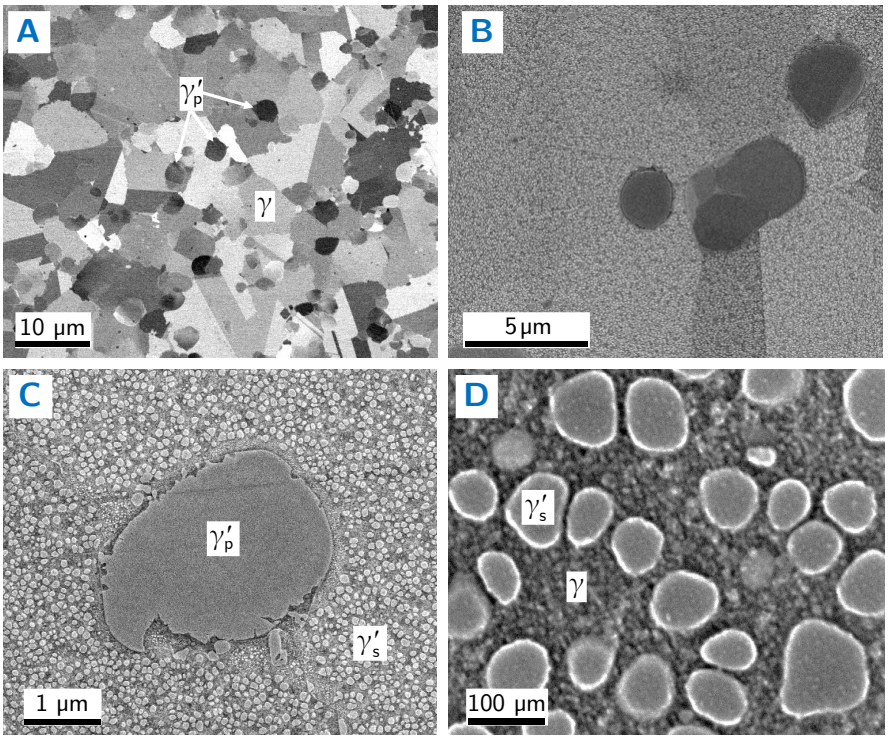

Figure 4.2. BSE (A) and SE (C – D) images of Udimet 720 material in initial (as-forged) state. Images of increasing magnification showing intergranular primary γ' (A – C) and intragranular secondary γ' (B – D) in a γ-matrix.

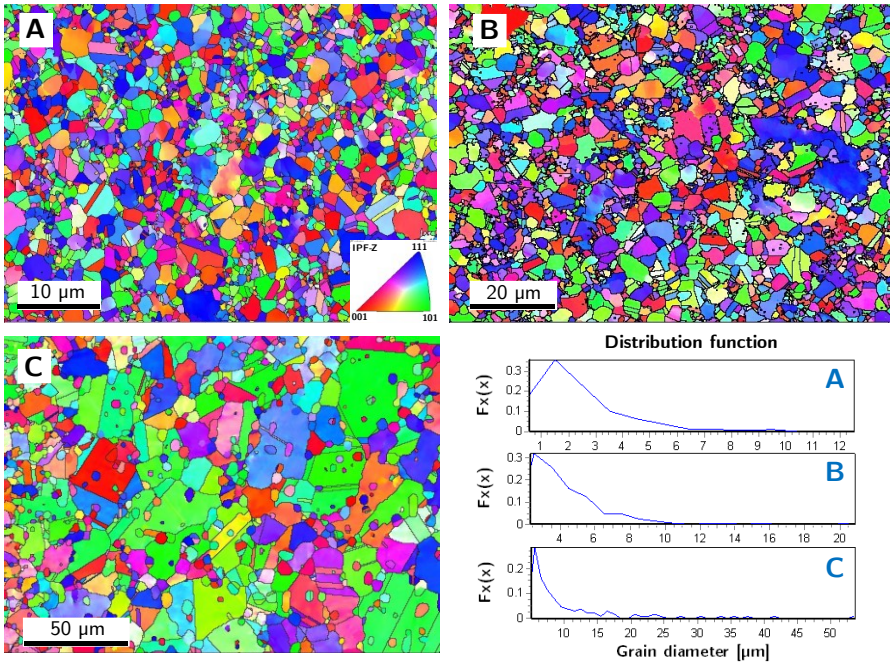

Figure 4.3. For the as-forged Udimet 720 material: EBSD inverse pole figure (IPF) maps and corresponding grain size distribution functions of different regions of the pancake. The colours indicate which crystal direction of the stereographic triangle is normal to the sampling plane.

area fraction of 32%, and their mean size is 80 nm ± 40 nm, where the measurement uncertainty is taken as the standard deviation. In this context, it is important to distinguish between the actual volume fraction occupied by a certain phase and the area fraction that can be measured experimentally from 2D micrographs. All area fraction measurements of this research work were obtained from uniform, random samples. Hence, according to Delesse's principle, the expected value of the area fraction is equal to the volume fraction [252]. Hereafter, a single variable (f) is often used to represent both quantities.

Certain variability in grain size is found across the pancake. Grains span from ~ 1 µm in some regions (Figure 4.3A) to ~ 10 µm in others (Figure 4.3C). The mean grain diameters for the EBSD maps of Figure 4.3A–C are 2 µm ± 2 µm, 4 µm ± 2 µm, and 10 µm ± 8 µm, respectively. In addition, regions of finer grains pinned by smaller γ'_p precipitates are identified (see Figure 4.4). Heaney et al. [33] reported similar structures in René 65; they stated that these are a carry-over from the billet microstructure where the volume fraction and composition of γ' are equivalent to other areas.

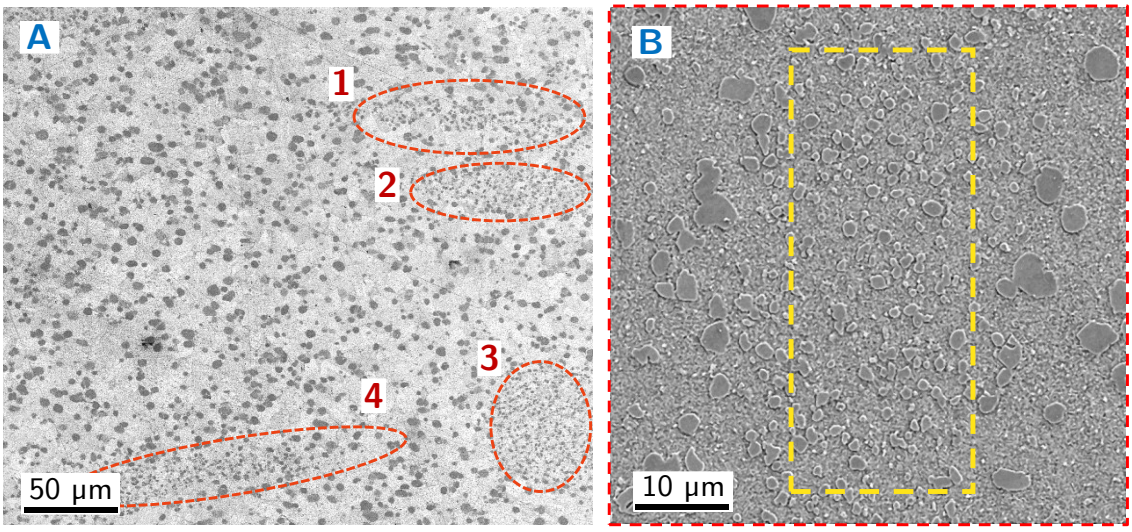

Figure 4.4. (A) SE SEM micrograph of the as-forged Udimet 720 material showing regions of finer grains and finer primary γ' precipitates (1 – 4). (B) Higher magnification micrograph with one such area highlighted.

4.3 Heat-treatments

Udimet 720 specimens were heat treated for 20 minutes or 4 hours near the limits of the exploratory hot die forging window – at 1030°C or 1150°C. Based on the thermal analysis results, samples were also heat treated at 1100°C – slightly below the γ'_s solvus – and at the intermediate temperature of 1060°C. The heat treatment time of 4 hours is selected to represent typical industrial furnace times prior to forging. Due to the unavailability of industrial data, the sub-solvus solutionising time for Udimet 720Li reported by Gopinath et al. [253] is used as a proxy. The 20-minute heat treatment is selected as an intermediate step, and to ascertain whether this time is long enough to achieve equilibrium. The latter consideration has implications for thermo-mechanical testing, as detailed in Section 6.1.

SE SEM images of heat treated and γ-etched specimens are shown in Figure 4.5. In this analysis, secondary γ' (γ'_s) refers to the unimodal distribution of intragranular γ' precipitates observed in the as-forged condition (Figure 4.2C,D) and retained upon heat treatment. Tertiary γ' (γ'_t) denotes newly formed γ' – for example those observed below in Figure 4.5R. Henceforth, this nomenclature will be employed consistently in this thesis. The volume fraction and mean size of γ'_p and γ'_s measured with ImageJ are plotted in Figure 4.6. γ'_p is observed at the grain boundaries in all low magnification (Figure 4.5A–F) and medium magnification images (Figure 4.5G–L). For the 4 hours heat treatments, $f_{\gamma'_p}$ decreases modestly from 17% in as-forged condition to 14% at 1030°C. As the temperature increases to 1060°C and 1100°C, it drops slightly further to 13% and 11%. γ'_p dissolution is even less significant for the 20-minute heat treatments (see Figure 4.6A), with $f_{\gamma'_p} = 13\%$ at 1100°C. γ'_p is consistently smaller in size after heat treatment, although substantial dispersion exists.

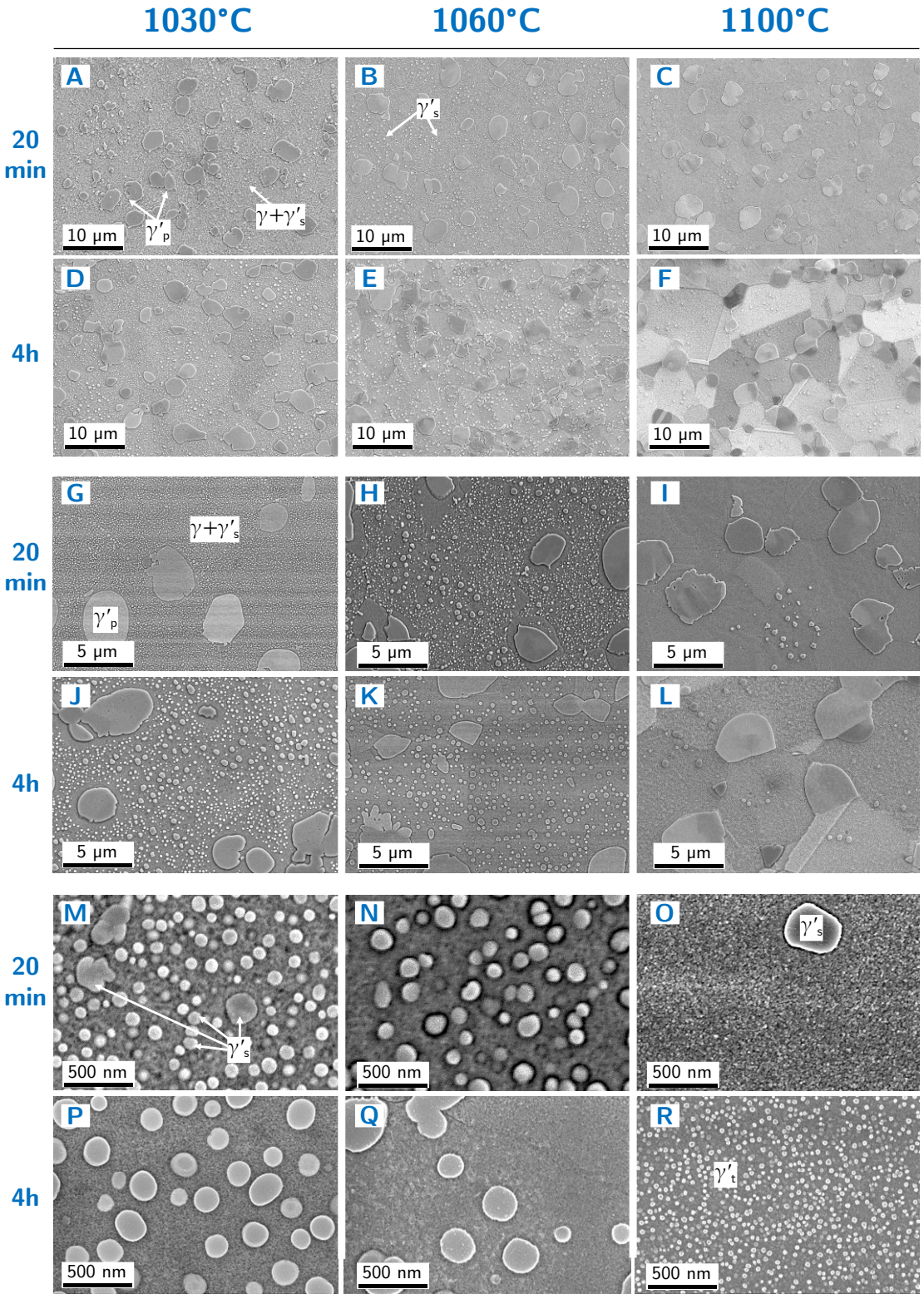

Figure 4.5. SE SEM images of heat treated Udimet 720 specimens at low magnification (A – F), medium magnification (G – L), and high magnification (M – R). Primary, secondary, and tertiary precipitates γ are labelled γ'_{p}, γ'_{s}, and γ'_{t}.

Significant γ'_s coarsening by Ostwald ripening occurs upon heating. This phenomenon is well documented for γ' precipitates in nickel-based superalloys [254,255]. Coarsened precipitates are visible at low magnification in the samples heat treated at 1030°C for 4 hours (Figure 4.5D), 1060°C for 20 minutes (Figure 4.5B) and 4 hours (Figure 4.5E), and 1100°C for 20 minutes (Figure 4.5C) and 4 hours (Figure 4.5F). Medium and high magnification images (Figure 4.5G,M) reveal that γ'_s also coarsens in the sample heat treated at 1030°C for 20 minutes.

Incomplete γ'_s coarsening is found in the samples heat treated for 20 minutes. In particular, the 1030°C – 20 minute sample (Figure 4.5G,M) displays smaller and more numerous γ'_s precipitates than the 1030°C – 4 hours one (see Figure 4.5J,P). The mean γ'_s particle size is 80 nm for 20 minutes versus 200 nm for 4 hours, and their area fractions are 20% and 14% respectively. The 1060°C – 20 minutes sample (Figure 4.5H) shows a bimodal distribution of coarse and fine γ'_s. The sizes of each population are 400 nm ± 50 nm and 80 nm ± 40 nm; their combined mean size is 100 nm and their combined volume fraction 18%. After 4 hours (Figure 4.5E,K,Q) the fine γ'_s dissolves, and only the coarse particles remain. Their mean size increases to 300 nm and the volume fraction decreases to $f_{\gamma's} = 14\%$. γ' coarsening kinetics appear to accelerate at higher temperatures: the 1100°C – 20 minutes sample (Figure 4.5C,I,O) contains very few γ'_s, and almost none are present after 4 hours (Figure 4.5F,L). In all cases, γ'_s precipitates morph from quasi-cuboidal to spherical, with no signs of ageing. Interestingly, very finely dispersed γ'_t are observed in the 1100°C – 4 hours sample (Figure 4.5R); they are believed to form during water quenching owing to the increased availability of γ' forming elements in the matrix.

The γ'_s area fraction decreases as the heat treatment temperature increases (Figure 4.6). The decline in $f_{\gamma's}$ is particularly pronounced from 1060°C to 1100°C. At 1100°C, almost all γ'_s dissolves. Similarly to the trend described for γ'_s particle sizes, the difference in $f_{\gamma's}$ between the 20 minutes and 4 hours heat treatments is less significant at higher temperatures, indicating faster kinetics. At 1030°C, $f_{\gamma's}$

is ~ 8% higher for the 20-minute treatment, yet at 1100°C that difference narrows to ~ 0.3%. Overall, the dissolution of virtually all γ'_s at 1100°C is consistent with the γ'_s solvus obtained through thermal analysis. Moreover, the intergranular γ'_p remaining largely unaffected in the 1030°C to 1100°C window is also in accordance with the onset of γ'_p dissolution at 1100°C found via DSC.

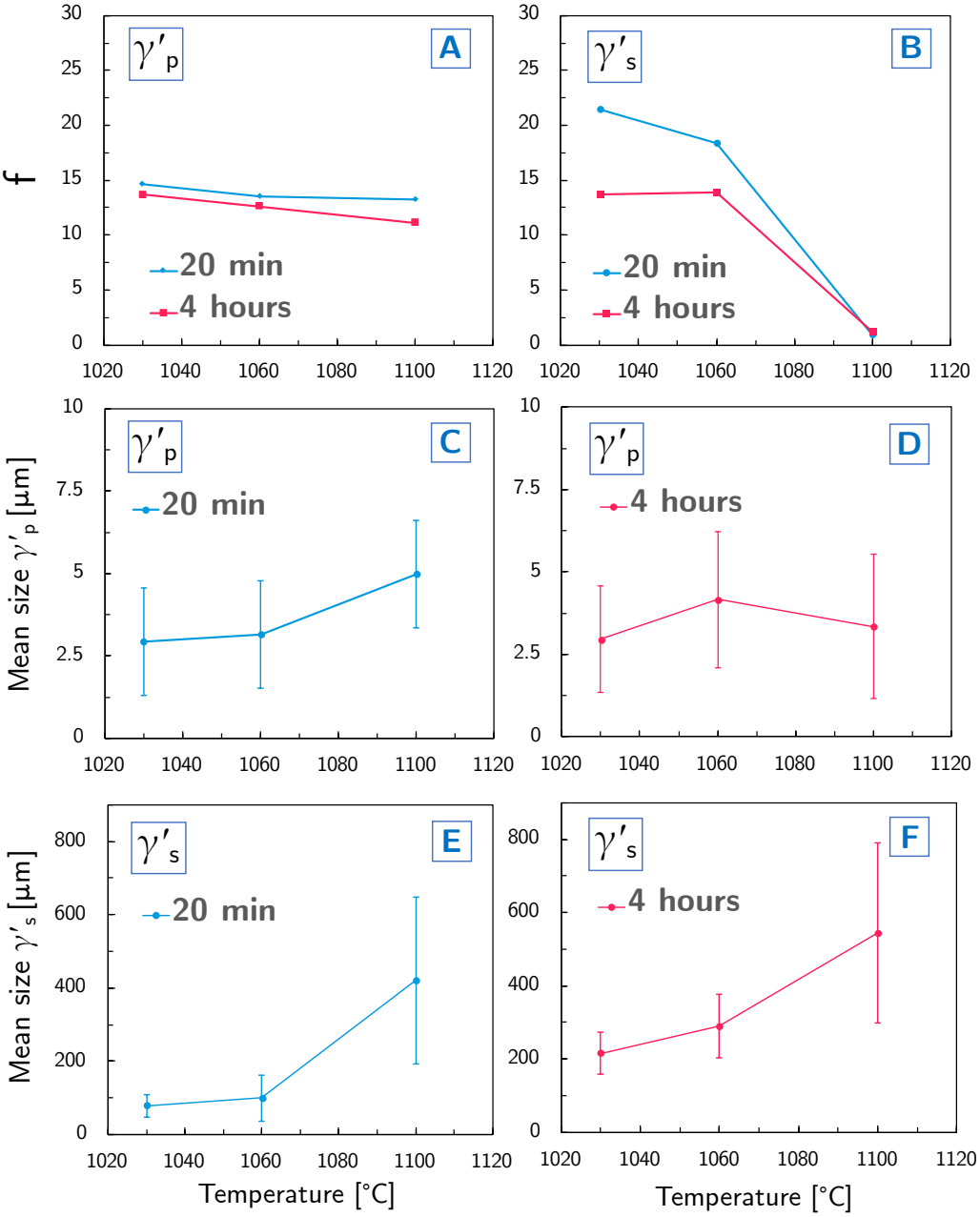

Figure 4.6. Measured volume fraction (A, B), mean size of γ'_p (C, D), and mean size of γ'_s (E, F) as a function of heat treatment temperature and time. The error bars represent the standard deviation of the sample.

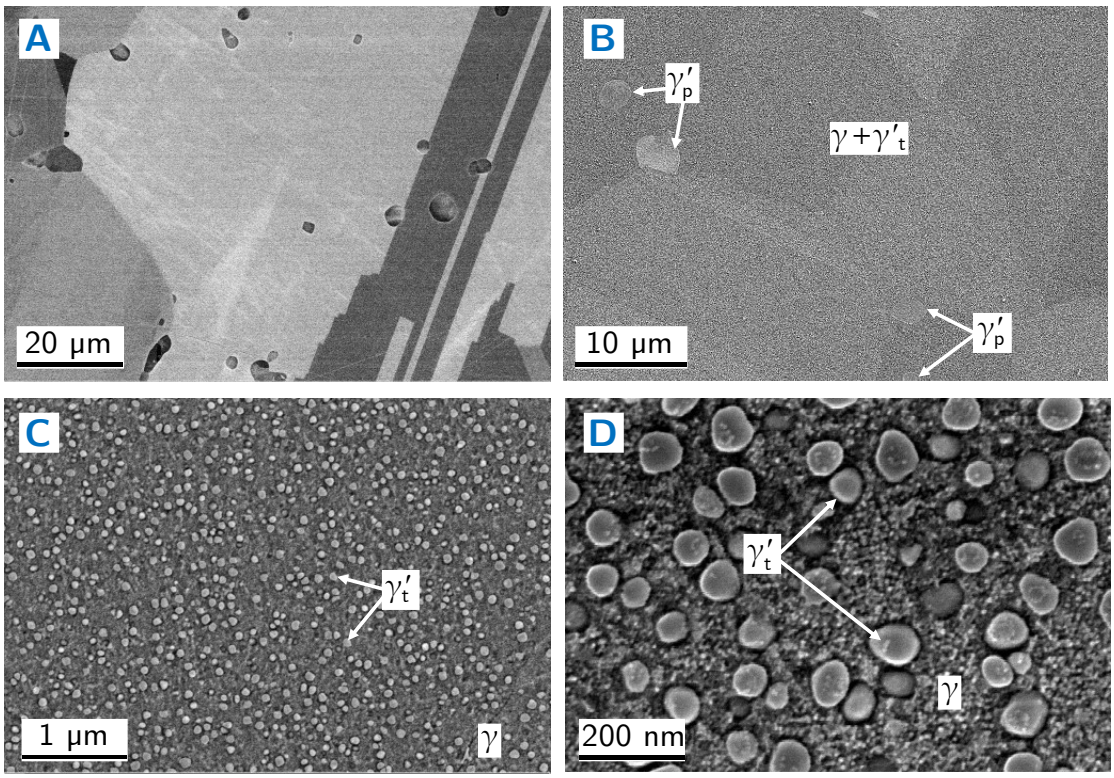

Figure 4.7. BSE (A) and SE (C – D) images of Udimet 720 heat treated for 4 hours at 1150°C. Images of increasing magnification showing intergranular primary γ' (A, B) and intragranular tertiary γ' (C,D) in the γ matrix.

Figure 4.7 shows BSE and SE micrographs of a specimen heat treated for 4 hours at 1150°C. Here, notable differences are seen with respect to previous conditions. First, the microstructure is not bimodal γ'_p/γ'_s but bimodal γ'_p/γ'_t; in other words, all the γ'_s precipitates dissolve, and numerous new γ'_t precipitates form upon cooling (Figure 4.7C,D). This finding further supports the hypothesis that the dissolution of greater amounts of γ'_s at higher heat treatment temperature gives rise upon cooling to a dispersion of very fine γ'_t precipitates. Secondly, a significant fraction of γ'_p dissolves into the matrix (Figure 4.7C,D). Yet, although $\sim$1150°C lies within the equilibrium solvus temperature range reported in the literature, intergranular γ'_p can be clearly seen in Figure 4.7A,B. This agrees with the γ'_p dissolution temperature obtained via thermal analysis and indicates that the material necessitates more than 4 hours at 1150°C to reach equilibrium. Finally, it is apparent that significant grain growth occurs; γ'_p precipitates appear to be in the interior of grains, and large annealing twins are

found (Figure 4.7A). This is attributed to the partial dissolution of γ'_p particles and their resulting diminished capacity to pin the grains during grain growth.

4.4 Comparison with thermodynamic simulations

The results of Section 4.3 were compared against equilibrium thermodynamic calculations. Thermo–Calc was used to obtain $f_{\gamma'}$ predictions in the 800 – 1200°C temperature range for the five typical nickel-based superalloys of Table 2.1. These results are shown in Figure 4.8A. In Figure 4.8B, the $f_{\gamma'}$ for Udimet 720 is compared with the $f_{\gamma'}$ (where $f_{\gamma'} = f_{\gamma'_p} + f_{\gamma'_s}$) obtained through heat treatment and image analysis.

For all five considered alloys, $f_{\gamma'}$ decreases monotonically above 800°C as the temperature increases. Moreover, the rate of change (i.e. $|\, df_{\gamma'} / dT \,|$) also increases with temperature. Both high γ' cast-and-wrought alloys – René 65 and Udimet 720 – have significantly larger $f_{\gamma'}$ than the two 718-type alloys. Their equilibrium γ' solvus temperatures are also higher: 1096°C for René 65 and 1127°C for Udimet 720 versus 975°C for Alloy 718 and 991°C for 718Plus. In turn, Udimet 720 has not only a higher $T_{\gamma'solvus}$ than René 65 but also a consistently greater $f_{\gamma'}$. The predicted solvus for René 65 agrees with that reported by Bond et al. [54] ($T_{\gamma'solvus} \sim 1111$°C), whereas for Udimet 720 it appears to be significantly underestimated.

The equilibrium predictions for Udimet 720 are below the measurements obtained through heat treatment. Importantly, the low $T_{\gamma'solvus}$ suggests that the $f_{\gamma'}$ prediction is underestimated, and hence the difference between $f_{\gamma'}$ in equilibrium and the measured data points is presumably narrower than shown in Figure 4.8B. The gap between equilibrium predictions and experimental data points is larger for the 20-minute than for the 4-hour heat treatments. It shows that $f_{\gamma'}$ measurements tend to the predicted $f_{\gamma'}$ curve as the heat treatment time increases. Such behaviour is in accordance with the observations of Sections 4.2

and 4.3. Therefore, the material is not in equilibrium after a 4-hour heat treatment but is relatively close to it. Moreover, the gap between the equilibrium prediction and the 20-minute heat treatment measurements decreases as the temperature increases, suggesting that γ' dissolution kinetics accelerate at higher temperatures.

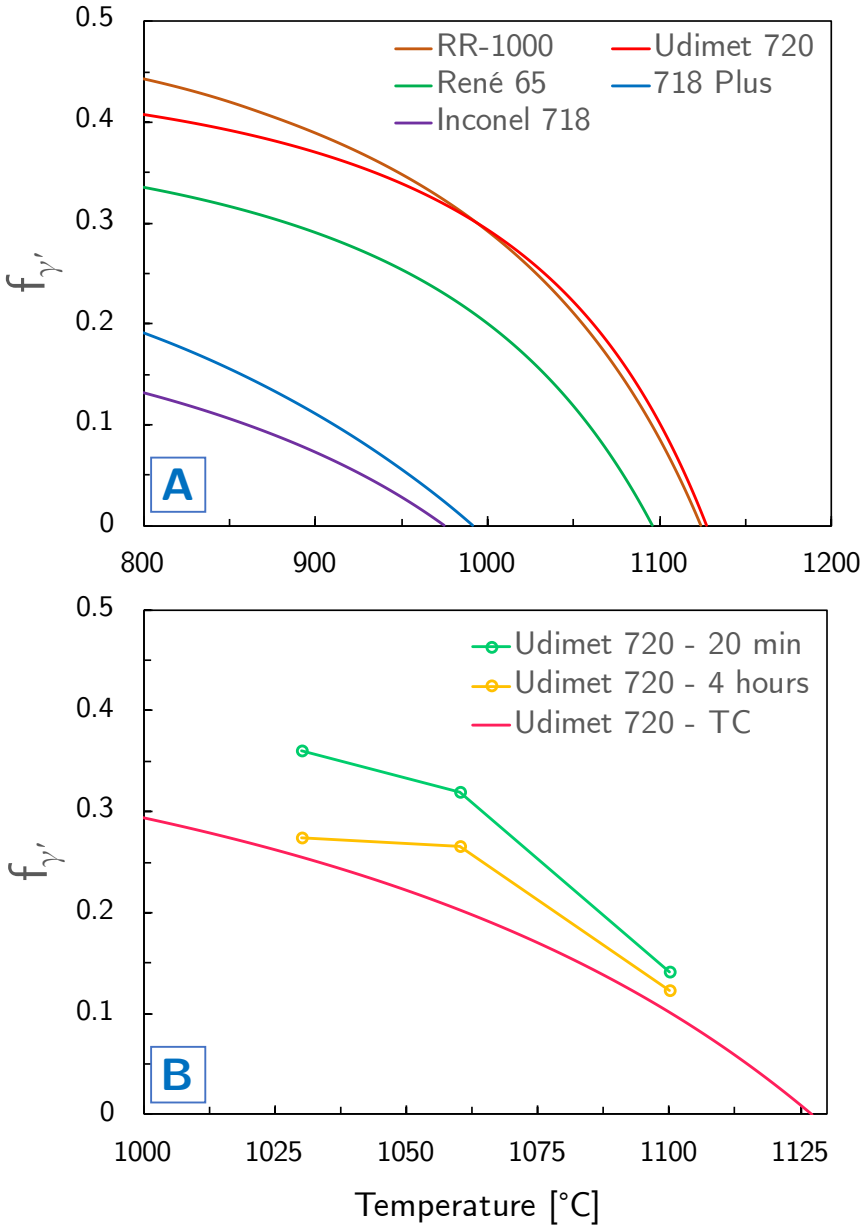

Figure 4.8. (A) Thermo-Calc predictions of the equilibrium γ'-phase volume fraction versus temperature for five typical nickel-based superalloys. (B) Equilibrium Thermo-Calc prediction for Udimet 720 and heat treatment experimental measurements.

4.5 Summary

The results and discussion of Sections 4.1 – 4.4 allow drawing several conclusions on the microstructural evolution and hot die forgeability of Udimet 720. First, DSC data and Thermo-Calc equilibrium predictions reveal a monotonic decrease of $f_{\gamma'}$ with temperature and no other phase transformations in the preliminary forging window. DSC is successfully employed to study the dissolution of different populations of γ' in the multimodal material. The previously unreported γ'_s and γ'_t solvi are found to be ~ 1110°C and ~ 840°C. Heat treatment and EM analysis reveal that a 4-hour heat treatment at 1150°C causes partial γ'_p dissolution and significant grain growth. Together with the mechanical testing experiments of Fahrmann and Suzuki [134] and Sczerzenie and Maurer [31], a clear picture emerges that the upper limit of the hot die forging window is ~ 1100°C. Below that temperature, γ'_p precipitates remain largely unaltered, their grain pinning effect is maintained, and undesirable grain growth is avoided. Therefore, an updated preliminary forging window can be established as 1000 – 1100°C. In addition, a trend is identified whereby higher heat treatment temperature dissolves a larger fraction of γ'_s precipitates up until ~ 1110°C, and of γ'_p thereafter. Upon rapid cooling, greater amounts of γ' forming elements in the matrix precipitate as a fine distribution of γ'_t.

5

Full-scale forging: FEM simulations

The forgeability of metallic materials depends on the interplay between processing parameters and microstructural evolution. Following the microstructural analyses of Chapter 4, in this chapter finite element modelling (FEM) is used to study the full-scale hot die forging of Udimet 720. This serves two purposes. First, it allows understanding for this and similar superalloys how the relevant thermo-mechanical variables evolve during processing. In this context, relevant variables refer to those which affect forgeability and surface cracking either directly or inducing microstructural changes. The most crucial of these are the stress, strain, strain rate, temperature, and cooling rate fields across the workpiece. Secondly, the results of this analysis are used to design the thermo-mechanical experiments that follow in Chapter 6. These experiments aim to simulate hot die forging through laboratory-scale tests. Therefore, obtaining data on the evolution of the said variables in the workpiece during full-scale hot die forging is essential to build accurate simulated tests. The chapter starts with a description of the physical model simulated through FEM. Then, results are presented and discussed for each of the five variables of interest. A summary of the most significant findings of the chapter is presented last.

5.1 Model description

The model used to study the hot die forging of a turbine disc is depicted in Figure 5.1. It consists of a two-step closed-die forging process. The first step is termed 'pre-forging' and involves deforming a Udimet 720 pancake into an intermediate shape. In the second operation or 'forging', the resulting workpiece is deformed into its final shape. Subsequently, a 3,600 s cooling time exists where no load is applied and the workpiece is allowed to cool naturally. Heat transfer happens between the workpiece, the dies, and the surrounding atmosphere; friction acts between the dies and the workpiece. The heat transfer and friction coefficients are detailed in Section 3.4.

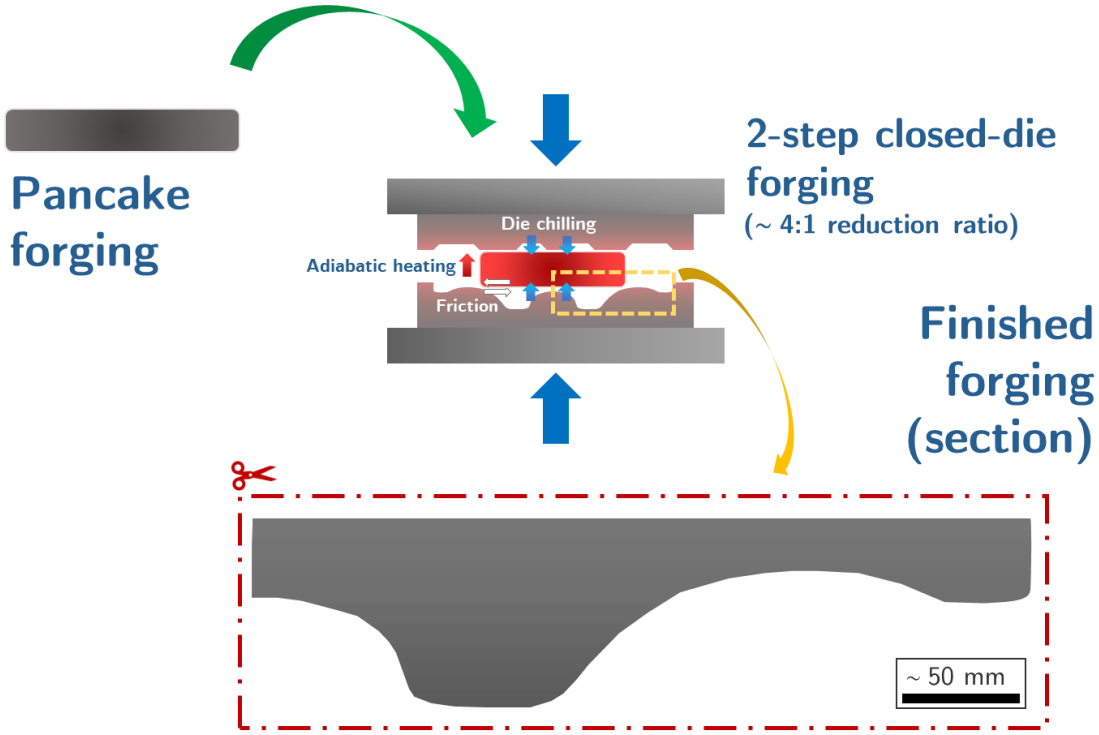

Figure 5.1. Schematic of the physical model used to simulate the hot die forging of a Udimet 720 turbine disc.

In both pre-forging and forging, the material is initially at a homogenous forging temperature T_0, which represents the temperature of the workpiece in the furnace prior to forging. Based on the findings of Chapter 4, three temperatures

were selected: 1030°C, 1060°C, and 1100°C. The latter sits below $T_{\gamma' s\ solvus}$, and the remaining two are spaced within the updated preliminary hot die forging window. The transfer of the workpiece from the furnace to the dies is simulated adding a 15 second lag time where heat transfer occurs without deformation. The ram speed is constant of 15 mm/s.

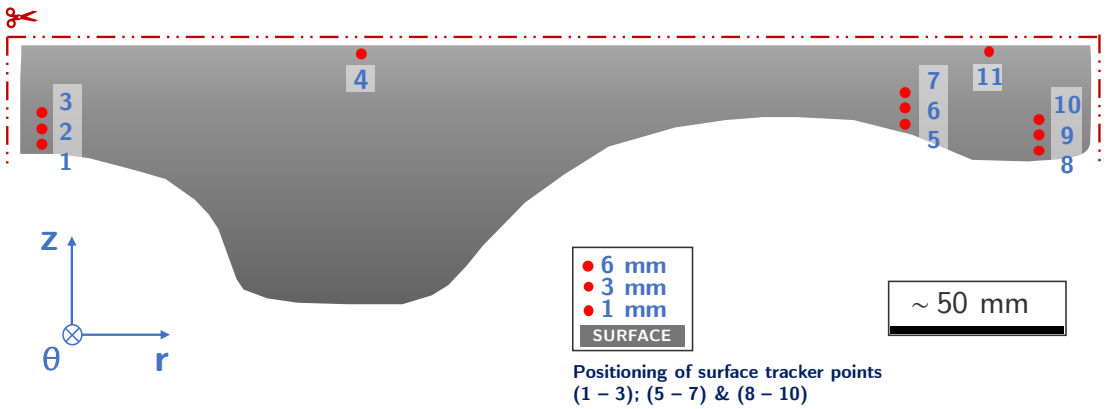

Figure 5.2. Schematic of the section of turbine disc analysed via FEM simulations. Points (1 – 11) designate the tracer points where data were extracted. The system of reference (r, θ, z) is shown at the bottom left of the figure.

The physical model was built into an FEM simulation by Otto Fuchs KG with the commercial package FORGE® and using proprietary information. The constitutive data for Udimet 720 were obtained through isothermal tests. To save computational costs, only the 2D section highlighted in Figure 5.1 and shown in Figure 5.2 is simulated. This is possible as the workpiece is axisymmetric and is assumed to be almost symmetric about the radial axis. Data are collected at 11 tracer points shown in Figure 5.2. Three sets of 3 tracer points each are placed at sections by the surface with different curvatures – these are designated as (1 – 3), (5 – 7), and (8 – 10). In addition, 2 tracer points (4, 11) are located at inner sections of the workpiece. Data are collected on temperature, strain, strain rate, and stress against time. For tensor and vector variables, the reference frame is shown in Figure 5.2; the coordinate functions (r, θ, z) correspond to the radial, tangential, and axial directions respectively. The FEA raw data provided by Otto

Fuchs were subsequently curated and visualised with MATLAB R2018a and Microsoft Excel to produce the analyses that follow.

5.2 Temperature and cooling rate evolution

Figure 5.3 shows temperature versus time during pre-forging and forging for a forging temperature (T_0) of 1100°C. In the analyses that follow, this forging temperature is taken as the benchmark against which results for $T_0 = 1030$°C and $T_0 = 1060$°C are compared. Similarly, various figures plot only data of the outermost sensors 1, 5, and 8 as illustrative of phenomena at the surface, and of sensor 4 to reflect the behaviour of the inner sections of the workpiece.

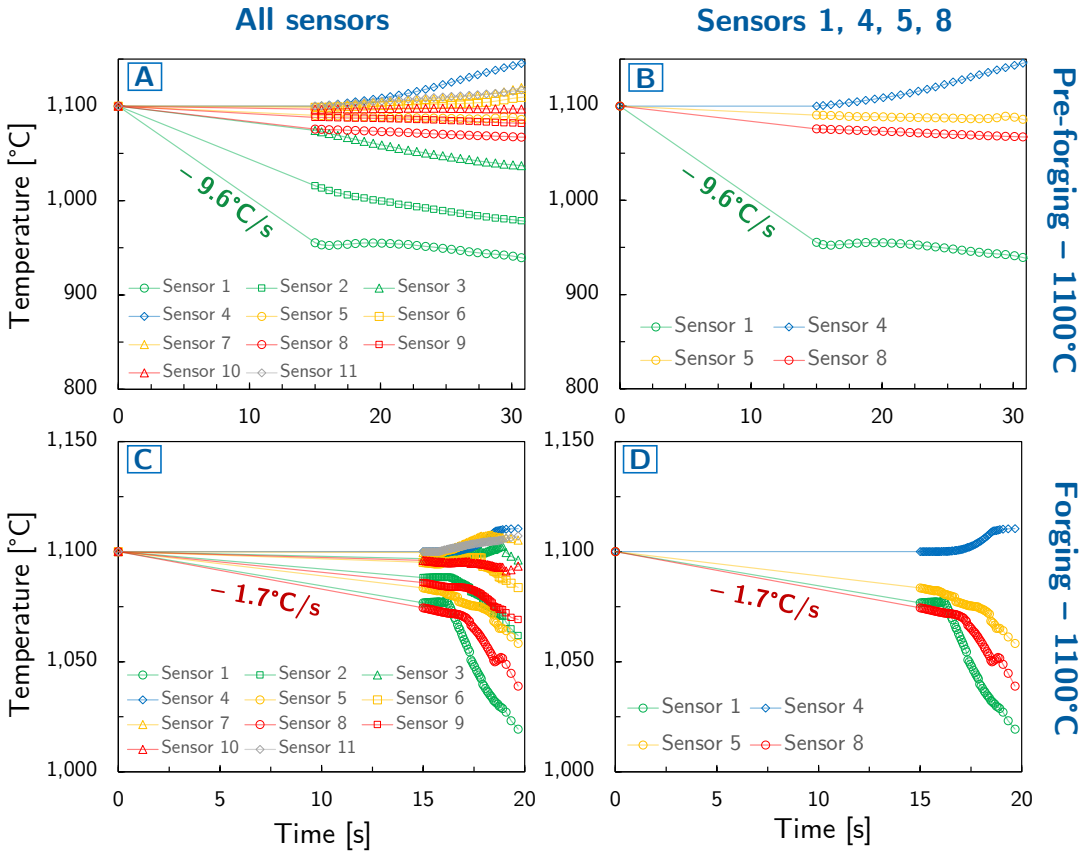

Figure 5.3. Temperature versus time at sensors 1 – 11 (A,C) and sensors 1, 4, 5, and 8 only (B,D) during pre-forging (A,B) and forging (C,D) for a forging temperature $T_0 = 1100$°C. The dots represent the numerical (simulated) solution at each time step.

In both pre-forging and forging, a distinct region is observed at $0 < t < 15$ s where the temperature decreases linearly. This corresponds to the transfer time between the furnace and the dies. Here, the cooling rate differs greatly across tracer points. During pre-forging, the temperature stays constant at the innermost tracer points (4, 11) and decreases slightly (< 25°C) at two of the three surface locations (sensors $5-7$ and $8-10$). By contrast, the temperature drops substantially at sensors $1-3$. Sensor 1 undergoes cooling at a rate of 9.6°C/s and reaches ~ 956°C by the time deformation starts. In forging, the innermost sensors behave in the same way, but all three surface sensors (1,5, and 8) see cooling rates of ~ 1.5°C/s and reach ~ 1075°C prior to deformation. An analysis of the deformation path for sensor 1 (not displayed) revealed that the $\sim 400\%$ difference in cooling rate is due to the displacement of the sensors during deformation. In pre-forging, sensor 1 is close to the surface where intense die chilling is acting, whereas in forging it has moved inwards and undergoes milder cooling. Overall, these results indicate that the surfaces of the workpiece can be cooled at rapid rates of up to ~ -10°C/s during transfer operations.

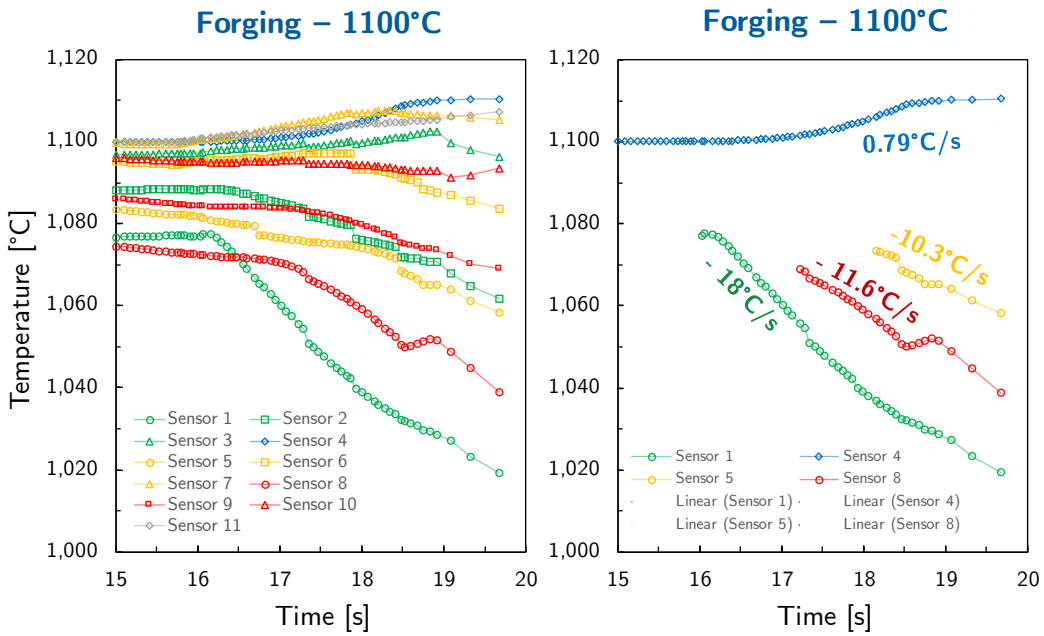

Figure 5.4. Temperature versus time at sensors $1-11$ (left) and sensors 1, 4, 5, and 8 only (right) during forging for $t > 15$ s and $T_0 = 1100$°C. On the right, a linear regression model is used to obtain cooling rates.

Figure 5.4 shows a close-up view of the subplots of Figure 5.3C,D for $t > 15$ s. This region corresponds to the deformation period, and both heat transfer and adiabatic heating occur. Similarly to the transfer operation, there are substantial differences across tracer points. The temperature drop is most significant at the outermost sensors 1, 5, and 8, and it diminishes with distance from the surface. Interestingly, the three innermost of the surface sensors (3, 7, and 10) effectively see no cooling. This suggests that die chilling only affects a narrow band of material (< 6 mm) in contact with the dies. Furthermore, it is observed that the temperature increases at the core of the workpiece (sensors 4 and 11) due to adiabatic heating outweighing heat transfer. A linear temperature drop is observed at the outermost surface sensors 1, 5, and 8 starting at ~ 16 s, ~ 17 s, and ~ 18 s. Their respective cooling rates obtained through linear regression are -18°C/s, -11.6°C/s and -10.3°C/s. The largest temperature drop of ~ 60°C happens at sensor 1. This linear regime is understood to begin when the workpiece and the die come into contact locally. The temperature stays nearly constant prior to the linear regime, further supporting the idea that noticeable workpiece cooling requires close proximity to the die.

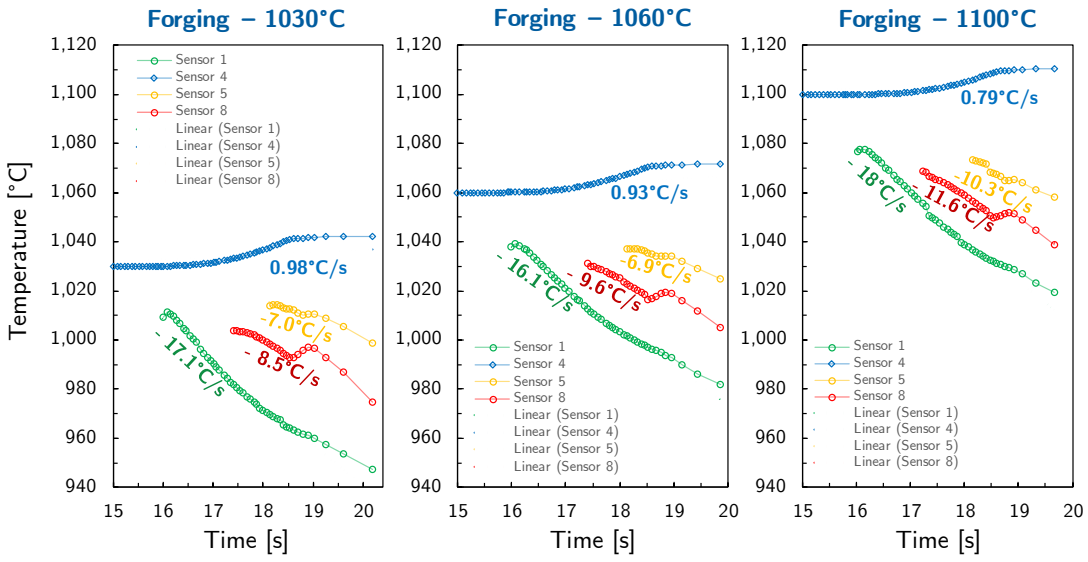

Figure 5.5. Temperature versus time at sensors 1, 4, 5, and 8 during forging for $t > 15$ s and $T_0 = 1030$°C, 1060°C, and 1100°C. Linear regression models are fitted to obtain cooling rates.

A comparison of temperature evolution for forging temperatures of 1030°C, 1060°C, and 1110°C is shown in Figure 5.5. No difference is noted in the temperature profiles as the forging temperature decreases, except for the initial temperature (T_0) shift. The cooling rates decrease slightly at lower forging temperatures, but not enough to change the overall decrease in temperature. For example, the temperature drop seen by sensor 1 consistently remains ~ 60°C.

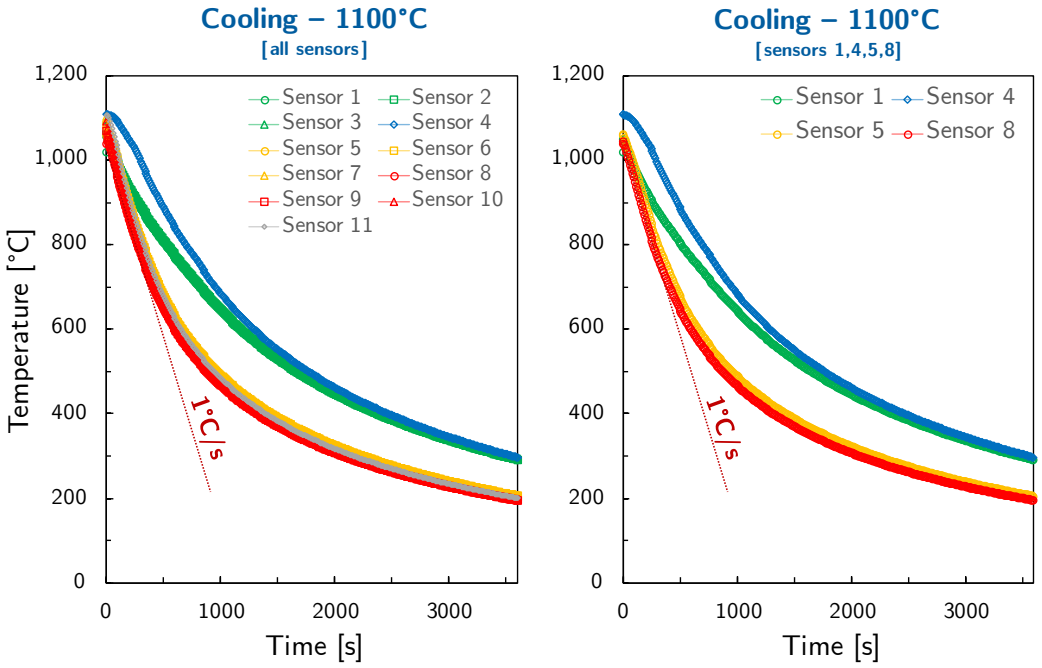

Figure 5.6. Temperature versus time at sensors 1 – 11 (left) and sensors 1, 4, 5, and 8 only (right) during cooling following forging for $T_0 = 1100$°C. Also plotted is a linear model of cooling at a rate of 1°C/s.

Temperature versus time data corresponding to the 3,600 s cooling period subsequent to forging are shown in Figure 5.6. In this case, the temperature drops more uniformly across tracer points. In addition, cooling is slower than during transfer or forging, with a fastest cooling rate of ~ 1°C/s. Since no rapid temperature drops or significant stresses or strains happen upon cooling, this step is unlikely to affect forgeability or surface cracking. Hence, it is not considered in subsequent analyses.

In summary, hot die forging operations induce cooling rates from $\sim 1°C/s$ to $\sim 20°C/s$ at the surface of the workpiece, resulting in temperature drops of up to $\sim 150°C$. Conversely, the temperature at the inner regions of the workpiece remains constant or increases slightly.

5.3 Strain evolution

The radial (ε_r), tangential (ε_θ), axial (ε_z), and shear (ε_{rz}) strain components corresponding to forging at $T_0 = 1100°C$ are shown in Figure 5.7. The shear strain components $\varepsilon_{r\theta}$ and $\varepsilon_{\theta z}$ are not shown since they are null for the entire domain. All strain components are bounded above by ~ 0.75 and below by ~ -0.8. As expected, the axial strain is greatest at most tracer points, although large radial and shear strains are also recorded at several locations. The tangential strain is generally lower and is bounded above by 0.4. Both tensile and compressive strains are seen across the workpiece for all except the tangential component, which stays consistently in tension. There appears to be a certain degree of symmetry of the radial and axial strains about the horizontal axis, whereby high tensile radial strains correlate with high compressive axial strains. The surface sensors ($1-3$, $5-7$, and $8-10$) largely display tensile radial strains and compressive axial strains, while no clear pattern is detected for shear. Concerning the outermost sensors (1, 5, 8), sensor 5 shows the largest radial, axial, and shear strain; however, the tangential strain is highest at sensor 8. Remarkably, no clear tendency is identified for the innermost sensors: sensor 11 behaves similarly to the surface points, but sensor 4 shifts from tensile to compressive radial, axial, and shear strains.

Although the geometry of the workpiece plays a major role in determining the deformation path during forging, certain differences across tracer points could be ascribed to thermal effects. In particular, there is a positive correlation between temperature and strain at sensors 4 (inner region) and 5 (surface). These sensors

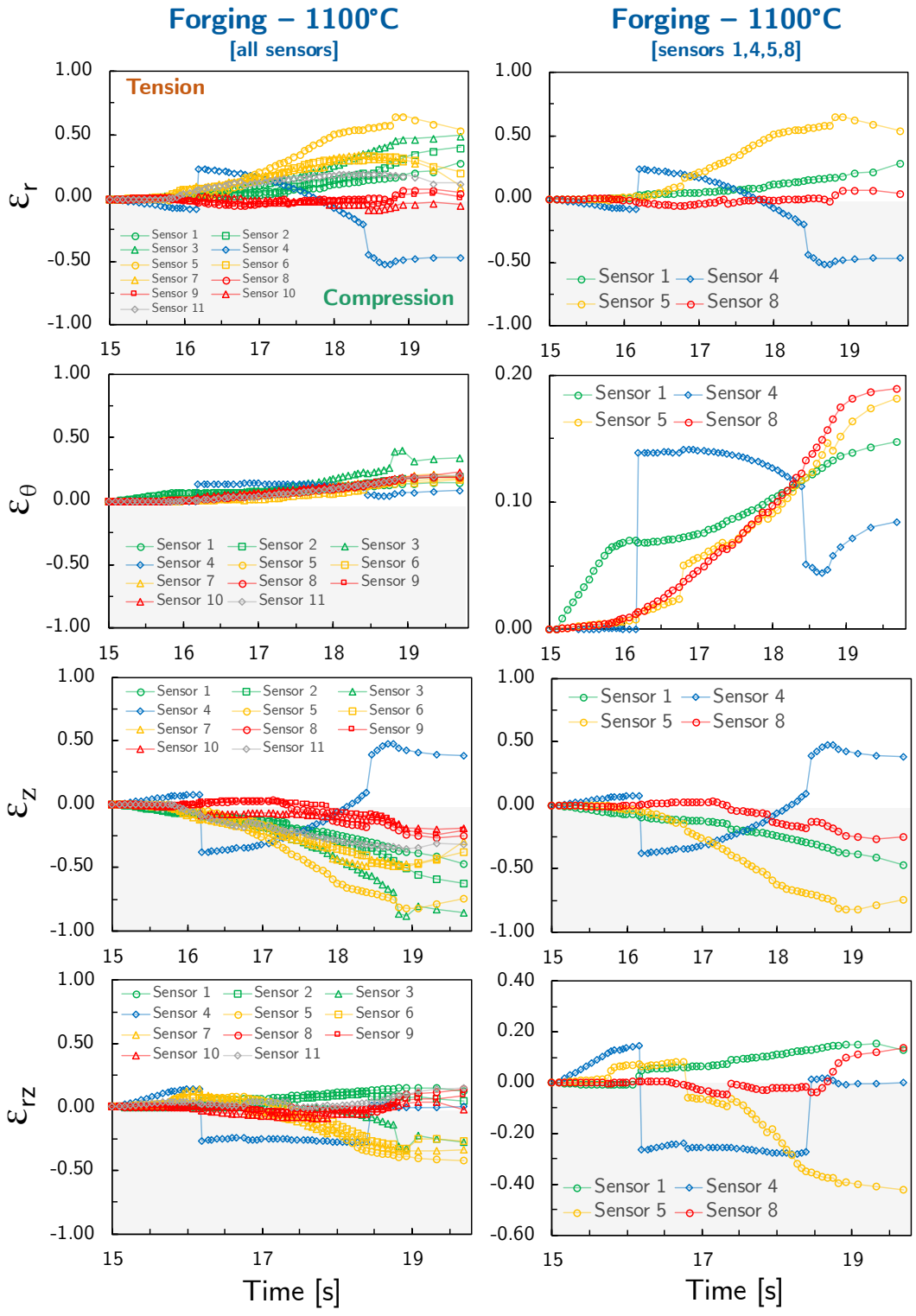

Figure 5.7. Strain components (radial, tangential, axial, and shear) versus time at sensors 1 – 11 (left column) and sensors 1, 4, 5, and 8 only (right column) during forging for t > 15 s and $T_0 = 1100°C$.

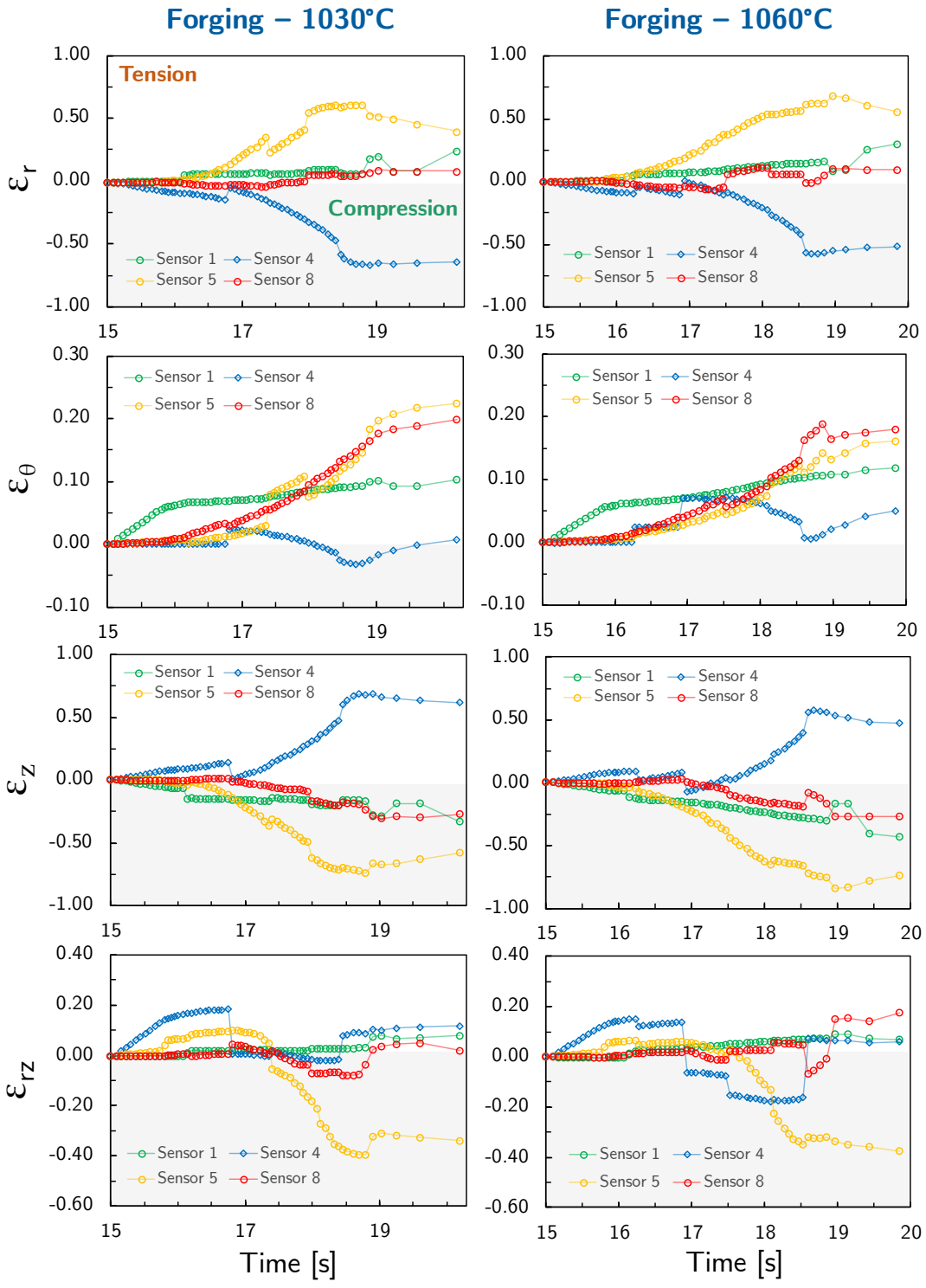

Figure 5.8. Strain components (radial, tangential, axial, and shear) versus time at sensors 1, 4, 5, and 8 during forging for t > 15 s and forging temperature T_0 = 1030°C (left column) and T_0 = 1060°C (right column).

maintain the highest temperatures during deformation (see Figure 5.4) and are subject to the highest strains. However, this trend does not hold for sensors 1 and 8; this is discussed further in Section 5.5.

The strain components for the remaining forging temperatures are shown in Figure 5.8. No variation in trends is observed, and therefore the analysis of $T_0 = 1100°C$ can be extended to $T_0 = 1060°C$. Minor differences are seen in tangential strain for $T_0 = 1030°C$: sensors 5 and 8 show higher tensile strains, and it is now sensor 5 that attains the highest tangential strain.

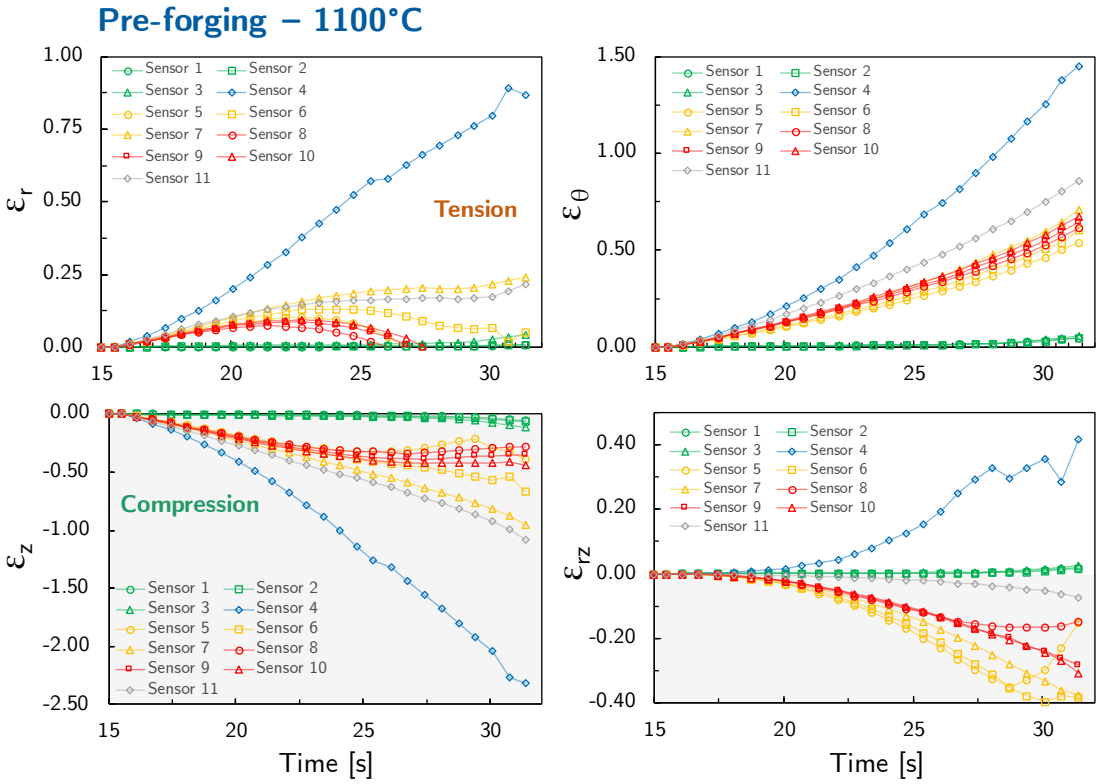

Figure 5.9. Strain components (radial, tangential, axial, and shear) versus time during pre-forging for t > 15 s and $T_0 = 1100°C$.

Figure 5.9 presents the strain components corresponding to pre-forging at $T_0 = 1100°C$. In this case, visible disparities exist with respect to forging. Sensor 4 attains much greater radial, tangential, and axial strains; while sensors 1, 2, and 3 see almost no strain. The remaining tracer points show generally lower radial

strains and larger tangential and axial strains. In addition, no tension to compression transitions are observed: both the radial and tangential strains are consistently in tension, and the axial strain is always in compression. Despite these differences, some trends noted for the forging step remain valid in pre-forging. Except for sensor 4, a similar upper boundary of $\varepsilon \lesssim 1$ exists. Besides, in both forging and pre-forging the radial and tangential strains are largely tensile and the axial strain compressive.

In summary, the greatest strain components across the workpiece are axial and radial – and indeed the maximum tensile strain is ~ 0.75 (radial) and the maximum compressive strain is ~ -0.8 (axial). At the surface, the radial strain is largely in tension, the axial strain is in compression, and the tangential strain is consistently in tension with an upper limit of 0.4.

5.4 Strain rate evolution

The strain rates during pre-forging and forging at different forging temperatures are plotted in Figure 5.10. These strain rates are obtained from the equivalent (von Mises) strain. In pre-forging, sensors $4-11$ show broadly constant strain rates of $\sim 0.1\ s^{-1}$; sensors $1-3$ display constant strain rates of $\sim 0.001\ s^{-1} - 0.01\ s^{-1}$, in line with their low strain values (see Figure 5.9). In forging, strain rates fluctuate around $0.1\ s^{-1}$ and are bounded below by $\sim 0.01\ s^{-1}$ and above by $\sim 1\ s^{-1}$. No dependence with temperature is noticeable for either forging or pre-forging. It is concluded that $\sim 0.1\ s^{-1}$ is a representative strain rate for a typical surface section of the workpiece.

5.5 Stress evolution

Figure 5.11 shows the radial (σ_r), tangential (σ_θ), axial (σ_z), and shear (τ_{rz}) stress components plotted against their corresponding strains during forging at

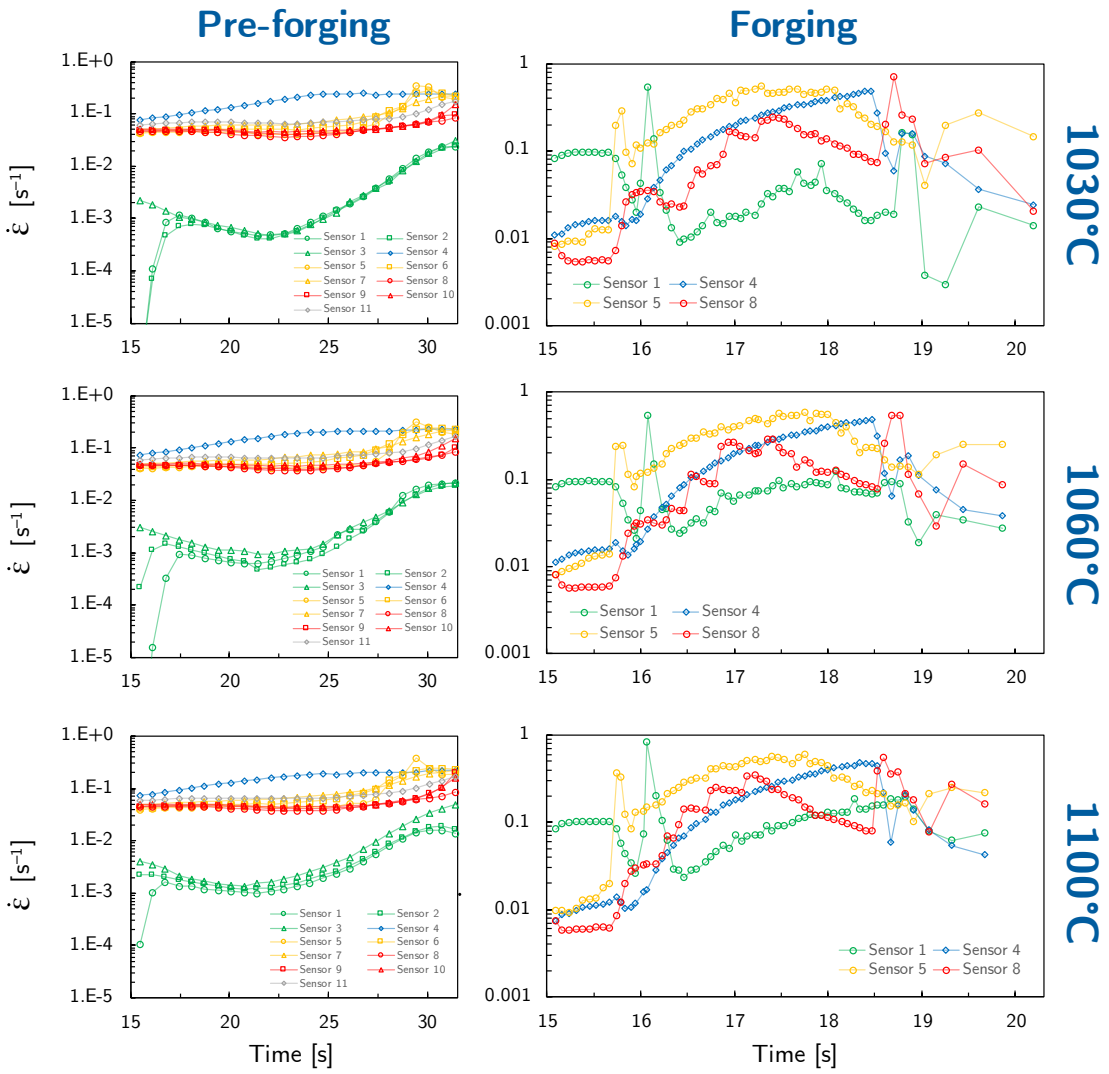

Figure 5.10. Strain rate versus time for pre-forging and forging during deformation (t > 15 s) and forging temperatures (T_0) of 1030°C, 1060°C, and 1100°C.

T_0 = 1100°C. Figure 5.12 shows the same stress components versus time. The shear stress components $\tau_{r\theta}$ and $\tau_{\theta z}$ are not presented since they are null for the entire domain – as their corresponding strains. It is found that high normal stresses of up to ~ 1800 MPa exist across the workpiece. The shear stress attains more moderate values and is bounded below by – 100 MPa and above by 300 MPa. Plotted against time (Figure 5.12), the normal stresses evolve similarly at all tracer points: a first quasi-steady regime in tension or low-stress compression

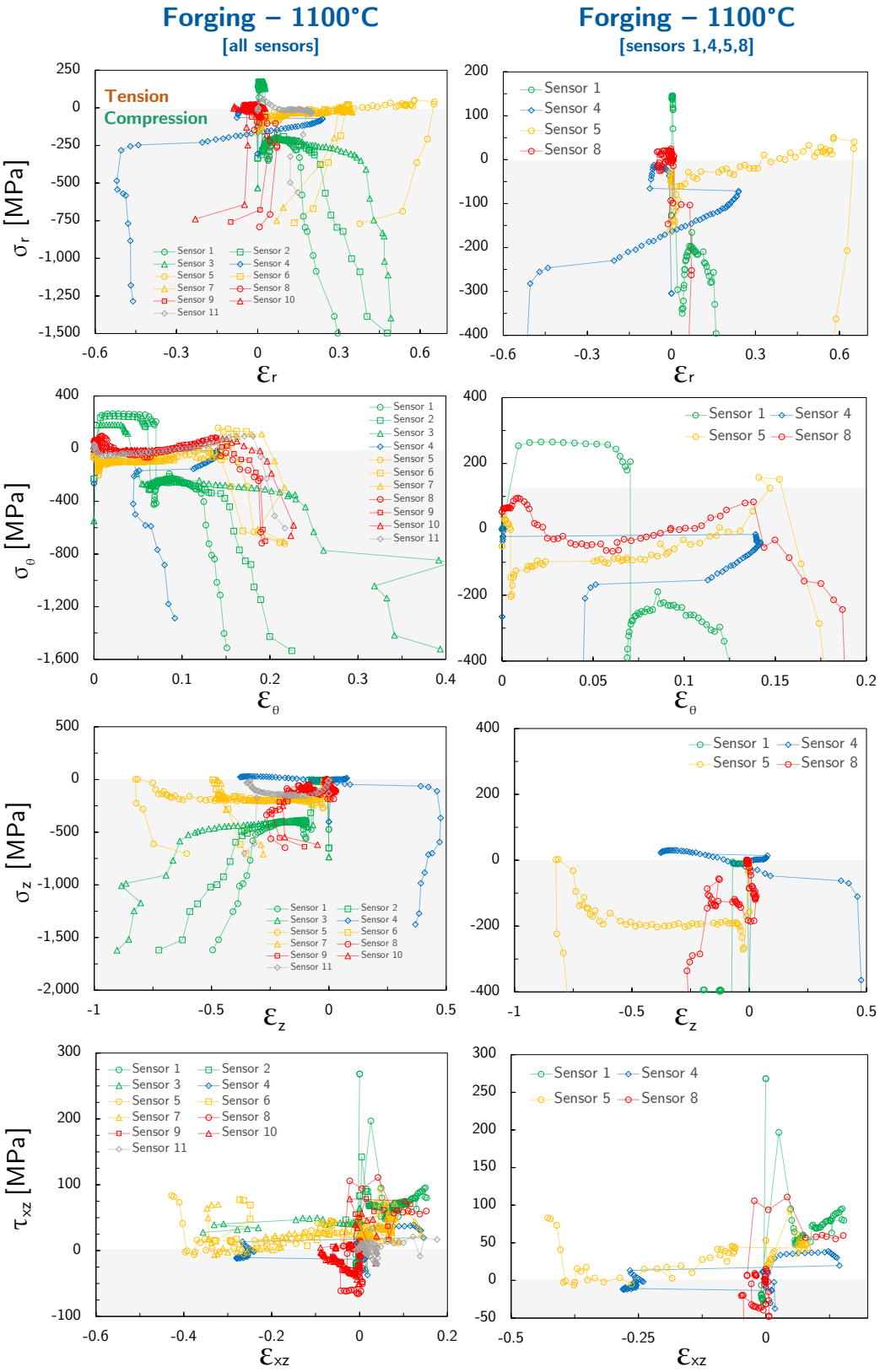

Figure 5.11. Stress components (radial, tangential, axial, and shear) versus corresponding strains at sensors 1 – 11 (left column) and sensors 1, 4, 5, and 8 only (right column) during forging for $T_0 = 1100°C$.

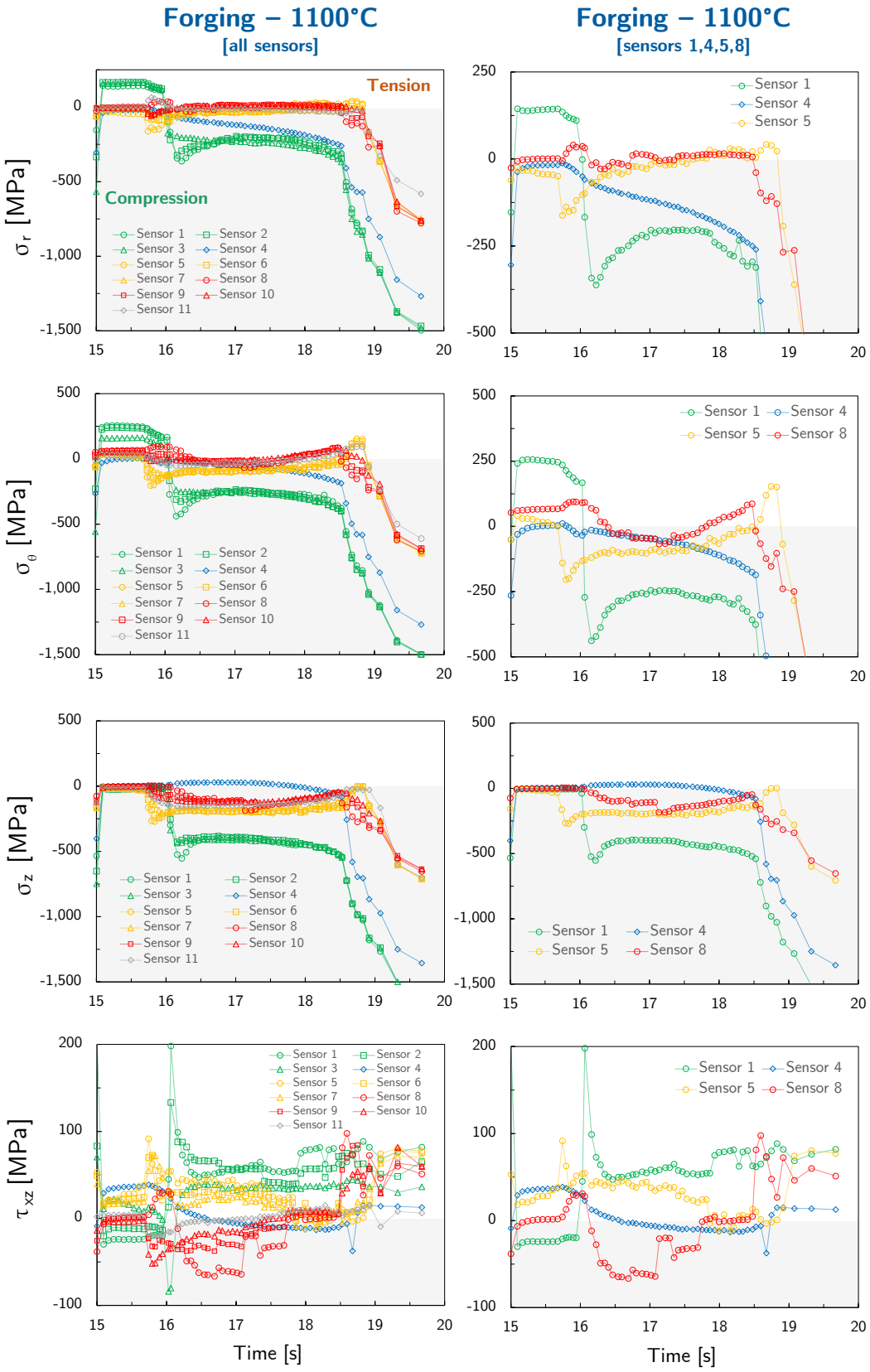

Figure 5.12. Stress components (radial, tangential, axial, and shear) versus time at sensors 1 – 11 (left column) and sensors 1, 4, 5, and 8 only (right column) during forging at 1100°C.

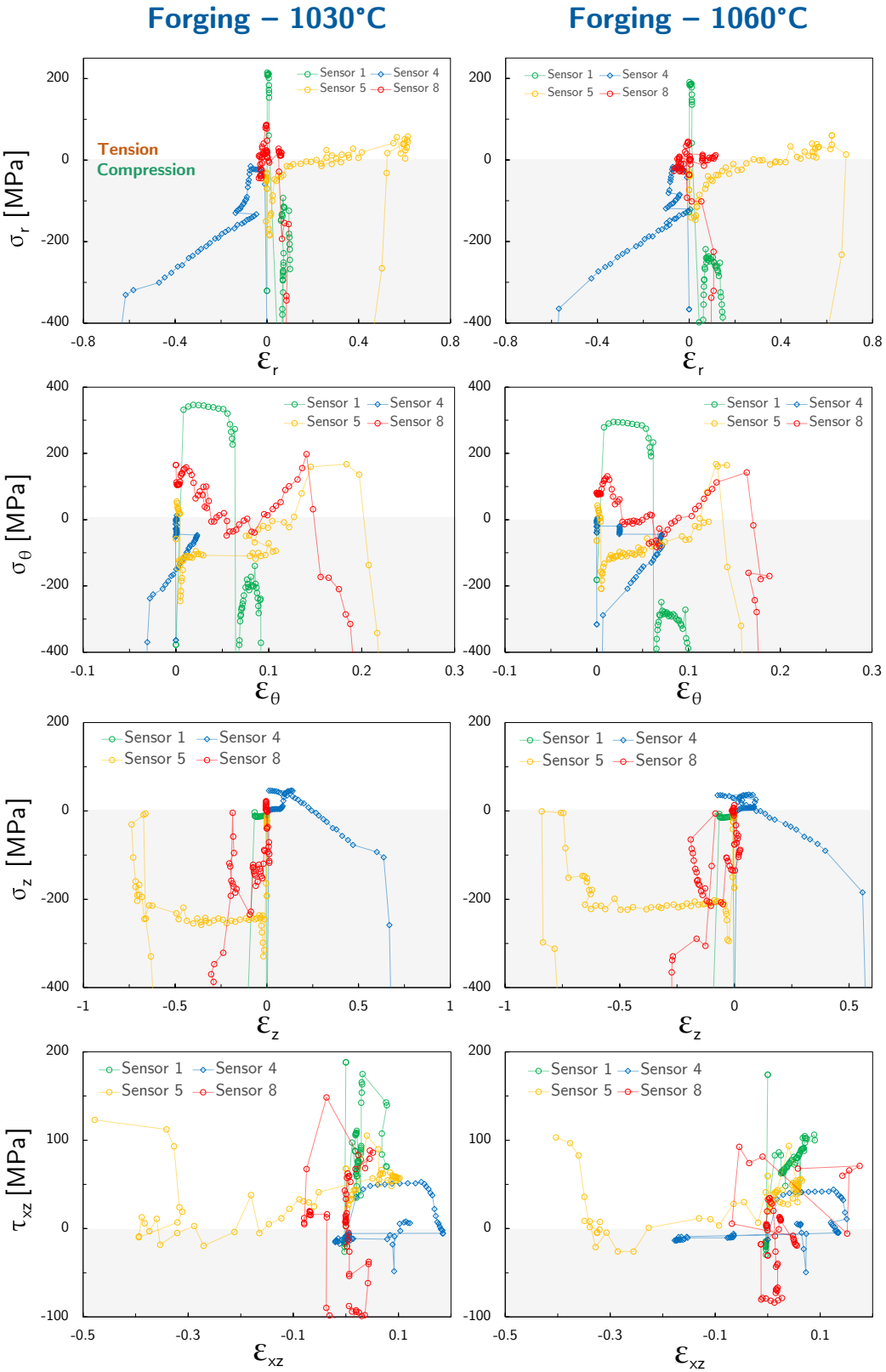

Figure 5.13. Stress components (radial, tangential, axial, and shear) versus corresponding strains at sensors 1, 4, 5, and 8 for forging temperatures of 1030°C and 1060°C.

is followed by a steep descent into compression. For the radial stress, surface sensors 1 – 3 show tensile stresses of $\sim 100 - 150$ MPa before shifting to compression. Sensors 5 – 11 see low tensile stresses until ~ 18.5 s, when they start exhibiting compression stresses of up to – 750 MPa. The tangential stress follows a similar pattern, although here sensors 5 – 11 display several peaks of tensile stress in the initial regime. By contrast, axial stresses stay consistently in compression or show negligible tension stresses in the quasi-steady region. For their part, the innermost sensors 4 and 11 show low stresses until ~ 18.5 s prior to displaying higher compression stress. Concerning shear stress, no clear pattern can be discerned.

Considered together with the strain data analysis (see Figure 5.11), a clearer picture emerges of the thermal effects discussed in Section 5.3. Among the outermost tracer points, sensor 1 sees the highest stress and sensor 8 the lowest stress. Sensor 1 displays high stress and high strain in the normal directions, whereas sensor 5 shows comparatively low stress and even higher strains. Moreover, the temperature at sensor 1 is ~ 40°C lower than at sensor 5 (see Figure 5.4). Hence, it is thought that thermal effects are significant in determining the material's response, and even relatively modest temperature drops can cause notable hardening. Sensor 8 shows both low strain and low stress, which is attributed to the geometry of the workpiece.

Figure 5.13 presents the stress components versus their respective strains for $T_0 = 1030$°C and $T_0 = 1060$°C. No qualitative difference is found between the three forging temperatures, although minor changes in stress amplitude occur, most likely due to higher or lower flow stresses at the given temperature. In particular, tensile radial and tangential stresses increase slightly at the surface sensors 1 and 8, but these stresses remain bounded above by ~ 200 MPa and ~ 350 MPa respectively. Importantly, the observation that neither the stresses nor the strains change substantially with the forging temperature could suggest that the thermal effects discussed in in Section 5.3 are caused by local and not

global drops in temperature. In other words, as the temperature decreases locally, the flow stress increases, and deformation concentrates in sections of the workpiece where the temperature is higher.

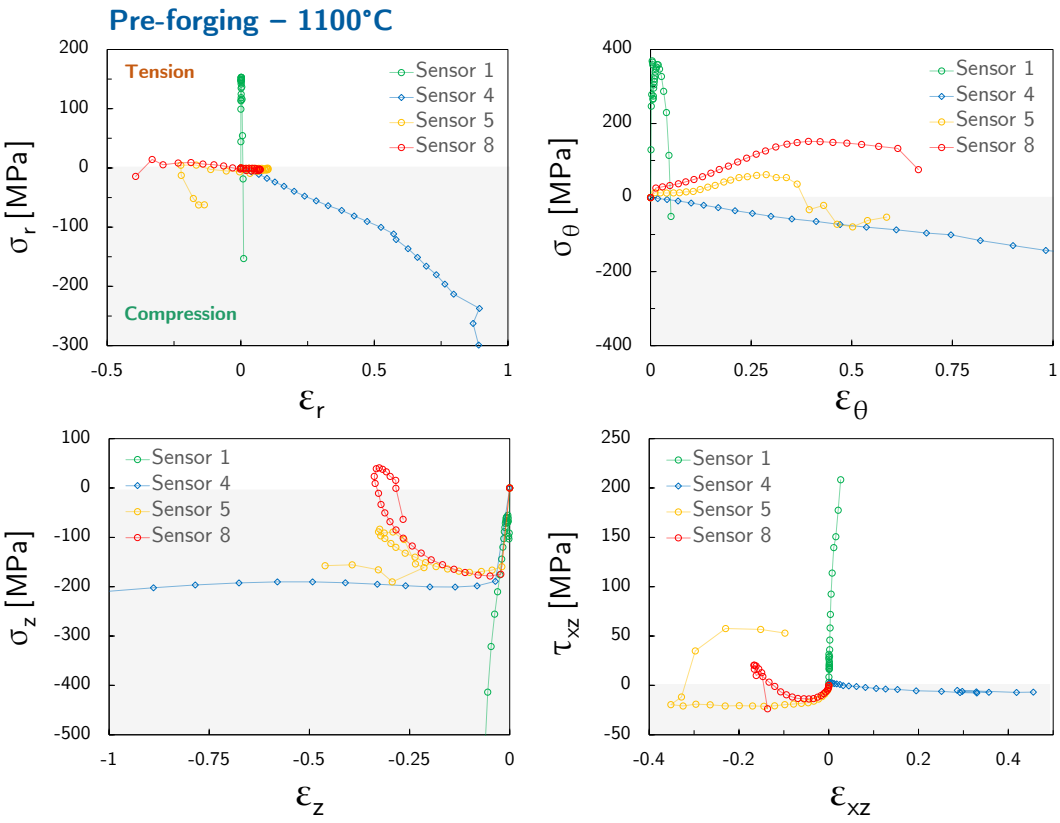

Figure 5.14. Stress components (radial, tangential, axial, and shear) versus time during pre-forging for t > 15 s and T_0 = 1100°C.

The stress components corresponding to pre-forging at a temperature of 1100°C are plotted in Figure 5.14. Here, the trends outlined for forging stay largely valid. The innermost sensor shows consistent compressive stresses. At surface sensors 1, 5, and 8, a transition from tensile to compressive tangential stresses is clearly observed. As in forging, only sensor 1 shows tensile radial stress although with low values below ~ 150 MPa.

5.6 Conclusions and discussion

The results of the FEM simulations presented and discussed in this chapter provide valuable insights into the response of Udimet 720 to hot die forging at different temperatures. Several key conclusions can be drawn:

- The surface of the workpiece undergoes rapid cooling at rates from ~ 1°C/s to ~ 10°C/s during the transfer from the furnace to the dies. For a forging temperature of 1100°C, the surface temperature can drop as much as 150°C before deformation starts. Conversely, the inner regions of the workpiece see almost no thermal losses.

- Thermal losses at the surface increase during deformation, with cooling rates from ~ 10°C/s to ~ 20°C/s. This results in temperature drops of up to 60°C. The temperature in the innermost regions of the workpiece can increase due to adiabatic heating outweighing heat transfer.

- Die chilling effects are confined to a narrow (~ 5 mm) band of material surrounding the surface of the workpiece.

- In forging, all true strain components are bounded above by 0.75 and below by – 0.8. The greatest strain components across the workpiece are axial and radial. At the surface, the radial strain is largely in tension, whereas the axial strain is in compression. The tangential strain has an upper limit of 0.4 and is consistently in tension.

- No significant variation in strain values is found between forging temperatures of 1030°C, 1060°C, and 1100°C.

- The strain rates for pre-forging and forging fluctuate between 10^{-3} s^{-1} and 1 s^{-1} with an average of 0.1 s^{-1}. No strong dependence is observed between strain rate and forging temperature.

- High stresses values of up to ~ 1800 MPa occur across the workpiece during forging. The three normal stress components show relatively similar values, whereas shear stress is lower. In like manner to strain, tensile radial and tangential stress are observed, although a transition to compression takes place as deformation develops. Axial stresses are consistently compressive.

- The presence of secondary radial and tangential tensile stresses is particularly relevant to this investigation since forging cracks are a manifestation of localised tensile stresses.

- Representative hot die forging temperatures, cooling rates (1°C/s – 20°C/s), maximum strains ($\varepsilon_z \sim 0.8$), and strain rates (~ 0.1 s^{-1}) were obtained and are used in the chapter that follows to design the forging simulation experiments; this is developed in Section 6.4.

- The existence of a region of material surrounding the surface where intense die chilling occurs is highly relevant to surface cracking. Indeed, it is shown that relatively modest local temperature drops can increase the stress or reduce the strain seen by the material locally. And crucially, these FEM simulations use constitutive data obtained empirically through isothermal tests. Thus, they do not capture the effect of die chilling on the microstructure and through it on the thermo-mechanical response of the material.

- There is very likely an error linked to the FEM model not accounting for microstructural phenomena. This error is unlikely to compromise substantially the accuracy of the temperature results presented above, since the thermal properties of the material will not change significantly. The strain results can be affected; yet since the process is fundamentally strain controlled (the geometry of the dies and the ram speed are fixed), the largest inaccuracy is likely to come from the stresses.

- These results are hence approximative, but they show the trends of the relevant thermo-mechanical variables and provide order of magnitude values for the experimental design section that follows.

6

Laboratory-scale forging: experimental design

This chapter proposes a hypothesis and an experimental methodology to identify and understand the optimal forging route for highly γ' reinforced cast-and-wrought superalloys. The results presented in Chapter 4 and 5 provide a basic understanding of how Udimet 720 behaves during hot die forging. Based on limited literature results and microstructural analyses, a preliminary hot die forging window of 1000°C – 1100°C was established. Then, FEM simulations were used to understand the thermo-mechanical response of the material during forging and obtain estimates of the relevant variables to design representative experiments. This chapter builds on these results to further narrow down the forging window of Udimet 720. This requires unravelling the unexpected phenomenon described in Section 2.4.3 whereby ductility decreases at higher forging temperatures in the preliminary forging window. Thus, the chapter starts by presenting a hypothesis to explain this behaviour. Then, a novel thermo-mechanical testing method is proposed to mimic hot die forging through laboratory-scale experiments. FEM modelling is used to find an appropriate specimen geometry for these experiments. This new method serves two purposes. First, it allows assessing how the material responds locally to different forging parameters without resorting to expensive and time-consuming full scale trials.

Furthermore, it is used to validate the said hypothesis on forgeability and surface cracking. Finally, an experimental matrix is presented for the thermo-mechanical tests.

6.1 Hypothesis: secondary-γ' controlled surface cracking

In conventional industrial practice, the forging of nickel-based superalloys is performed at temperatures at or closely below the γ' solvus [9,150,256]. This promotes annealing phenomena, reduces the volume fraction of reinforcing γ' precipitates, and precludes grain growth. Yet to date it is not known if this paradigm applies to high γ' cast-and-wrought alloys. Indeed, the results reported by Fahrmann and Suzuki [134] and Sczerzenie and Maurer [31] for Udimet 720 and Bond et al. [54] for René 65 seem to disprove it. For both alloys, ductility increases as the forging temperature decreases in the $\sim 1000°C - 1100°C$ temperature range. Recently, Otto Fuchs KG reported similar findings concerning surface cracking during the hot die forging of these alloys. The hypothesis that follows aims to explain the physical mechanism behind this anomalous hardening and increased surface cracking.

In hot die forging, forging stock is heated to high temperature in a furnace. Once the workpiece is in equilibrium – or at least in a thermal and microstructural steady state – it is removed from the furnace and deformed using pre-heated dies. As the temperature of the dies is lower than that of the workpiece, deformation is accompanied by thermal transfer from the workpiece to the dies, and the surface temperature of the workpiece decreases. This process is illustrated in Figure 6.1.

The microstructure of typical forging stock material is studied in Section 4.2 and is found to consist of a bimodal distribution of intergranular γ'_{p} and fine intragranular γ'_{s}. The heat treatments of Section 4.3 show that as the temperature increases up to $T_{\gamma'\mathrm{s\ solvus}}$ ($\sim 1110°C$), γ'_{s} increasingly dissolves into the matrix and $f_{\gamma'\mathrm{s}}$ declines, whereas $f_{\gamma'\mathrm{p}}$ is broadly unaffected. Thus, insets A and B

of Figure 6.1 depict a typical microstructure of an industrial workpiece after leaving the furnace and prior to hot die forging.

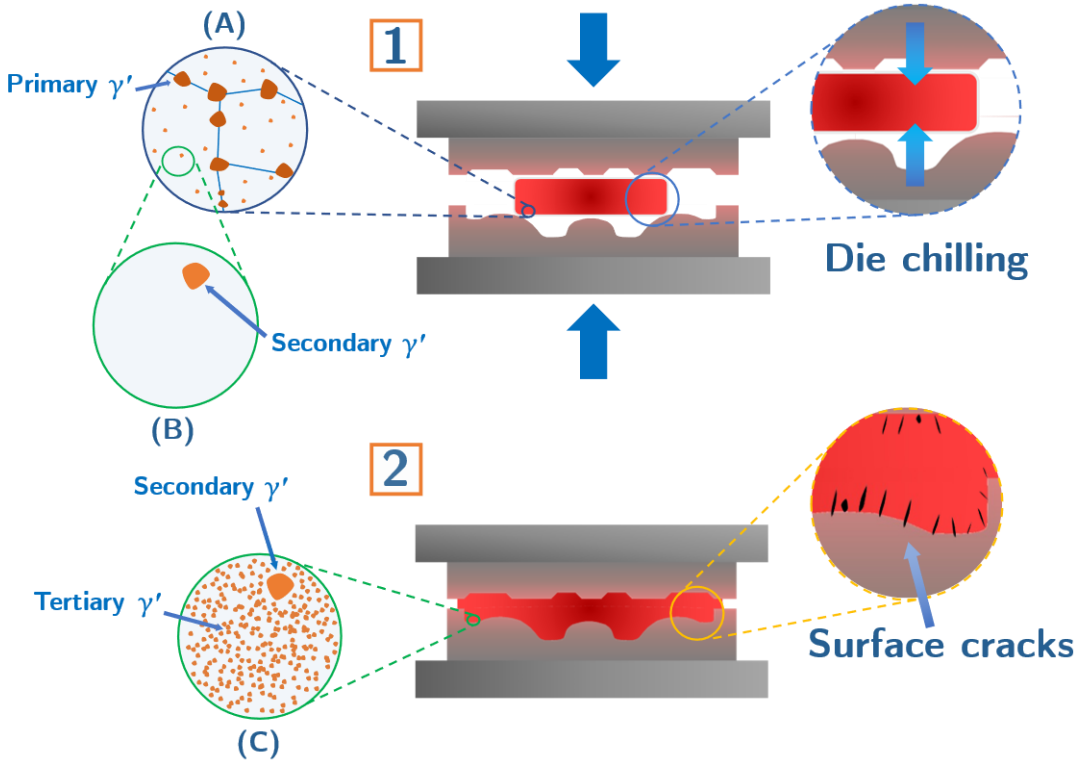

Figure 6.1. Proposed mechanism to explain hardening and increased surface cracking at higher forging temperatures in hot die forging. High forging temperatures induce great dissolution of relatively coarse γ'_s (A, B). Upon surface cooling, γ' reprecipitates as very fine, highly reinforcing γ'_t (C). These γ'_t substantially strengthen the alloy and lead to surface cracking.

It is hypothesised that greater γ'_s dissolution increases the amount of γ' forming elements in the matrix, which upon cooling reprecipitate as a fine distribution of γ'_t (Figure 6.1C). Such γ'_t precipitates are observed in Udimet 720 specimens heat treated for 4 hours at 1100°C (Figure 4.5R) or 1150°C (Figure 4.7C,D). These fine precipitates impede dislocation motion, reduce ductility, and increase the susceptibility to surface cracking. This follows from the discussion in Section 2.1.4II that maximum hardening lies at the transition between weak and strong pair coupling (see Figure 2.12). For Udimet 720Li, Jackson and Reed [122] found that the maximum theoretical critical resolved

shear occurred for particle diameters ~ 40 nm. It is noteworthy that the proposed hypothesis satisfactorily explains the results of Sczerzenie and Maurer [31] and is consistent with Fahrmann and Suzuki [134]. The continuing decline of ductility – measured as reduction of area – at temperatures higher than the $T_{\gamma' \text{s solvus}}$ reported in these studies is attributed to the start of γ'_{p} dissolution, which provides additional γ' forming elements for nucleation and growth of γ'_{t}.

The hypothesis introduced above refers exclusively to the forging temperature, yet the results of Fahrmann and Suzuki [134] suggest that the cooling rate could be as crucial as the nominal forging temperature. The hypothesis can be extended to account for this variable. At high cooling rates, the rapid drop in temperature provides a strong driving force for nucleation and not enough time for precipitate coarsening. Thus, copious amounts of fine γ'_{t} result at the surface. But as the cooling rate decreases, coarsening increasingly dominates over nucleation, and a distribution of coarser γ'_{t} particles ensues. Therefore, the unexpected hardening and increased surface cracking arise as the cooling rate increases.

6.2 Forging simulation: experimental design

A robust experimental method is required to test the hypothesis. The most obvious method involves the hot die forging of full-scale workpieces. However, testing full-scale forgings is costly, time-consuming, and environmentally damaging. Therefore, a more efficient testing method is proposed that replicates hot die forging on small-scale specimens. The complexity of ensuring that laboratory-scale tests are representative of larger forgings has been recently acknowledged by Hardy et al. [29] in their comprehensive review of the challenges for novel cast-and-wrought superalloys. Laboratory-scale tests must be designed so that the microstructures, the thermal variables (temperatures, heating rates, and cooling rates), and the mechanical variables (stresses, strains, strain rates) mimic the (non-uniform) conditions of full-scale forging.

The method uses a Gleeble 3800-GTC thermal-mechanical simulation system to replicate hot die forging through compression tests on cylindrical and double cone specimens. It allows exploring hot die forgeability in a broad sense – microstructure, flow stress, and defects – but it is unique in that it is designed to target specifically the occurrence of surface cracking. Therefore, a metric of success for the method is whether it can reproduce on small scale specimens the surface cracking observed for Udimet 720 workpieces under certain forging parameters. The mechanical dimension to these tests and the rationale behind the chosen specimen geometries are presented in Section 6.3. In particular, the section demonstrates that for these tests the relevant mechanical variables are comparable to full scale forging. The discussion that follows pertains exclusively to the microstructural and thermal dimension of the experiments.

Figure 6.2 proposes an experiment where samples of Udimet 720 are heated up to three temperatures (1), (2), or (3), where (3) corresponds to $T_{\gamma' s\ solvus}$. Then, samples are cooled down at a fixed rate (Θ) to a final (or deformation) temperature T_f and compressed. This thermal cycle is characteristic of hot die forging: temperatures (1), (2), and (3) are denoted by T_0 and correspond to the forging (furnace) temperature, while the cooling segment simulates die chilling effects. The initial state of the material is depicted at the bottom left corner of the figure: a bimodal distribution of intergranular γ'_p and fine intragranular γ'_s. Insets (1), (2), and (3). represent schematically the pattern observed through heat treatment investigations: as the temperature increases up to $T_{\gamma' s\ solvus}$, γ'_s increasingly dissolves into the matrix and $f_{\gamma' s}$ declines, whereas $f_{\gamma' p}$ is unaffected. According to the hypothesis, greater γ'_s dissolution increases the amount of γ' forming elements in the matrix, which upon cooling precipitate as a fine distribution of γ'_t. In turn, these fine γ'_t reduce ductility and increase the susceptibility to surface cracking. Hence, if the hypothesis is correct, samples forged at higher temperatures (T_0) should show increasing amounts of surface cracking (insets A – C).

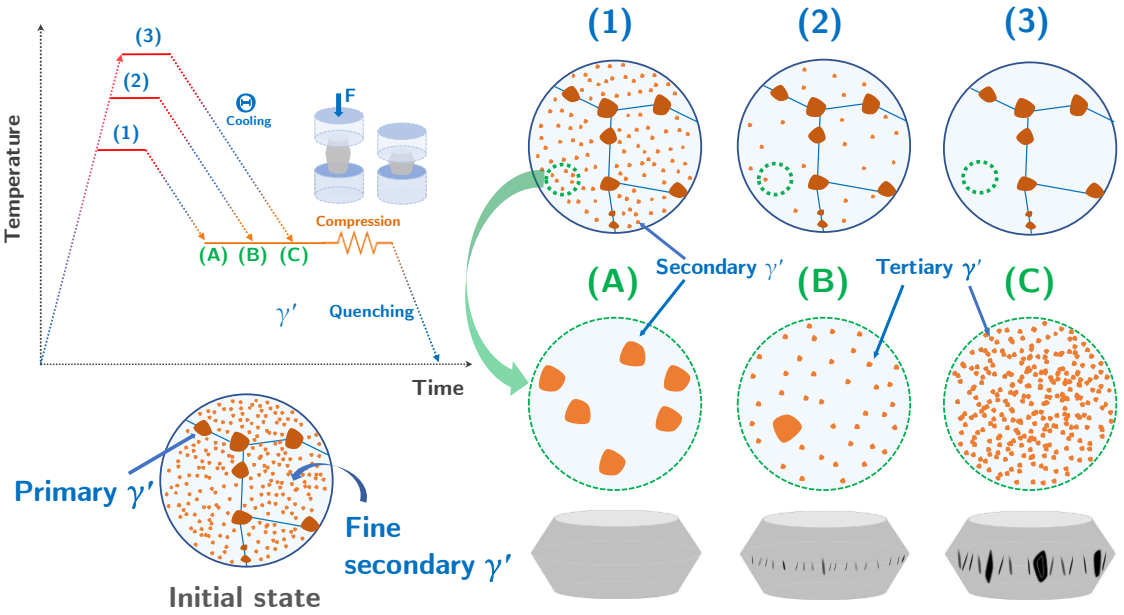

Figure 6.2. Thermo-mechanical experiment to investigate the effect of forging temperature on hot die forgeability and surface cracking. According to the hypothesis, higher forging temperatures increase the dissolution of the initial relatively coarse γ'_s precipitates (1 – 3). Upon cooling, γ' reprecipitates as very fine, highly reinforcing γ'_t (A – C) that assist surface cracking.

The experiment proposed above and the mechanism depicted in Figure 6.2 serve to study the effect of the forging temperature, yet the hypothesis proposes that the cooling rate (Θ) is also a key processing variable. Figure 6.3 proposes a second experiment to study the influence of the cooling rate on the microstructure and mechanical behaviour of the material. In this case, Udimet 720 material in the same initial state is heated up to a certain T_0 where a substantial amount of γ'_s is dissolved. Then, it is cooled down at one of three cooling rates $\Theta_3 < \Theta_2 < \Theta_1$ to a temperature T_f prior to compression. The expected microstructures are schematised in insets (1), (2), and (3). At the highest cooling rate (Θ_1), the rapid drop in temperature provides a strong driving force for nucleation and not enough time for precipitate coarsening. Thus, copious amounts of fine γ'_t result. But as the cooling rate decreases (Θ_2 and Θ_1), coarsening increasingly dominates over nucleation, and a distribution of coarser γ'_t particles ensues. Therefore, hardening and increased surface cracking arise as the cooling rate increases.

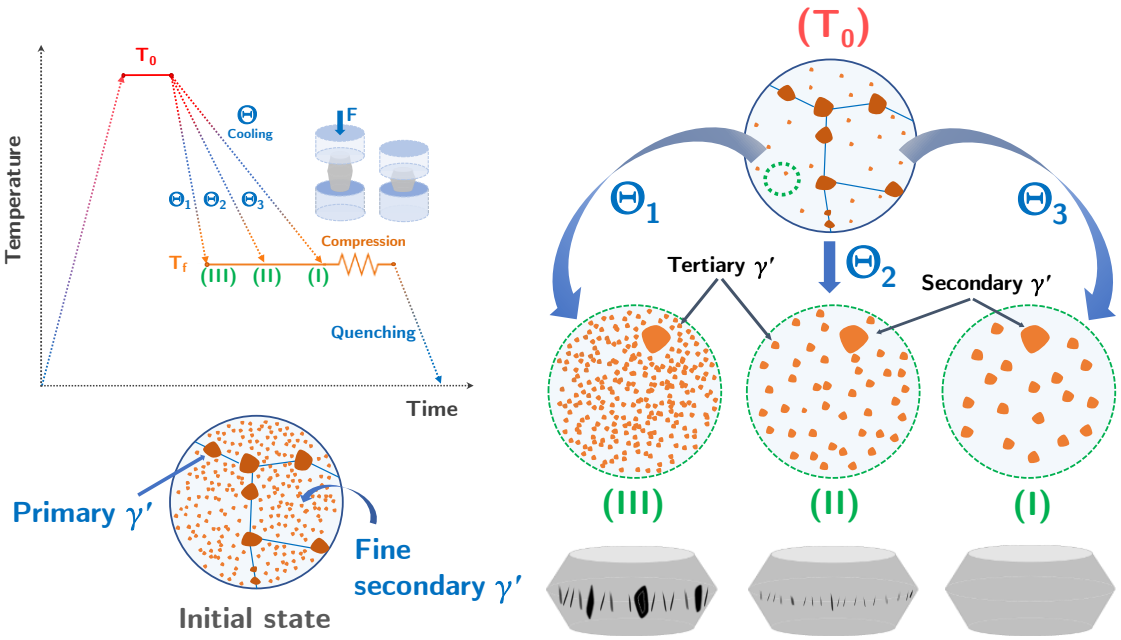

Figure 6.3. Thermo-mechanical experiment to investigate the effect of the cooling rate on hot die forgeability and surface cracking. If the hypothesis holds, rapid cooling (Θ_1) results in fine dispersions of γ'_t, reducing ductility and increasing the susceptibility to surface cracking (III). Slow cooling (Θ_3) allows particle coarsening, thereby precluding hardening and surface cracking.

The experiments proposed in Figure 6.2 and Figure 6.3 can be merged into a single testing method. This unified thermo-mechanical cycle is shown in Figure 6.4. Starting at room temperature, samples are heated up at a rate of 30°C/s to a forging temperature T_0 and held at that temperature for 15 minutes. Then, they are cooled down at a cooling rate Θ to a deformation or final temperature T_f, held at that temperature for 10 s – 20, deformed to a strain ε at a strain rate $\dot{\varepsilon}$, and air quenched to room temperature. The 15 minutes dwelling time is discussed in the next paragraph; the stabilisation dwelling serves to attain a homogenous temperature across the sample after cooling. The forging temperature, the cooling rate, the strain, the strain rate, and the deformation temperature are independent variables, while the heating rate, dwelling time, and stabilisation dwelling time are fixed parameters.

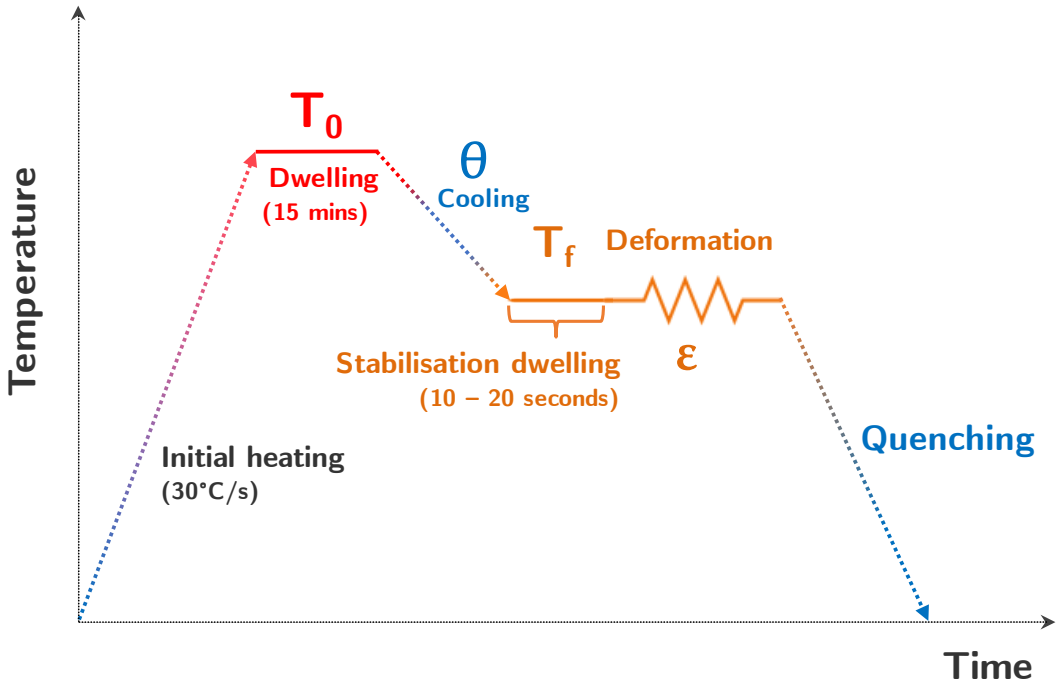

Figure 6.4. Thermo-mechanical testing cycle used to mimic hot die forging.

In order to attain representative microstructures, specimens are heat treated prior to thermo-mechanical testing. The heat treatments explored in Section 4.3 reveal that Udimet 720 billet material does not attain equilibrium after 20 minutes at high temperature, but a steady state is achieved after 4 hours. This has important implications for the experimental design. In full-scale hot die forging, workpieces are heated up in a furnace for hours to achieve temperature and microstructural homogeneity. However, holding samples at high temperature for hours is not feasible on a Gleeble 3800-GTC system: it is not technically sound for the apparatus and can introduce undesired deformation before the start of the tests. Heat treatments allow reducing the dwelling time on the Gleeble to 15 minutes, which suffices to attain temperature homogeneity across the sample. The heat treatments consist of holding the samples for 4 hours at their forging temperature (T_0) followed by swift water quenching. So, microstructures are achieved where γ'_p and γ'_p are equivalent to full-scale forging and any reprecipitating γ' exists as fine tertiaries. The presence of fine tertiaries is not considered problematic, since they readily dissolve during the 15 minutes dwelling step.

6.3 Sample design for laboratory-scale tests

The standard bulk workability test involves upsetting cylindrical specimens into flat pancakes. Cylindrical samples are easy to prepare, require simple grips, and when compressed produce similar stress and strain fields to those seen in a workpiece during forming. Compression testing also saves the hurdles that occur in tension testing of premature fracture when cracks form and necking instabilities. However, the method does not provide a full picture of the forgeability of an alloy. In particular, it fails to capture the effect of large secondary tensile stresses, which can lead to free surface fracture or cavitation. Such stresses are not significant in the upsetting of cylinders but can be large in industrial forgings. Several methods have been employed to overcome this issue: among others, the notched-bar and double cone tests [184]. Double cones offer the advantage of inducing in the sample a strain gradient and a non–uniform stress state [185], and indeed some variations of this test have been used in recent studies to study the forgeability of nickel-based superalloys [177,185,257]. Finite element analysis is normally combined with double cone compression tests to correlate the mechanical response of the material with microstructural and fracture observations [184].

In this section, finite element modelling is used to study the hot die forging of Udimet 720 laboratory-scale testing specimens in order to obtain optimal specimen geometries. The physical model implemented in FEM is shown in Figure 6.5. This model does not reproduce the bespoke testing method to mimic hot die forging introduced in Section 6.2. Rather, it models the forging of small samples in the same manner that the forging of full-scale turbine discs is simulated in Chapter 5. This ensures the validity of the analysis irrespective of the forging simulation method, since it was initially not known whether the said bespoke method would be successful. Three geometries are studied: a cylinder, a truncated double cone (‘double cone’), and a truncated double cone with a central cylindrical section (‘cylindrical double cone’). The three geometries are selected to produce

different stress and strain conditions at the equator, where cracks are expected, and thus controlled cracking. They are compressed to a test (global) axial strain of 0.8, at a test axial strain rate of 0.1, and at temperatures of 1030°C, 1060°C, or 1100°C. Friction, adiabatic heating, and die chilling effects are included. The tungsten carbide anvils initially are at a temperature of 550°C. Tracer points where data series are recorded are located at the edge and the core of the specimens.

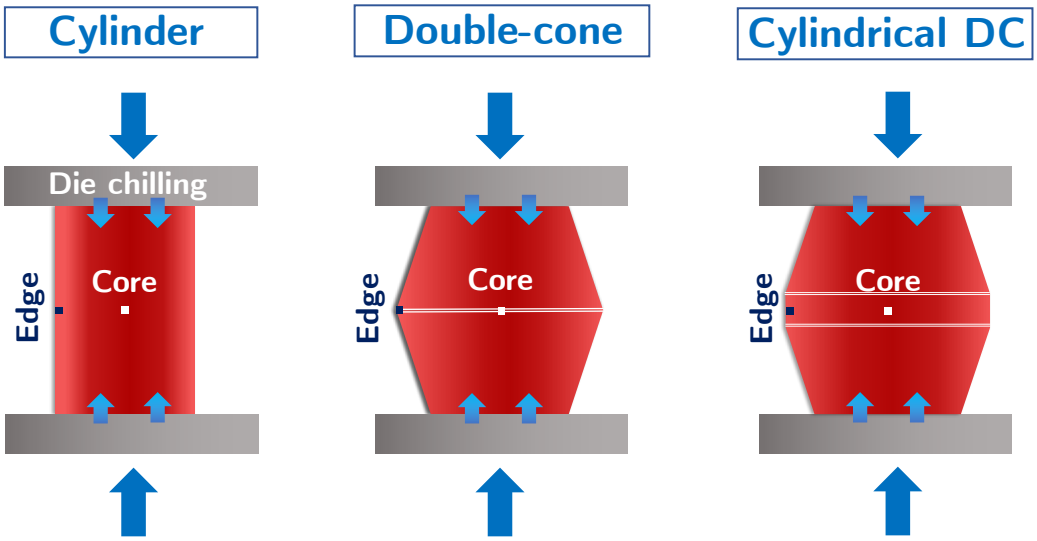

Figure 6.5. Schematic of the physical model of laboratory-scale hot die forging tests. FEM simulations of the model were used to study the three geometries displayed.

Figure 6.6 shows the temperature versus time for the three geometries and three forging temperatures (A – C) and a comparison of the three geometries at a forging temperature of 1100°C (D). The temperature decreases monotonically with time for all forging temperatures, geometries, and locations, indicating that heat transfer outweighs adiabatic heating. Cooling at the surface (edge) starts when the specimen comes into contact with the die (t = 0 s), whereas a slight time lag is observed for the inner (core) tracer points. This produces a temperature gradient between the core and the edge that peaks at ~ t = 2 s and dissipates by t = 8 s. Other than the expected shift along the vertical axis, no significant difference is observed among specimens forged at 1030°C, 1060°C, or

1100°C. The biggest temperature drop corresponds to the cylindrical specimen, with a cooling rate of 20°C/s. The variation in temperature between the double cone and the cylindrical double cone is negligible, with cooling rates of 14.8°C/s and 14.4°C/s respectively. The difference between the cylinders and the double cones is relatively modest; for a forging temperature of 1100°C, it peaks by the end of the deformation at ∼ 30°C. Overall, the temperature drop at the edge corresponding to a forging temperature of 1100°C is 150°C for a cylinder, 127°C for a double cone, and 123°C for a cylindrical double cone.

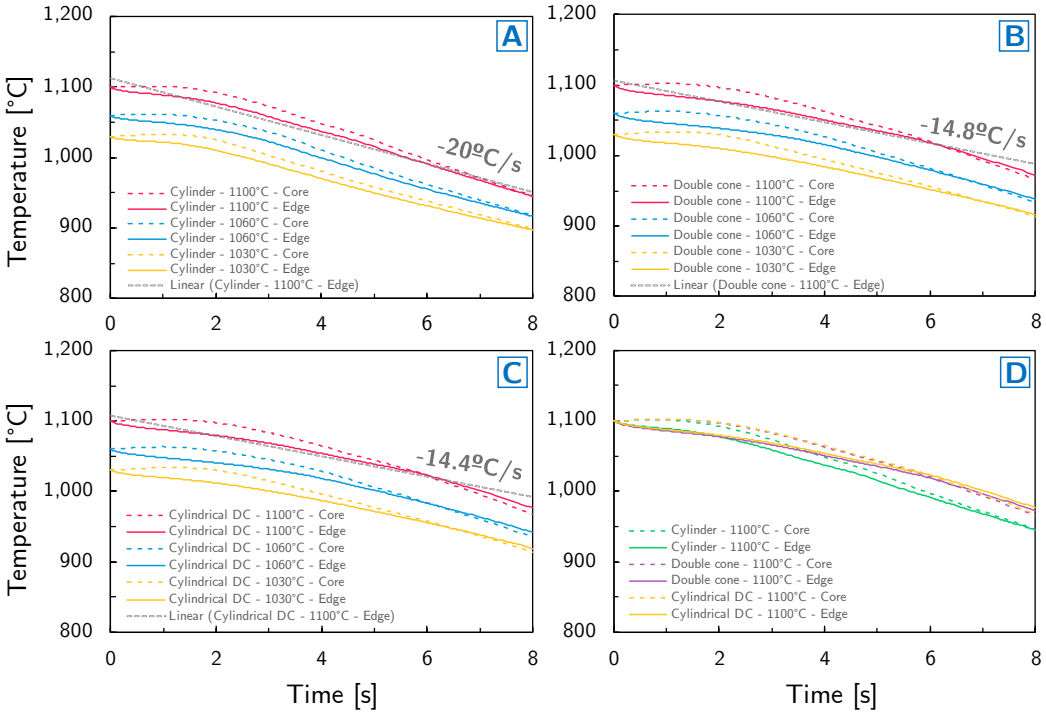

Figure 6.6. (A – C) Temperature versus time during the forging of cylindrical (A), double cone (B), and cylindrical double cone (C) samples. Data recorded at the core and the edge of samples forged at 1030°C, 1060°C, or 1100°C. (D) Temperature versus time for cylindrical, double cone, and cylindrical double cone samples forged at 1100°C.

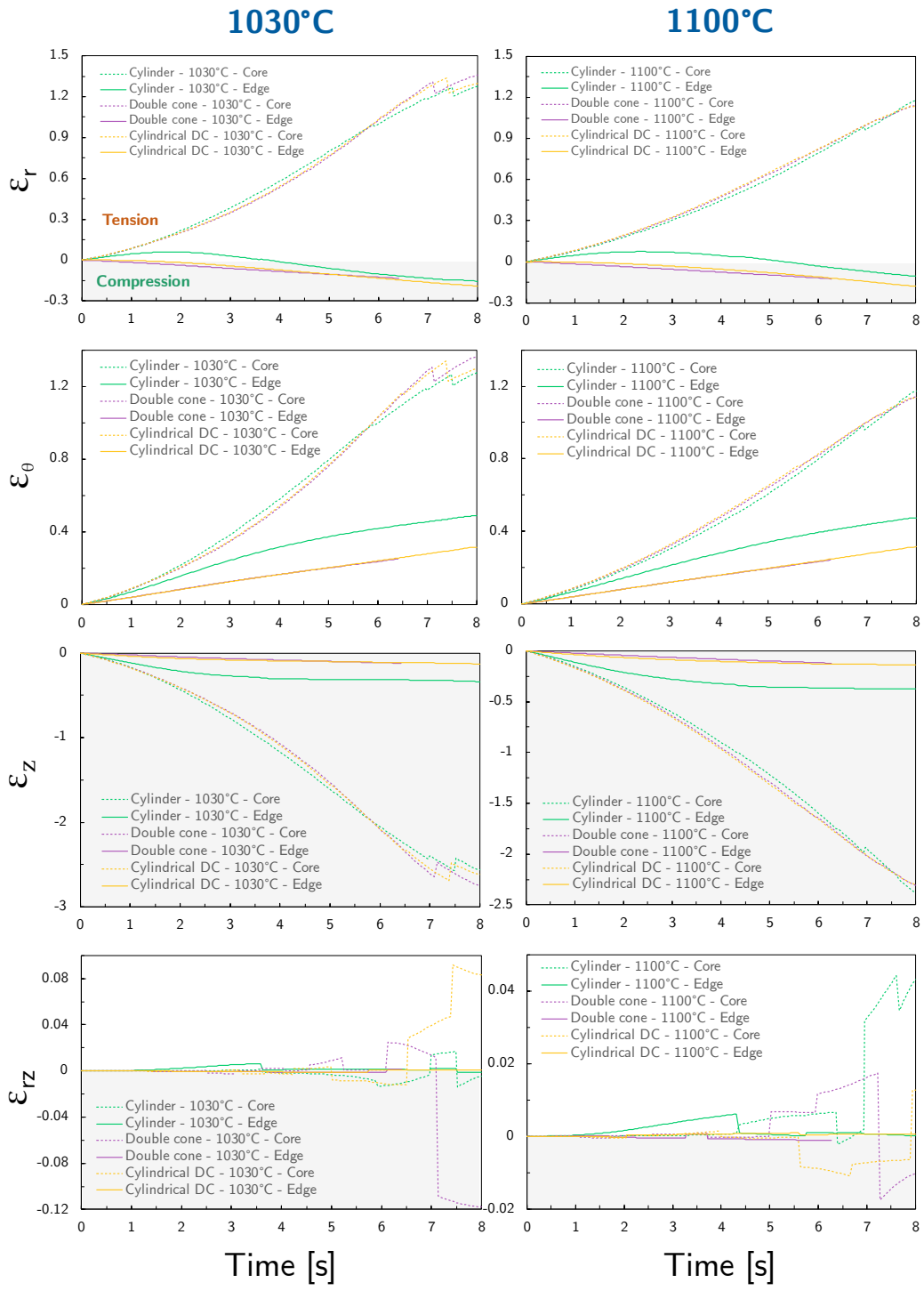

Figure 6.7. Strain components (radial, tangential, axial, and shear) versus time for cylindrical, double cone, and cylindrical double cone samples forged at 1030°C (left column) or 1100°C (right column). Data recorded at the core and the edge of the samples.

Figure 6.7 shows the radial, tangential, axial, and shear strain against time corresponding to the three specimen geometries forged at 1030°C or 1100°C. The shear strain shows negligible values throughout deformation and lacks a clear pattern, so the analysis below pertains exclusively to the remaining components. The behaviour of the central and the peripheral regions diverges significantly, with substantially greater deformation at the core of the samples. Conversely, the forging temperature does not seem to significantly affect the strain evolution or distribution. In particular, certain variation is observed in the radial and axial strains at the edges, but this deviation is below ~ 0.2 for a total radial deformation of ~ 1.2 and ~ 0.3 for a total axial deformation of ~ 2.5. Concerning the geometry, the strain at the core regions is highly comparable for all three specimens. The strain at the edge is greater (in absolute value) for the cylinder, while the double cone specimens display almost identical values. The greatest strain absolute value corresponds to the axial strain, followed by the radial and tangential strains. For all conditions and tracer point locations, the axial strain is consistently in compression and the tangential strain in tension. In addition, the radial strain is consistently in tension at the core, whereas for the edge it is largely in compression, but a transition is noted for cylinders from tension to compression.

The strain rate versus time for different geometries and forging temperatures is shown in Figure 6.8. The 0.1 s^{-1} overall axial strain rate of the test (imposed by the dies) was selected to match the strain rates of full-scale forging (see Section 5.4). It is observed that strain rates are bounded below by 0.03 s^{-1} and above by 0.5 s^{-1}. Strain rates are one order of magnitude greater in the inner than in the peripheral regions. The strain rate at the core increases as deformation progresses for all geometries, whereas at the edge it decreases for the cylinder and remains largely constant for both double cone specimens. The variation between the double cones and the cylindrical double cones is marginal. Figure 6.8B reveals that temperature does not significantly affect the strain rate, besides producing slightly higher values at the core as the temperature decreases.

It is concluded that the global axial strain rate of 0.1 s^{-1} results in good agreement with full-scale forging conditions for every geometry and condition considered

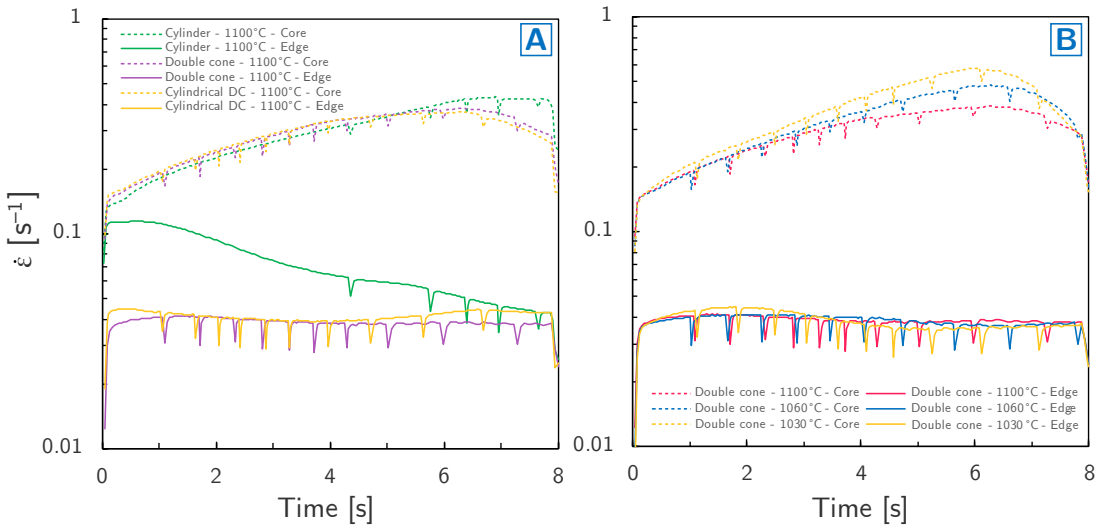

Figure 6.8. (A) Strain rate versus time for cylindrical, double cone, and cylindrical double cone samples forged at 1100°C. (B) Strain rate versus time for double cone samples forged at 1030°C, 1060°C, or 1100°C. Data recorded at the core and the edge of the samples.

Figure 6.9 displays maps of the normal stresses corresponding to a cylindrical and a double cone specimen at the end of deformation. The shear stress is negligible and thus not shown (see Figure 6.10 and Figure 6.11). A transition from tensile to compression stress is observed for all three normal stresses. Specifically, the radial component is compressive in the central regions of the sample and tensile in the peripheral regions. The maximum tensile stress of ~ 180 MPa appears at the top and bottom surfaces, which are in contact with the dies. The tangential stress exhibits a pattern characteristic of upset cylindrical specimens: a cross-shaped region of high compressive stress that peaks at the core, a region of low stress (dead-metal zone) around it, and moderate tensile stress at the top and bottom surfaces. In addition, a gradient of increasing tensile stress towards the lateral surfaces is observed that peaks at ~ 500 MPa. This is similar to the axial stress, which increases radially from ~ – 1100 MPa in compression at

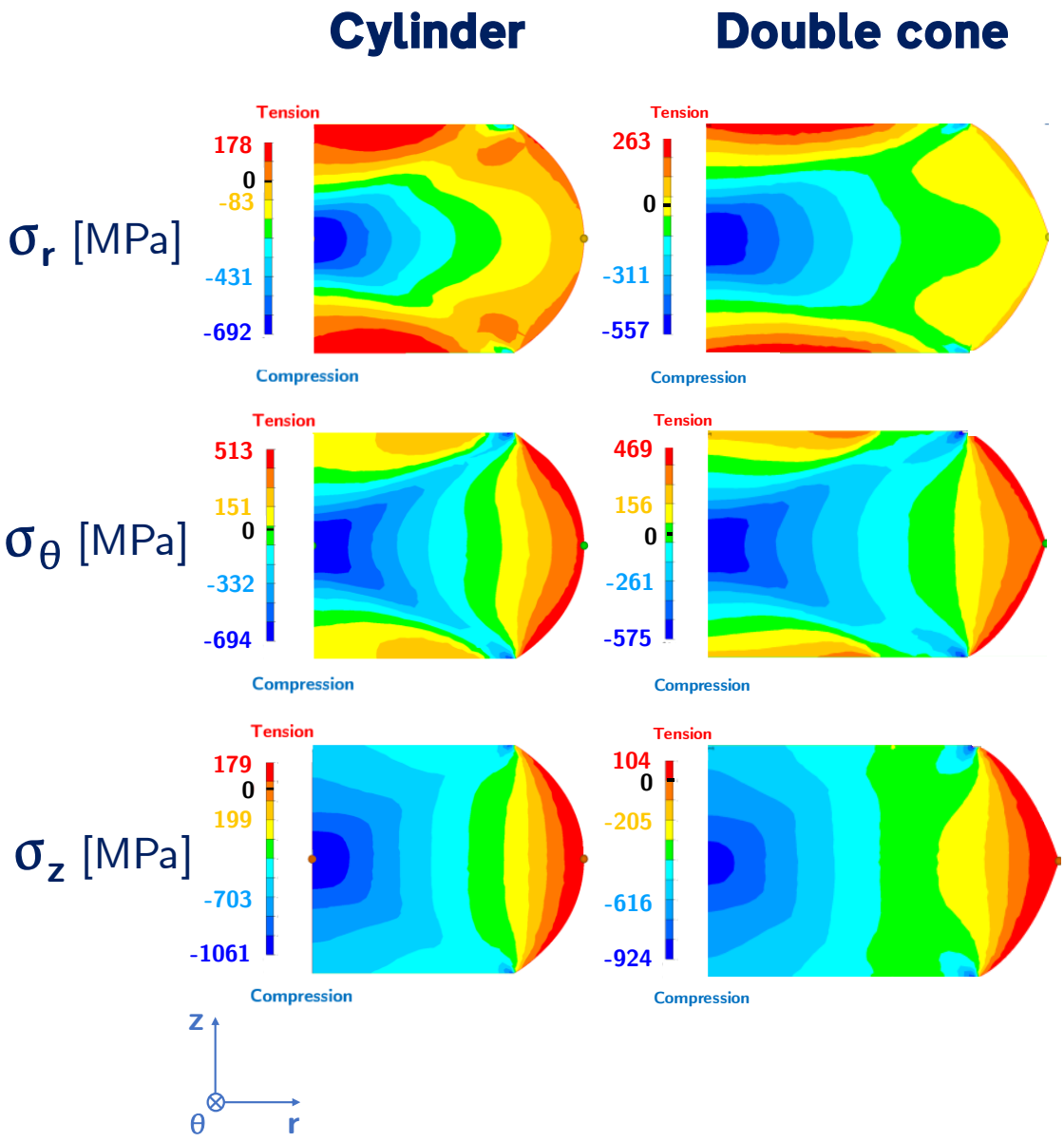

Figure 6.9. Normal stress (radial, tangential, axial) maps corresponding to the forging of cylindrical and double cone specimens at a temperature of 1100°C. The tracer points shown at the middle section indicate where the core (left) and edge (right) data are extracted.

the core to ~ 180 MPa in tension at the edge. Interestingly, the stress gradient is less steep for the double cones, indicating that cracking could be less sensitive to deformation inhomogeneities and shape changes; in other words, cracking is likely

to be more localised at the edge of the sample, whereas crack initiation regions in the cylinder could be less consistent and more sensitive to the final shape that barrelling induces on the sample.

Figure 6.10 shows the radial, tangential, axial, and shear stresses against strains at the edge and the core of double cone specimens forged at 1100°C. It is observed that the stress and strain distributions in the inner and peripheral regions are markedly different, whereas the divergence between different geometries is less significant. The radial stress is negligible at the edge and large (in compression) at the core, where it reaches ∼ – 550 MPa for both double cones and ∼ – 700 MPa for the cylinder. The tangential stress at the core behaves in the same manner. But at the edge, tangential tensile stresses of ∼ 400 MPa exist. The axial stress behaves similarly, although there is a vertical shift downwards that causes a compression to tension transition at the edge. Both the shear stress and strain are negligible. Comparing the three geometries, the largest stress divergence between the cylinder and the double cones corresponds to radial stress at the core. At the edges, although they attain generally similar stress values, the cylinder does so at higher strain values. Interestingly, the double cone displays significantly lower axial stress at the edge than the cylindrical double cone; for all variables considered, this is the only major difference between these two geometries.

The normal and shear stress components versus their corresponding strains for double cone samples forged at 1030°C, 1060°C, and 1100°C are shown in Figure 6.11. The shear stress is negligible and has no clear pattern, so the analysis that follows pertains exclusively to the normal stresses. The trends noted in Figure 6.10 remain valid for the three forging temperatures. It is seen that lower forging temperatures translate into higher (in magnitude) stresses, both at the edge and at the core. These changes are significant: the maximum radial stress shifts in compression from ∼ – 570 MPa to ∼ – 940 MPa. The tangential stress

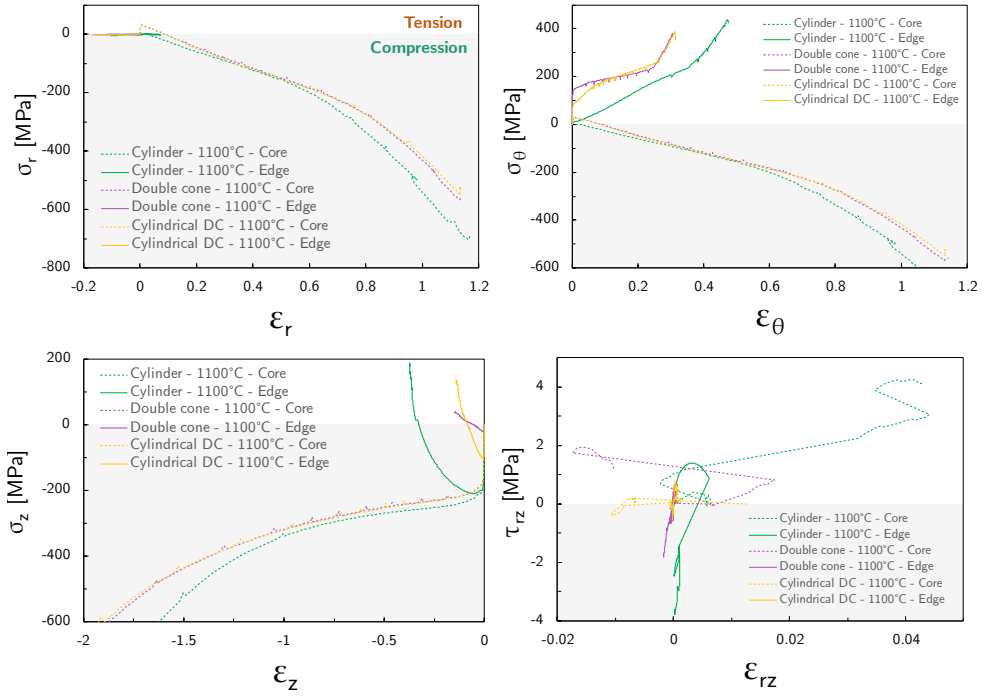

Figure 6.10. Stress components (radial, tangential, axial, and shear) versus corresponding strains for cylindrical, double cone, and cylindrical double cone samples forged at 1100°C. Data recorded at the core and the edge of the samples.

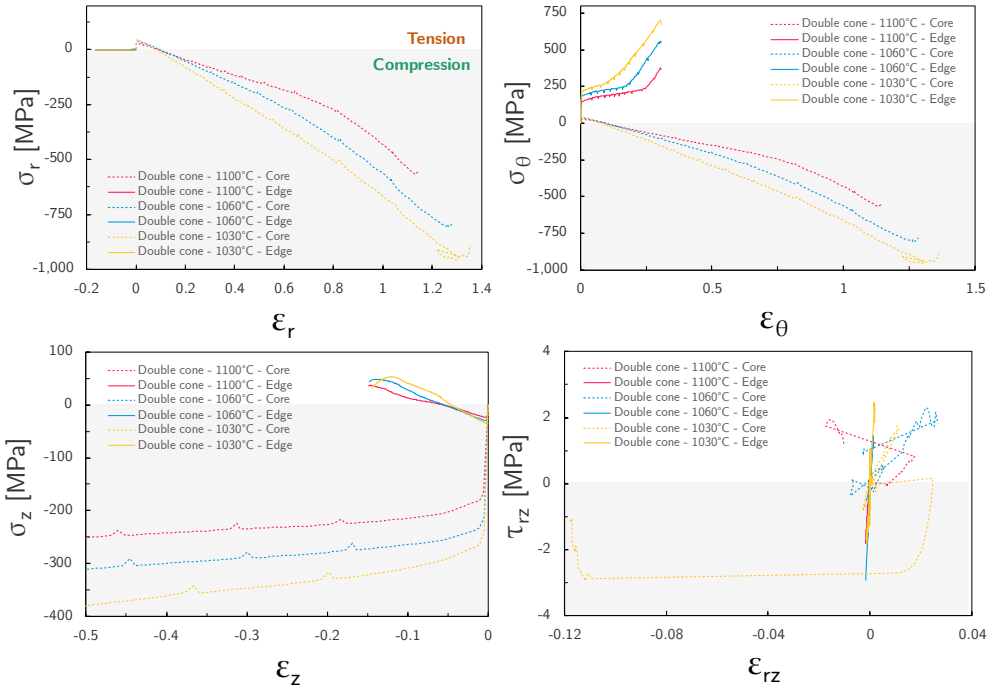

Figure 6.11. Stress components (radial, tangential, axial, and shear) versus corresponding strains for double cone samples forged at 1030°C, 1060°C, or 1100°C. Data recorded at the core and the edge of the samples.

shifts in compression from ~ – 560 MPa to ~ – 940 MPa at the core and in tension from ~ 370 MPa to ~ 700 MPa at the edge. The axial stress at the core varies in compression from ~ – 250 MPa to ~ – 380 MPa. By contrast, the axial stress at the edge does not seem to depend substantially on the forging temperature.

6.3.1 Highlights of sample design and FEM simulations

Several key conclusions can be extracted from the results presented above:

- The temperature evolution for the hot die forging of laboratory-scale specimens is comparable to full-scale (industrial) workpieces. Specifically, heat transfer outweighs adiabatic heating, and cooling rates of up to ~ 15°C/s – 20°C/s occur at both the interior and peripheral regions of the specimens. This is true for the three geometries and forging temperatures considered, bringing the results in line with those of Section 5.2.

- Normal strain components at the edge of the specimens are similar in order of magnitude to full-scale forging, but they are significantly higher at the core. The strain is not markedly affected by temperature. The three geometries behave similarly, although strains at the periphery are slightly higher for cylindrical samples.

- A test axial strain rate of 0.1 s^{-1} delivers strain rates of the same order of magnitude as full-scale forging (see Figure 5.10) for all conditions.

- The distribution of stresses across the specimens is comparable to full-scale forging. In particular, Figure 6.9 and Figure 6.10 reveal that significant secondary tensile stresses (stresses caused by the deformation resulting from the applied compressive force) exist. Broadly speaking, a transition occurs from compression stresses at the interior of the specimens to tension stresses in their peripheral regions. As expected, these secondary tensile stresses arise more readily (at lower strains) for double cones than for

cylindrical specimens. Contrary to the other variables, stresses are noticeably temperature dependent and increase as the forging temperature decreases.

- Overall, the difference in the thermo-mechanical variables between the double cone and the cylindrical double cone geometry is minimal. Conversely, some variation is noted between the cylinders and the double cones.

- The stress distribution discussed above – and in particular the secondary tensile stresses – suggests that cracking is more likely to occur on the double cones. Thus, double cones may provide better cracking control as cracking should be less sensitive to deformation inhomogeneities.

It must be noted that these FEM simulations (just as those of Chapter 5) use constitutive material data from isothermal tests and thus, they do not appropriately capture the thermo-mechanical effects caused by die chilling. In particular, assuming that the hypothesis of Section 6.1 holds, the simulations do not reflect the hardening caused by the precipitation of fine γ'_t – particularly at higher forging temperatures.

Following these results, it was decided that thermo-mechanical tests were to be conducted using cylinders and double cones but not cylindrical double cones. Cylinders are the standard sample of the Gleeble thermal-mechanical simulation system, and preliminary trials indicated that they deliver slightly more accurate thermal control. In addition, the interpretation of stress versus strain data for cylindrical samples is more straightforward. Double cones deliver a gradient of stresses and strains across the surface and higher secondary tensile stresses. Both these features are beneficial to study surface cracking. Since no substantial difference was found between the double cones and the cylindrical double cones, the former were selected on the basis of ease of manufacturing.

6.4 Experimental matrix

After designing a thermo-mechanical cycle to simulate hot die forging and selecting suitable specimen geometries, the last step of the experimental design process consists of determining the variables for testing Udimet 720 specimens. The experimental matrix for the tests is shown in Table 6.1. Specimens are forged at temperatures of 1030°C, 1060°C, or 1100°C, and cooled at rates of 1°C/s, 10°C/s, or 30°C/s. The strain and the strain rates are kept constant at 0.8 and 0.1 s^{-1}, respectively; the deformation temperature (T_f) is also kept constant at 880°C. The rationale for these values is detailed below.

Table 6.1. Experimental matrix containing the forging temperatures (T_0), cooling rates (Θ) used to study the forgeability of Udimet 720. Other variables which were fixed are shown at the bottom of the matrix.

θ	T_0		
	1030°C	1060°C	1100°C
1°C/s	X	X	X
10°C/s	X	X	X
30°C/s	X	X	X
Udimet 720; $\varepsilon = 0.8$; $\dot{\varepsilon} = 0.1\ s^{-1}$; $T_f = 880$°C			

- The forging temperatures (T_0) of 1030°C, 1060°C, and 1100°C are selected following the findings of Chapter 4, where a potential forging window 1000 – 1100°C is established. The temperature of 1100°C lies just below the secondary gamma prime solvus ($T_{\gamma's\ solvus}$), while the 1030°C and 1060°C temperatures are spaced within the hot die forging window.

- The cooling rates of 1°C/s, 10°C/s, or 30°C/s are chosen based on the FEM simulations of full-scale workpieces. In these, cooling rates of 1°C/s are recorded in the inner regions of the forging and ~ 10°C/s by the surface.

The cooling rate of 30°C/s is selected based on preliminary trials with the Gleeble; this is the maximum cooling rate that can be achieved with the instrument.

- The final (or deformation) temperature (T_f) of 880°C is selected through a 'reasonable worst-case scenario' methodology. The largest temperature drop recorded through FEM simulations for full-scale workpieces is ~ 150°C corresponding to sensor 1 in pre-forging (see Figure 5.3). When this temperature drop is considered together with a forging temperature of 1030°C, T_f = 880°C results. The final temperature is set at 880°C for all three forging temperatures rather than subtracting 150°C to each T_0. This allows decoupling the effect of T_0 (furnace temperature) and T_f (deformation temperature) on cracking – although these are linked in full-scale hot die forging. In this set of experiments, T_f is fixed because the hypothesis being tested relates primarily to the dissolution of greater amounts of γ'_s. Yet in general, nothing precludes varying T_f to explore the latter mechanism.

- The strain of 0.8 derives from the FEM simulation of a full-scale disc turbine, for which the maximum compressive strain (ε_z) is ~ 0.8 (see Figure 5.7 and Figure 5.8).

- Similarly, the strain rate of 0.1 s^{-1} is selected based on Figure 5.10, as this the value around which strain rates fluctuate.

It must be noted that the strain, strain rate, and final temperature could have been varied. In particular, it is expected that for any combination of variables there exists a critical strain above which surface cracks appear. However, preliminary trials with the Gleeble indicated that the deformation path and thermal evolution of the specimens are critically dependent on the initial conditions. For example, minor misalignments result in highly inhomogeneous deformation, and cooling at the highest rate (30°C/s) not always yields the

expected temperature control. Hence, a decision was made to prioritise the two variables necessary to test the hypothesis: the forging temperature and the cooling rate. This allowed obtaining a sufficient number of valid experiments despite the said hurdle. In general, these variables could be varied to get a more comprehensive picture of the forging map of an alloy.

6.5 Summary

This chapter introduces a new conceptual framework and a novel testing methodology to deliver on the general aim of studying the hot die forgeability and the specific objective of exploring surface cracking for Udimet 720. The main findings of the chapter can be summarised as follows:

- The conventional hot die forging window of Udimet 720 corresponds to the temperature range 1000°C – 1100°C.
- In this temperature range, an unusual phenomenon is reported whereby ductility decreases and more intense surface cracking arises at higher forging temperatures below the γ' solvus. This suggests that the accepted knowledge in industrial practice that nickel-based superalloys ought to be forged at temperatures below but close to the γ' solvus does not hold for the highly reinforced cast-and-wrought grades.
- A hypothesis is presented to explain this phenomenon: the decreased ductility and more extensive surface cracking follow the dissolution of increasing amounts of γ'_s at higher forging temperatures and its reprecipitation as a fine dispersion of reinforcing γ'_t precipitates due to die chilling.
- A novel testing methodology is presented to simulate hot die forging that uses a Gleeble thermo-mechanical simulator and a bespoke thermo-

mechanical cycle to mimic die chilling and microstructural changes at the surface.

- Through extensive FEM modelling cylindrical and double cone specimens are found to be appropriate for these experiments.
- An experiments matrix is selected for Udimet 720 based on FEM simulations and previous results.

In the chapter that follows, the method devised here will be used in to test the validity of the hypothesis.

7

Thermo-mechanical testing

This chapter presents the results of the thermo-mechanical testing of Udimet 720 material. The methodology introduced in Chapter 6 is employed on laboratory-scale specimens to explore the forgeability of the alloy and its susceptibility to surface cracking. These tests can be considered as a middle step of the experimental suite developed to tackle the research questions of this project. In simple terms, Chapters 4 – 6 lay the foundation for the macroscopic results presented here, while Chapter 8 validates and delves deeper into the microstructural origin of these results. This methodological reflection is relevant and is discussed in further depth in Section 7.4. In the first part of this chapter, the test results are shown, classified qualitatively according to the extent of surface cracks, and discussed. Secondly, stress versus strain curves are presented and analysed. Then, a novel approach is employed to quantify surface cracking employing panoramic imaging and image analysis on sectioned samples. The said quantitative data are fed into a multiple linear regression model to predict surface cracking in the forging design space. The last section summarises the key findings of the chapter and discusses their implications in relation to the objectives of this thesis.

7.1 Gleeble compression-testing results

Figure 7.1 shows 9 representative double cones samples following thermo-mechanical testing at the cooling rates and forging temperatures defined in the experimental matrix of Section 6.4. Successful outcomes were achieved for all nine conditions of the experimental matrix. A total of 26 double cone specimens were tested of which 18 are considered valid. Tests are considered valid if both the thermal cycle and the deformation characteristics are acceptably accurate. There exists moderate deformation inhomogeneity across the samples; this is most clearly observed in the $(T_0, \Theta) = (1030°C, 30°C/s)$ condition, where the axial strain is slightly larger on one side of the sample.

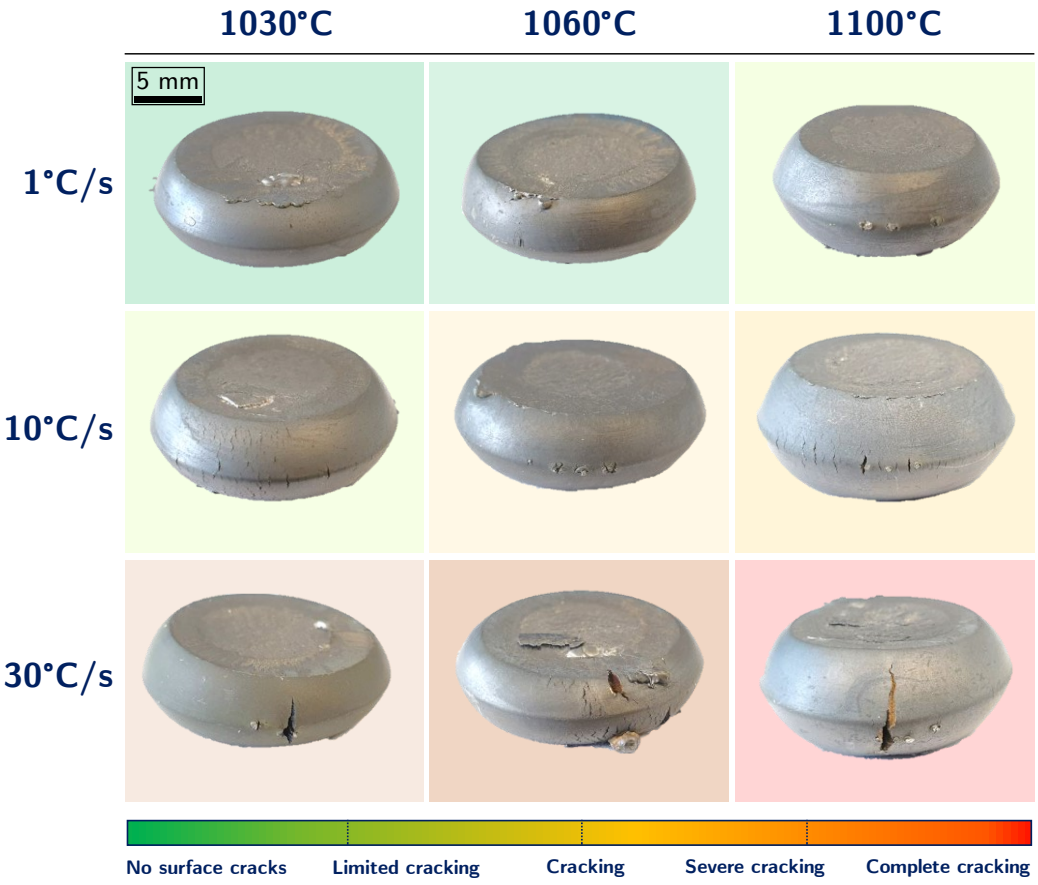

Figure 7.1. Representative double cone samples tested at different forging temperatures (T_0) and cooling rates (Θ). The forging temperature for each sample is indicated at the top of its column; the cooling rate is indicated at the left of its row. The background colour denotes the degree of cracking as per the gradient legend below.

A clear pattern exists whereby the severity of cracking increases with both the forging temperature and the cooling rate; here severity of cracking refers to both the number of surface cracks and their depth. Thus, these results provide solid support for the hypothesis. In addition, it is observed that the nine specimens display varying degrees of surface cracking, ranging from no cracks for the (1030°C, 1°C/s) sample to full cracking for the (1100°C, 30°C/s) condition. This demonstrates the soundness of the novel experimental method. Interestingly, surface cracking seems to be more sensitive to the cooling rate than to the forging temperature. Cracking is minimal for the slowest cooling rate of 1°C/s irrespective of the forging temperature, whereas at the medium cooling rate of 10°C/s it is only significant for a forging temperature of 1100°C. Conversely, all three samples cooled at 30°C/s show substantial cracking. In particular, the (1030°C, 30°C/s) sample shows one large crack and the (1060°C, 30°C/s) sample an even distribution of large cracks. The (1100°C, 30°C/s) sample displays fracture with notable loss of material, and in the context of forging it can be considered to have failed catastrophically.

The full data corresponding to the double cone specimens are shown in tabular form in Table 7.1. This includes the specimens shown in Figure 7.1 and the remaining 9 valid samples. Samples are designated by their true axial strain after deformation – obtained through calliper measurements and direct calculations. Although a fixed (nominal) strain of 0.8 was set on the Gleeble thermo-mechanical simulator, the actual results varied. Only samples with strains between 0.6 and 0.9 are considered valid. By definition, the full set of data displays the same patterns described for the representative samples of Figure 7.1: higher forging temperature and especially higher cooling rates cause greater surface cracking. In addition, there is a positive correlation between strain and surface cracking that is clearly seen in the (1060°C, 30°C/s) and (1100°C, 10°C/s) conditions. This behaviour is expected, but it is noteworthy that the axial strain appears to be a weaker indicator of surface cracking than the forging temperature or the cooling rate. For example, the thermo-mechanical testing of both

(1100°C, 30°C/s) samples resulted in complete failure despite attaining relatively low strain values.

Table 7.1. For all double cone samples tested at different forging temperatures (T_0) and cooling rates (Θ): global axial strain (ε) and degree of cracking. The degree of cracking is indicated by the background colour as per the gradient legend below.

θ	T_0		
	1030°C	1060°C	1100°C
1°C/s	$\varepsilon = 0.82$	$\varepsilon = 0.80$	$\varepsilon = 0.71$
10°C/s	$\varepsilon = 0.74$	$\varepsilon = 0.75$	$\varepsilon = 0.62$ $\varepsilon = 0.63$
	$\varepsilon = 0.75$	$\varepsilon = 0.86$	$\varepsilon = 0.69$ $\varepsilon = 0.71$ $\varepsilon = 0.77$
30°C/s	$\varepsilon = 0.82$	$\varepsilon = 0.69$ $\varepsilon = 0.82$ $\varepsilon = 0.86$	$\varepsilon = 0.63$ $\varepsilon = 0.67$
Udimet 720; $\varepsilon = 0.8$; $\dot{\varepsilon} = 0.1\ s^{-1}$; $T_f = 880°C$			

No surface cracks | Limited cracking | Cracking | Severe cracking | Complete cracking

Figure 7.2 shows representative thermo-mechanically tested cylindrical specimens. Successful results are attained for 8 out the 9 intended conditions. The samples show varying degrees of surface cracking and behave equivalently to the double cones concerning forging temperatures, cooling rates, and surface cracking. Consequently, these results provide additional backing for the validity of the hypothesis and the effectiveness of the forging simulation methodology. Surface cracking is negligible or marginal for the slowest cooling rate. For a cooling rate of 10°C/s, samples forged at 1060°C display limited cracking, but when the forging temperature increases to 1100°C surface cracking appears. Severe cracking occurs for all three samples cooled at a rate of 30°C/s. As in the double cones,

catastrophic failure occurs for the (1100°C, 30°C/s) condition. Here again, the cooling rate seems to affect cracking more than the forging temperature. This is evidenced by the shift for a forging temperature of 1100°C from no cracking at 1°C/s to catastrophic failure at 30°C/s. However, it is clear that the forging temperature also plays a significant role; for example, for a cooling rate of 30°C cracking is much more limited at 1030°C and 1060°C than at 1100°C.

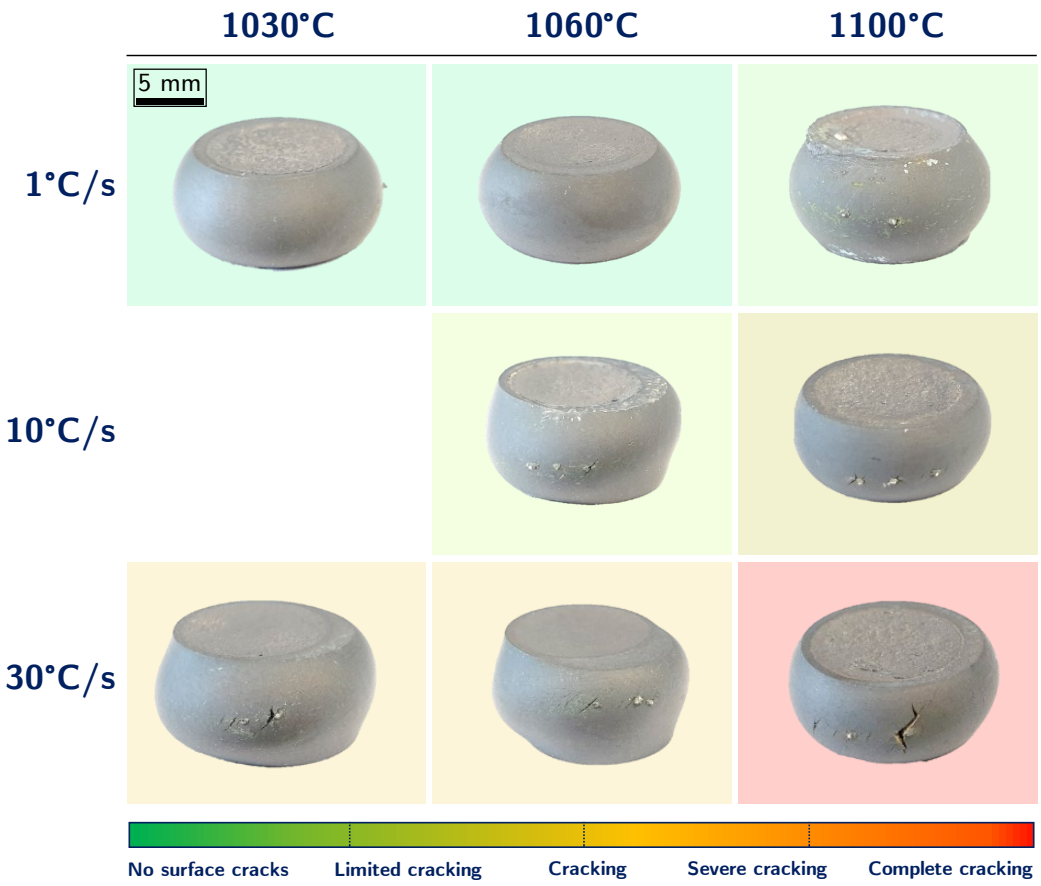

Figure 7.2. Representative cylindrical samples tested at different forging temperatures (T_0) and cooling rates (Θ). The forging temperature for each sample is indicated at the top of its column; the cooling rate is indicated at the left of its row. The background colour denotes the degree of cracking as per the gradient legend below.

Overall, 12 specimens from a total of 15 completed tests are considered valid. Nevertheless, it is apparent from Figure 7.2 that deformation is more inhomogeneous than for the double cone specimens. Deformation inhomogeneities alter the local strain and stress states in the samples, thereby reducing accuracy.

Besides, the cylindrical specimens show generally less surface cracking, which makes identifying patterns more difficult. This is due to the shortcoming identified in Section 6.3 that the compression of cylinders cannot capture the effect of large secondary tensile stresses, which are frequently behind surface cracking or cavitation. For these reasons, double cone specimens are prioritised in this research work, and only 15 cylindrical specimens are tested.

Table 7.2. For all cylindrical samples tested at different forging temperatures (T_0) and cooling rates (Θ): global axial strain (ε) and degree of cracking. The degree of cracking is indicated by the background colour as per the gradient legend below.

θ	T_0		
	1030°C	1060°C	1100°C
1°C/s	$\varepsilon = 0.79$	$\varepsilon = 0.82$	$\varepsilon = 0.70$ $\varepsilon = 0.82$
10°C/s	N/A	$\varepsilon = 0.73$ $\varepsilon = 0.84$	$\varepsilon = 0.71$ $\varepsilon = 0.81$
30°C/s	$\varepsilon = 0.72$	$\varepsilon = 0.71$	$\varepsilon = 0.70$ $\varepsilon = 0.82$
Udimet 720; $\varepsilon = 0.8$; $\dot{\varepsilon} = 0.1\ s^{-1}$; $T_f = 880°C$			

No surface cracks | Limited cracking | Cracking | Severe cracking | Complete cracking

The full set of data corresponding to the cylindrical samples is shown in Table 7.2. In addition to the observations noted for Figure 7.2, there is additional evidence that for each condition there exists a critical strain above which surface cracking is significant. This can be inferred from conditions (1060°C, 10°C/s) and (1100°C, 10°C/s), despite the limited number of samples. The critical strain can be thought of as a link between the macroscopic deformation variables (ε and σ) and the microstructural phenomena controlled by T_0 and Θ. In effect, the critical strain correlates positively with the forging temperature and the cooling rate. For example, a strain of $\varepsilon \sim 0.8$ for the (1060°C, 1°C/s) condition results in no cracking, for (1100°C, 10°C/s) limited cracking occurs, and for (1100°C, 30°C/s)

it results in catastrophic failure. Naturally, the global axial strain and the critical strain for each condition are correlated to the local strain at the equator of the samples where surface cracks emerge; this correlation can be established via the FEA simulations of Section 6.3.

7.2 Stress-strain curves

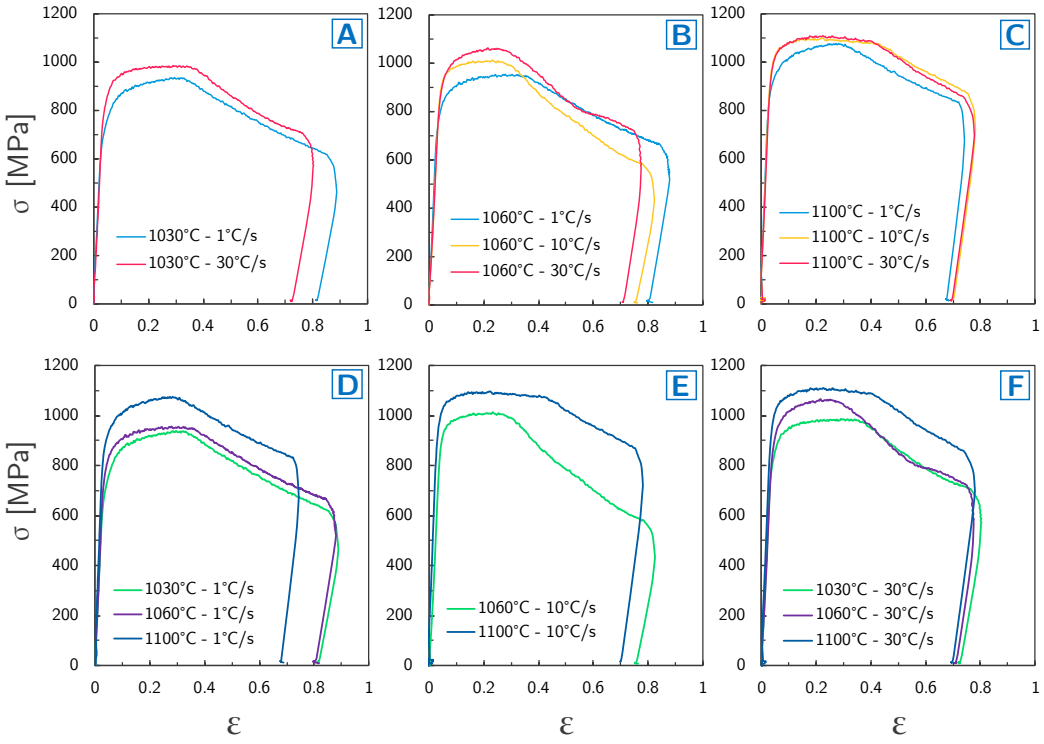

Figure 7.3. Stress versus strain curves for selected cylindrical specimens deformed at different forging temperatures and cooling rates. (A – C) Each subplot presents curves corresponding to different cooling rates at the same forging temperature. (D – F) Subplots for different forging temperatures at the same cooling rate.

Figure 7.3 shows the stress versus strain data corresponding to the representative cylindrical samples of Figure 7.2. The subplots (A – C) display data for different cooling rates at each forging temperature; the subplots (D – F) display data for different forging temperatures at the same cooling rate. Despite the shortcomings noted in Section 7.1, there is value in using cylindrical samples along with double cones, because cylinders provide stress versus strain data that

can be interpreted in a more straightforward manner. This is discussed in further depth at the end of the section.

The flow stress increases with the cooling rate at all forging temperatures. The difference in peak flow stress at 1030°C between specimens cooled at a rate of 1°C or 30°C/s is 5.5%, while at 1060°C it increases to 11.5%. Conversely, the gap is narrower ($\sim 1\%$) at 1100°C. Equally, the flow stress increases with the forging temperature for constant cooling rates. For a cooling rate of 1°C/s, the peak flow stress increases by 13% when the forging temperature rises from 1030°C to 1100°C. For a cooling rate of 10°C/s the peak flow stress increases by 9%, and for 30°C/s by $\sim 12\%$.

The stress versus strain results are broadly in line with the hypothesis and the results presented thus far. In particular, higher T_0 (greater γ'_s dissolution) and higher Θ (finer γ'_t) raise the flow stress. Yet some inconsistencies are noted. For example, it is unexpected that the difference in flow stress is minimal for specimens forged at 1100°C when the cooling rate changes (subplot C). Indeed, in Figure 7.2 and Table 7.2 it is seen that the largest transition in surface cracking occurs for these three conditions. In addition, the flow stress for the (1030°C, 30°C/s) condition is lower than for the (1100°C, 1°C/s) sample, but surface cracking is observed on the former and not the latter. These inconsistencies can be attributed to inhomogeneities in deformation. This is most clearly seen in subplot B, where the inconsistent intersections between curves are likely due to the non-ideal deformation observed in the (1060°C, 10°C/s) and (1060°C, 30°C/s) samples in Figure 7.2. Besides, all samples show a degree of barrelling, meaning that they are not following the deformation path assumption on which the stress versus strain curves rely. In summary, stress versus strain curves are useful indicators of how the processing conditions relate to surface cracking, but they should be accompanied by additional assessments before conclusions can be extracted with confidence. Such examinations can be either a macroscopic qualitative analysis as that presented in Section 7.1 or a systematic

quantitative approach as the one introduced in the following section. It is noteworthy that FEM simulations can be fed with geometric data from the deformed specimens to 'backtrack' the deformation path and thereby obtain actual stress and strain fields in the specimens. This could improve the accuracy and insight provided by the stress versus strain data and will be listed as future work in Chapter 10.

7.3 Quantification of cracking behaviour

Figure 7.4 shows two panoramic images and close-ups in the peripheral and inner regions for two double cone specimens: one for which no surface cracks are observed (1060°C, 1°C/s), and another one which shows catastrophic failure (1100°C, 30°C/s). The macroscopic examinations and the qualitative classification set out in Section 7.1 are a straightforward but effective approach to study forgeability and surface cracking. However, the method is limited in two aspects: first, macroscopic examinations do not show the depth of surface cracking, which is of the utmost importance in industrial practice; secondly, quantitative measurements are required to develop predictive statistical models. To the knowledge of the author, no previous study has produced a robust procedure to quantify surface cracking, so a bespoke method is designed and employed. In brief, specimens were cut along their 'equator' and imaged via SEM. Then, the SEM micrographs were assembled into panoramic images, and image analysis was performed to measure the cracked surface area. Finally, the data were fed into a multiple linear regression model. The experimental procedure is described in detail in Sections 3.8.3 and 3.8.4.

The panoramic images reveal the full extent of surface cracking. Image analysis confirms that for the samples classified as 'non-cracked' in Section 7.1, the crack surface area is negligible, whereas for the (1100°C, 30°C/s) condition it reaches ~ 16% – indicating a large loss of material. Surprisingly, low values (<1%) were obtained for the (1030°C, 30°C/s) and (1100°C, 10°C/s) conditions; this is

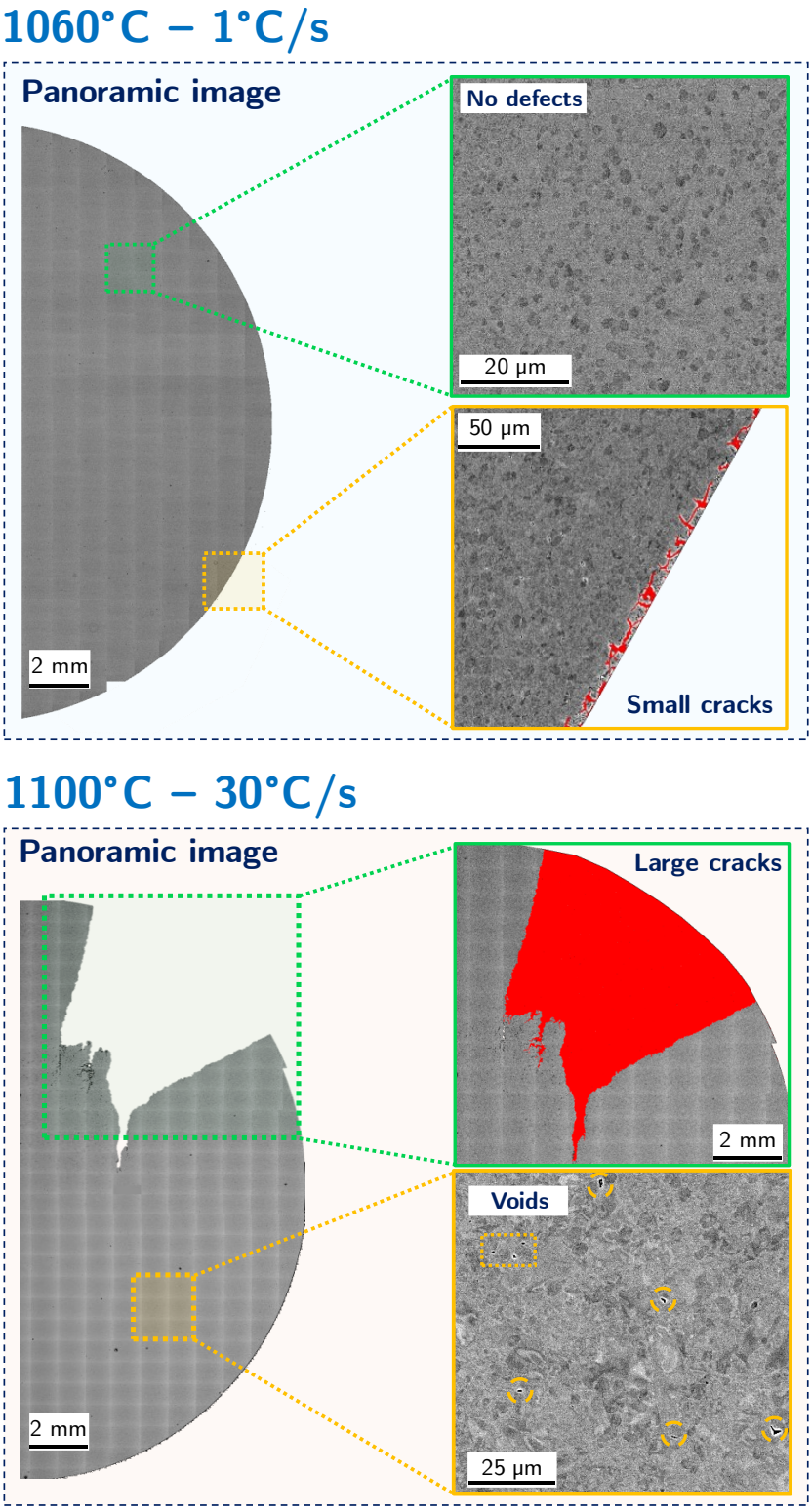

Figure 7.4. Representative panoramic images showing close-ups of the inner and peripheral (edge) regions. The top sample was forged at 1060°C and cooled down at 1°C/s; it displays minimal surface cracking and no internal defects. The bottom sample was forged at 1100°C and cooled at 30°C/s; it shows significant loss of material and internal voids. Void density is not quantified.

not in agreement with the observations of Figure 7.1 and could indicate that cracks are highly superficial despite their seemingly large extension. Nevertheless, more measurements are needed before this can be affirmed with confidence. The close-up images reveal that large surface cracking is accompanied by cavitation. A gradient of voids exists from the peripheral region, where the density of voids is maximum, to the inner region, where voids are sparser. Conversely, on the non-cracked samples voids are observed solely in the immediate surroundings of the edge.

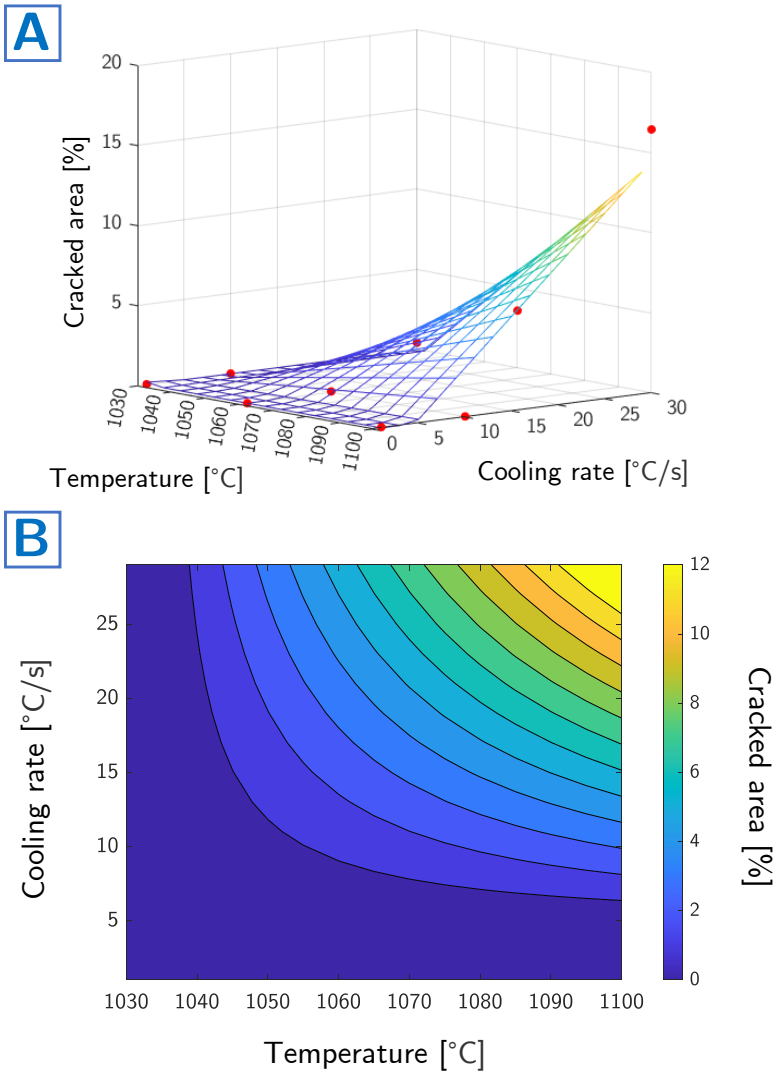

Figure 7.5. Multiple linear regression model for cracked area (%) versus forging temperature and cooling rate for Udimet 720 in the 1030°C – 1100°C temperature range and 0°C/s – 30°C/s cooling rate range. (A) Surface plot and experimental data points; (B) Contour plot.

A multiple linear regression model was built using the surface crack area measurements. The predictive model is given by Eq.7.1 and 7.2, where the input variables are the forging temperature (T_0) in [°C] and the cooling rate (Θ) in [°C s^{-1}], and the response variable is the cracked area (κ). Figure 7.5 shows a surface plot of the model. The model reflects the tendencies mentioned in this chapter regarding the relationship between cooling rate, temperature, and surface cracking. It also shows graphically the observation made above that the (1100°C, 10°C/s) data point could be an outlier. An appraisal of this method follows in the next section.

$$\kappa = \beta_0 + \beta_1 T_0 + \beta_2 \Theta + \beta_3 T_0 \Theta \tag{7.1}$$

$$\kappa \sim 41.45 - 0.04\ [°C^{-1}]\ T_0 - 8.95\ [s\ °C^{-1}]\ \Theta + 0.00865\ [s\ °C^{-2}]\ T_0 \Theta \tag{7.2}$$

It must be noted that this model has a number of limitations. Firstly, it is a basic linear model that uses limited data; naturally, increasing the number of data points fed into it would increase its accuracy. Secondly, a linear model is employed to model a phenomenon which is non-linear in nature, and thus non-linear regression would be more appropriate with additional data. This is clear as, for example, the model predicts that the cracked area continues to increase with forging temperature and cooling rates outside the dominion shown in Figure 7.5. This is not obvious from a metallurgical perspective, and unlikely to be accurate in mechanical terms, since there is an upper limit to the cracked surface area before catastrophic failure occurs. Finally, this model is exclusively observational and does not account for the physics of the problem.

7.4 Summary and discussion

Establishing an optimal forging window for Udimet 720 is a key milestone of this research project. From an industrial point of view, it paves the way for

reduced material waste and increased environmental and cost efficiency. Scientifically, learning how the optimal microstructure looks like provides insight into the relationship between processing parameters, microstructural evolution, and thermo-mechanical behaviour for this class of alloys. Therefore, this chapter contains the arguably most crucial results of this thesis. First, strong evidence is presented to sustain the validity of the hypothesis. Secondly, it is demonstrated that the novel forging simulation methodology is effective and accurate.

The thermo-mechanical testing results robustly contest the notion that the optimal forging window for high γ'-reinforced cast-and-wrought lies below but close to the γ' solvus. Instead, they suggest that lower forging temperatures improve ductility and reduce surface cracking. Based on the analysis of 30 valid double cones and cylindrical samples tested at different forging temperatures and cooling rates, it can be affirmed with confidence that Udimet 720 behaves in line with the hypothesis. For a constant deformation temperature (T_f), the severity of surface cracking increases with both the forging temperature and the cooling rate. Among these, cracking appears to be most sensitive to the cooling rate. Moreover, the experimental data indicate the existence of a critical strain above which surface cracks appear that is dependent on T_0 and Θ. Stress versus strain data align with the hypothesis and the qualitative results, although some inconsistencies are noted. Quantitative data obtained via panoramic imaging and image analysis validate the findings outlined above, as does the multiple linear regression model built with these data. Minor disagreements were observed between the qualitative analysis and the quantitative analysis whereby samples forged at intermediate T_0 and Θ appeared to show qualitatively significant cracking but that panoramic imaging showed to be highly superficial, resulting in low cracking surface. Extensive surface cracking is associated with the presence of a gradient of voids that is maximum in the peripheral regions and minimum at the core of the specimens.

An important corollary of the results is the validation of the forging simulation method. This is worthy of attention: 41 tests of laboratory-scale specimens provided 30 valid samples covering 9 combinations of forging temperatures and cooling rates. It is a significantly more efficient and economical method of appraising hot die forgeability than conventional full-scale trials. Acquiring comparable data through full-scale trials would require testing different forging temperatures, performing several tests at each condition for repeatability, and – if at all possible – employing complex temperature measurement apparatus to determine cooling rates. The novel method delivers a wide range of surface cracking states for Udimet 720. Importantly, these results show good accordance with those reported by Otto Fuchs KG for full-scale forgings; this matter is explored in further depth in Section 9.1. Double cone specimens are shown to be particularly robust for assessing susceptibility to surface cracking, confirming the importance of large secondary tensile stresses in cracking (see Section 6.3). Nevertheless, cylindrical samples also result in satisfactory outcomes and have the advantage of providing readily understandable stress versus strain curves. Despite the limited number of points due to the time constraints of this research project, the results show that panoramic imaging, image analysis, and statistical quantification are an effective supplement to the novel hot die forging simulation method. It can thus be considered a successful proof of concept. A reliable model can be used to find states of minimum cracking in the forging design space, for both industrial and scientific applications.

If the thermo-mechanical tests are the arguably most insightful results of this research project, the reader could pose the question: why not starting with these, followed by EM, thermal analysis, and FEM simulations to understand the subjacent physical mechanisms? Such a view is reasonable but misses one fundamental point: the results shown here rely on the extensive preliminary work presented previously. In other words: without DSC, heat treatments, finite element analysis, and a fitting conceptual framework, it is unlikely that the same results had been obtained. For example, it would not be known that 4 hours heat

treatments are required to obtain representative microstructures, and which thermo-mechanical testing parameters are best to replicate hot die forging. In this sense, this work demonstrates the value of planned, structured explorations to target certain research problems. However, it is undoubtful that EM examinations of the Udimet 720 specimens after thermo-mechanical testing are a necessary check to further validate the hypothesis; this content is covered in the next chapter.

8

Microstructural analysis of forged specimens

Following the thermo-mechanical tests of Chapter 7, this chapter presents and discusses the EM analyses of the resulting specimens. The thermo-mechanical tests prove that for Udimet 720, surface cracking increases and ductility decreases as the temperature increases below its γ' solvus. Together with the DSC analysis, heat treatments, EM examinations of heat-treated specimens, and FEM forging simulations, a clear picture emerges that surface cracking is controlled by the dissolution and reprecipitation of γ'_s. However, validating with confidence the hypothesis requires one additional step: examining the specimens after thermo-mechanical testing. This provides direct evidence of previously unobserved mechanisms, such as the reprecipitation of fine γ'_t in the severely cracked, high forging temperature, high cooling rate samples. Crucially, it also ensures that other microstructural phenomena caused by the combination of both deformation and heat – and hence not captured through the heat treatments of Section 3.3 – are not at play in surface cracking. Such phenomena could include shear bands, abnormal grain growth (AGG), or others. Therefore, the ultimate validation for the hypothesis and the testing methodology is that the microstructures after thermo-mechanical testing resemble those observed through heat treatments.

The chapter starts with a fractographic analysis of the specimens that show significant surface cracking. Then, the microstructures of selected specimens corresponding to every combination of forging temperature and cooling rate of the experimental matrix are studied via BSE and SE imaging – including a comparison between the inner and outer regions of the samples. The PSD of the γ' phase for these samples is quantified via image analysis on the BSE or SE images and discussed. Next, additional BSE imaging, EDX analysis, and EBSD analyses are used to infer the dominant deformation and fracture mechanisms for different forging conditions. The final section outlines the conclusions of the chapter.

8.1 Fractography

Figure 8.1 shows SE SEM fractographic images corresponding to the thermo-mechanical testing conditions which resulted in substantial surface cracking. It is noteworthy that the difference in resolution between images is due to the exposure and extension of the surface cracks. For example, the (1060°C, 10°C/s) specimens show minimal cracking (see Figure 7.1), which makes surface cracks difficult to image. Conversely, the (1100°C, 30°C/s) samples contain large surface cracks that can be readily imaged with good resolution (see Figure 8.1E,J). To avoid inducing additional cracking or other preparation artifacts, the specimens were ultrasonically only cleaned before being imaged.

A pattern is observed whereby specimens thermo-mechanically tested at lower cooling rates and temperatures show elongated grains and dimpled fracture surfaces, whereas higher cooling rates and temperatures result in more equiaxed and faceted surfaces. The (1060°C, 10°C/s) sample (Figure 8.1A,F) shows highly elongated grains, substantial dimpling, and secondary cracking. The (1100°C, 10°C/s) sample (Figure 8.1B,G) resembles the (1060°C, 10°C/s) condition, although grains appear to be slightly less deformed. Intergranular γ'_{p} precipitates are visible, and the exposed grains show no signs of transgranular

fracture – e.g. river patterns, terraces, smooth areas – suggesting that fracture occurs intergranularly. The same pattern is observed for the (1030°C, 30°C/s) sample (Figure 8.1C,H).

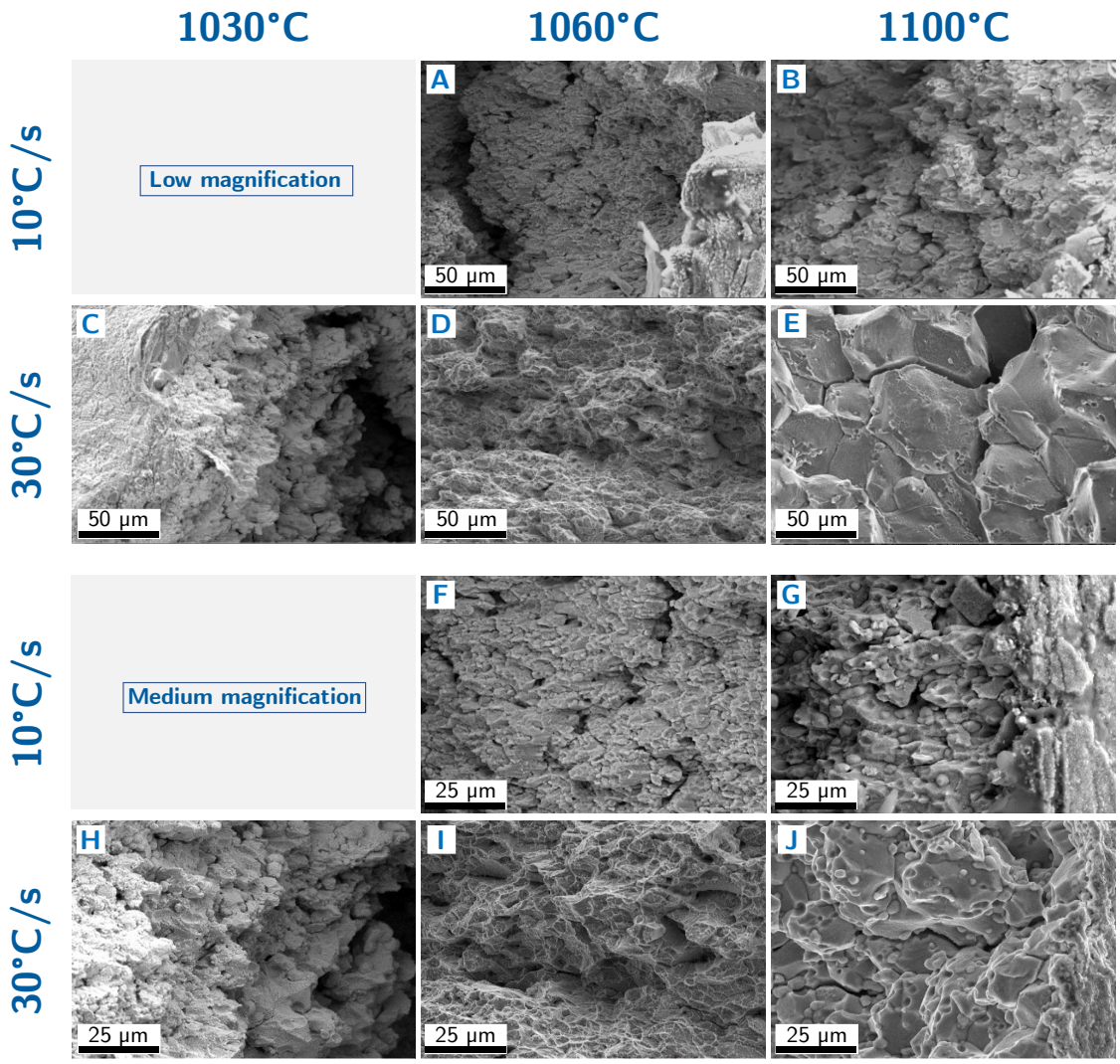

Figure 8.1. Fractographic SE SEM images of the surface cracks on double cone specimens thermo-mechanically tested at forging temperatures of 1030°C, 1060°C, or 1100°C and cooling rates of 10°C/s or 30°C/s. The (1030°C, 10°C/s) condition is not shown as it did not display significant surface cracks.

For the (1060°C, 30°C/s) sample (Figure 8.1D,I), significant differences are noted. The grains are more equiaxed than in the previous condition, and the surface is more faceted – i.e. less dimpled. This indicates a shift from ductile to brittle fracture. Although the faceted surface is indicative of intergranular

fracture, the grains also show river patterns characteristic of transgranular fracture, suggesting a possible mixed mode of fracture [258]. The trend toward brittle fracture continues for the most cracked condition, specimen (1100°C, 30°C/s), as seen in Figure 8.1E,J; this sample displays more equiaxed grains and a faceted 'rock candy' cracking surface [259].

In conclusion, fractography reveals that surface cracks for Udimet 720 are primarily intergranular, with a ductile to brittle transition at higher cooling rates and forging temperatures. This is aligned with the hypothesis: it is expected that the material accommodates deformation and releases larger amounts of energy via more extensive surface cracking as greater amounts of fine γ'_t harden the microstructure.

8.2 Backscattered and secondary electron analyses.

Figure 8.2 shows low (~ 100 μm) and medium-low magnification (~ 10 μm) BSE micrographs of the outer regions of the thermo-mechanically tested specimens for all conditions of the experimental matrix. At low magnification (Figure 8.2A–I), no relevant microstructural differences are noted between specimens: all conditions show several surface cracks, voids, and a dispersion of intergranular γ'_p particles. In line with the heat treatments of Section 4.3, γ'_p is not noticeably affected by either the forging temperature or the cooling rate. At medium magnification (Figure 8.2J–R), additional features become visible. All samples but the (1060°C, 10°C/s) condition contain voids, which are located primarily at γ'_p particles. Moreover, Figure 8.2O shows a surface crack growing by void coalescence in the (1060°C, 10°C/s) sample. γ'_s precipitates are seen in all 1030°C and 1060°C conditions but are absent in the samples forged at a T_0 of 1100°C. For a T_0 of 1030°C, γ'_s precipitates are finer and more numerous, whereas the samples forged at 1060°C contain fewer and coarser γ'_s precipitates. This is also in accordance with the observations of Section 4.3: as the

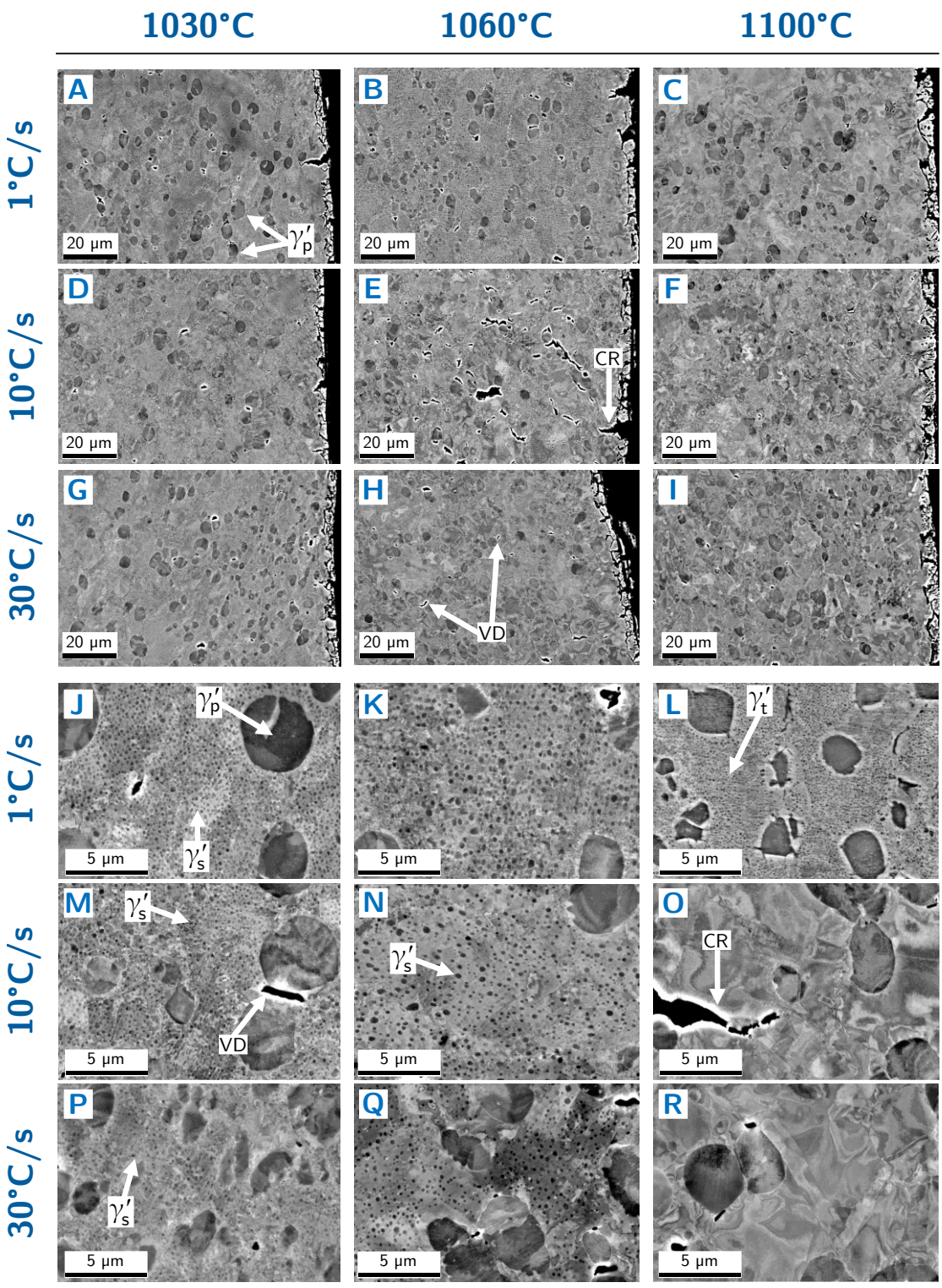

Figure 8.2. BSE SEM micrographs of the outer regions of specimens thermo-mechanically tested at various forging temperatures (columns) and cooling rates (rows). Low magnification (A – I) and low-medium magnification images (J – R). Primary, secondary, and tertiary γ' precipitates are labelled γ'_p, γ'_s, and γ'_t; cracks are labelled 'CR' and voids 'VD'.

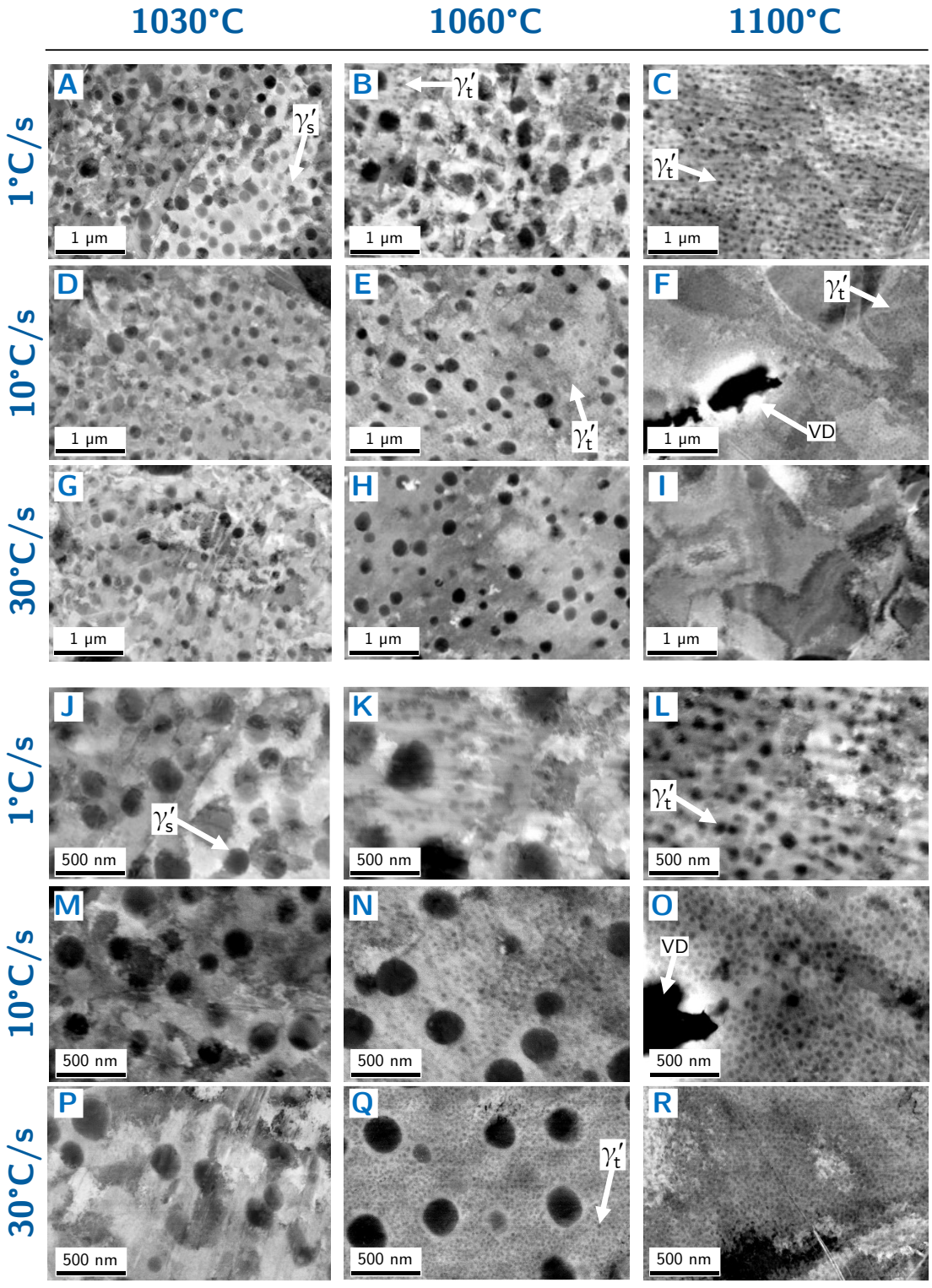

Figure 8.3. Medium-high magnification (A – I) and high magnification (J – R) BSE SEM micrographs of the outer regions of Udimet 720 specimens thermo-mechanically tested at various forging temperatures (columns) and cooling rates (rows). Secondary and tertiary γ' precipitates are labelled γ'_s and γ'_t; voids are labelled 'VD'.

temperature increases, coarsening occurs via Ostwald ripening. At 1100°C, no γ'_s precipitates are observed as this temperature lies just below $T_{\gamma's\ solvus}$ (~ 1110°C). Fine γ' precipitates are noted for the (1100°C, 1°C/s) condition in Figure 8.2L. These, however, are not γ'_s but γ'_t particles, as seen in greater resolution in Figure 8.3.

Figure 8.3 presents medium-high and high magnification (~ 1 µm) BSE micrographs for the same thermo-mechanical testing conditions and sample areas of Figure 8.2. Very high magnification (~ 100 nm) micrographs corresponding to the highest temperatures (1060°C and 1100°C) and cooling rates (10°C/s and 30°C/s) are shown in Figure 8.4. The evolution of γ'_s with the forging temperature described above is also observed in Figure 8.3A–I. Furthermore, lower cooling rates also result in γ'_s coarsening – see Figure 8.3A,D,G and Figure 8.3B,E,H. This phenomenon is particularly evident as the cooling rate drops from 10°C/s to 1°C/s and is due to the dissolution of γ'-forming elements into the matrix and their reprecipitation upon cooling. As the cooling rate decreases, more time is available for γ'-forming elements to deposit onto γ'_s precipitates and for ripening of the newly formed γ'_t.

In Figure 8.3C, it is clear that the aforementioned γ' precipitates for the (1100°C, 1°C/s) condition belong to a different population to the γ'_s of Figure 8.3A,B,D,E,G,H. Specifically, these are γ'_t particles that have reprecipitated upon cooling and which can also be seen in Figure 8.3F for the (1100°C, 10°C/s) condition. At higher magnification, γ'_t precipitates are detected for all samples forged at 1060°C and 1100°C (Figure 8.3K,L,N,O,Q,R). Equivalently to γ'_s, γ'_t precipitates are found to coarsen as the cooling rate decreases. However, the effect for γ'_t is more intense than for γ'_s; indeed, Figure 8.3K,N,Q and Figure 8.3L,O,R show an order of magnitude difference in the PSD (size and density) of γ'_t precipitates as the cooling rate changes. No γ'_t precipitates are seen in samples thermo-mechanically tested at 1030°C. The samples thermo-mechanically tested at a forging temperature of 1100°C contain

greater amounts of γ'_t than the 1060°C samples – this is most clearly seen in Figure 8.3K,L and Figure 8.3N,O. As per the hypothesis, this is due to the greater dissolution of γ'_s as the forging temperature increases and the concomitant rise in γ'-forming elements that reprecipitate upon cooling. Interestingly, γ'_t precipitates seem to have a comparable size or be finer for $T_0 = 1060°C$ than for $T_0 = 1100°C$ (see Figure 8.3K,L and Figure 8.4A-D). Since finer γ'_t precipitates tend to diminish ductility, this seems to be at odds with the fact that surface cracking increases with the forging temperature. However, this can be explained in terms of the overall lower γ'_t volume fraction at 1060°C, or the finer γ'_t lying below the peak strength (see Figure 2.12) and blocking dislocation glide less effectively than the slightly coarser ones.

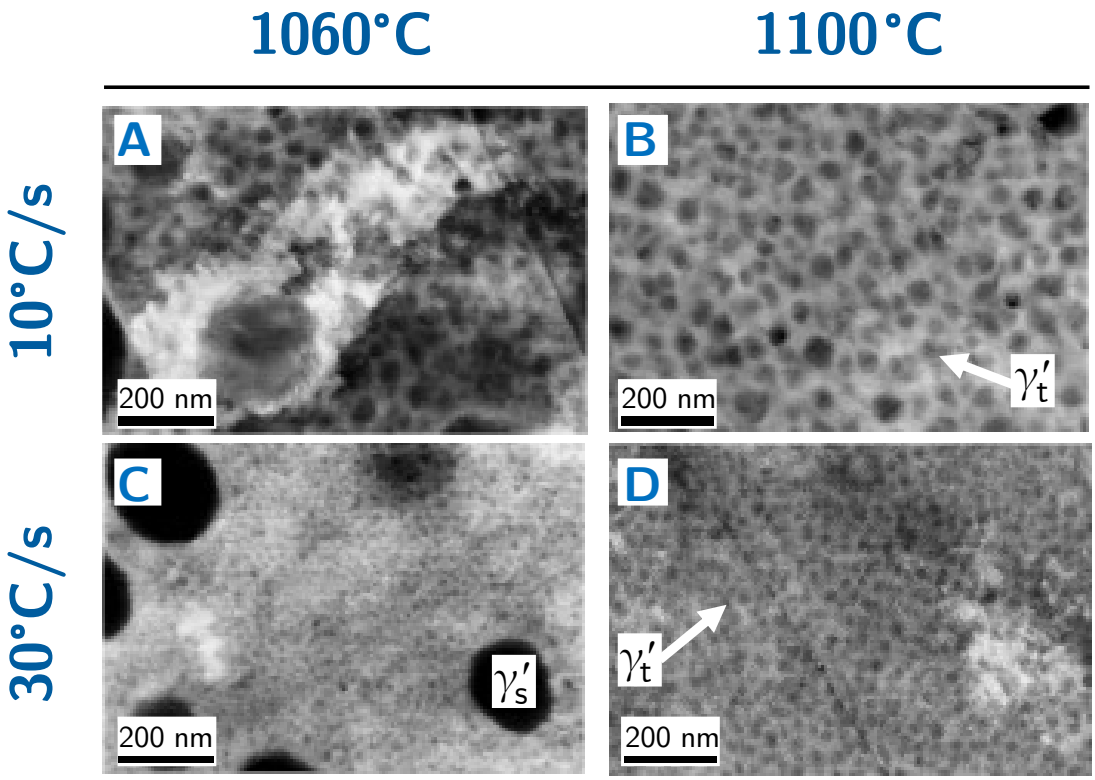

Figure 8.4. Very high magnification BSE SEM micrographs of the outer regions of Udimet 720 specimens thermo-mechanically tested at forging temperatures of 1060°C or 1100°C and cooling rates of 10°C/s or 30°C/s. Secondary and tertiary γ' precipitates are labelled γ'_s and γ'_t.

Following their characterisation by BSE imaging, the thermo-mechanically tested and EM-prepared samples were γ-etched electrolytically using a 10% phosphoric acid solution. SE SEM micrographs of these materials are shown in Figure 8.5. The micrographs at low magnification (Figure 8.5A–I) and high magnification (Figure 8.5J–R) provide additional evidence for the phenomena described above, namely:

- γ'_{p} precipitates are largely unaffected by either the forging temperature or the cooling rate; this is attributed to their different chemical composition together with their smaller interface area.
- Greater amounts of γ'_{s} precipitates dissolve as the forging temperature increases. γ'_{s} precipitates coarsen as the cooling rate decreases.
- For all samples thermo-mechanically tested at forging temperatures of 1060°C or 1100°C, reprecipitated γ'_{t} particles are detected. These are particularly fine (~ 50 nm) for cooling rates of 10°C/s and 30°C/s.

A small number of γ'_{s} precipitates are seen for the (1100°C, 10°C/s) condition (Figure 8.5F), which are not seen in the BSE micrographs; this is consistent with the $T_{\gamma's\ solvus}$ (~ 1110°C) obtained via DSC. Moreover, no γ'_{t} are observed for the (1030°C, 30°C/s) condition in either Figure 8.3P or Figure 8.5P. This is despite this condition resulting in significant surface cracking (see Figure 7.1). It is hypothesised that – in line with the observation that γ'_{t} are finer at 1060°C than at 1100°C for the same cooling rate – γ'_{t} precipitates in Figure 8.3P or Figure 8.5P are too fine to be resolved via SEM. This could be confirmed via TEM but was left outside of this research project due to time constraints.

Figure 8.6 presents BSE SEM micrographs corresponding to the outer and inner regions of the thermo-mechanically tested specimens. Specifically, BSE

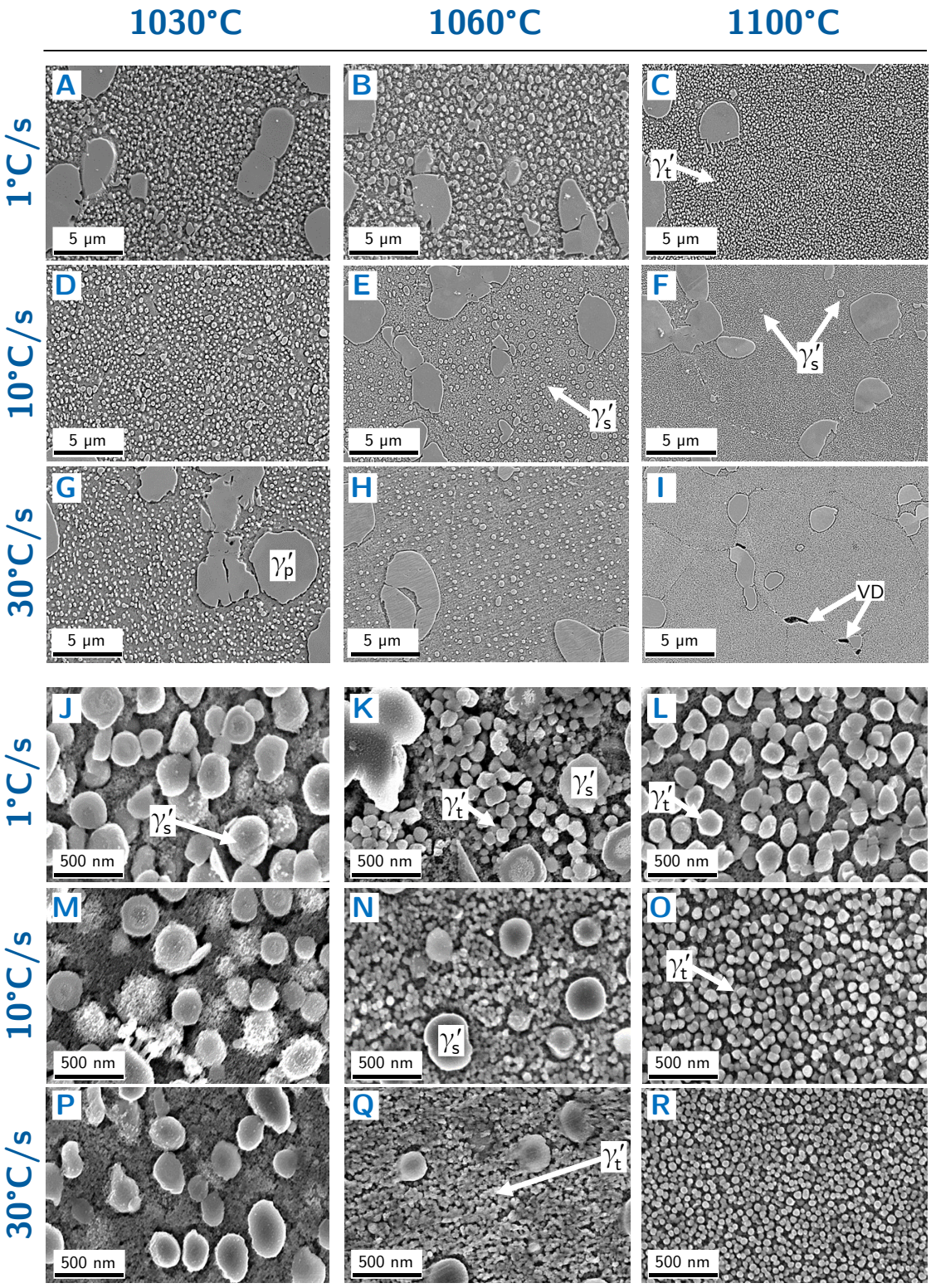

Figure 8.5. SE SEM micrographs of the outer regions of Udimet 720 specimens thermo-mechanically tested at various forging temperatures (columns) and cooling rates (rows). Low-medium magnification (A – I) and high magnification images (J – R). Primary, secondary, and tertiary γ' precipitates are labelled γ'_{p}, γ'_{s}, and γ'_{t}; voids are labelled 'VD'.

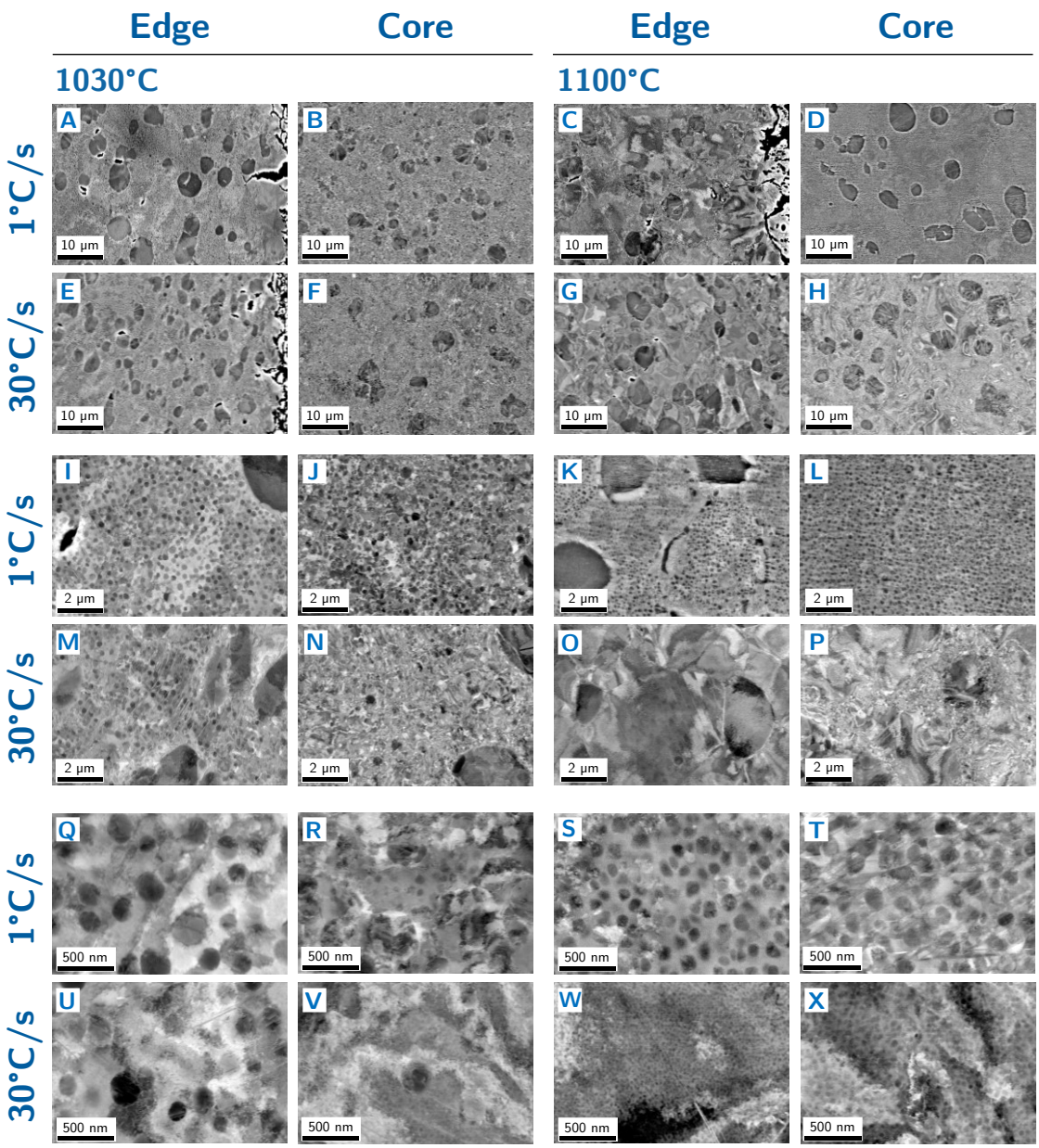

Figure 8.6. BSE SEM images of the outer ('edge') and inner ('core') regions of specimens thermo-mechanically tested at forging temperatures of 1030°C or 1100°C and cooling rates of 1°C/s or 30°C/s. Low magnification (A – H), medium magnification (I – P), and high magnification images (Q – X).

micrographs are shown corresponding to the upper and lower bounds of the experimental matrix for cooling rate (1°C/s and 30°C/s) and forging temperature (1030°C and 1100°C). This analysis explores whether microstructural inhomogeneities exist across the specimen that could affect the thermo-mechanical behaviour of the material – and hence the accuracy of the tests. It is noteworthy

that the FEM simulations (see Figure 6.6) indicate that the temperature gradient between the inner and the outer regions is modest and short-lived.

No significant differences are noted between the inner and the outer regions of the specimens for any forging temperature or cooling rate. In the low magnification micrographs (Figure 8.6A–H) it is seen that – equivalently to the outer regions – intergranular γ'_{p} particles in the inner regions remain unaffected by thermo-mechanical processing. In the medium magnification images (Figure 8.6I–P), γ'_{s} particles are present in the inner regions at 1030°C and 1060°C; these are of comparable size to those present in the outer regions. Interestingly, the high dislocation density in Figure 8.6N,P suggests that the core of the samples undergoes greater deformation that the edges – in agreement with the FEM results of Figure 6.7. Finally, γ'_{t} precipitates are observed in the high magnification micrographs (Figure 8.6Q–X) for which only minor differences are found. In particular, several γ'_{t} precipitates are present in the core for the (1030°C, 30°C/s) condition – adding evidence to the idea proposed above that for a forging temperature of 1030°C γ'_{t} precipitates are too small to be resolved via SEM. Since cooling at the core is slightly slower, γ'_{t} coarsens to a size where it can be resolved. Likewise, for the (1100°C, 30°C/s) condition, γ'_{t} precipitates in the outer regions (Figure 8.6W) seem to be marginally finer than in the inner regions (Figure 8.6X).

8.3 Image analysis and quantification

Figure 8.7 plots the volume fraction of γ'_{p} (Figure 8.7A) and γ'_{s} (Figure 8.7B) as a function of the forging temperature and cooling rate; these data correspond to image analysis measurements. Consistent with the 4-hour heat treatments of Section 3.3, $\mathrm{f}_{\gamma'\mathrm{p}}$ is bounded above by $\sim 15\%$ and below by $\sim 10\%$. For the 1°C/s and 10°C/s conditions, $\mathrm{f}_{\gamma'\mathrm{p}}$ increases by $\sim 5\%$ at a forging temperature of 1060°C. This could indicate that for sufficiently slow cooling rates, γ' forming elements deposit onto γ'_{p} particles upon cooling, or that γ'_{p} coarsens

at the expense of smaller precipitates. However, further measurements are required to validate this finding.

$f_{\gamma's}$ decreases monotonically with the forging temperature and is negligible at 1100°C. As observed qualitatively, $f_{\gamma's}$ increases as the cooling rate decreases, particularly between 1°C/s and 10°C/s. Importantly, the divergence in $f_{\gamma's}$ between specimens cooled at different rates is maximum at 1060°C. Since surface cracking is found to be controlled by the dissolution of $\gamma's$, this result suggests that surface cracking for Udimet 720 is most sensitive to the cooling rate when hot die forged at a temperature of 1060°C, whereas for 1030°C the difference is marginal once the cooling rate surpasses 10°C/s.

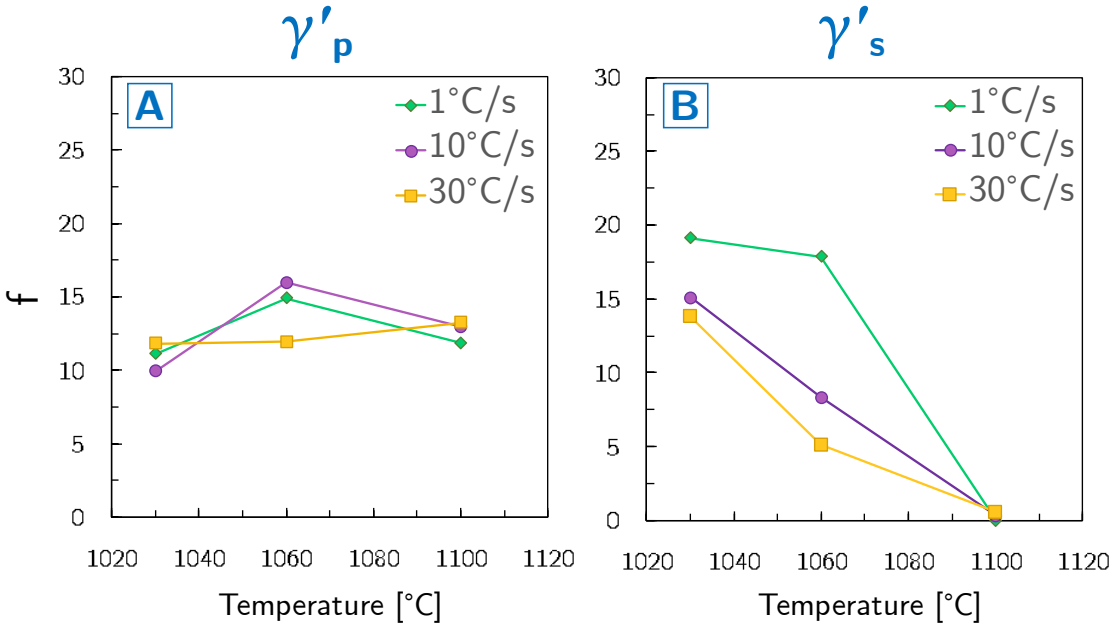

Figure 8.7. For thermo-mechanically tested Udimet 720 specimens: measured volume fraction of γ'_p (A) and $\gamma's$ precipitates (B) as a function of heat treatment temperature (x-axis) and cooling rate (1°C/s, 10°C/s, or 30°C/s).

The $f_{\gamma's}$ data corresponding to cooling rates of 10°C/s and 30°C/s are in good agreement with the 4-hour heat treatments data; conversely, it is significantly higher for a cooling rate of 1°C/s. This is to be expected, noting that the heat treated specimens were water quenched – i.e. cooled very swiftly; hence,

as the cooling rate increases, the $f_{\gamma's}$ vs temperature curves tend to the 4-hour heat treatment curve of Figure 4.6. It is noteworthy that the difference in $f_{\gamma's}$ between curves can be used as a proxy to quantify Ostwald ripening of γ'_t precipitates for different cooling rates – i.e. it can be assumed that any increase in $f_{\gamma's}$ comes from an equivalent decrease in $f_{\gamma't}$. This is useful, since $f_{\gamma't}$ could not be accurately quantified via SEM.

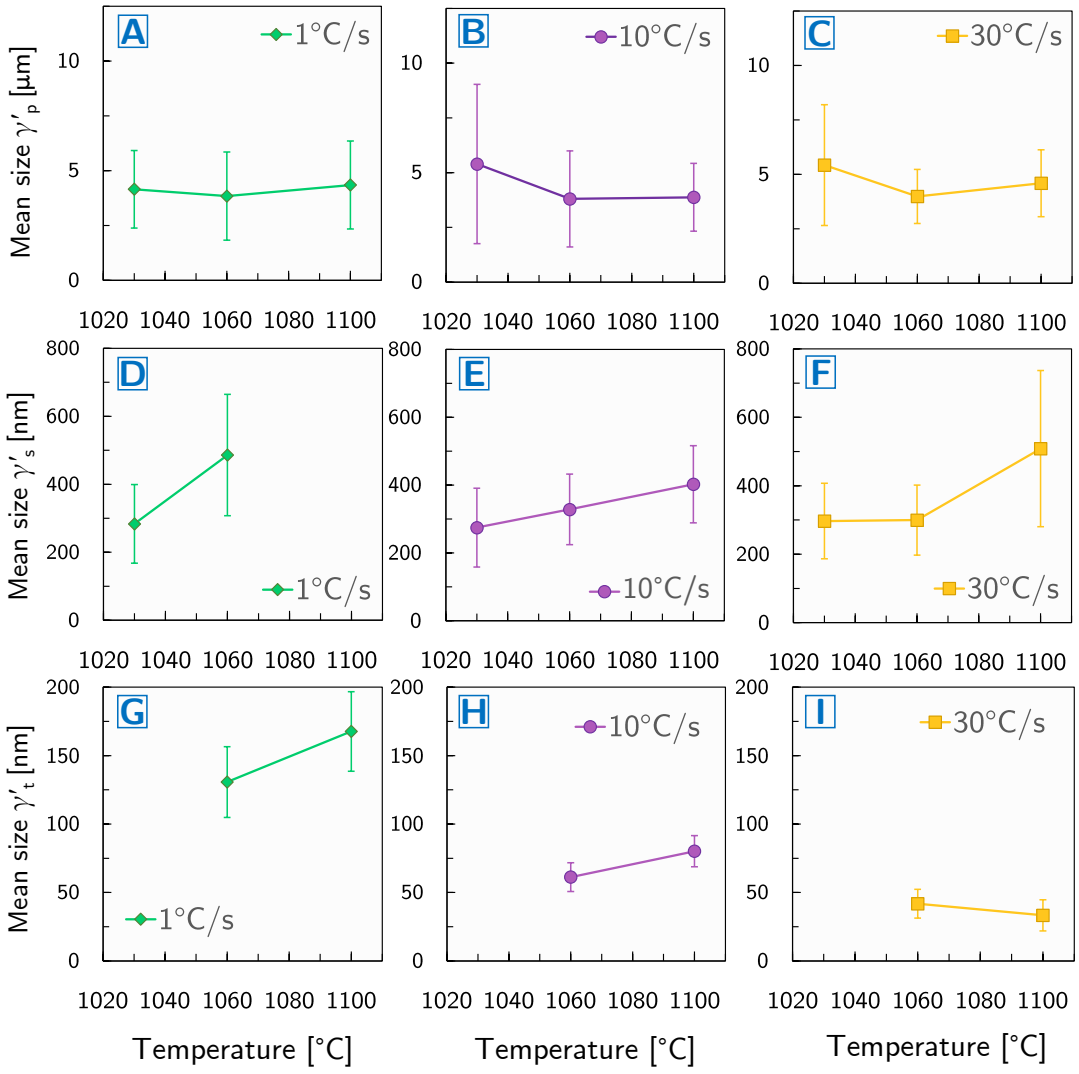

Figure 8.8. For thermo-mechanically tested Udimet 720 specimens: measured mean size of γ'_p (A – C), γ'_s (D – F), and γ'_t precipitates (G – I) as a function of heat treatment temperature (x-axis) and cooling rate (1°C/s, 10°C/s, or 30°C/s). The error bars represent the standard deviation of the sample.

The mean size of γ'_p (A – C), γ'_s (D – F), and γ'_t (G – I) precipitates as a function of the forging temperature and the cooling rate are shown in Figure 8.8. The average size of γ'_p particles is found to be ~ 5 μm and not correlated with either the temperature or the cooling rate. Accounting for the dispersion of particle sizes, this result is consistent with the heat treatment data.

Also in accordance with the results of the 4-hour heat treatments, γ'_s particles grow in size with the forging temperature. Contrarily, the size of γ'_s does not strongly correlate with the cooling rate – the exception being that for a forging temperature of 1060°C, γ'_s precipitates are substantially larger for a cooling rate of 1°C/s than for 10°C/s or 30°C/s. The size of γ'_s for (1030°C; 1°C/s) is not quantified as not enough γ'_s precipitates were observed.

γ'_t precipitates behave in the opposite manner: their size correlates strongly with the cooling rate. Specifically, it decreases substantially as the cooling rate increases, particularly in the 1°C/s to 10°C/s range. As for the effect of the forging temperature on γ'_t, the results show that for cooling rates of 1°C/s, 10°C/s, or 30°C/s the average size of γ'_t stays approximately constant. The size of γ'_t for T_0 = 1030°C is not quantified as precipitates cannot be resolved via SEM.

For additional insight, it is interesting to utilise the data above to estimate how each population of γ' strengthens the alloy. The strengthening contributions can be calculated using the formulae presented in Section 2.1.3 for weak or strong coupling. For simplicity, since the observed γ'_s and γ'_t particles are in all cases close to or above the peak strength for Udimet 720 (~ 40 nm [122]), the strong coupling Eq. 2.3 is used. The model requires the (temperature-dependent) antiphase boundary energy (γ_{APB}) of the γ' precipitates and the shear modulus (μ). These are calculated using Eq. 8.1 and 8.2 from Galindo-Nava et al. [91] for Udimet 720's low interstitial grade, where T is the temperature (in K); a Burger's vector value b = 0.248 nm is used. Since the fraction of γ'_t could not be measured experimentally, it was estimated for each condition by subtracting from the total

fraction of γ' in the initial (as-received) state the fractions of γ'_p and γ'_s – i.e. assuming that the fraction of γ' remains approximately constant. The results of these calculations are presented in Table 8.1.

$$\gamma_{APB} = 0.3 - 0.000007\ T - 0.00000003\ T^2\ [J/m^2] \quad 8.1$$

$$\mu = 87.32 - 0.0009\ T - 0.0000019\ T^2\ [GPa] \quad 8.2$$

Table 8.1. Strength contribution of secondary γ' precipitates ($\tau_{\gamma's}$) and tertiary γ' precipitates ($\tau_{\gamma't}$) in Udimet 720 samples heated up to different forging temperatures (T_0) and cooled down to 880°C under different cooling rates (Θ).

$\tau_{\gamma's}$	T_0		
θ	1030°C	1060°C	1100°C
1°C/s	70 MPa	60 MPa	0 MPa
10°C/s	70 MPa	50 MPa	0 MPa
30°C/s	50 MPa	40 MPa	0 MPa
$\tau_{\gamma't}$	T_0		
θ	1030°C	1060°C	1100°C
1°C/s	N/A	100 MPa	100 MPa
10°C/s	N/A	200 MPa	200 MPa
30°C/s	N/A	300 MPa	300 MPa
Udimet 720; T_f = 880°C			

The results of Table 8.1 align with previous observations. For lower forging temperatures and cooling rates, γ'_s precipitates strengthen the alloy by ~ 70 MPa; however, for $T_0 = 1060$°C and $\Theta = 30$°C/s, the strengthening effect has diminished significantly to ~ 40 MPa. For a forging temperature of 1100°C, the residual fraction of γ'_s precipitates results in a negligible strengthening. The strengthening effect of γ'_t precipitates is more significant, with $\tau_{\gamma't}$ ~ 100 MPa for

low cooling rates, and up to ~ 300 MPa for high cooling rates. The strengthening effect of γ'_t for $T_0 = 1030°C$ could not be estimated, as the size of the precipitates could not be resolved with SEM. Hence, these figures further support the hypothesis that the observed strengthening is due principally to the precipitation of significant amounts of fine γ'_t at high cooling rates. In the absence of data for $T_0 = 1030°C$, the effect of the forging temperature is not clear; higher resolution imaging (via TEM) could provide additional insight.

8.4 Deformation and fracture mechanisms

The results of the previous section demonstrate robustly that the microstructures of the thermo-mechanically tested specimens agree with the predictions of the hypothesis (see Figure 6.2 and Figure 6.3) and the heat treatments of Section 4.3. However, two questions remain open. Firstly, it is yet to be established if other microstructural phenomena besides changes in the γ'-PSD, such as abnormal grain growth, could contribute to surface cracking. Secondly, it has not been determined how deformation and fracture occur, and if they are affected by differences in the γ'-PSD. This section sheds light on these questions.

8.4.1 Backscattered electron imaging

Figure 8.9 shows BSE images of the outer regions (Figure 8.9A–D) and SE images of the inner regions (Figure 8.9E–G) of thermo-mechanically tested specimens corresponding to the main diagonal of the experimental matrix. In the outer regions, voids are detected for all conditions. No differences are noted in the voids between any of the three conditions: they are located at γ'_p particles and are not accompanied by particle cracking. Moreover, the (1100°C, 30°C/s) condition (Figure 8.9C,D) shows a surface crack growing by coalescence of the said voids.

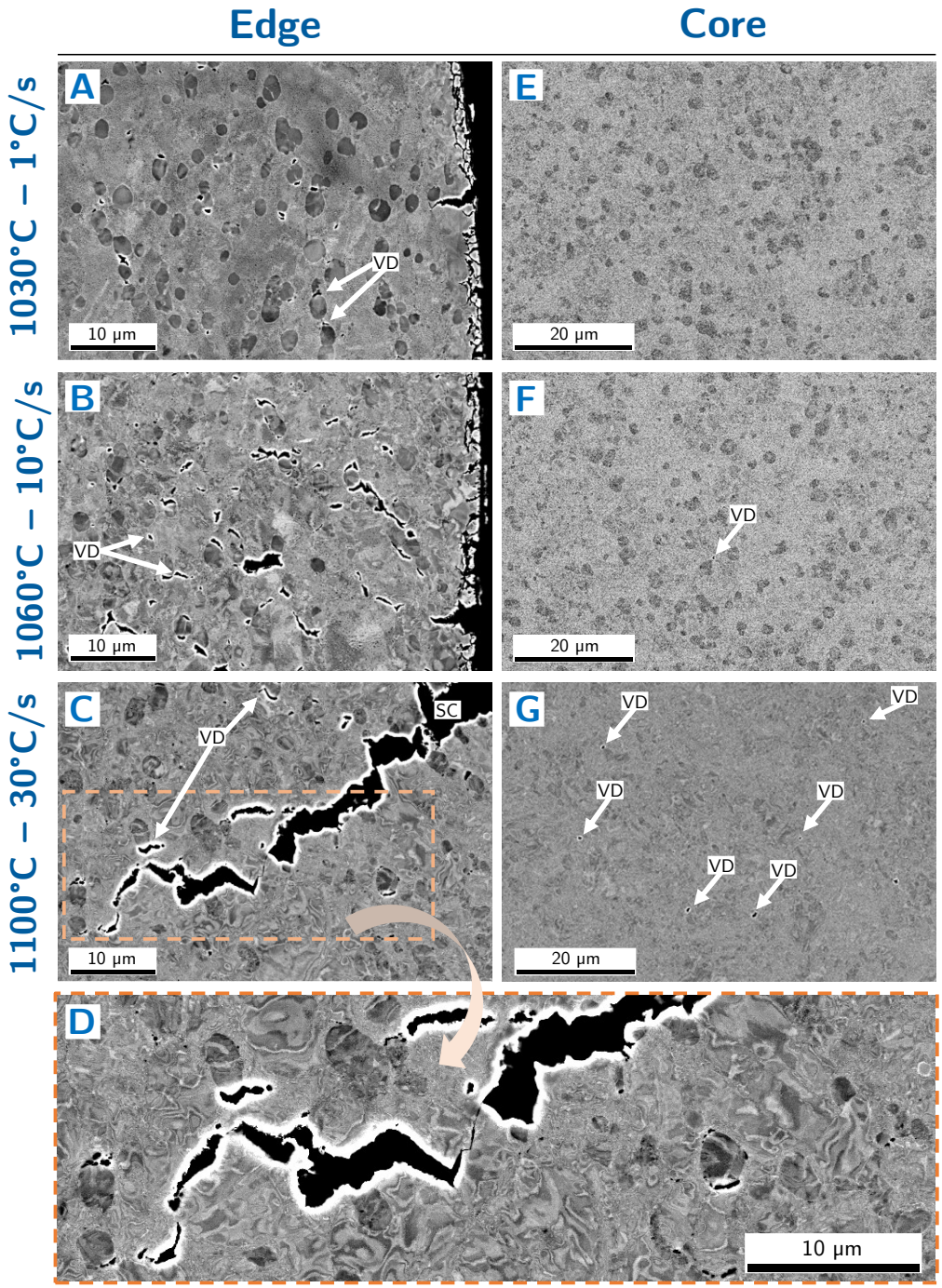

Figure 8.9. Voids at γ'_p particles (A – G) and surface crack growth via void coalescence (C – D) on BSE/SE SEM images of the outer ('edge') and inner ('core') regions of specimens thermo-mechanically tested at various forging temperatures and cooling rates. Voids are labelled 'VD'; surface cracks are labelled 'SC'.

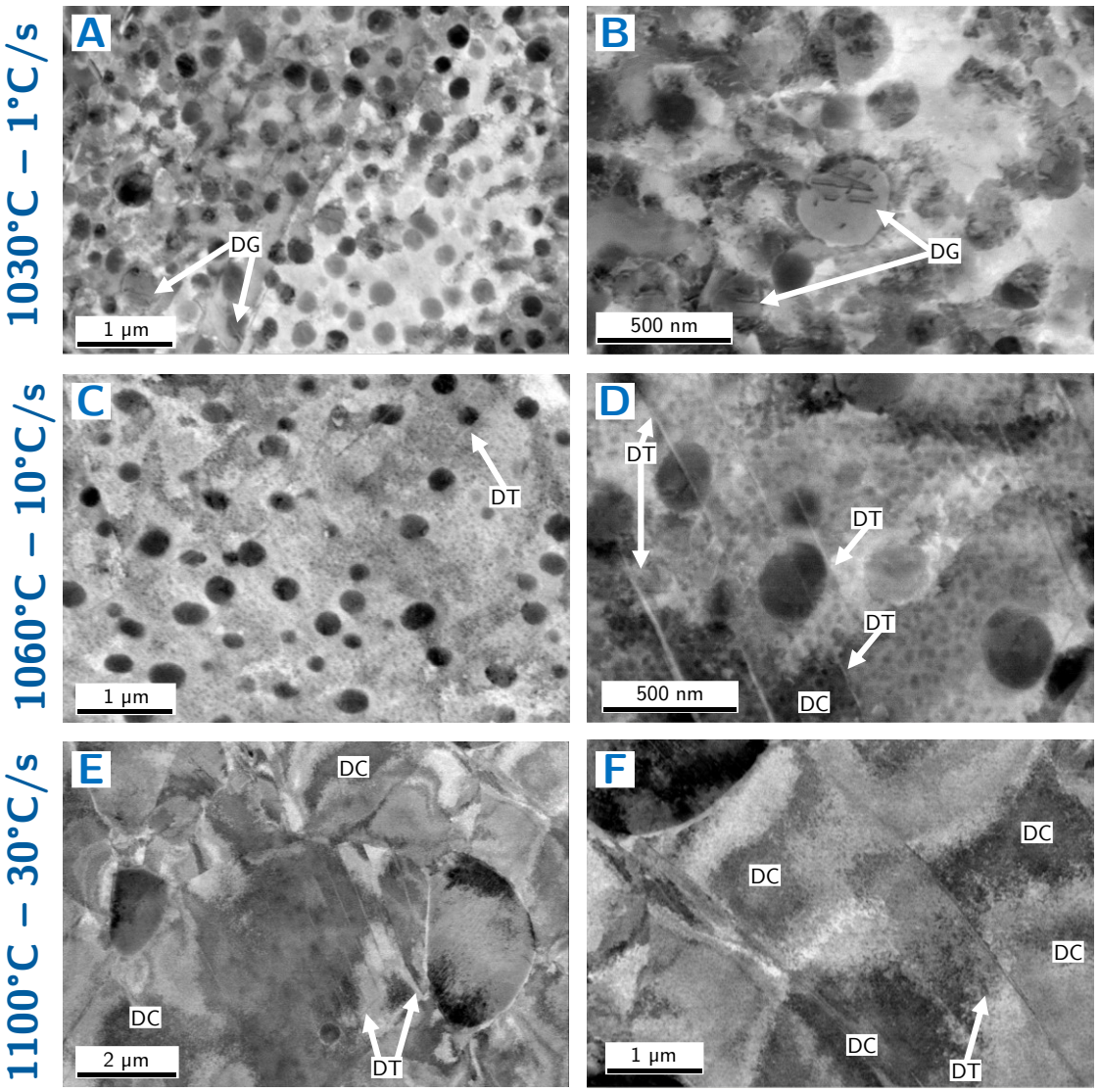

Figure 8.10. Deformation structures on BSE SEM images of the outer regions of specimens thermo-mechanically tested at various forging temperatures and cooling rates. 'DG' refers to deformation glide, 'DT' to deformation twins, and 'DC' to dislocation cells.

For the inner regions, a gradient of void density exists between the lower cooling rate and lower forging temperature condition – which shows no voids (Figure 8.9E) – and the high cooling rate, high forging temperature condition, which shows a significant number of voids (Figure 8.9G). The last result is interesting in itself: it suggests that for Udimet 720, the presence of surface cracking is associated with the occurrence of voids deep inside the forging. In that sense, surface cracks are not only a defect that ought to be removed, but an

indicator of the presence of highly undesirable internal voids. Internal voids may force that a forging be discarded altogether, so this result adds to the evidence that high cooling rates and forging temperatures are to be avoided.

Overall, the results suggest that the fracture mechanism behind surface cracking is common across all forging temperatures and cooling rates. Voids nucleate due to plastic flow concentration at non-deforming inclusions [186] and grow by decohesion at the particle-matrix interface; when sufficiently large surface cracks appear, they advance via coalescence of the said voids. Although the formation of these voids is not the focus of this study, it is hypothesised that void nucleation may happen by crack formation at the particle-matrix interface (e.g. by clustering of vacancies), followed by dislocation emission from the crack tip. According to Noell et al.'s [260] review of the microstructural aspects of void nucleation, FCC metals at high loading rates or stresses (above 1GPa) exhibit this behaviour; interestingly, the same review notes that there is increasing evidence that particle debonding is associated with dislocation boundaries and deformation twins [260]. Once nucleated, voids grow at a higher rate than the matrix; elongate and become ellipsoidal (see Figure 8.9); and ultimately coalesce causing or facilitating fracture [186]. Hence, the lesser severity of cracking at lower forging temperatures and cooling rates can then be ascribed to the lower void density and flow stress (see Figure 7.3), both of which hinder crack growth. Conversely, for the harder microstructures linked to high cooling rates and forging temperatures, dislocation glide is impeded by fine γ'_{t}; this favours the emergence of voids and increases the flow stress, paving the way for surface crack growth.

Figure 8.10 displays additional BSE micrographs of the outer regions of thermo-mechanically tested specimens corresponding to the main diagonal of the experimental matrix. They show that – contrary to fracture – the dominant deformation mechanism changes with the forging temperatures and the cooling rate. For the (1030°C, 1°C/s) condition (Figure 8.10A,B), particle shearing by strongly coupled dislocation pairs is observed in several γ'_{s} precipitates, and the

material appears to show a lower dislocation density than for the other two conditions. This suggests that for this forging temperature and cooling rate, dislocation glide and particle shear are the main deformation mechanisms.

The (1060°C, 10°C/s) condition (Figure 8.10C,D) shows no direct evidence of dislocation glide or γ' shearing. However, dislocation cells are observed, indicating that dislocation density is higher and dislocation mobility is lower than in the previous case. Moreover, several line structures of thickness ~ 10 nm are observed in Figure 8.10D; these are believed to be microtwins, pointing at the activation of twinning as an alternative deformation mode less inhibited by dislocation density. The trend is maintained for the (1100°C, 30°C/s) condition (Figure 8.10E,F), which shows more extensive dislocation cells and higher dislocation density. Line structures alike to the presumed twins of Figure 8.10D are seen in Figure 8.10F, but with significantly larger thicknesses of ~ 1 μm.

Based on the observations described above, it is hypothesised that dislocation glide and particle shear are the dominant deformation mechanisms at lower forging temperatures and cooling rates. Yet for higher cooling rates and forging temperatures, dislocation motion is increasingly impeded by fine γ'_{t}, and at sufficiently high strains another deformation mechanism is triggered: twinning. Twinning requires dislocation activity as a precursor, so it is believed that this deformation regime entails dislocation and twinning operating concurrently. These observations are in agreement with the reports of Fahrmann and Suzuki [134] for Udimet 720 and Kienl et al. [94] for ATI 718Plus®. Based on this, the question arises of whether the activation of twinning as a significant deformation mechanism precipitates failure. Indeed, deformation twins are known to impede dislocation motion and increase strength [261,262], and profuse twinning has been linked to reduced ductility due to twinning impingement – which causes local stress concentrations and triggers cracking [263]. Although this merits further investigations, it is not believed that twinning directly triggers failure, since cracking is systematically observed to start at γ'_{p} particles rather than in highly

twinned areas for every cooling rate and forging temperature considered. It cannot be discarded, however, that the emergence of deformation twins causes notable strengthening and indirectly contributes to the ultimate failure of the material.

8.4.2 Energy-dispersive X-ray spectroscopy

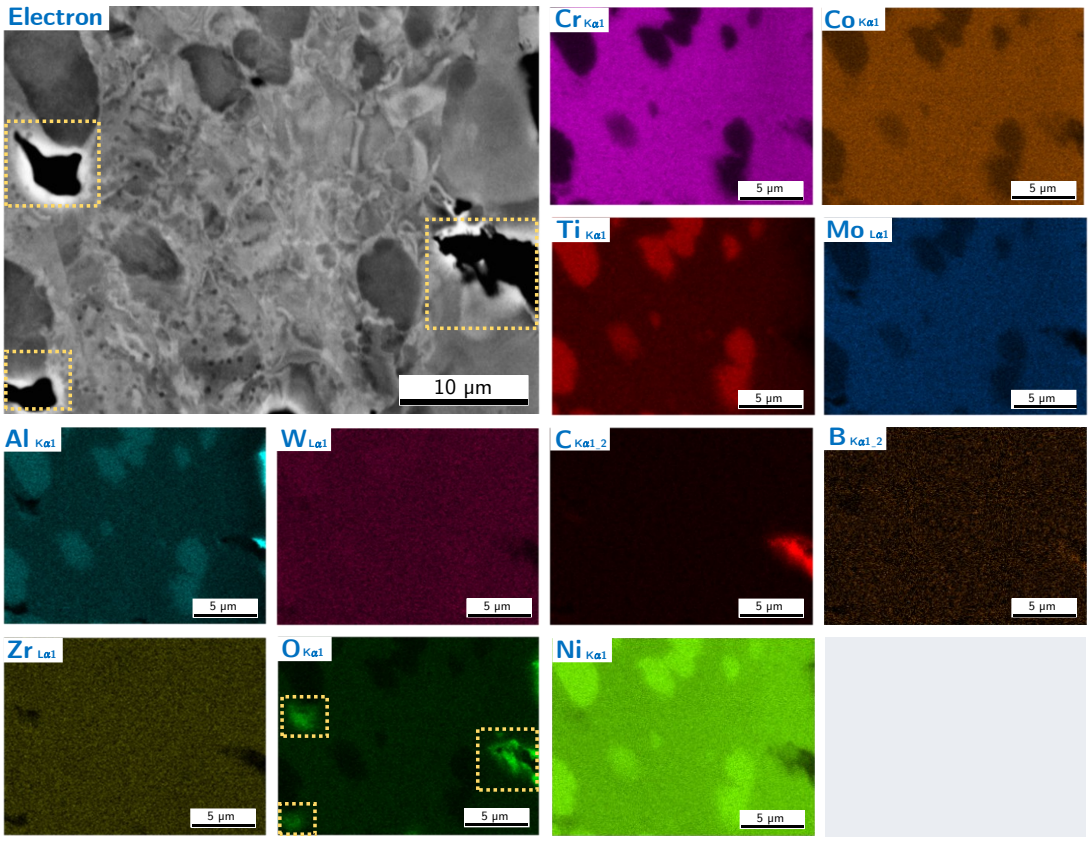

Figure 8.11. EDX maps of the outer region of a Udimet 720 sample thermo-mechanically tested at a forging temperature of 1060°C and a cooling rate of 10°C/s. The dashed yellow squares enclose the oxygen rich voids and cracks.

Figure 8.11 shows an electron (SE) image and energy-dispersive X-ray spectroscopy (EDX) maps corresponding to the outer region of a sample thermo-mechanically tested at a forging temperature of 1060°C and a cooling rate of 10°C/s. The EDX analysis has a twofold purpose. Firstly, it seeks to confirm that the regions that have so far been presumed to be voids are indeed so – and not an unknown phase. Secondly, it serves to investigate the occurrence of

compositional effects – or lack thereof – in the surroundings of surface cracks or voids, which could be causing or assisting cracking.

The SE image shows several γ'_p particles as well as a number of γ'_s precipitates. It also displays one surface crack (right side of the image) and two voids (left side of the image), which are marked with yellow dashed frames. A distinctive compositional contrast is noted between the γ matrix and the γ'_p particles; γ'_p are rich in Ti, Al, and Ni; and depleted in Cr, Co, and Mo. The γ'_s precipitates are not resolved in the EDX maps. The presumed voids and the surface crack are rich in O and depleted of Mo, Al, and Zr. This indicates that oxygen permeation has occurred and supports that the dark contrast areas are voids. Similarly, the surface crack is rich in C; this is an artifact of the metallographic preparation method, and it is due to the surface crack being filled by the phenolic mounting resin. Considered together with the edge effect seen around the black regions, it is proved that they are indeed voids. No other compositional effects are detected.

8.4.3 Electron backscatter diffraction analysis

Figure 8.12 displays electron backscatter diffraction (EBSD) maps of the outer regions of specimens thermo-mechanically tested corresponding to each condition of the experimental matrix. In the sample-plane-normal inverse pole figures (IPF-Z) maps of Figure 8.12A–I, grains appear equiaxed and do not show signs of strong crystallographic texture. Similarly, no evident grain growth is observed for any condition. Voids at the intergranular γ'_p particles are detected for several conditions: (1030°C, 1°C/s), (1030°C, 10°C/s), (1030°C, 30°C/s), (1060°C, 1°C/s), and (1060°C, 10°C/s), as shown in Figure 8.12A–E,G,H. Furthermore, surface cracks are observed for the (1060°C, 10°C/s), (1060°C, 30°C/s), (1100°C, 1°C/s), (1100°C, 10°C/s), and (1100°C, 30°C/s) conditions. The surface cracks grow into the specimens intergranularly, as seen most clearly

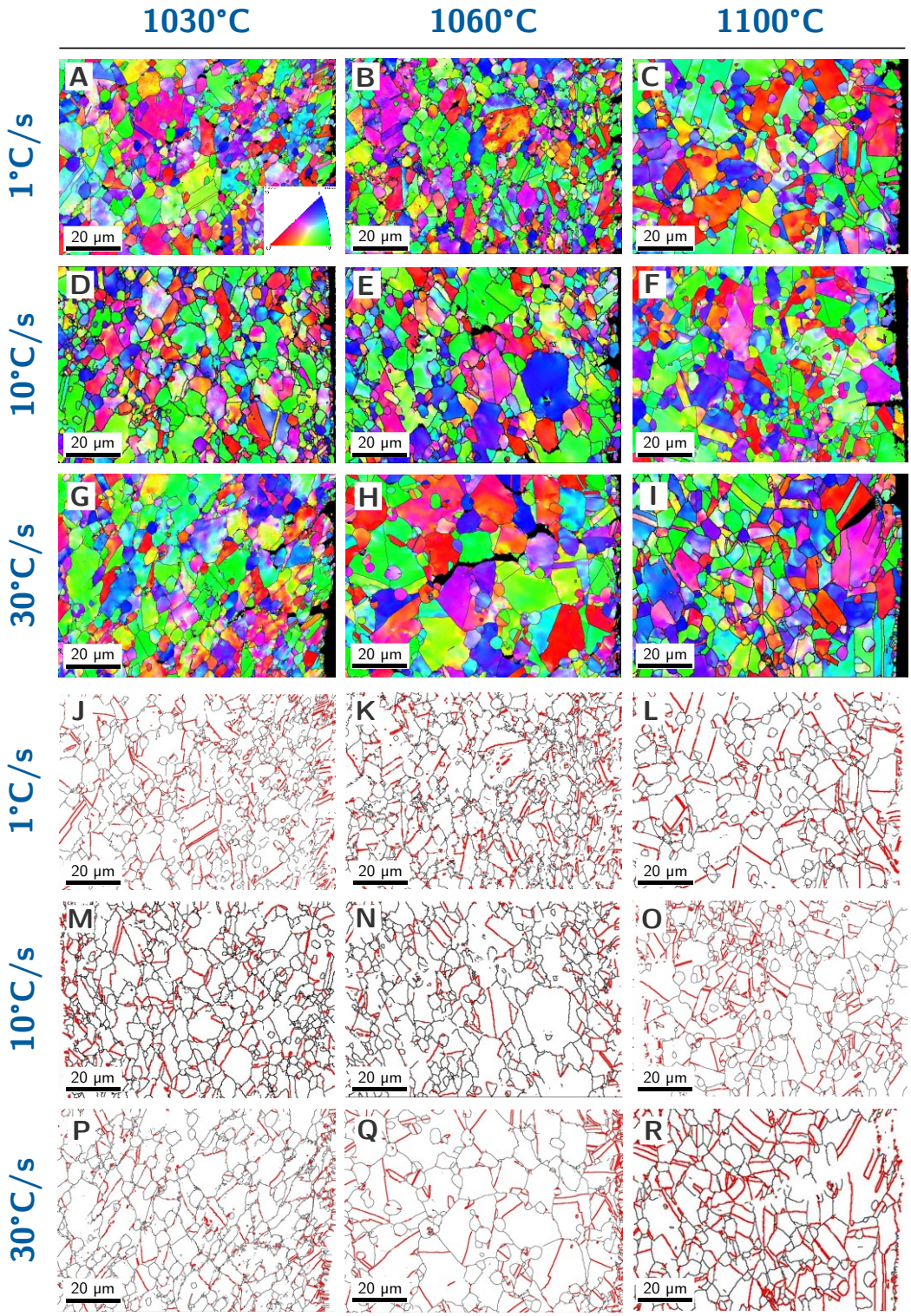

Figure 8.12. (A – I) EBSD inverse pole figure (IPF) maps of the outer regions of specimens thermo-mechanically tested at various forging temperatures and cooling rates. The colours indicate which crystal direction of the stereographic triangle is normal to the sampling plane. (J – R) High angle grain boundaries ($\alpha > 15°$; black) and twin boundaries (red) for the same regions.

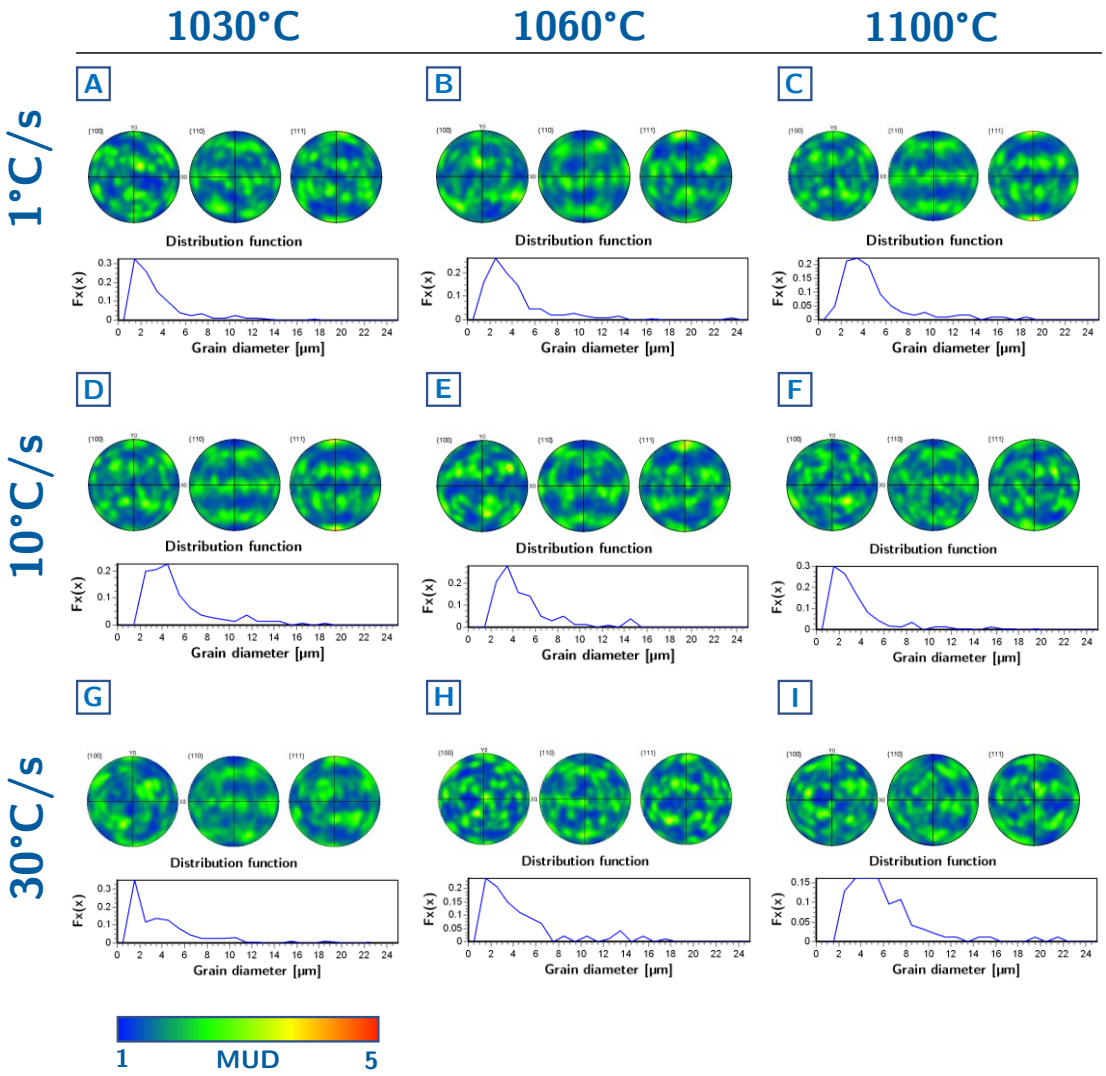

Figure 8.13. For the maps shown in Figure 8.12: {100}, {110}, and {111} pole figures in the sample plane and grain size distribution functions.

for the (1100°C, 10°C/s) condition (Figure 8.12H), in agreement with the fractographic and BSE examinations.

For the same specimens and regions, maps displaying the high angle grain boundaries ($\alpha > 15°$) and twin boundaries are shown in Figure 8.12J–R. Twins are observed for all conditions, but no noticeable difference is noted in either their morphology or density as the forging temperature or cooling rate changes. Moreover, the twin boundaries are flat rather than lenticular, suggesting that these are annealing twins and not deformation twins. These data could be

considered to conflict with the evidence presented in Section 8.4.1 that twinning is a significant deformation mechanism at high forging temperatures and cooling rates. Yet it must be noted that the EBSD maps are collected at a lower magnification than the BSE images of Figure 8.10. Therefore, it can only be concluded that no mechanical twins occur at this scale, but additional EBSD examinations are required to further validate the hypothesis proposed in Section 8.4.1 concerning the deformation mechanisms.

Figure 8.13 displays the grain size distribution functions and the {100}, {110}, and {111} pole figures in the sample plane for the maps of Figure 8.12. In agreement with the findings for the IPF-Z maps, no crystallographic texture is observed on the pole figures. Likewise, no correlation is found between grain size, forging temperature, and cooling rate. Indeed, the average grain size is fairly consistent and varies between ~ 3.5 µm and ~ 6.5 µm, with standard deviations from $\sim \pm 3$ µm to $\sim \pm 5$ µm. These figures lie within the range of grain sizes measured in the as-received material (see Section 4.2), demonstrating that no grain growth occurs during either heat treatment or thermo-mechanical testing. Consequently, abnormal grain growth – or indeed grain growth – is discarded as a cause behind surface cracking at high forging temperatures and cooling rates. Moreover, these data further support the finding in Chapter 4 that γ'_{p} particles are effective in pinning the γ grains for temperatures of up to 1100°C.

8.5 Conclusions

The fractographic and EM analyses presented and discussed in this chapter provide additional evidence that surface cracking is controlled by the dissolution of γ'_{s} and its reprecipitation as fine γ'_{t}; the observations also exclude alternative mechanisms that could be causing or assisting surface cracking; and they offer new insight into the deformation and fracture mechanisms that dominate at different forging temperatures and cooling rates. The main conclusions can be summarised as follows:

- The fractographic analysis shows that for the thermo-mechanical processing of Udimet 720, surface cracking is primarily intergranular, and a transition from ductile to brittle fracture occurs as the cooling rate and forging temperature increase.

- The results of the EM examinations are in good agreement with both the heat treatment data and the assumptions made in Section 6.1 which underpin the hypothesis, namely:

- γ'_{p} does not change with either the forging temperature or the cooling rate.

- EBSD analyses show that grain growth does not occur for any of the conditions considered. This proves that γ'_{p} particles are effective in pinning the grains in the hot die forging window (1000°C to 1100°C). Moreover, no crystallographic texture is observed via EBSD for any forging temperature of cooling rate.

- Since no grain growth or abnormal grain growth occur, these can be rejected as causes behind surface cracking at high forging temperatures and high cooling rates.

- The previously noted behaviour whereby larger amounts of γ'_{s} dissolve at higher forging temperatures is observed for the thermo-mechanically tested samples. Furthermore, evidence is presented that this causes the reprecipitation of larger amounts of γ'_{t} upon cooling, which correlates with more extensive surface cracking.

- Likewise, evidence is presented that higher cooling rates at the same forging temperature lead to finer γ'_{t} precipitates and more extensive surface cracking – in line with the hypothesis and classical precipitation theories. Estimations of the strengthening contributions of the different populations of γ' confirm that the main strengthening effect is due to the fine γ'_{t} precipitates occurring at high cooling rates and forging temperatures.

- No substantial microstructural differences exist between the core and the outer regions of the thermo-mechanically tested specimens. This is consistent with the thermal data from FEM analysis. Experiments are designed so that each test explores the material's response to different stresses and strains for one microstructural state (controlled by T_0 and Θ). Hence, microstructural homogeneity across the core and outer regions is desirable, and these results support the accuracy of the tests

- Surface cracks are accompanied by internal voids. In particular, void density correlates positively with the severity of surface cracking. For samples which show substantial surface cracking, even the innermost regions of the samples show significant void density.

- No compositional effects are observed through EDX at the voids or surface cracks.

- BSE examinations suggest that the surface fracture mechanism is common for all forging temperatures and cooling rates: voids nucleate and grow by decohesion at the particle-matrix interface, and surface cracks grow by coalescence of the voids.

- SEM data suggest that dislocation motion is the dominant deformation mechanism at lower forging temperatures and cooling rates, whereas for higher cooling rates and forging temperatures it is accompanied by twinning.

Overall, this and previous chapters present substantive evidence to support the main hypothesis of this research project and refute alternative surface cracking mechanisms. Hence, it can be considered that for Udimet 720, the hypothesis is proved. Similarly, the consistency of the analyses presented leads to the conclusion that the bespoke thermo-mechanical testing method devised to assess hot die forgeability is a success, in that it effectively replicates full-scale forging conditions. And yet, a scientific hypothesis can arguably never be considered fully

proved; the metric for its explanatory power are the instances where it predicts the outcome of an experiment. In this vein, the chapter that follows aims to provide additional validation and expand the scope of the hypothesis. This is done by conducting a full-scale forging experiment for Udimet 720 and performing selected analyses on another high γ' content cast-and-wrought alloys: René 65.

9

Further validation

The last chapter of this thesis provides additional validation to the findings of previous chapters. The objective is twofold. Firstly, validating and comparing the novel methodology against conventional testing methods. To this end, a full scale forging trial on Udimet 720 is performed, analysed, and compared with the relevant laboratory-scale results. The second objective is extending this investigation to a second material belonging to the same class of alloys: René 65. Thus, selected experiments are conducted on René 65 to establish whether parallels can be drawn with the behaviour of Udimet 720.

The chapter starts by looking at the full-scale forging trial, including macroscopic examinations of the resulting workpiece and SEM examinations of several regions of interest. The second part of the chapter contains the analyses for René 65. Using a condensed version of the experimental suite, DSC is first used to track phase transformations and γ' dissolution and to establish a potential hot die forging window for René 65. Then, heat treatments are used to study in detail its microstructural evolution in this forging window. Finally, thermo-mechanical tests are used to explore the forgeability of the material and the occurrence of surface cracking in its forging window.

9.1 Full-scale forging trials

A full-scale turbine disc forging trial was conducted by Otto Fuchs KG in Meinerzhagen, Germany. The trial involves heating up Udimet 720 material for 4 hours at 1100°C in a furnace prior to being pre-forged, re-heated, and forged into a final shape. Due to material and time constraints, only one full-scale forging trial was performed and analysed in this research project. A forging temperature of 1100°C is employed, since the hypothesis and previous results indicate that this forging temperature triggers the precipitation of large fractions of fine γ'_t and thus more extensive surface cracking. It is clear that validating the emergence of surface cracks and the presence of fine γ'_t at 1100°C provides more solid proof for the hypothesis than the lack thereof at 1030°C or 1060°C.

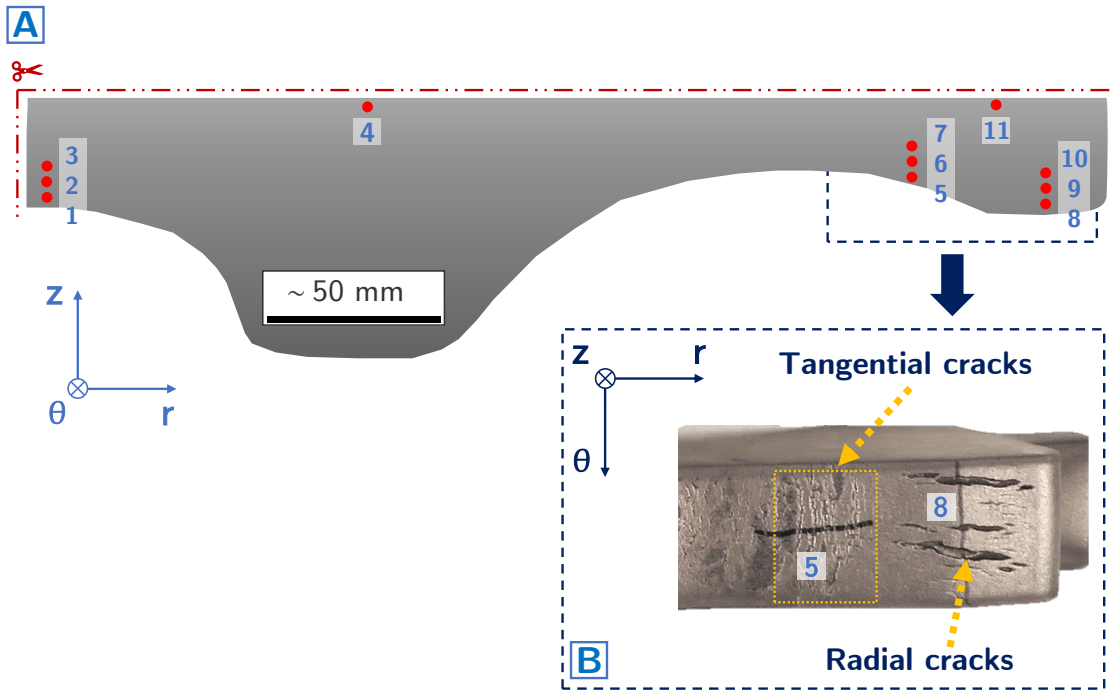

Figure 9.1. (A) Schematic of the full-scale Udimet 720 workpiece following hot die forging. The points (1 – 11) indicate the location of the tracer points on the FEM model of Chapter 5. (B) Section of the full-scale Udimet 720 forged workpiece showing surface cracks above tracer point 5 (tangential cracks) and tracer point 8 (radial cracks).

A schematic of the final shape of the workpiece following hot die forging is shown in Figure 9.1. Naturally, this is equivalent to the physical model of Chapter 5, where FEM analysis is used to simulate this forging process. The tracer points used in those analyses are shown in Figure 9.1. As expected, surface cracks are observed with the unaided eye at various surface points of the forging. A representative section displaying surface cracks is shown in Figure 9.1B, which extends from the surroundings of tracer point 5 to those of tracer point 8. In this section, two types of surface cracks are observed. Low depth (< 1 mm) cracks extending in the tangential (θ) direction are observed above tracer point 5, whereas deep (> 1 mm) cracks in the radial direction (r) exist above tracer point 8. To determine whether the difference in cracking between these regions is due to mechanical (stress, strain) or metallurgical (microstructural) factors, samples from both areas are examined via SEM. Figure 9.2 shows BSE micrographs with increasing magnification corresponding to the tangential cracks above tracer point 5; NB tracer point 5 lies 1 mm below the surface. The microstructures are highly similar to those observed in the laboratory-scale samples forged at 1100°C. Surface cracks advancing intergranularly by coalescence of voids are noted in Figure 9.2A. Moreover, voids at the interface between the matrix and the γ'_{p} particles are observed up to $\sim$ 100 µm inside the material, far ahead of the crack tips (Figure 9.2A–C). Intergranular γ'_{p} particles are seen that show no sign of coarsening or dissolution with respect to the initial (as received) state, suggesting effective pinning of the γ grains and no grain growth.

As expected for a forging temperature of 1100°C, a very small number of intragranular γ'_{s} precipitates are observed in Figure 9.2C,D. In line with the hypothesis, abundant γ'_{t} precipitates are observed in Figure 9.2C–F. But interestingly, these precipitates are to some extent different to those observed in the laboratory-scale thermo-mechanical testing specimens. The laboratory-scale specimens contain unimodal γ'_{t} precipitates that are finer as the cooling rate

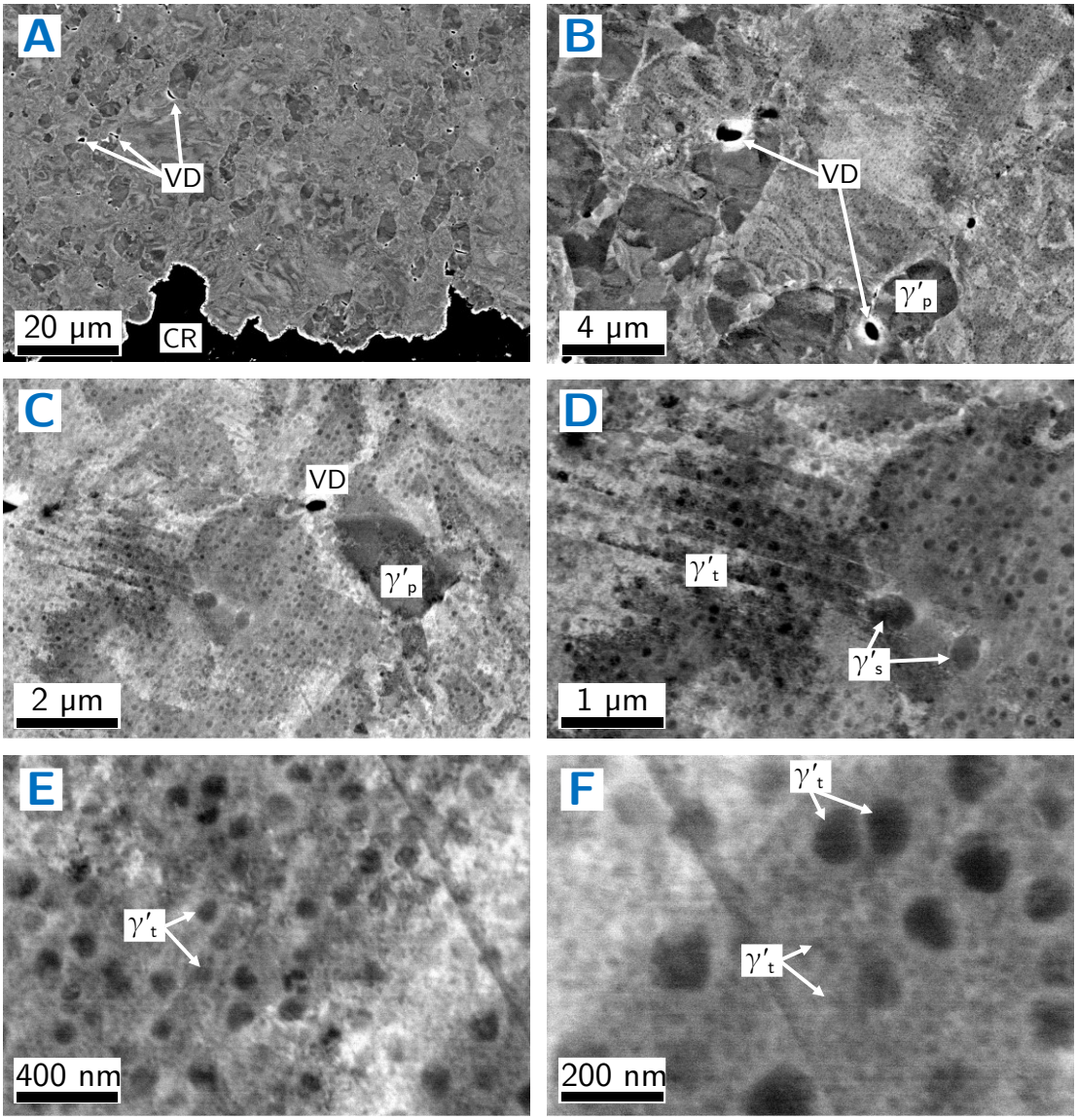

Figure 9.2. BSE SEM micrographs with increasing magnification corresponding to the tangential cracks (above tracer point 5 in Figure 9.1) on the full-scale Udimet 720 forged workpiece. Primary, secondary, and tertiary γ' precipitates are labelled γ'_{p}, γ'_{s}, and γ'_{t}; cracks are labelled 'CR' and voids 'VD'.

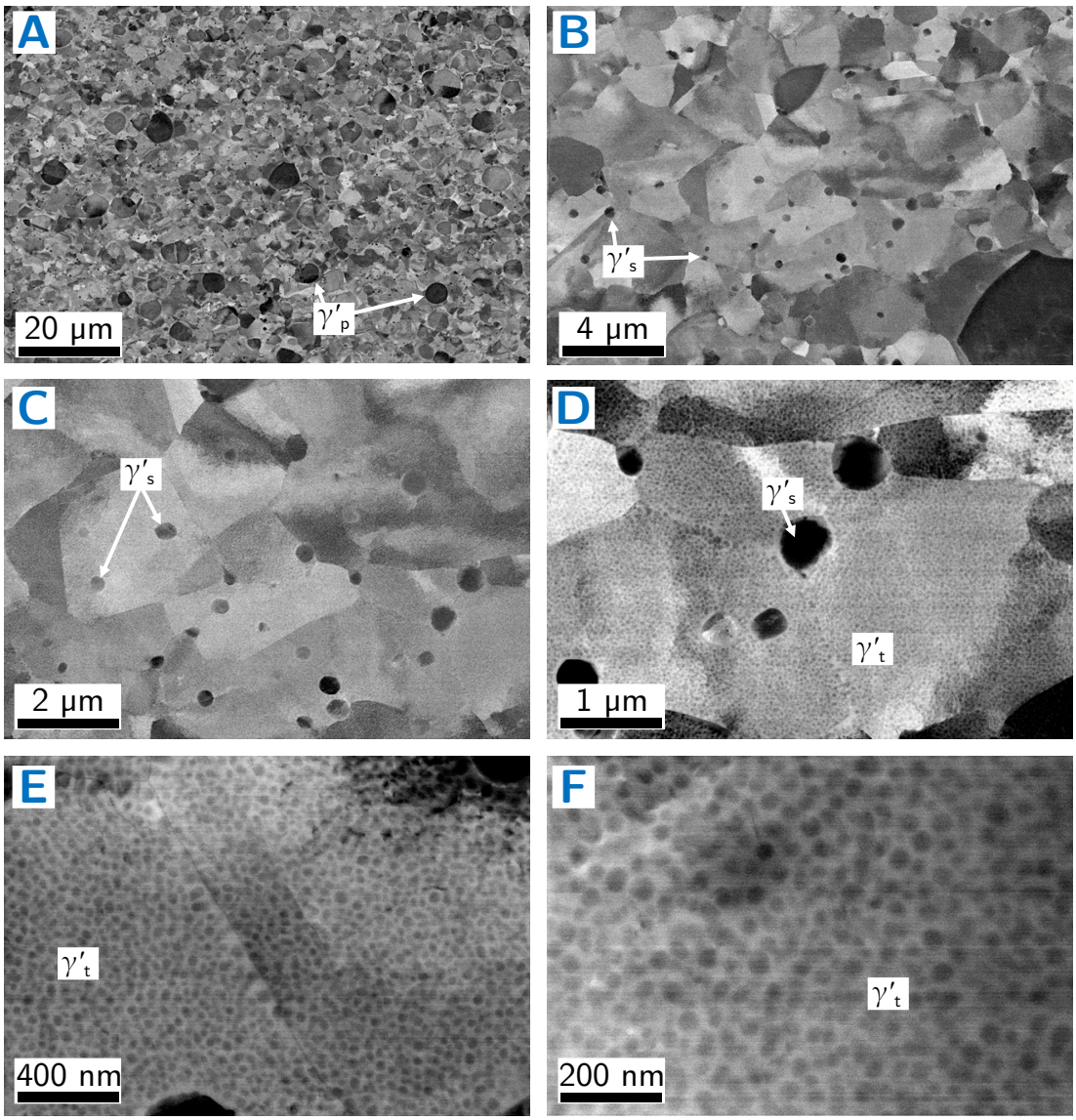

Figure 9.3. For the full-scale Udimet 720 forged workpiece: BSE SEM micrographs with increasing magnification corresponding to tracer point 5 in Figure 9.1. Tracer point 5 lies ~ 1 mm below the surface where tangential cracks are found. Primary, secondary, and tertiary γ' precipitates are labelled γ'_p, γ'_s, and γ'_t.

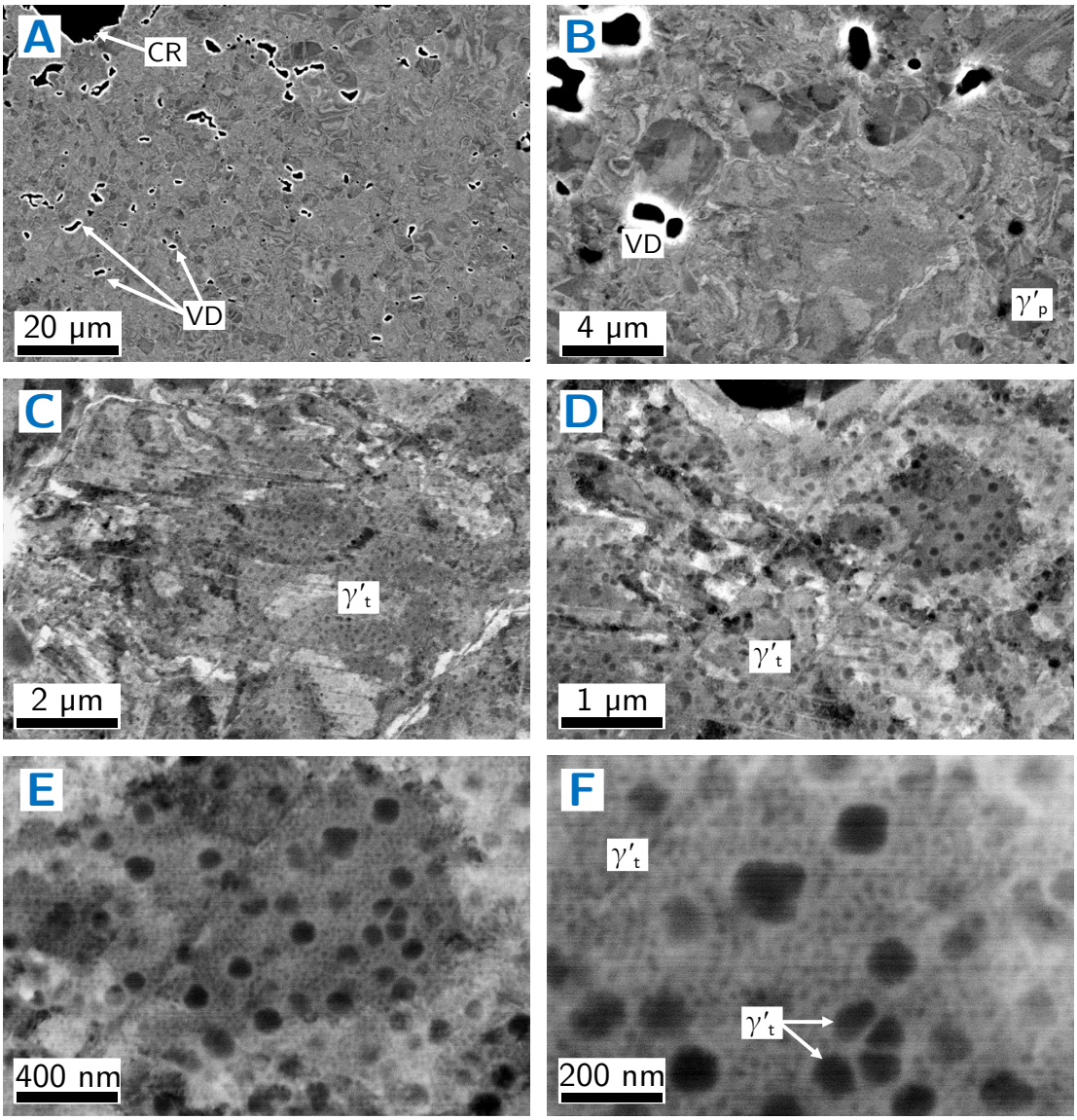

Figure 9.4. BSE SEM micrographs with increasing magnification corresponding to the radial cracks (above tracer point 8 in Figure 9.1) on the full-scale Udimet 720 forged workpiece. Primary and tertiary γ' precipitates are labelled γ'_p and γ'_t; cracks are labelled 'CR' and voids 'VD'.

decreases. Conversely, γ'_t precipitates in Figure 9.2 are bimodal, with a population of larger (~ 100 nm) precipitates (Figure 9.2C–F) and another population of very fine (~ 10 nm) precipitates only resolved in Figure 9.2F. This is believed to be caused by slow cooling to temperatures close to γ'_s solvus prior to the start of the forging operation at the outermost surface region. Indeed, the coarser γ'_t precipitates suggest a slow cooling rate and are similarly sized to the γ'_t observed in the laboratory-scale samples forged at 1100°C and a cooling rate of 1°C/s (see Figure 8.3C,L). In Figure 9.3, the sub surface region (tracer point 5) contains a unimodal distribution of fine γ'_t similar to those seen in the laboratory tests for cooling rates higher than 10°C/s. Although further investigations are required to confirm the mechanism behind the formation of the bimodal γ'_t precipitates in Figure 9.2, it is noteworthy that these observations are aligned with the hypothesis. In particular, the microstructure shows what the hypothesis predicts: the near total dissolution of γ'_s, the reprecipitation of large amounts of fine γ'_t, and the concomitant presence of surface cracks. Furthermore, dislocation cells and deformation twins are observed in Figure 9.2C–F. This agrees with the results of Chapter 8 and suggests that γ'_t hinders dislocation motion, increasing dislocation density and activating deformation by twinning.

Figure 9.3 shows BSE micrographs of tracer point 5, i.e. 1 mm below the tangential cracks examined in Figure 9.2. No cracks or voids are observed in this region. Intergranular γ'_p particles are present in the usual condition. Coarse γ'_s precipitates are seen scattered inside the γ grains (Figure 9.3B–D); there is, however, a very limited number of them, indicating that almost total dissolution of γ'_s occurs. At high magnification, a population of high density fine γ'_t is observed. Correlating this with the results of thermomechanical testing (Figure 8.3 and Figure 8.4), it appears that locally the material undergoes cooling at rates higher than 10°C/s. This is in accordance with the FEM simulations, which predict a cooling rate of ~ 10°C at tracer point 5 for a forging temperature of 1100°C. The line structure of Figure 9.3E is believed to be a deformation twin; despite this, the region has a lower dislocation density compared to the surface.

Overall, this microstructure is highly consistent with those observed in the laboratory-scale specimens. Since those experiments are designed to simulate this forging operation, it is clear that Figure 9.3 constitutes solid validation for the accuracy of the method and, by extension, for the hypothesis.

BSE images of the section of the surface containing radial cracks (above point 8) are presented in Figure 9.4. The microstructure is broadly equivalent to the region containing tangential cracks. Figure 9.4A,B shows γ'_{p} in the usual condition, surface cracks growing by coalescence of voids at the interface of γ'_{p}, and a high density of voids extending at least ~ 100 μm inside the workpiece. No γ'_{s} precipitates are detected, indicating that locally all γ'_{s} has dissolved. A bimodal distribution of γ'_{t} is observed in Figure 9.4C–F; this is accompanied by a large number of twins, high dislocation density, and dislocation cells.

Once established that the sections of the surface displaying low depth tangential cracks or deep radial cracks have equivalent microstructures, it is clear that the local mechanical states (stress and strain) drive cracking severity. The differences in cracking can be rationalised using a strain based approach, commonly employed on workability diagrams [184]. The FEM simulations presented in Figure 5.7 predict that at tracer point 5, the radial strain at the end of deformation is $\varepsilon_r \sim 0.53$, the tangential strain is $\varepsilon_\theta \sim 0.18$, and the axial strain $\varepsilon_z \sim -0.74$. In turn, the strain components at the tracer point 8 are $\varepsilon_r \sim 0.05$, $\varepsilon_\theta \sim 0.19$, and $\varepsilon_z \sim -0.25$. Surface cracks grow under tensile stress and are hampered by compression. Hence, it is believed that tangential cracks appear above tracer point 5 due to the significant radial strain but are absent at tracer point 8, where radial strain is lower. Conversely, radial cracks are driven by tangential strains. Tangential strains are equivalent at both tracer points, but at tracer point 5 their growth is hampered by the high compressive axial strain – and as a consequence they only emerge above tracer point 8. Although this matter is not explored in further depth in this section, determining the stress and strain conditions that lead to fracture (fracture loci) for each forging temperature and

cooling rate is a natural future step of this project; this will be discussed in Chapter 10. Overall, the results presented in this section are in good agreement with previous findings and provide further support to the hypothesis.

9.2 Second alloy system: René 65

The analyses that follow pertain to René 65. This is a cast-and-wrought alloy for turbine disc applications derived from the P/M alloy René 88DT. It has a $f_{\gamma'} \sim 40\%$ and is forgeable via hot die forging and ring-rolling [54,216]. The composition of René 65 is provided in Section 3.1.

9.2.1 Thermal analysis

The DSC thermogram of René 65 from initial (as-forged) state is shown in Figure 9.5. The figure also shows the thermogram of Udimet 720 from as-forged state for comparison purposes. For René 65, an endothermic occurs between ~ 600°C and ~ 900°C that is believed to correspond to the onset of γ' dissolution, specifically the dissolution of γ'_t. This event overlaps with another endothermic peak that starts at ~ 880°C and lasts until ~ 1080°C, and which is associated to the dissolution of γ'_s. The maximum deviation from the baseline for this peak occurs at ~ 1065°C, which is therefore the temperature where γ'_s dissolution is maximum. A final endothermic peak occurs between ~ 1080°C and ~ 1200°C due to the dissolution of intergranular γ'_p. No other phase transformations are identified.

The DSC thermograms of René 65 and Udimet 720 are highly similar. Yet importantly, the event corresponding to the dissolution of γ'_s for René 65 is shifted down by ~ 30°C with respect to Udimet 720. Since it has been demonstrated that for Udimet 720 surface cracking is controlled by γ'_s, a potential forging window can be established for René 65 by shifting down accordingly the forging window

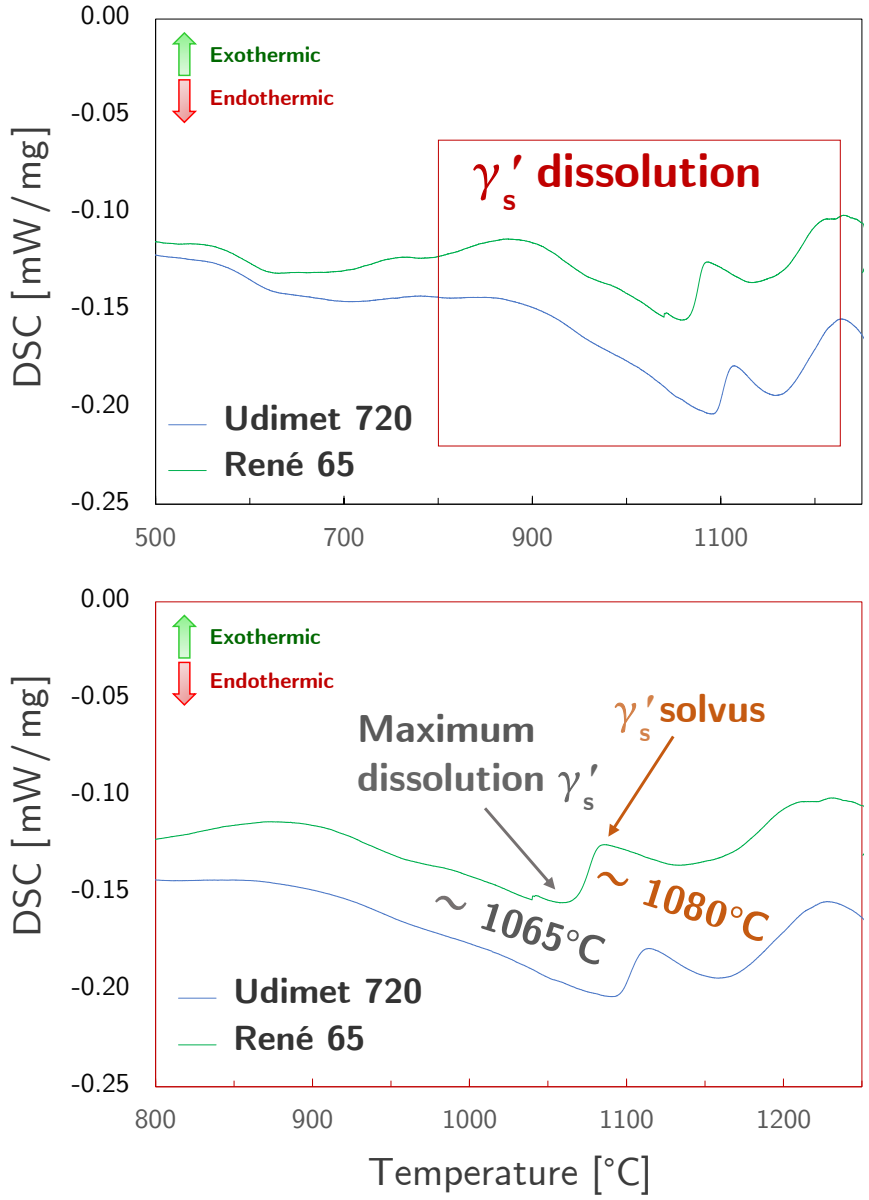

Figure 9.5. DSC thermogram of René 65 and Udimet 720 material in the as-received state. The bottom figure is a close-up version of the γ'_s dissolution window shown at the top. The indicated temperature of maximum dissolution of γ'_s and the γ'_s solvus correspond to René 65.

of Udimet 720 (1030°C – 1100°C) by 30°C. Hence, the forging temperatures considered for René 65 in subsequent sections are 1000°C, 1030°C, and 1070°C. As it will be seen below, this assumption yields successful results, demonstrating that DSC together with the Udimet 720 benchmark can be used to establish the working window of this class of alloys in a straightforward manner.

9.2.2 Heat treatments

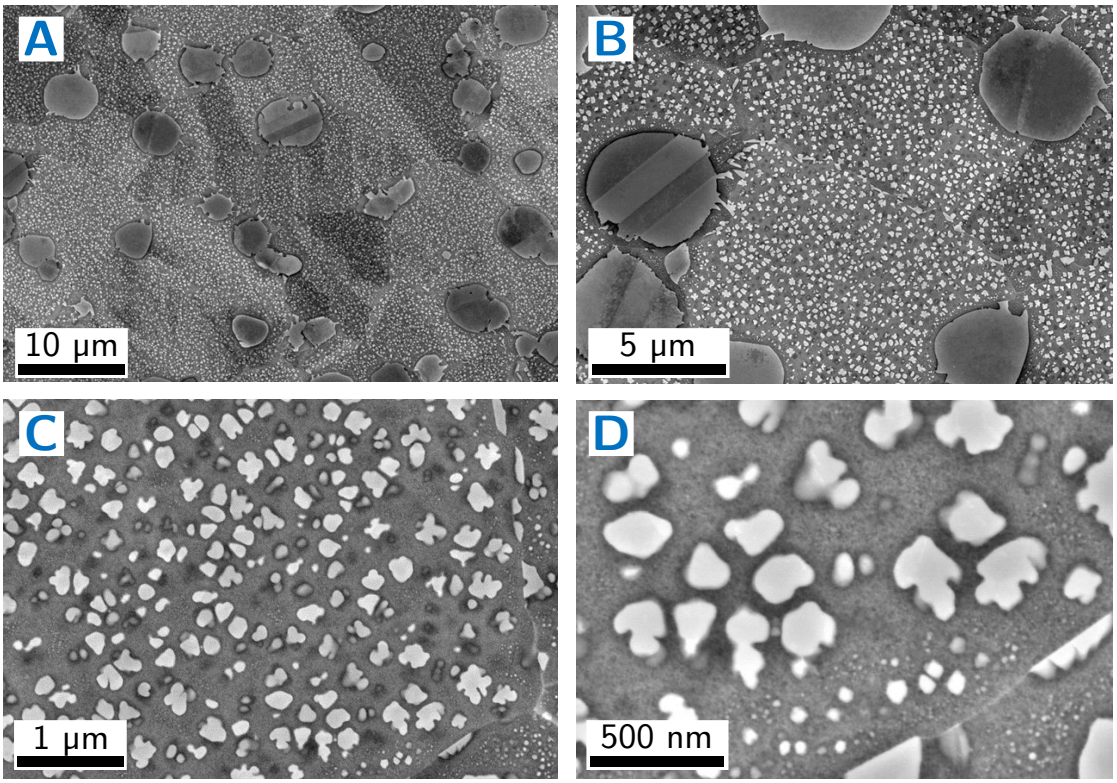

Figure 9.6. SE SEM images with increasing magnification of René 65 material in the initial (as-forged) state. The sample is γ-etched electrolytically using a 10% phosphoric acid solution.

Figure 9.6 displays SEM images of γ-etched René 65 in as-forged state, prior to heat treatment. The material highly resembles Udimet 720 in as-received condition (Figure 4.2). Firstly, intergranular γ'_{p} particles are observed in Figure 9.6A,B with similar sizes (~ 5 µm) and area fractions. Moreover, the γ grains are filled with moderately aged γ'_{s} precipitates which are butterfly shaped and, in some cases, split. Although their size is also similar (~ 100 nm) to those of Udimet 720, their area fraction is noticeably lower. This is consistent with the literature, where $f_{\gamma'}$ is reported to be $\sim 4\%$ lower for René 65, and the Thermo-Calc results in Figure 4.8. Furthermore, a limited number of γ'_{t} precipitates are seen in Figure 9.6C,D, particularly in the proximity of grain boundaries.

René 65 material was heat treated for 20 minutes or 4 hours at temperatures of 1000°C, 1030°C, or 1070°C followed by water quenching. SEM micrographs of the resulting samples are shown in Figure 9.7. At low magnification (Figure 9.7A– F), γ'_p particles are visible for all conditions. These look equivalent to the as-received condition, confirming that below ~ 1080°C no γ'_p dissolution occurs. No grain growth is noticeable for any configuration, suggesting that γ'_p is effective at pinning the γ grains up to 1070°C.

In the medium magnification images (Figure 9.7G–L), intergranular γ'_s precipitates are visible for all conditions except the sample heat treated at 1070°C for 4 hours. As expected, the fraction of γ'_s decreases with temperature. The fact that the sample heat treated at 1070°C for 4 hours does not contain γ'_s precipitates is broadly consistent with the γ'_s solvus obtained via DSC (~ 1080°C). Incomplete coarsening of the γ'_s precipitates is observed in the samples heat treated for 20 minutes, indicating that this time does not suffice to achieve equilibrium. This is most clearly seen in the samples heat treated at 1030°C, where the 4 hours condition (Figure 9.7K) contains fewer and significantly coarser γ'_s than the 20 minutes condition (Figure 9.7H). Furthermore, as noted above, for a temperature of 1070°C γ'_s are only observed in the sample heat treated for 20 minutes.

At the highest magnification (Figure 9.7M–R), it is seen that the γ'_s precipitates have changed in shape: from butterfly shaped before heat treatment to spherical after it. No γ'_t are observed for any condition. It is noteworthy that for Udimet 720, the sample heat treated at the highest temperature (1100°C) for 4 hours does show γ'_t precipitation upon water quenching. The lack of visible γ'_t precipitation for René 65 is likely due to its lower $f_{\gamma'}$. It is expected that precipitation of very fine γ'_t occurs but cannot be resolved through SE SEM on γ-etched specimens. This could be confirmed with BSE SEM or TEM. Despite this difference, it is clear that the microstructures of René 65 and

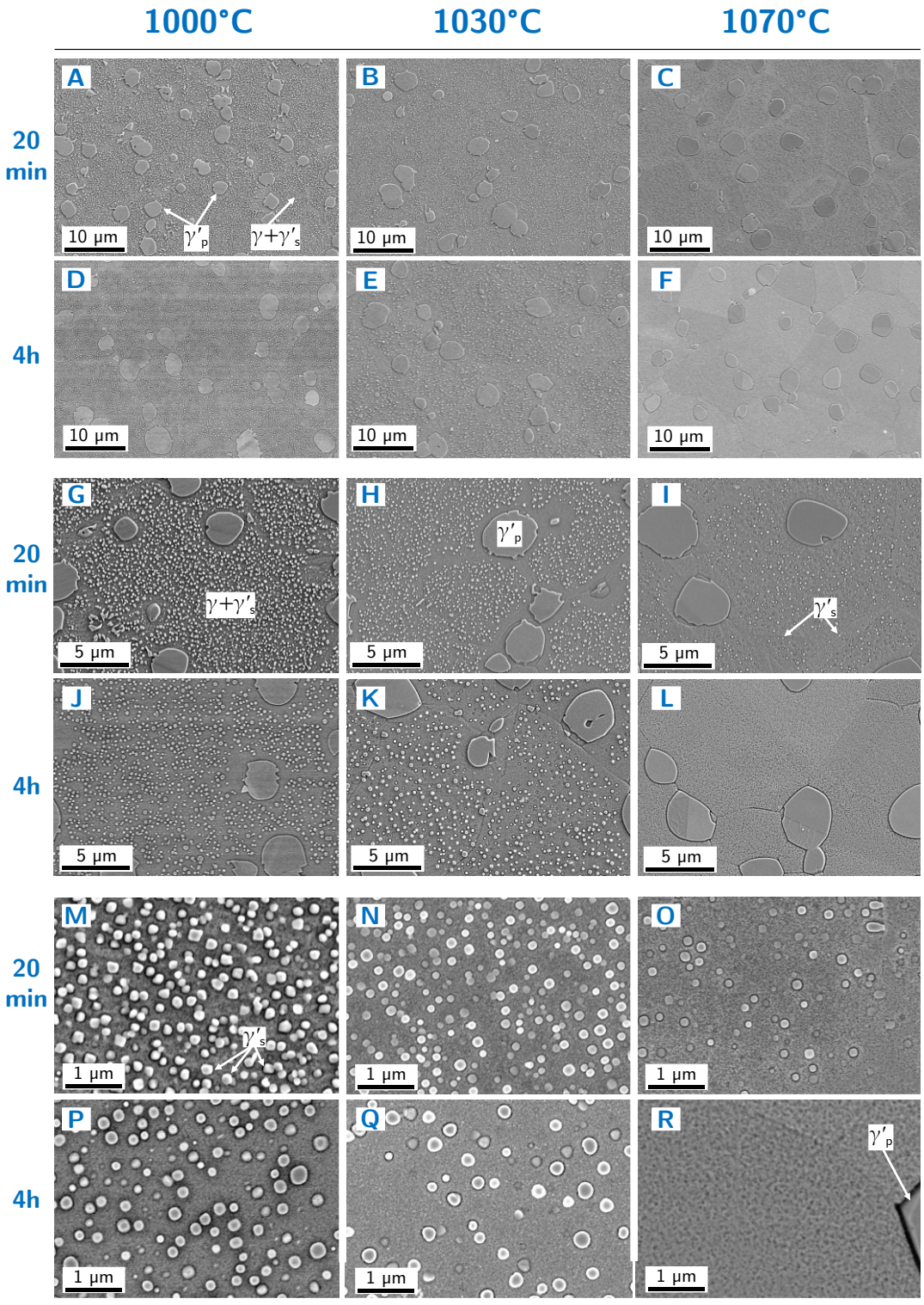

Figure 9.7. SE SEM images of heat treated René 65 specimens at low magnification (A – F), medium magnification (G – L), and high magnification (M – R). Primary and secondary precipitates γ are labelled γ'_{p} and γ'_{s}.

Udimet 720 evolve similarly with temperature and heat treatment time in their hot die forging windows. In short, René 65 behaves largely like Udimet 720 but shifting down the relevant temperatures by – 30°C. This finding is employed in the mechanical tests that follow.

9.2.3 Mechanical testing

Once a potential forging window for René 65 is determined through DSC and heat treatments, the next step of the experimental suite consists of conducting thermo-mechanical Gleeble compression tests to appraise the occurrence of surface cracking under different forging conditions. Strictly speaking, heat treatments would be followed by FEM simulations to predict the range of relevant thermal and mechanical variables during hot die forging. However, this lengthy step can be bypassed on account of the similarities between Udimet 720 and René 65 by making the following assumptions:

- This research project focuses on the hot die forging of Udimet 720 and René 65 into turbine discs. Despite certain differences in the constitutive behaviour of the two alloys (see Figure 9.8), the FEM analyses of Chapter 5 are assumed to be a reasonable approximation to the deformation path of René 65 forging stock material into a turbine disc. Hence, thermo-mechanical testing is conducted using the same nominal strain ($\varepsilon = 0.8$) and strain rates ($\dot{\varepsilon} = 0.1$) employed for Udimet 720.

- René 65 and Udimet 720 have similar chemistries; thus, their thermal properties are assumed to be sufficiently similar so that the thermal evolution analyses of Chapter 5 remain valid. Because of this, thermo-mechanical tests are conducted using the same cooling rates of 1°C/s, 10°C/s, and 30°C/s.

- The forging window for René 65 is shifted by – 30°C with respect to Udimet 720. Therefore, the forging temperatures (T_0) employed are

1000°C, 1030°C, and 1070°C; likewise, the final temperature (T_f) is 850°C. The interested reader is referred to Figure 6.4. to review what these variables denote in the thermo-mechanical testing cycle.

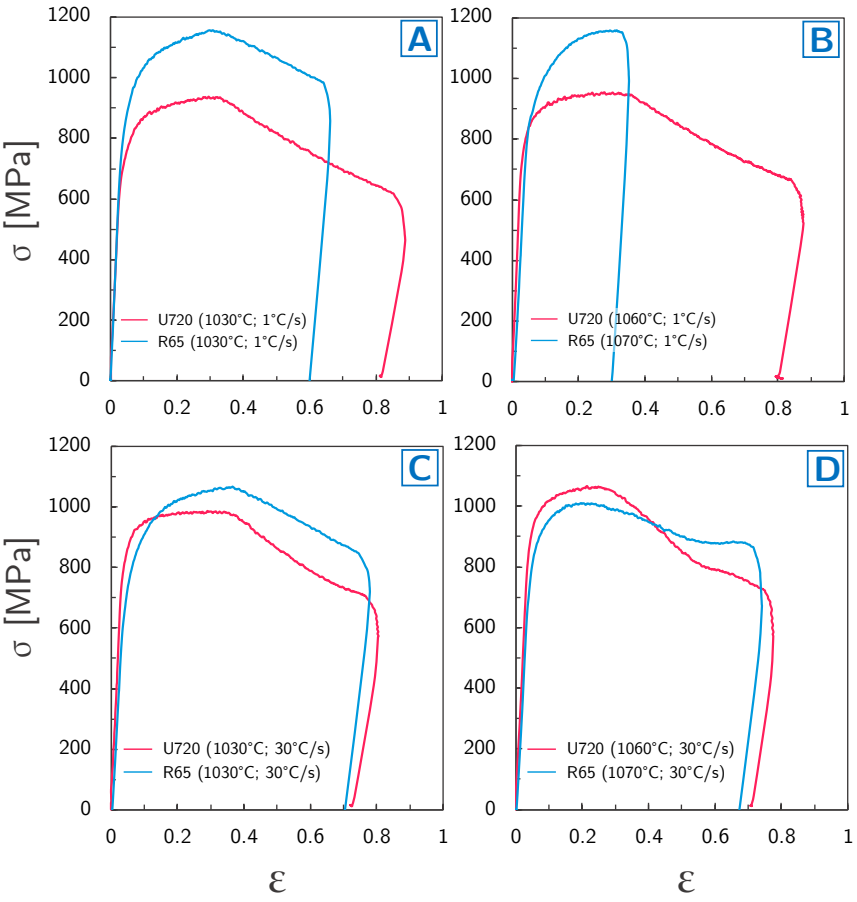

Figure 9.8. Stress versus strain curves for selected René 65 (blue) and Udimet 720 (red) cylindrical specimens deformed at different forging temperatures and cooling rates: A: (1030°C; 1°C/s); B: Udimet 720 (1060°C; 1°C/s), René 65 (1070°C; 10°C/s); C: (1030°C; 30°C/s); D: Udimet 720 (1060°C; 30°C/s), René 65 (1070°C, 30°C/s).

The stress versus strain curves for selected René 65 and Udimet 720 specimens are shown in Figure 9.8. As noted above, significant differences are observed for the specimens deformed following cooling at slow rates of $\Theta = 1$°C/s (Figure 9.8A,B). These disparities warrant further investigation, yet the fact that the curves start to diverge at yield suggests that deformation inhomogeneities may be at play once plastic deformation starts. The curves corresponding to high

cooling rates (Figure 9.8C,D) are in close agreement, with René 65 showing a higher flow stress for a forging temperature $T_0 = 1030°C$ and Udimet 720 having a higher flow stress at $T_0 = 1060°C$ versus $T_0 = 1070°C$. Although this may seem surprising on account of Udimet 720's higher γ' fraction, it is consistent with the hypothesis of this thesis. In particular, since the γ'_s solvus of René 65 is $\sim 30°C$ lower than for Udimet 720, more dissolution of γ'_s precipitates will have occurred, and the observed strengthening is due to its reprecipitation as γ'_t.

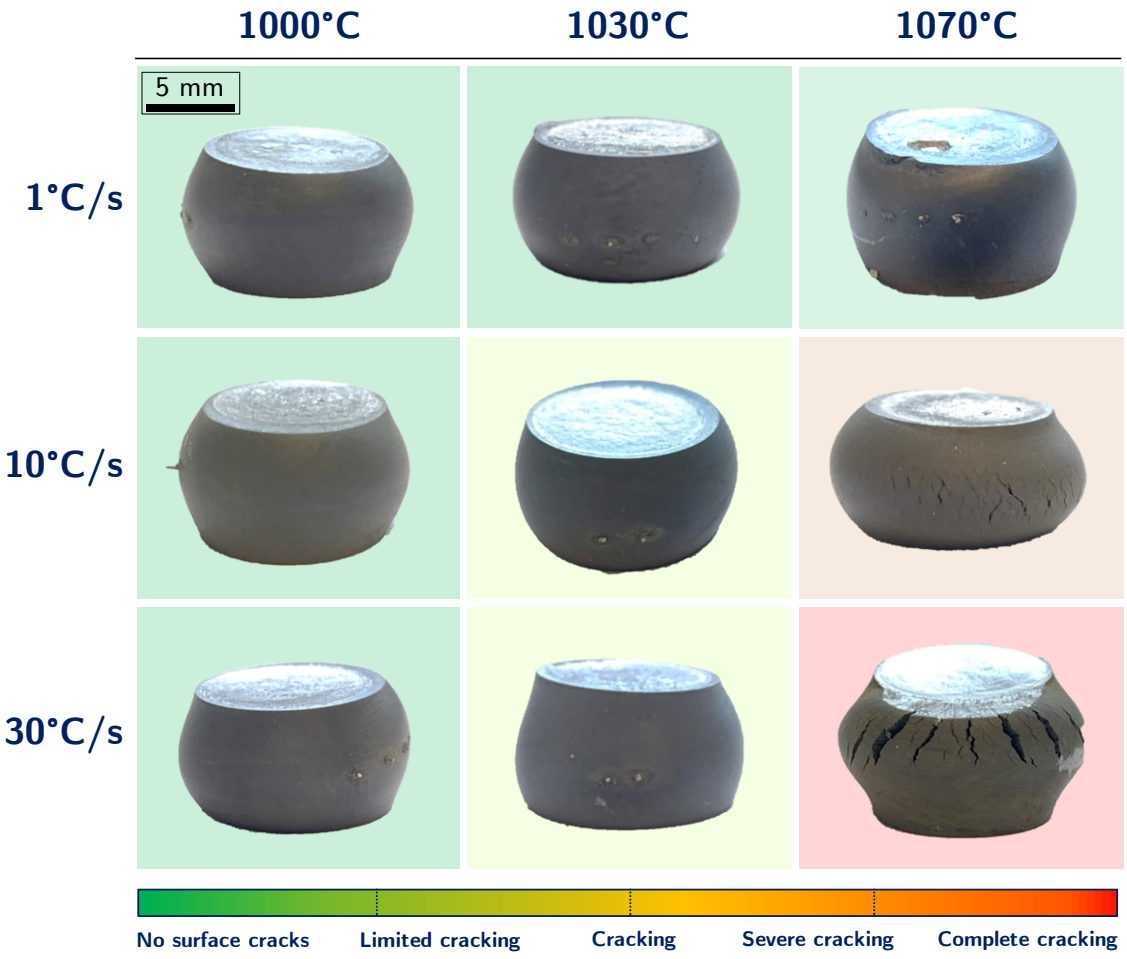

Figure 9.9. Representative René 65 cylindrical samples tested at different forging temperatures (T_0) and cooling rates (Θ). The forging temperature for each sample is indicated at the top of its column; the cooling rate is indicated at the left of its row. The background colour denotes the degree of cracking as per the gradient legend below. The (1030°C, 10°C/s) and the (1030°C, 30°C/s) samples show small cracks that are not resolved on the macroscopic photographs.

Figure 9.9 shows representative cylindrical samples tested using the parameters detailed above. Similarly, Figure 9.10 shows three representative double cone specimens tested at different cooling rates for a forging temperature of 1070°C. It ought to be noted that – due to time and material constraints – these results are partial and affected by two main limitations. Firstly, results for all forging temperatures and cooling rates are available for the cylindrical specimens (Figure 9.9) but not the double cones. Secondly, final axial strains of 0.4 – 0.5 are achieved despite the nominal target being 0.8. This hinders one-to-one comparisons with Udimet 720, but the partial results provide valuable insight into the thermo-mechanical behaviour and the occurrence of surface cracking for René 65.

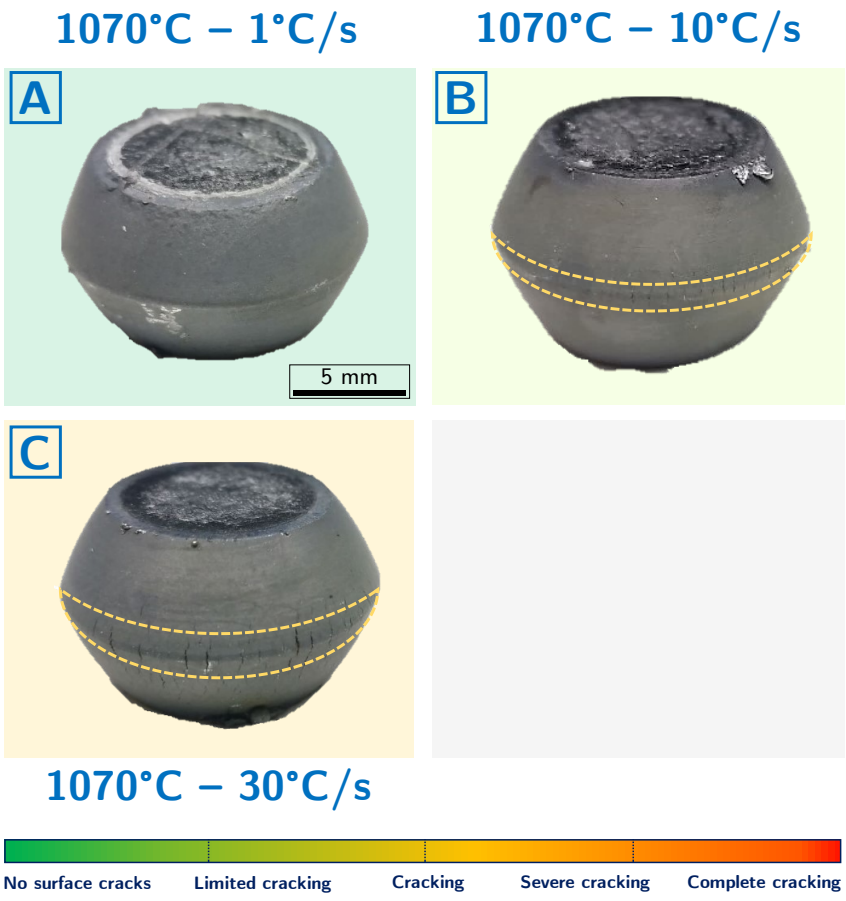

Figure 9.10. Selected René 65 double-cone samples tested at different cooling rates (Θ) for a forging temperature (T_0) of 1070°C. The background colour denotes the degree of cracking as per the gradient legend below.

In Figure 9.9, a clear pattern is noted whereby surface cracking increases along the main diagonal. In other words, cracking increases with both the cooling rate and the forging temperature. In particular, no cracking is observed for any of the 1000°C samples. For a forging temperature of 1030°C, the sample cooled at 1°C/s shows no cracking, whereas the samples cooled at 10°C/s and 30°C/s show limited cracking. Conversely, for a forging temperature of 1070°C, cracking shifts from very limited at 1°C/s to significant at 10°C/s and complete cracking at 30°C/s. The same behaviour is noted for the double cone specimens tested at 1070°C (Figure 9.10): the low cooling rate conditions show no cracking, and surface cracking increases with the cooling rate. It appears that surface cracking for René 65 could be as sensitive to the forging temperature as to the cooling rate. For example, both a cooling rate of 1°C/s and a forging temperature of 1000°C result in no cracking irrespective of the other variable. This is unlike Udimet 720, where at the highest cooling rate, substantial cracking occurs for all forging temperatures, indicating greater sensitivity to the cooling rate. This, however, requires further exploration given that the results for René 65 correspond to lower final axial strains.

The hot die forging window for René 65 is concluded to extend from 1000°C to 1030°C, both of which are suitable forging temperatures. Overall, the thermo-mechanical testing results are highly aligned with those of Udimet 720 and the hypothesis. With the caveats discussed above, the data suggest that forging René 65 at or close below its γ'_s solvus temperature ($\sim$ 1080°C) results in extensive surface cracking, and that cracking is aggravated by high cooling rates. On the other hand, reducing the cooling rate or lowering the forging temperature into the 1000°C to 1030°C range – where substantial fractions of γ'_s remain undissolved – results in limited to no surface cracking.

9.3 Conclusions

The results presented and discussed in this chapter provide additional validation and expand on the findings of previous chapters. The main conclusions can be summarised as follows:

- The full-scale hot die forging of a Udimet 720 turbine disc at a forging temperature of 1100°C was successfully completed. As predicted by the hypothesis, for this temperature significant surface cracking is observed in several sections of the workpiece.

- The SEM analyses of these sections show that surface cracking is associated with the complete or near complete dissolution of γ'_s precipitates and their reprecipitation as very fine γ'_t precipitates. This is a key result, as it not only further validates the hypothesis. It also proves that the laboratory-scale thermo-mechanical tests are an accurate model of full-scale hot die forging.

- A disparity is identified whereby the microstructures of regions directly on the surface contain coarser γ'_t precipitates than in regions 1 mm below the surface. Further research is required to elucidate this phenomenon; importantly, this result does not contradict the hypothesis.

- A condensed version of the experimental suite developed for Udimet 720 is employed for René 65. DSC and heat treatments show that the microstructure of René 65 evolves with temperature very similarly to Udimet 720, but the dissolution of γ'_s precipitates is shifted down by – 30°C.

- Thermo-mechanical compression tests are adapted accordingly by shifting the forging temperatures and final temperature by – 30°C. The results suggest that the γ'_s mechanism that controls surface cracking for Udimet

720 also operates in René 65 and, presumably, other highly γ'-reinforced cast-and-wrought nickel-based superalloys.

- This discovery and the successful application of the experimental suite to a second alloy paves the way for improved processing of these alloys. In particular, it is shown that DSC, targeted heat treatments, and selected thermo-mechanical tests can be used to determine the hot die forging window of an alloy in a straightforward manner.

This chapter concludes the presentation, analysis, and discussion of the results obtained in this research project. The chapter that follows summarises the main conclusions of this work and discusses their scientific and industrial significance. It also outlines several proposals for further work.

10

Conclusions and future work

This work substantially advances the current understanding of the forging of highly γ'-reinforced cast-and-wrought superalloys. Although forgeability is investigated holistically, the focus has been on the emergence of surface cracking – a phenomenon that has received virtually no attention despite its high relevance. Through a series of key findings, this work challenges established notions in industrial practice and provides evidence-based scientific insights to reduce environmental impacts and drive cost efficiencies. It does so by using experimental and conceptual tools to link the macroscopic thermo-mechanical behaviour of these alloys with the microstructural phenomena that govern cracking. To this end, a novel forging simulation methodology and a conceptual framework have been devised. The work is, thus, both scientifically and industrially relevant.

The last chapter of this thesis starts with a summary of the main findings of the project. Then, several lines of further work are suggested to advance the knowledge on this subject leveraging these findings.

10.1 Conclusions

10.1.1 Development of a forging simulation method to study surface cracking

A novel experimental method was devised to investigate at laboratory-scale surface cracking and chilling effects in hot die forging of high γ' content cast-and-wrought alloys. The method uses a Gleeble 3800-GTC thermal-mechanical simulation system to replicate hot die forging through compression tests on double cone and cylindrical specimens. A multi-step thermo-mechanical cycle is used to mimic the die chilling effects characteristic of hot die forging. Finite element analyses are used to estimate the evolution and distribution of the relevant variables (temperatures, strains, strain rates) in full-scale forgings and feed into the forging simulation. The method serves to investigate hot die forgeability in a broad sense – microstructure, flow stress, and defects – but it is unique in that it is designed to target specifically the occurrence of surface cracking.

The complexity of researching hot die forging – and in particular surface cracking – through laboratory-scale tests lies in attaining for small scale specimens microstructural, thermal, and evolutions representative of full-scale forgings. To this end, FEA was employed to optimise the specimen geometry and demonstrate that the temperatures, cooling rates, stresses, strains, and strain rates seen by the specimens are equivalent to the forging of a turbine disc. In particular, that the secondary tensile stresses that drive surface cracking are comparable for the laboratory specimens and full-scale forgings. Out of the three geometries considered during specimen design, cylinders and double cones were selected following finite element analyses. Cylinders are the standard sample of the Gleeble thermal-mechanical simulation system and deliver slightly better thermal control. Double cones deliver a gradient of stresses and strains across the surface and higher secondary tensile stresses which are beneficial to study surface cracking.

Crucially, heat treatments and EM investigations showed that specimens need to be heat treated prior to thermo-mechanical testing to achieve microstructural equivalence.

The methodology was shown to be effective and robust. For Udimet 720, it delivered a wide range of surface cracking states for different forging temperatures and cooling rates. Since the method is designed to study specifically the occurrence of surface cracking, the key evidence of its success is that it reproduces on small scale specimens the surface cracks that have been reported to occur on full-scale Udimet 720 workpieces for some forging parameters. Double cone specimens were shown to be particularly robust for assessing susceptibility to surface cracking, confirming the essential role of large secondary tensile stresses in cracking. Cylindrical samples also result in satisfactory outcomes, but surface cracking occurred in a less controlled fashion. Furthermore, the results showed that panoramic imaging, image analysis, and statistical analysis are an effective supplement to the method; through these, a reliable model can be built and used to find states of minimum cracking in the forging design space. A full-scale Udimet 720 workpiece was hot die forged to validate the results; the laboratory- and full-scale tests were found to be highly consistent, demonstrating the accuracy of the method.

To the knowledge of the author, this is the first study where hot die forging simulation was successfully employed to produce laboratory-scale testing specimens showing varying degrees of cracking as a function of the forging parameters. Thus, the method paves the way for a better scientific understanding of the phenomenon as well as knowledge transfer to industrial practice, where surface cracking poses a major problem

10.1.2 Establishing the processing route for Udimet 720

The novel methodology was used to study the forgeability of Udimet 720. DSC was successfully employed to study the dissolution of the multimodal γ' phase. In particular, it was shown that DSC can be used to determine the solvi of γ'_t (~ 840°C) and γ'_s (~ 1110°C) that were previously unreported for Udimet 720. Heat treatment and EM analyses revealed that at 1150°C partial γ'_p dissolution and significant grain growth occur. Thus, the potential hot die forging window was established as 1000°C – 1100°C. FEA simulations were used to estimate the evolution of key thermo-mechanical variables during the forging of a turbine disc – which were fed into the thermo-mechanical forging simulation method.

Thermo-mechanical tests showed that for a constant deformation temperature (T_f), surface cracking correlates positively with the cooling rate and the forging temperature in the 1000°C – 1100°C temperature range. Severe cracking appears for high cooling rates and forging temperatures, while limited to no surface-cracking occurs for lower cooling rates and forging temperatures. Importantly, cracking appeared to be more sensitive to the cooling rate than to the forging temperature. Quantitative data obtained via panoramic imaging and image analysis supported these results, as did the multiple linear regression model built with these data. The forging of a full-scale workpiece at 1100°C validated the finding that substantial surface cracking occurs at this forging temperature. Stress versus strain data revealed that the ductility drop was associated to hardening (higher stress flows).

Based on the regression model and the cooling rates obtained via FEA, the hot die forging window for Udimet 720 was concluded to be $\sim$ 1030°C – 1040°C. This is a relevant result that can improve the industrial processing of the alloy. Yet the most remarkable implication of the findings discussed above is that they contest the idea that the optimal forging window for high γ'-reinforced cast-and-

wrought lies below but close to the γ' solvus. Instead, they suggest that lower forging temperatures improve ductility and reduce surface cracking. These results are subject to certain limitations. Most notably, a limited number of specimens and conditions were tested, and the final strain attained was not fully consistent across specimens. Although the physical trends noted above are well substantiated, the limitations affect the accuracy of e.g. the regression model and the forging window. Several further work proposals to overcome these limitations are presented in Section 10.2 below.

10.1.3 Microstructural origins of the constitutive behaviour

A hypothesis was presented to explain this phenomenon. It postulates that decreased ductility and more extensive surface cracking follow the dissolution of increasing amounts of γ'_s at higher forging temperatures and its reprecipitation as highly reinforcing γ'_t precipitates owing to die chilling.

The hypothesis was tested through extensive experimental explorations. Four-hour heat treatments revealed the dissolution of increasing amounts of γ'_s in the 1000°C – 1100°C range, with negligible fractions of γ'_s remaining undissolved at 1100°C (i.e. 10°C below γ'_s solvus). They also showed that γ'_p is almost unaffected in this range of temperatures, thereby precluding undesirable grain growth. In addition, the thermo-mechanically tested specimens were analysed via EM. The results were in agreement with the observations noted above for γ'_s and γ'_p. Crucially, larger amounts of γ'_t were found in the severely cracked samples forged at higher temperatures. Similarly, evidence was presented that higher cooling rates at the same forging temperature lead to finer γ'_t precipitates and more extensive surface cracking. These observations all align with the hypothesis. EBSD was employed to confirm that no significant grain growth or crystallographic texture occurs in the forging window, and EDX showed no compositional effects in the surroundings of the surface cracks. These results allowed rejecting other explanations for the unexpected drop of ductility – such

as abnormal grain growth. Considering the substantial evidence supporting the hypothesis and having rejected alternative mechanisms, the hypothesis was considered proved.

Fractographic analysis showed that for all forging temperatures and cooling rates, surface cracking is primarily intergranular. Moreover, surface cracks were found to be accompanied by internal voids, with void density correlating positively with the severity of surface cracking. BSE examinations suggested a common surface fracture mechanism: void nucleation and growth by decohesion at the particle-matrix interface and surface crack growth by coalescence of the voids. In addition, EM data suggested that dislocation motion is the dominant deformation mechanism at lower forging temperatures and cooling rates, whereas for higher cooling rates and forging temperatures it is accompanied by twinning.

10.1.4 Forgeability of new generation cast-and-wrought superalloys

Considered together, the forging simulation and microstructural examinations lead to a clear conclusion: surface cracking and forgeability for Udimet 720 are controlled by the dissolution of γ'_s. To determine whether this result applies to other highly γ'-reinforced cast-and-wrought superalloys, the forgeability of a second commercial alloy – René 65 – was investigated using a condensed version of the experimental suite developed for Udimet 720.

DSC and heat treatments showed that the microstructural evolutions with temperature are highly similar for both alloys, but for René 65 the γ'_s dissolution window is ~ 30°C below that of Udimet 720; the γ'_s solvus temperature for René 65 was determined to be ~ 1080°C. Forging simulation experiments were conducted employing the same cooling rates but decreasing the forging temperatures accordingly by 30°C. The same pattern was observed whereby higher forging temperatures and cooling rates correlate positively with surface cracking severity, validating the hypothesis.

Therefore, the optimal hot die forging window for highly γ'-reinforced cast-and-wrought superalloys does not lie below but close to the γ' solvus – but to the γ'_s solvus. This is arguably the most significant result of this research project and holds dual relevance. From a technological standpoint, it provides a simple yet robust guideline for the industrial forging of these alloys. Scientifically, it expands the understanding of the relationship between composition, microstructural evolution, processing, and properties for nickel-based superalloys. This new knowledge is complemented by the investigations on how deformation and surface fracture occur at the micro-scale.

As a final remark, the investigation for René 65 showed that a condensed version of the set of experiments employed for Udimet 720 suffices to establish the forging window. This set of experiments – DSC, heat treatments, and forging simulation on a Gleeble thermo-mechanical simulator – was proved to be an effective experimental suite to explore hot die forgeability. The experimental suite could include with panoramic imaging, crack quantification, and statistical analysis as described in Section 7.3, which could not be completed for René 65 due to time constraints.

10.2 Further work

In the previous section, several limitations of this work have been discussed. And naturally, while this research project was bounded in time, research itself has no end, and new findings give rise to new research questions. This section presents several proposals for further work to expand on the results of this project and answer some of these questions. These proposals revolve around modelling the evolution of γ' PSD leveraging the data produced in this project, developing a FEA cracking criterion and linking it to that microstructural evolution model, investigating the microstructural deformation and fracture mechanisms in further depth via advanced EM techniques, improving the forging

simulation technique, and using these to investigate other forging parameters and alloy systems.

Modelling the kinetics of γ′ dissolution and reprecipitation

In this research project, it has been established that for highly γ'-reinforced cast-and-wrought superalloys, surface cracking and hot die forgeability are controlled by the γ' PSD. Substantial data were produced on the γ' PSD of Udimet 720 during typical hot die forging operations – including particle size and volume fraction for the various populations of precipitates. Data were also obtained for René 65 in the form of SEM micrographs. These data allowed understanding the microstructural evolution during heat treatment and thermo-mechanical testing, and in particular the relationship between forging temperature and cooling rate and γ' PSD.

However, the γ' PSD is only known with accuracy for the discrete temperatures and cooling rates that were tested experimentally. Thermodynamic simulations were used to obtain $f_{\gamma'}$ as a function of the temperature for both alloys, but these models are limited by the non-equilibrium (kinetic) nature of microstructural evolution during hot die forging. There is, therefore, significant value in developing analytical or numerical tools to predict the kinetics of PSD.

Kinetic modelling could be used to predict the dissolution and coarsening of γ' when the material is heated up prior to forging as well as the reprecipitation of γ' driven by die chilling. The former phenomenon could be simulated using the Lifshitz, Slyozov, and Wagner (LSW) theory or semi-analytical models calibrated by experiments [264–266]. Combined with FEA heat transfer simulations, such a model would allow optimising the furnace time of workpieces. By determining the minimum time required at T_0 before deformation to achieve the desired microstructure homogeneously across the workpiece, furnace time and hence energy waste could be minimised. Likewise, the reprecipitation of γ' could be

modelled through semi-analytical models; for example, Masoumi et al. [78] employed a modified Johnson-Mehl-Avrami (JMA) model to study the precipitation of γ' during cooling for alloy AD730™. Coupled with the previous model, it would allow obtaining the evolution of γ' PSD throughout the entire hot die forging operation, which is key to controlling surface cracking.

Development of a surface crack criterion and FEA integration

The investigations on laboratory-scale and full-scale workpieces demonstrated that surface cracking is the result of γ'-driven embrittlement combined with specific stress and strain states. In particular, it was shown that surface cracking requires substantial secondary (strain induced) tensile stresses and that cracking severity correlates positively with strain. Yet similarly to the microstructural case discussed in the previous section, forging simulation experiments only revealed the severity of surface cracking for the limited range of strains that were tested experimentally. Hence, a criterion to determine whether a local stress and strain state will result in surface cracking would be a highly valuable design tool. There are, however, significant challenges: any such criterion would be specific to a particular microstructure. Besides, it would need to account for the fact that the deformation path affects cracking; for example, compression stresses can close voids and cracks.

In addition, experimental investigations showed that a gradient of voids occurs ahead of the crack front. The surface cracking model could be developed to predict this deleterious phenomenon; for example, through a function that takes stresses and strains as arguments to produce the density of cracking as output. Ultimately, the ideal hot die forging modelling suite would couple microstructural evolution and macroscopic (FEA) thermo-mechanical and cracking predictions. This, however, would require an intermediate step: building a model capable of delivering a constitutive equation for each γ' PSD configuration.

Enhancing strain control and streamlining the forging simulation method

The main experimental limitation encountered in this research project concerned the control of axial strain during the forging simulation experiments. Due to the very high strength of these alloys, the Gleeble thermo-mechanical simulator did not provide consistent final strain outputs. Although a satisfactory range of strains was finally achieved, there is significant value in improving the strain control of the apparatus. This would allow more accurate and straightforward comparisons between samples and reduce the number of invalid samples, hence driving efficiencies. A straightforward means to accomplish it would be reducing the size of the samples. Alternatively, a different system could be employed, such as Instron's Electro-Thermal Mechanical Testing System (ETMT).

Moreover, there is scope for streamlining the forging simulation investigations. For example, in this research project, panoramic imaging was conducted using an SEM. This provided high resolution panoramic images that allowed resolving small-scale features – such as voids. However, it is worth investigating whether the cracked area of thermo-mechanically tested specimens can be measured with sufficient accuracy using an optical microscope. This could be significantly less time consuming than the SEM route employed here, and it would allow generating more data to feed the multiple linear regression model for improved accuracy.

Additional EM microstructural investigations

The deformation and fracture mechanisms driving surface crack growth were explored in this work. SEM investigations suggested that when large fractions of fine γ'_t precipitates hamper dislocation glide, deformation twinning becomes a significant deformation mechanism. Deformation twinning is generally considered a relevant mechanism at low homologous temperatures or high strain

rates. Yet investigations by Fahrmann and Suzuki [134] for Udimet 720 and Kienl et al. [94] for ATI 718Plus® question that notion. The results of this project are highly aligned with those of Fahrmann and Suzuki, adding evidence to the need to revisit this idea.

In this work, SEM and EBSD were employed to observe deformation twinning. While structures believed to be deformation twins were consistently observed through SEM, they could not be detected via EBSD – possibly due to lack of resolution. There is thus ample scope for using other techniques – such as electron channelling contrast imaging (ECCI), TEM, or t-EBSD – to explore the deformation mechanisms active for different thermo-mechanical processing parameters. This investigation has scientific relevance. For example, it could shed light on the mechanism whereby twins nucleate and grow; but it would also expand the overall understanding of deformation for these alloys, which is crucial to inform the solution to current and future applied challenges. Ultimately, a better understanding of these phenomena could serve as basis to develop a physics-based model to predict cracking.

Investigating additional test parameters and alloy systems

This investigation has focused on the die chilling effect characteristic of hot die forging and its impact on surface cracking. Accordingly, thermo-mechanical experiments were conducted using different cooling rates and forging temperatures, and other relevant parameters – such as the strain or the strain rate – representative values were obtained via FEA simulations and were fixed for all experiments. However, in full-scale forging the strain and the strain rate can be controlled by adjusting the geometry of the dies and the deformation speed, respectively. Expanding the thermo-mechanical experiments to investigate how different strains and strain rates affect surface cracking would allow expanding the prediction power of the statistical model for industrial applications. Similarly, studying how deformation kinetics (via the strain rate) affects cracking and which

deformation and fracture mechanisms are at play is highly scientifically relevant and would be aligned with the additional EM microstructural investigations proposed above. Similarly, this work could leverage the proposal above concerning streamlining the forging investigations and improving strain control.

Finally, Udimet 720 has been employed in this work, and the results obtained for this alloy were compared with a similarly composed alloy: René 65. There is clear value in expanding this investigation to account for the effect of chemical composition. This could include new generation highly γ'-reinforced cast-and-wrought superalloys such as AD730$^{\text{TM}}$ or the niobium rich VDM Alloy 780, as well as bespoke compositions.

Bibliography

[1] The World Bank, World Bank Open Data: Air transport, passengers carried., 2019. https://data.worldbank.org/indicator/IS.AIR.PSGR.

[2] The World Bank, World Bank Open Data: Air transport, freight, 2019. https://data.worldbank.org/indicator/IS.AIR.GOOD.MT.K1?end=2019&start=1970.

[3] T.R. Lakshmanan, The broader economic consequences of transport infrastructure investments, J. Transp. Geogr. 19 (2011) 1–12. https://doi.org/10.1016/j.jtrangeo.2010.01.001.

[4] J. Larsson, A. Kamb, J. Nässén, J. Åkerman, Measuring greenhouse gas emissions from international air travel of a country's residents methodological development and application for Sweden, Environ. Impact Assess. Rev. 72 (2018) 137–144. https://doi.org/10.1016/j.eiar.2018.05.013.

[5] International Energy Agency (IEA), Aviation, Paris, 2021. https://www.iea.org/reports/aviation.

[6] S. Gössling, P. Upham, Climate change and aviation: Issues, challenges and solutions, Earthscan, 2009.

[7] M.J. Donachie, S.J. Donachie, Superalloys: A Technical Guide, 2nd Edition, America (NY). (2002). https://doi.org/10.1361.

[8] C.T. Sims, A history of superalloy metallurgy for superalloy metallurgists, in: Proc. 5th Int. Symp. Superalloys (Superalloys 1984), 1984: pp. 399–419.

[9] R.C. Reed, The superalloys: fundamentals and applications, Cambridge University Press, 2008.

[10] G.C. Oates, Aerothermodynamics of gas turbine and rocket propulsion, AIAA, 1997.

[11] A. Faghri, Y. Zhang, Introduction To Transport Phenomena, Transp. Phenom. Multiph. Syst. (2006) 1–106. https://doi.org/10.1016/b978-0-12-370610-2.50006-4.

[12] F.J. Hale, Introduction to Aircraft Performance and Design, Wiley, 2003.

[13] C. Soares, Gas Turbine Major Components and Modules, 2015.

https://doi.org/10.1016/b978-0-12-410461-7.00004-3.

[14] Rolls Royce Holdings plc, The Jet Engine, John Wiley & Sons, 2015.

[15] Z. Xu, Y. Wang, Electrochemical machining of complex components of aero-engines: Developments, trends, and technological advances, Chinese J. Aeronaut. 34 (2021) 28–53. https://doi.org/10.1016/j.cja.2019.09.016.

[16] B.V.R.R. Kumar, A Review on Blisk Technology, Int. J. Innov. Res. Sci. Eng. Technol. 2 (2013) 1353–1358.

[17] R.J. Mitchell, J.A. Lemsky, R. Ramanathan, H.Y. Li, K.M. Perkins, L.D. Connor, Process development & microstructure & mechanical property evaluation of a dual microstructure heat treated advanced nickel disc alloy, Proc. 11th Int. Symp. Superalloys (Superalloys 2008). (2008) 347–356. https://doi.org/10.7449/2008/superalloys_2008_347_356.

[18] J. Gayda, T.P. Gabb, P.T. Kantzos, The effect of dual microstructure heat treatment on an advanced nickel-base disk alloy, in: Proc. 10th Int. Symp. Superalloys (Superalloys 2004), 2004: pp. 323–329. https://doi.org/10.7449/2004/superalloys_2004_323_329.

[19] C. Kienl, Hot forging of the nickel-base superalloy ATI 718Plus, Cambridge Univ. (2019). https://www.repository.cam.ac.uk/handle/1810/299543.

[20] Rolls Royce Holdings plc, Annual Report 2020, 2021. https://www.rolls-royce.com/~/media/Files/R/Rolls-Royce/documents/annual-report/2020/2020-full-annual-report.pdf.

[21] Flight Airline Business, Market share of the leading commercial aircraft engine manufacturers worldwide in 2020 [Graph], Statista. (2021). https://www.statista.com/statistics/1099835/global-aircraft-engine-manufacturer-market-share/ (accessed January 18, 2022).

[22] European Union Aviation Safety Agency, Type-certificate data sheet (No. EASA E.047) for RB211 Trent 800 series engines, 2019. https://www.easa.europa.eu/sites/default/files/dfu/EASA E 047 TCDS issue 04.pdf.

[23] A.E.B. Hernández, T. Beno, C. Fredriksson, Energy and Cost Estimation of a Feature-based Machining Operation on HRSA, Procedia CIRP. 61 (2017) 511–516. https://doi.org/10.1016/j.procir.2016.11.141.

[24] D.S. Lee, D.W. Fahey, A. Skowron, M.R. Allen, U. Burkhardt, Q. Chen, S.J. Doherty, S. Freeman, P.M. Forster, J. Fuglestvedt, A. Gettelman, R.R. De León, L.L. Lim, M.T. Lund, R.J. Millar, B. Owen, J.E. Penner, G. Pitari, M.J. Prather, R. Sausen, L.J. Wilcox, The contribution of

global aviation to anthropogenic climate forcing for 2000 to 2018, Atmos. Environ. 244 (2021). https://doi.org/10.1016/j.atmosenv.2020.117834.

[25] S.L. Semiatin, F. Zhang, R. Larsen, L.A. Chapman, D.U. Furrer, Precipitation in powder-metallurgy, nickel-base superalloys: review of modeling approach and formulation of engineering methods to determine input data, Integr. Mater. Manuf. Innov. (2016). https://doi.org/10.1186/s40192-016-0046-3.

[26] R.M.F. Jones, L.A. Jackman, The structural evolution of superalloy ingots during hot working, JOM. (1999). https://doi.org/10.1007/s11837-999-0007-9.

[27] T. Altan, G. Ngaile, G. Shen, Cold and Hot Forging: Fundamentals and Applications, Volume 1, AMS Int. 1 (2005) 341. https://books.google.ca/books/about/Cold_and_Hot_Forging.html?id=ieisfCEvObIC&pgis=1.

[28] C.P. Blankenship, M.F.F. Henry, J.M. Hyzak, R.B. Rohling, E.L. Hall, C.P. Blankenship, Jr, M.F.F. Henry, J.M. Hyzak, R.B. Rohling, E.L. Hall, Hot-die forging of P/M Ni-base superalloys, Proc. 8th Int. Symp. Superalloys (Superalloys 1996). (1996) 653–662. https://doi.org/10.7449/1996/superalloys_1996_653_662.

[29] M.C. Hardy, M. Detrois, E.T. McDevitt, C. Argyrakis, V. Saraf, P.D. Jablonski, J.A. Hawk, R.C. Buckingham, H.S. Kitaguchi, S. Tin, Solving Recent Challenges for Wrought Ni-Base Superalloys, Metall. Mater. Trans. A Phys. Metall. Mater. Sci. (2020). https://doi.org/10.1007/s11661-020-05773-6.

[30] A. Devaux, B. Picqué, M.F. Gervais, E. Georges, T. Poulain, P. Héritier, AD730™ - A New Nickel-Based Superalloy for High Temperature Engine Rotative Parts, in: Proc. 12th Int. Symp. Superalloys (Superalloys 2012), 2012. https://doi.org/10.1002/9781118516430.ch100.

[31] F.E. Sczerzenie, G.E. Maurer, Development of Udimet 720 for High Strength Disk Applications, (2012) 573–580. https://doi.org/10.7449/1984/superalloys_1984_573_580.

[32] A. Devaux, E. Georges, P. Héritier, Development of new C&W superalloys for high temperature disk applications, in: Adv. Mater. Res., 2011. https://doi.org/10.4028/www.scientific.net/AMR.278.405.

[33] J.A. Heaney, M.L. Lasonde, A.M. Powell, B.J. Bond, C.M. O'Brien, Development of a new cast and wrought alloy (René 65) for high temperature disk applications, in: 8th Int. Symp. Superalloy 718 Deriv.

2014, TMS (The Minerals, Metals & Materials Society), 2014: pp. 67–77. https://doi.org/10.1002/9781119016854.ch6.

[34] H. Monajati, M. Jahazi, S. Yue, A.K. Taheri, Deformation characteristics of isothermally forged UDIMET 720 nickel-base superalloy, Metall. Mater. Trans. A Phys. Metall. Mater. Sci. 36 (2005) 895–905. https://doi.org/10.1007/s11661-005-0284-z.

[35] M. Preuss, J.Q. da Fonseca, B. Grant, E. Knoche, R. Moat, M. Daymond, The effect of γ' particle size on the deformation mechanism in an advanced polycrystalline nickel-base superalloy, Proc. 11th Int. Symp. Superalloys (Superalloys 2008). 11 (2008) 405–414.

[36] J.G. Wang, D. Liu, T. Wang, Y.H. Yang, Characterization of hot deformation behavior of Udimet720Li superalloy using processing map, Adv. Mater. Res. 887 (2014) 1161–1168. https://doi.org/10.4028/www.scientific.net/AMR.887-888.1161.

[37] Q.Y. Yu, Z.H. Yao, J.X. Dong, Hot deformation behavior of uniform fine-grained GH4720Li alloy based on its processing map, Int. J. Miner. Metall. Mater. 23 (2016) 83–91. https://doi.org/10.1007/s12613-016-1214-3.

[38] J.M. Morra, R.R. Biederman, F.R. Tuler, The Deformation Behavior of P/M Rene'95 Under Isothermal Forging Conditions, in: Proc. 6th Int. Symp. Superalloys (Superalloys 1988), TMS, Pennsylvania, 1988: pp. 505–14. https://doi.org/10.7449/1988/superalloys_1988_505_514.

[39] J. long Qu, Z. nan Bi, J. hui Du, M. qing Wang, Q. zeng Wang, J. Zhang, Hot Deformation Behavior of Nickel-Based Superalloy GH4720Li, J. Iron Steel Res. Int. 18(10) (2011) 59–65. https://doi.org/10.1016/S1006-706X(12)60023-5.

[40] M.O. Alniak, F. Bedir, Modelling of deformation and microstructural changes in P/M Rene 95 under isothermal forging conditions, Mater. Sci. Eng. A. 429(1–2) (2006) 295–303. https://doi.org/10.1016/j.msea.2006.05.030.

[41] G. He, F. Liu, L. Huang, L. Jiang, Analysis of Forging Cracks during Hot Compression of Powder Metallurgy Nickel-Based Superalloy on Simulation and Experiment, Adv. Eng. Mater. 18 (2016) 1823–1832. https://doi.org/10.1002/adem.201600270.

[42] A.P. Mouritz, Introduction to aerospace materials, Elsevier, 2012.

[43] B. Geddes, H. Leon, X. Huang, Superalloys: alloying and performance, ASM International, 2010.

[44] F.C. Campbell Jr, Manufacturing technology for aerospace structural materials, Elsevier, 2011.

[45] J.K. Tien, R.N. Jarrett, Effects of cobalt in nickel-base superalloys, in: High Temp. Alloy. Gas Turbines 1982, Springer, 1982: pp. 423–446.

[46] T.J. Garosshen, T.D. Tillman, G.P. McCarthy, Effects of B, C, and Zr on the structure and properties of a P/M nickel base superalloy, Metall. Trans. A. 18 (1987) 69–77.

[47] M.A. Burke, J. Greggi Jr, G.A. Whitlow, The effect of boron and carbon on the microstructural chemistries of two wrought nickel base superalloys, Scr. Metall. 18 (1984) 91–94.

[48] P. Kontis, H.A.M. Yusof, S. Pedrazzini, M. Danaie, K.L. Moore, P.A.J. Bagot, M.P. Moody, C.R.M. Grovenor, R.C. Reed, On the effect of boron on grain boundary character in a new polycrystalline superalloy, Acta Mater. 103 (2016) 688–699. https://doi.org/10.1016/j.actamat.2015.10.006.

[49] H. Wang, J. Yang, J. Meng, S. Ci, Y. Yang, N. Sheng, Y. Zhou, X. Sun, Effects of B content on microstructure and high-temperature stress rupture properties of a high chromium polycrystalline nickel-based superalloy, J. Alloys Compd. 860 (2021) 157929. https://doi.org/10.1016/j.jallcom.2020.157929.

[50] O.P. Sinha, M. Chatterjee, V.V.R.S. Sarma, S.N. Jha, Effect of residual elements on high performance nickel base superalloys for gas turbines and strategies for manufacture, Bull. Mater. Sci. 28 (2005) 379–382. https://doi.org/10.1007/BF02704253.

[51] J.B. Wahl, K. Harris, Advances in single crystal superalloys-Control of critical elements, in: 7th Parsons Conf., 2007.

[52] B. Hassan, J. Corney, Grain boundary precipitation in Inconel 718 and ATI 718Plus, Mater. Sci. Technol. (United Kingdom). 33 (2017) 1879–1889. https://doi.org/10.1080/02670836.2017.1333222.

[53] R.C. Reed, C.M.F. Rae, Physical Metallurgy of the Nickel-Based Superalloys, Fifth Edit, Elsevier, 2014. https://doi.org/10.1016/B978-0-444-53770-6.00022-8.

[54] B.J. Bond, C.M. O'Brien, J.L. Russell, J.A. Heaney, M.L. Lasonde, René 65 billet material for forged turbine components, in: 8th Int. Symp. Superalloy 718 Deriv. 2014, TMS (The Minerals, Metals & Materials Society), 2014: pp. 107–118. https://doi.org/10.1002/9781119016854.ch9.

[55] C. Chen, Q. Wang, C. Dong, Y. Zhang, H. Dong, Composition rules of

Ni-base single crystal superalloys and its influence on creep properties via a cluster formula approach, Sci. Rep. 10 (2020) 1–13. https://doi.org/10.1038/s41598-020-78690-8.

[56] A.K. Jena, M.C. Chaturvedi, The role of alloying elements in the design of nickel-base superalloys, J. Mater. Sci. 19 (1984) 3121–3139. https://doi.org/10.1007/BF00549796.

[57] A. Nowotnik, Nickel-Based Superalloys, Ref. Modul. Mater. Sci. Mater. Eng. (2016) 1–7. https://doi.org/10.1016/b978-0-12-803581-8.02574-1.

[58] O.I. Gorbatov, I.L. Lomaev, Y.N. Gornostyrev, A. V. Ruban, D. Furrer, V. Venkatesh, D.L. Novikov, S.F. Burlatsky, Effect of composition on antiphase boundary energy in Ni3Al based alloys: Ab initio calculations, Phys. Rev. B. 93 (2016) 1–8. https://doi.org/10.1103/PhysRevB.93.224106.

[59] N.S. Stoloff, Physical and mechanical metallurgy of Ni3Al and its alloys, Int. Mater. Rev. 34 (1989) 153–184. https://doi.org/10.1179/imr.1989.34.1.153.

[60] Y. Tu, Z. Mao, D.N. Seidman, Phase-partitioning and site-substitution patterns of molybdenum in a model Ni-Al-Mo superalloy: An atom-probe tomographic and first-principles study, Appl. Phys. Lett. 101 (2012). https://doi.org/10.1063/1.4753929.

[61] WT Loomis, JW Freeman, DL Sponseller, Influence of molybdenum on the U- phase in experimental nickelbase superalloys, Met Trans. 3 (1972) 989–1000.

[62] C. Joseph, C. Persson, M. Hörnqvist Colliander, Influence of heat treatment on the microstructure and tensile properties of Ni-base superalloy Haynes 282, Mater. Sci. Eng. A. 679 (2017) 520–530. https://doi.org/10.1016/j.msea.2016.10.048.

[63] R.W. Cahn, P.A. Siemers, J.E. Geiger, P. Bardhan, The order-disorder transformation in Ni3Al and Ni3Al- Fe alloys—I. Determination of the transition temperatures and their relation to ductility, Acta Metall. 35 (1987) 2737–2751.

[64] F.J. Bremer, M. Beyss, H. Wenzl, The order–disorder transition of the intermetallic phase Ni3Al, Phys. Status Solidi. 110 (1988) 77–82.

[65] R.A. Ricks, A.J. Porter, R.C. Ecob, The growth of γ' precipitates in nickel-base superalloys, Acta Metall. 31 (1983) 43–53.

[66] G.H. Meier, Thermodynamics of surfaces and interfaces: concepts in inorganic materials, Cambridge University Press, 2014.

[67] A. Baldan, Progress in Ostwald ripening theories and their applications in nickel-base super alloys, J. Mater. Sci. 37 (2002) 2379–2405.

[68] M. Doi, T. Miyazaki, Microstructural Development Under the Influence of Elastic Energy in Nickel-Base Alloys Containing gamma' Precipitates, Proc. 6th Int. Symp. Superalloys (Superalloys 1988). (1988) 663–672.

[69] A.J. Goodfellow, Factors contributing to the yield strength of polycrystalline nickel-based superalloys, University of Cambridge, 2019. https://doi.org/10.17863/CAM.40855.

[70] M. Fährmann, P. Fratzl, O. Paris, E. Fährmann, W.C. Johnson, Influence of coherency stress on microstructural evolution in model Ni-Al-Mo alloys, Acta Metall. Mater. 43 (1995) 1007–1022.

[71] T.P. Gabb, J. Gayda, J. Telesman, A. Garg, The effects of heat treatment and microstructure variations on disk superalloy properties at high temperature, in: Proc. 11th Int. Symp. Superalloys (Superalloys 2008), 2008: pp. 121–130. https://doi.org/10.7449/2008/superalloys_2008_121_130.

[72] R.J. Mitchell, M.C. Hardy, M. Preuss, S. Tin, Development of γ' morphology in P/M rotor disc alloys during heat treatment, in: Proc. 10th Int. Symp. Superalloys (Superalloys 2004), 2004: pp. 361–370. https://doi.org/10.7449/2004/superalloys_2004_361_370.

[73] M.A. Charpagne, P. Vennégueès, T. Billot, J.M. Franchet, N. Bozzolo, Evidence of multimicrometric coherent γ' precipitates in a hot-forged γ–γ' nickel-based superalloy, J. Microsc. 263 (2016) 106–112. https://doi.org/10.1111/jmi.12380.

[74] S. Vernier, J.M. Franchet, C. Dumont, P. Vennéguès, N. Bozzolo, γ' precipitates with a twin orientation relationship to their hosting grain in a γ-γ' nickel-based superalloy, Scr. Mater. 153 (2018) 10–13. https://doi.org/10.1016/j.scriptamat.2018.04.037.

[75] R. Radis, M. Schaffer, M. Albu, G. Kothleitner, P. Pölt, E. Kozeschnik, Multimodal size distributions of γ' precipitates during continuous cooling of UDIMET 720 Li, Acta Mater. 57 (2009) 5739–5747. https://doi.org/10.1016/j.actamat.2009.08.002.

[76] Y.Q. Chen, E. Francis, J. Robson, M. Preuss, S.J. Haigh, Compositional variations for small-scale gamma prime (γ') precipitates formed at different cooling rates in an advanced Ni-based superalloy, Acta Mater. 85 (2015) 199–206. https://doi.org/10.1016/j.actamat.2014.11.009.

[77] A.J. Goodfellow, E.I. Galindo-Nava, K.A. Christofidou, N.G. Jones, T.

Martin, P.A.J. Bagot, C.D. Boyer, M.C. Hardy, H.J. Stone, Gamma Prime Precipitate Evolution During Aging of a Model Nickel-Based Superalloy, Metall. Mater. Trans. A Phys. Metall. Mater. Sci. 49 (2018) 718–728. https://doi.org/10.1007/s11661-017-4336-y.

[78] F. Masoumi, D. Shahriari, M. Jahazi, J. Cormier, A. Devaux, Kinetics and Mechanisms of γ' Reprecipitation in a Ni-based Superalloy, Sci. Rep. 6 (2016) 1–16. https://doi.org/10.1038/srep28650.

[79] M. Sundararaman, P. Mukhopadhyay, S. Banerjee, Some aspects of the precipitation of metastable intermetallic phases in INCONEL 718, Metall. Trans. A. 23 (1992) 2015–2028. https://doi.org/10.1007/BF02647549.

[80] M. Sundararaman, S. Banerjee, H. Mori, The Stability of γ'' and γ' Phases in Alloy 718 Under Electron Irradiation, in: E.A. Loria (Ed.), Supcralloys 718, 625, 706, Var. Deriv., TMS (The Minerals, Metals &Materials Society), 2001: pp. 379–387. https://doi.org/10.7449/2001/superalloys_2001_379_387.

[81] P.M. Mignanelli, N.G. Jones, E.J. Pickering, O.M.D.M. Messé, C.M.F. Rae, M.C. Hardy, H.J. Stone, Gamma-gamma prime-gamma double prime dual-superlattice superalloys, Scr. Mater. 136 (2017) 136–140. https://doi.org/10.1016/j.scriptamat.2017.04.029.

[82] Y. Desvallées, M. Bouzidi, F. Bois, N. Beaude, Delta phase in Inconel 718: mechanical properties and forging process requirements, in: Superalloys 718, 625, 706 Var. Deriv., TMS (The Minerals, Metals & Materials Society), 1994: pp. 281–291.

[83] G.K. Bouse, Eta η and Platelet Phases in Investment Cast Superalloys, Proc. 8th Int. Symp. Superalloys (Superalloys 1996). 8 (1996) 163–172.

[84] J.R. Davis, ASM specialty handbook: heat-resistant materials, ASM International, 1997.

[85] A. Casanova, M. Hardy, C.M.F. Rae, Morphology and kinetics of grain boundary precipitation in alloy ATI 718Plus®, in: 8th Int. Symp. Superalloy 718 Deriv., TMS (The Minerals, Metals & Materials Society), 2014: pp. 573–586.

[86] L. Xiao, D. Chen, M.C. Chaturvedi, Effect of boron and carbon on the fracture toughness of in 718 superalloy at room temperature and 650°C, J. Mater. Eng. Perform. 14 (2005) 528–538. https://doi.org/10.1361/105994905X56106.

[87] C.M.F. Rae, M.S.A. Karunaratne, C.J. Small, R.W. Broomfield, C.N. Jones, R.C. Reed, Topologically Close Packed Phases in an Experimental

Rhenium-Containing Single Crystal Superalloy, Proc. 9th Int. Symp. Superalloys (Superalloys 2000). (2000) 767–776. https://doi.org/10.7449/2000/superalloys_2000_767_776.

[88] G.D. Pigrova, TCP-phases in nickel-base alloys with elevated chromium content, Met. Sci. Heat Treat. 47 (2005) 544–551. https://doi.org/10.1007/s11041-006-0029-7.

[89] R. Darolia, D.F. Lahrman, R.D. Field, Formation of topologically closed packed phases in nickel base single crystal superalloys, Proc. 6th Int. Symp. Superalloys (Superalloys 1988). (1988) 255–264.

[90] R.R. Unocic, L. Kovarik, C. Shen, P.M. Sarosi, Y. Wang, J. Li, S. Ghosh, M.J. Mills, Deformation mechanisms in Ni-base disk superalloys at higher temperatures, in: Proc. 11th Int. Symp. Superalloys (Superalloys 2008), 2008: pp. 377–385. https://doi.org/10.7449/2008/superalloys_2008_377_385.

[91] E.I. Galindo-Nava, L.D. Connor, C.M.F. Rae, On the prediction of the yield stress of unimodal and multimodal γ' Nickel-base superalloys, Acta Mater. 98 (2015) 377–390. https://doi.org/10.1016/j.actamat.2015.07.048.

[92] S. Raujol, M. Benyoucef, D. Locq, P. Caron, F. Pettinari, N. Clement, A. Coujou, Decorrelated movements of Shockley partial dislocations in the γ-phase channels of nickel-based superalloys at intermediate temperature, Philos. Mag. 86 (2006) 1189–1200. https://doi.org/10.1080/14786430500254685.

[93] D. Barba, E. Alabort, S. Pedrazzini, D.M. Collins, A.J. Wilkinson, P.A.J. Bagot, M.P. Moody, C. Atkinson, A. Jérusalem, R.C. Reed, On the microtwinning mechanism in a single crystal superalloy, Acta Mater. 135 (2017) 314–329. https://doi.org/10.1016/j.actamat.2017.05.072.

[94] C. Kienl, F.D. León-Cázares, C.M.F. Rae, Deformation twinning during high temperature compression tests of the Ni-base superalloy ATI 718Plus®, Acta Mater. 000 (2020). https://doi.org/10.1016/j.actamat.2019.12.047.

[95] D. Barba, S. Pedrazzini, A. Vilalta-Clemente, A.J. Wilkinson, M.P. Moody, P.A.J. Bagot, A. Jérusalem, R.C. Reed, On the composition of microtwins in a single crystal nickel-based superalloy, Scr. Mater. 127 (2017) 37–40. https://doi.org/10.1016/j.scriptamat.2016.08.029.

[96] L. Kovarik, R.R. Unocic, J. Li, P. Sarosi, C. Shen, Y. Wang, M.J. Mills, Microtwinning and other shearing mechanisms at intermediate temperatures in Ni-based superalloys, Prog. Mater. Sci. 54 (2009) 839–

873. https://doi.org/10.1016/j.pmatsci.2009.03.010.

[97] T.M. Smith, R.R. Unocic, H. Deutchman, M.J. Mills, Creep deformation mechanism mapping in nickel base disk superalloys, Mater. High Temp. 33 (2016) 372–383. https://doi.org/10.1080/09603409.2016.1180858.

[98] T. Link, M. Feller-Kniepmeier, Shear mechanisms of the γ' phase in single-crystal superalloys and their relation to creep, Metall. Trans. A. 23 (1992) 99–105. https://doi.org/10.1007/BF02660857.

[99] C.M.F. Rae, R.C. Reed, Primary creep in single crystal superalloys: Origins, mechanisms and effects, Acta Mater. 55 (2007) 1067–1081. https://doi.org/10.1016/j.actamat.2006.09.026.

[100] E.M. Francis, B.M.B. Grant, J.Q. Da Fonseca, P.J. Phillips, M.J. Mills, M.R. Daymond, M. Preuss, High-temperature deformation mechanisms in a polycrystalline nickel-base superalloy studied by neutron diffraction and electron microscopy, Acta Mater. 74 (2014) 18–29. https://doi.org/10.1016/j.actamat.2014.04.028.

[101] F.R.N. Nabarro, M.S. Duesbery, Dislocations in solids, Vol 11, Elsevier, 2002.

[102] S. Karewar, J. Sietsma, M.J. Santofimia, Effect of pre-existing defects in the parent fcc phase on atomistic mechanisms during the martensitic transformation in pure Fe: A molecular dynamics study, Acta Mater. 142 (2018) 71–81. https://doi.org/10.1016/j.actamat.2017.09.049.

[103] L.B. Han, Q. An, R.S. Fu, L. Zheng, S.N. Luo, Melting of defective Cu with stacking faults, J. Chem. Phys. 130 (2009). https://doi.org/10.1063/1.3049799.

[104] A. Hunter, I.J. Beyerlein, T.C. Germann, M. Koslowski, Influence of the stacking fault energy surface on partial dislocations in fcc metals with a three-dimensional phase field dislocations dynamics model, Phys. Rev. B - Condens. Matter Mater. Phys. 84 (2011) 1–10. https://doi.org/10.1103/PhysRevB.84.144108.

[105] M. Shih, J. Miao, M. Mills, M. Ghazisaeidi, Stacking fault energy in concentrated alloys, Nat. Commun. 12 (2021) 1–10. https://doi.org/10.1038/s41467-021-23860-z.

[106] B. Burton, The influence of stacking fault energy on creep, Acta Metall. 30 (1982) 905–910.

[107] F. Pettinari, J. Douin, G. Saada, P. Caron, A. Coujou, N. Clément, Stacking fault energy in short-range ordered γ-phases of Ni-based superalloys, Mater. Sci. Eng. A. 325 (2002) 511–519.

https://doi.org/10.1016/S0921-5093(01)01765-8.

[108] W. Yang, P. Qu, J. Sun, Q. Yue, H. Su, J. Zhang, L. Liu, Effect of alloying elements on stacking fault energies of γ and γ' phases in Ni-based superalloy calculated by first principles, Vacuum. 181 (2020) 1–7. https://doi.org/10.1016/j.vacuum.2020.109682.

[109] B.E.P. Beeston, I.L. Dillamore, R.E. Smallman, The Stacking-Fault Energy of Some Nickel-Cobalt Alloys, Met. Sci. J. 2 (1968) 12–14. https://doi.org/10.1179/030634568790443468.

[110] H. Long, Y. Liu, D. Kong, H. Wei, Y. Chen, S. Mao, Shearing mechanisms of stacking fault and anti-phase-boundary forming dislocation pairs in the γ' phase in Ni-based single crystal superalloy, J. Alloys Compd. 724 (2017) 287–295. https://doi.org/10.1016/j.jallcom.2017.07.020.

[111] R.J. Taunt, B. Ralph, Observations of the fine structure of superdislocations in Ni3Al by field-ion microscopy, Philos. Mag. 30 (1974) 1379–1394. https://doi.org/10.1080/14786437408207288.

[112] D.P. Pope, Mechanical properties of Ni3Al and nickel-base alloys with high volume fraction of γ', Int. Met. Rev. 29 (1984) 136–167. https://doi.org/10.1179/imtr.1984.29.1.136.

[113] X. Gao, J. Wang, X. Wu, R. Wang, Z. Jia, Effects of alloying atoms on antiphase boundary energy and yield stress anomaly of L12 intermetallics: First-principles study, Crystals. 8 (2018) 1–18. https://doi.org/10.3390/cryst8020096.

[114] V. Paidar, D.P. Pope, V. Vitek, A theory of the anomalous yield behavior in L12 ordered alloys, Acta Metall. 32 (1984) 435–448. https://doi.org/10.1016/0001-6160(84)90117-2.

[115] R.W. Kozar, A. Suzuki, W.W. Milligan, J.J. Schirra, M.F. Savage, T.M. Pollock, Strengthening mechanisms in polycrystalline multimodal nickel-base superalloys, Metall. Mater. Trans. A Phys. Metall. Mater. Sci. 40 (2009) 1588–1603. https://doi.org/10.1007/s11661-009-9858-5.

[116] Y. Mishima, S. Ochiai, M. Yodogawa, T. Suzuki, Mechanical properties of Ni3Al with ternary addition of transition metal elements, Trans. Japan Inst. Met. 27 (1986) 41–50.

[117] A.J. Goodfellow, Strengthening mechanisms in polycrystalline nickel-based superalloys, Mater. Sci. Technol. (United Kingdom). 34 (2018) 1793–1808. https://doi.org/10.1080/02670836.2018.1461594.

[118] W. Hüther, B. Reppich, Interaction of dislocations with coherent, stress-

free, ordered particles, Int. J. Mater. Res. 69 (1978) 628–634.

[119] D.M. Collins, H.J. Stone, A modelling approach to yield strength optimisation in a nickel-base superalloy, Int. J. Plast. 54 (2014) 96–112. https://doi.org/10.1016/j.ijplas.2013.08.009.

[120] B. Reppich, Some new aspects concerning particle hardening mechanisms in γ' precipitating Ni-base alloys-I. Theoretical concept, Acta Metall. 30 (1982) 87–94. https://doi.org/10.1016/0001-6160(82)90048-7.

[121] B. Reppich, P. Schepp, G. Wehner, Some new aspects concerning particle hardening mechanisms in γ' precipitating nickel-base alloys-II. Experiments, Acta Metall. 30 (1982) 95–104. https://doi.org/10.1016/0001-6160(82)90049-9.

[122] M.P. Jackson, R.C. Reed, Heat treatment of UDIMET 720Li: the effect of microstructure on properties, Mater. Sci. Eng. A. 259 (1999) 85–97. https://doi.org/10.1016/S0921-5093(98)00867-3.

[123] G.B. Viswanathan, P.M. Sarosi, M.F. Henry, D.D. Whitis, W.W. Milligan, M.J. Mills, Investigation of creep deformation mechanisms at intermediate temperatures in René 88 DT, Acta Mater. 53 (2005) 3041–3057. https://doi.org/10.1016/j.actamat.2005.03.017.

[124] R.R. Unocic, G.B. Viswanathan, P.M. Sarosi, S. Karthikeyan, J. Li, M.J. Mills, Mechanisms of creep deformation in polycrystalline Ni-base disk superalloys, Mater. Sci. Eng. A. 483–484 (2008) 25–32. https://doi.org/10.1016/j.msea.2006.08.148.

[125] D. Locq, P. Caron, S. Raujol, F. Pettinari-Sturmel, A. Coujou, N. Clément, On the role of tertiary gamma prime precipitates in the creep behaviour at 700oC of a powder metallurgy disk superalloy, Proc. 10th Int. Symp. Superalloys (Superalloys 2004). (2004) 179–188. https://www.tms.org/superalloys/10.7449/2004/superalloys_2004_179_187.pdf.

[126] J. Telesman, T.P. Gabb, A. Garg, P. Bonacuse, JGayda, Effect of microstructure on time dependent fatigue crack growth behavior in a P/M turbine disk alloy, in: Proc. 11th Int. Symp. Superalloys (Superalloys 2008), 2008: pp. 807–816. https://doi.org/10.7449/2008/superalloys_2008_807_816.

[127] D. Raynor, J.M. Silcock, Strengthening mechanisms in γ' precipitating alloys, Met. Sci. J. 4 (1970) 121–130.

[128] Q.Z. Chen, N. Jones, D.M. Knowles, The microstructures of base/modified RR2072 SX superalloys and their effects on creep

properties at elevated temperatures, Acta Mater. 50 (2002) 1095–1112. https://doi.org/10.1016/S1359-6454(01)00410-4.

[129] D. Zhang, L. Jiang, B. Zheng, J.M. Schoenung, S. Mahajan, E.J. Lavernia, I.J. Beyerlein, J.M. Schoenung, E.J. Lavernia, Deformation Twinning (Update), Ref. Modul. Mater. Sci. Mater. Eng. (2016) 1–24. https://doi.org/10.1016/b978-0-12-803581-8.02878-2.

[130] Mechanism of Twinning in Metals, Nature. 123 (1929) 262–263. https://doi.org/10.1038/123262b0.

[131] S. Mahajan, D.F. Williams, Deformation Twinning in Metals and Alloys, Int. Metall. Rev. 18 (1973) 43–61. https://doi.org/10.1179/imtlr.1973.18.2.43.

[132] G.T. Gray Iii, Deformation twinning in Al-4.8 wt% Mg, Acta Metall. 36 (1988) 1745–1754.

[133] E. Pu, W. Zheng, Z. Song, H. Feng, H. Dong, Hot deformation characterization of nickel-based superalloy UNS10276 through processing map and microstructural studies, J. Alloys Compd. 694 (2017) 617–631. https://doi.org/10.1016/j.jallcom.2016.10.029.

[134] M. Fahrmann, A. Suzuki, Effect of cooling rate on Gleeble hot ductility of UDIMET alloy 720 billet, in: Proc. 11th Int. Symp. Superalloys (Superalloys 2008), TMS (The Minerals, Metals & Materials Society), 2008. https://doi.org/10.7449/2008/superalloys_2008_311_316.

[135] D. Hull, D.J. Bacon, Introduction to dislocations, 5th ed., Elsevier, 2011.

[136] N.T. Adelman, J. Dundurs, Instability of screw dislocation pile-ups, J. Appl. Phys. 44 (1973) 5631–5632. https://doi.org/10.1063/1.1662213.

[137] N.T. Adelman, J. Dundurs, Initiation of cross-slip near the head of a screw dislocation pile-up, J. Appl. Phys. 47 (1976) 4237–4238. https://doi.org/10.1063/1.323211.

[138] S.M. Hafez Haghighat, G. Eggeler, D. Raabe, Effect of climb on dislocation mechanisms and creep rates in γ'-strengthened Ni base superalloy single crystals: A discrete dislocation dynamics study, Acta Mater. 61 (2013) 3709–3723. https://doi.org/10.1016/j.actamat.2013.03.003.

[139] E. Arzt, J. Rösler, The kinetics of dislocation climb over hard particles-II. Effects of an attractive particle-dislocation interaction, Acta Metall. 36 (1988) 1053–1060. https://doi.org/10.1016/0001-6160(88)90159-9.

[140] H. Yang, M. Huang, Z. Li, The influence of vacancies diffusion-induced

dislocation climb on the creep and plasticity behaviors of nickel-based single crystal superalloy, Comput. Mater. Sci. 99 (2015) 348–360. https://doi.org/10.1016/j.commatsci.2014.12.035.

[141] S.M. Hafez Haghighat, G. Eggeler, D. Raabe, Effect of climb on dislocation mechanisms and creep rates in γ'-strengthened Ni base superalloy single crystals: A discrete dislocation dynamics study, Acta Mater. 61 (2013) 3709–3723. https://doi.org/10.1016/j.actamat.2013.03.003.

[142] F.X. Liu, A.C.F. Cocks, E. Tarleton, Dislocation dynamics modelling of the creep behaviour of particle-strengthened materials, Proc. R. Soc. A Math. Phys. Eng. Sci. 477 (2021). https://doi.org/10.1098/rspa.2021.0083.

[143] F. Liu, A.C.F. Cocks, E. Tarleton, A new method to model dislocation self-climb dominated by core diffusion, J. Mech. Phys. Solids. 135 (2020) 103783. https://doi.org/10.1016/j.jmps.2019.103783.

[144] J.-S. Zhang, High temperature deformation and fracture of materials, Elsevier, 2010.

[145] J. Hockin, Investment Casting of Superalloys, in: Proc. 2nd Int. Symp. Superalloys, Seven Spring, Pennsylvania, 1972: pp. 263–270. https://doi.org/10.7449/1972/superalloys_1972_c-1_c-9.

[146] T.M. Pollock, S. Tin, Nickel-based superalloys for advanced turbine engines: Chemistry, microstructure, and properties, J. Propuls. Power. 22 (2006) 361–374. https://doi.org/10.2514/1.18239.

[147] R.W. Hertzberg, R.P. Vinci, J.L. Hertzberg, Deformation and fracture mechanics of engineering materials, John Wiley & Sons, 2020.

[148] G.R. Thellaputta, P.S. Chandra, C.S.P. Rao, Machinability of Nickel Based Superalloys: A Review, Mater. Today Proc. 4 (2017) 3712–3721. https://doi.org/10.1016/j.matpr.2017.02.266.

[149] S.R. Schmid, M.Á.S. Cantó, T. Pasang, Tribology of Forging, in: Q.J. Wang, Y.-W. Chung (Eds.), Encycl. Tribol., Springer US, Boston, MA, 2013: pp. 3873–3880. https://doi.org/10.1007/978-0-387-92897-5_618.

[150] J.W. Brooks, Forging of superalloys, Mater. Des. 21 (2000) 297–303. https://doi.org/10.1016/s0261-3069(99)00069-2.

[151] J.H. Moll, B.J. McTiernan, Powder metallurgy superalloys, ASM Handb. 7 (1998) 887–902.

[152] M. Higashi, N. Kanno, Effect of initial powder particle size on the hot workability of powder metallurgy Ni-based superalloys, Mater. Des. 194

(2020) 108926. https://doi.org/10.1016/j.matdes.2020.108926.

[153] S.L. Semiatin, J.M. Shank, A.R. Shiveley, W.M. Saurber, E.F. Gaussa, A.L. Pilchak, The Effect of Forging Variables on the Supersolvus Heat-Treatment Response of Powder-Metallurgy Nickel-Base Superalloys, Metall. Mater. Trans. A Phys. Metall. Mater. Sci. 45 (2014) 6231–6251. https://doi.org/10.1007/s11661-014-2572-y.

[154] J.C. Borofka, R.D. Kissinger, J.K. Tien, HIP modeling of superalloy powders, in: Proc. 6th Int. Symp. Superalloys (Superalloys 1988), The Metallurgical Society, 1988: pp. 111–120.

[155] R. Thamburaj, W. Wallace, Y.N. Chari, T.L. Prakash, Influence of Processing Variables on Prior Particle Boundary Precipitation and Mechanical Behaviour in PM Superalloy APK1, Powder Metall. 27 (1984) 169–180. https://doi.org/10.1179/pom.1984.27.3.169.

[156] H.S. Liu, L. Zhang, X.B. He, X.H. Qu, H.M. Zhu, G.Q. Zhang, Effect of oxygen content and heat treatment on carbide precipitation behavior in PM Ni-base superalloys, Int. J. Miner. Metall. Mater. 19 (2012) 827–835. https://doi.org/10.1007/s12613-012-0635-x.

[157] R.G. Menzies, J.W. Edington, G.J. Davies, Superplastic behaviour of powder-consolidated nickel-base superalloy IN-100, Met. Sci. 15 (1981) 210–216.

[158] G.H. Gessinger, M.J. Bomford, Powder metallurgy of superalloys, Int. Metall. Rev. 19 (1974) 51–76. https://doi.org/10.1179/imtlr.1974.19.1.51.

[159] J.F. Radavich, The physical metallurgy of cast and wrought alloy 718, in: Superalloy 718-Metallurgy Appl., The Minerals, Metals & Materials Society Warrendale, PA, 1989: pp. 229–240. https://doi.org/10.7449/1989/superalloys_1989_229_240.

[160] C.Y. Lin, H.Y. Bor, C.N. Wei, C.H. Liao, Compositional Optimization of In718 Superalloy Powder for Additive Manufacturing, in: Mater. Sci. Forum, Trans Tech Publ, 2018: pp. 2167–2172.

[161] A. Kracke, Superalloys, the Most Successful Alloy System of Modern Times-Past, Present, and Future, (2016) 13–50. https://doi.org/10.7449/2010/superalloys_2010_13_50.

[162] J. Rösler, T. Hentrich, B. Gehrmann, On the development concept for a new 718-type superalloy with improved temperature capability, Metals (Basel). 9 (2019) 1–20. https://doi.org/10.3390/met9101130.

[163] R.L. Kennedy, Allvac® 718plus™, superalloy for the next forty years, Superalloys 718, 625, 706 Deriv. 2005. (2005) 1–14.

https://doi.org/10.7449/2005/superalloys_2005_1_14.

[164] W.D. Cao, R. Kennedy, Role of chemistry in 718-type alloys—Allvac 718Plus alloy development, Proc. 10th Int. Symp. Superalloys (Superalloys 2004). (2004) 91–99.

[165] J. Sharma, M.H. Haghighat, B. Gehrmann, C. Moussa, N. Bozzolo, Dynamic and Post-dynamic Recrystallization During Supersolvus Forging of the New Nickel-Based Superalloy—VDM Alloy 780, in: Proc. 14th Int. Symp. Superalloys (Superalloys 2020), Springer, 2020: pp. 450–460.

[166] J. Sharma, A. Nicolaÿ, M. De Graef, N. Bozzolo, Phase discrimination between δ and η phases in the new nickel-based superalloy VDM Alloy 780 using EBSD, Mater. Charact. 176 (2021) 111105. https://doi.org/10.1016/j.matchar.2021.111105.

[167] S.B. Kim, A. Evans, J. Shackleton, G. Bruno, M. Preuss, P.J. Withers, Stress relaxation of shot-peened UDIMET 720Li under solely elevated-temperature exposure and under isothermal fatigue, Metall. Mater. Trans. A Phys. Metall. Mater. Sci. 36 (2005) 3041–3053. https://doi.org/10.1007/s11661-005-0076-5.

[168] H. Hattori, M. Takekawa, D. Furrer, R.J. Noel, Evaluation of P/M U720 for Gas Turbine Engine Disk Application, (1996) 705–711. https://doi.org/10.7449/1996/superalloys_1996_705_711.

[169] M. Goto, D.M. Knowles, Initiation and propagation behaviour of microcracks in Ni-base superalloy Udimet 720 LI, Eng. Fract. Mech. 60 (1998) 1–18. https://doi.org/10.1016/S0013-7944(98)00003-4.

[170] Allegheny Technologies Incorporated (ATI), ATI 720 Alloy Technical Data Sheet, Pittsburgh, 2014. https://www.atimetals.com/Products/Documents/datasheets/nickel-cobalt/nickel-based/ati_720_tds_en_v1.pdf.

[171] R.C. Reed, M.P. Jackson, Y.S. Na, Characterization and Modeling of the Precipitation of the Sigma Phase in UDIMET 720 and UDIMET 720LI, Metall. Mater. Trans. A. 30 (1999) 521–533.

[172] P. Villechaise, J. Cormier, T. Billot, J. Mendez, Mechanical Behavior and Damage Processes of Udimet 720Li: Influence of Localized Plasticity at Grain Boundaries, in: Proc. 12th Int. Symp. Superalloys (Superalloys 2012), 2012: pp. 13–24. https://doi.org/10.1002/9781118516430.ch2.

[173] D. Helm, O. Roder, Influence of long term exposure in air on microstructure, surface stability and mechanical properties of Udimet 720Li, Proc. 9th Int. Symp. Superalloys (Superalloys 2000). (2000) 487–

493.

[174] T. Wojcik, M. Rath, E. Kozeschnik, Characterisation of secondary phases in Ni-base superalloy Rene 65, Mater. Sci. Technol. (United Kingdom). 34 (2018) 1558–1564. https://doi.org/10.1080/02670836.2018.1505227.

[175] Aubert&Duval, AD730 : New Ni-based Superalloy for High Temperature Applications, 2017. chrome-extension://efaidnbmnnnibpcajpcglclefindmkaj/https://www.aubertduval.com/wp-media/uploads/2017/05/2017_Brochure_AD730.pdf.

[176] T. Konkova, S. Rahimi, S. Mironov, T.N. Baker, Effect of strain level on the evolution of microstructure in a recently developed AD730 nickel based superalloy during hot forging, Mater. Charact. 139 (2018) 437–445. https://doi.org/10.1016/j.matchar.2018.03.027.

[177] M. Pérez, C. Dumont, O. Nodin, S. Nouveau, Impact of forging direction on the recrystallization behaviour of nickel base superalloy AD730 billet material at subsolvus temperatures, Mater. Charact. 146 (2018) 169–181. https://doi.org/10.1016/j.matchar.2018.10.003.

[178] A. Shyam, C.J. Torbet, S.K. Jha, J.M. Larsen, M.J. Caton, C.J. Szczepanski, T.M. Pollock, J.W. Jones, Development of ultrasonic fatigue for rapid, high temperature fatigue studies in turbine engine materials, Proc. 10th Int. Symp. Superalloys. (2004) 259–268. https://doi.org/10.7449/2004/superalloys_2004_259_268.

[179] B. Flageolet, O. Yousfi, Y. Dahan, P. Villechaise, J. Cormier, Characterization of microstructures containing abnormal grain growth zones in Alloy 718, in: 7th Int. Symp. Superalloy 718 Deriv. 2010, TMS (The Minerals, Metals & Materials Society), 2010: pp. 595–606. https://doi.org/10.1002/9781118495223.ch46.

[180] J. Miao, T.M. Pollock, J. Wayne Jones, Microstructural extremes and the transition from fatigue crack initiation to small crack growth in a polycrystalline nickel-base superalloy, Acta Mater. 60 (2012) 2840–2854. https://doi.org/10.1016/j.actamat.2012.01.049.

[181] N.A. Wilkinson, Forging of 718: The Importance of T.M.P., in: Superalloy 718-Metallurgy Appl., 1989: pp. 119–133. https://doi.org/10.7449/1989/superalloys_1989_119_133.

[182] M. Zhan, Z. Sun, H. Yang, Modeling of Hot Forging, Elsevier, 2014. https://doi.org/10.1016/B978-0-08-096532-1.00529-X.

[183] H.J. McQueen, Deformation mechanisms in hot working, Jom. 20 (1968) 31–38. https://doi.org/10.1007/bf03378692.

[184] G.E. Dieter, H.A. Kuhn, S.L. Semiatin, Handbook of workability and process design, ASM international, 2003.

[185] E.B. Marin, D.J. Bammann, A. Brown, H. El Kadiri, R.D. Costley, P.T. Wang, M.F. Horstemeyer, Modeling the hot forging of nickel-based superalloys: IN718 and alloy 718Plus, in: 7th Int. Symp. Superalloy 718 Deriv. 2010, TMS (The Minerals, Metals & Materials Society), 2010: pp. 331–342. https://doi.org/10.1002/9781118495223.ch25.

[186] M.F. Ashby, C. Gandhi, D.M.R. Taplin, M.F. Ashby, Overview No. 3 Fracture-mechanism maps and their construction for fcc metals and alloys, Acta Metall. 27 (1979) 699–729. https://doi.org/10.1016/B978-0-08-030541-7.50005-9.

[187] S.H. Goods, L.M. Brown, The nucleation of cavities by plastic deformation, Perspect. Creep Fract. (1983) 71–85.

[188] G. Le Roy, J.D. Embury, G. Edwards, M.F. Ashby, A model of ductile fracture based on the nucleation and growth of voids, Acta Metall. 29 (1981) 1509–1522. https://doi.org/10.1016/0001-6160(81)90185-1.

[189] M. Gologanu, D.-S. Comsa, A. Kami, D. Banabic, Modelling the voids growth in ductile fracture, in: Multiscale Model. Sheet Met. Form., Springer, 2016: pp. 135–203.

[190] A.K. Bhargava, C.P. Sharma, Mechanical behaviour and testing of materials, PHI Learning Pvt. Ltd., 2011.

[191] A. Bhaduri, Mechanical properties and working of metals and alloys, Springer, 2018.

[192] Y. Prasad, K.P. Rao, S. Sasidhar, Hot working guide: a compendium of processing maps, ASM international, 2015.

[193] W.F. Hosford, Mechanical behavior of materials, Cambridge university press, 2010.

[194] F.J. Humphreys, M. Hatherly, Recrystallization and related annealing phenomena, Elsevier, 2012.

[195] S. Kolupaeva, M. Semenov, The stored energy of plastic deformation in crystals of face- centered cubic metals, IOP Conf. Ser. Mater. Sci. Eng. 71 (2015). https://doi.org/10.1088/1757-899X/71/1/012077.

[196] H.J. McQueen, Development of dynamic recrystallization theory, Mater. Sci. Eng. A. 387–389 (2004) 203–208. https://doi.org/10.1016/j.msea.2004.01.064.

[197] R.N. Wright, Mechanical Properties of Wire and Related Testing, Wire

Technol. (2016) 129–157. https://doi.org/10.1016/b978-0-12-802650-2.00011-x.

[198] R.C. Buckingham, C. Argyrakis, M.C. Hardy, S. Birosca, The effect of strain distribution on microstructural developments during forging in a newly developed nickel base superalloy, Mater. Sci. Eng. A. 654 (2016) 317–328. https://doi.org/10.1016/j.msea.2015.12.042.

[199] Y. Wang, W.Z. Shao, L. Zhen, L. Lin, Y.X. Cui, Investigation on Dynamic Recrystallization Behavior in Hot Deformed Superalloy Inconel 718, Mater. Sci. Forum. 546–549 (2007) 1297–1300. https://doi.org/10.4028/www.scientific.net/msf.546-549.1297.

[200] C. Kienl, A. Casanova, O.M.D.M. Messé, C. Argyrakis, C.M.F. Rae, Characterization of the initial stages of dynamic recrystallization in ATI 718plus®, in: Proc. 9th Int. Symp. Superalloy 718 Deriv. Energy, Aerospace, Ind. Appl., Springer International Publishing, 2018: pp. 405–420. https://doi.org/10.1007/978-3-319-89480-5_25.

[201] M.E. Kassner, Fundamentals of creep in metals and alloys, Butterworth-Heinemann, 2015.

[202] S.C. Medeiros, Y.V.R.K. Prasad, W.G. Frazier, R. Srinivasan, Microstructural modeling of metadynamic recrystallization in hot working of IN 718 superalloy, Mater. Sci. Eng. A. 293 (2000) 198–207. https://doi.org/10.1016/S0921-5093(00)01053-4.

[203] S.L. Semiatin, D.S. Weaver, P.N. Fagin, M.G. Glavicic, R.L. Goetz, N.D. Frey, R.C. Kramb, M.M. Antony, Deformation and recrystallization behavior during hot working of a coarse-grain, nickel-base superalloy ingot material, Metall. Mater. Trans. A Phys. Metall. Mater. Sci. 35 A (2004) 679–693. https://doi.org/10.1007/s11661-004-0379-y.

[204] P.M. Mignanelli, N.G. Jones, K.M. Perkins, M.C. Hardy, H.J. Stone, Microstructural evolution of a delta containing nickel-base superalloy during heat treatment and isothermal forging, Mater. Sci. Eng. A. 621 (2015) 265–271. https://doi.org/10.1016/j.msea.2014.10.071.

[205] T. Sakai, Dynamic recrystallization microstructures under hot working conditions, J. Mater. Process. Tech. 53 (1995) 349–361. https://doi.org/10.1016/0924-0136(95)01992-N.

[206] L. Du, S. Yang, P. Zhang, H. Du, Pinning effect of different shape second-phase particles on grain growth in polycrystalline: numerical and analytical investigations, Compos. Interfaces. 25 (2018) 357–368. https://doi.org/10.1080/09276440.2018.1439625.

[207] W.D. Callister, Fundamentals of materials science and engineering, Wiley London, 2000.

[208] K. Song, M. Aindow, Grain growth and particle pinning in a model Ni-based superalloy, Mater. Sci. Eng. A. 479 (2008) 365–372. https://doi.org/10.1016/j.msea.2007.09.055.

[209] T. Sakai, A. Belyakov, R. Kaibyshev, H. Miura, J.J. Jonas, Dynamic and post-dynamic recrystallization under hot, cold and severe plastic deformation conditions, Prog. Mater. Sci. 60 (2014) 130–207. https://doi.org/10.1016/j.pmatsci.2013.09.002.

[210] C. Gandhi, M.F. Ashby, Overview no. 5. Fracture-mechanism maps for materials which cleave: F.C.C., B.C.C. and H.C.P. metals and ceramics, Acta Metall. 27 (1979) 1565–1602. https://doi.org/10.1016/0001-6160(79)90042-7.

[211] T.H. Courtney, Mechanical Behavior of Materials, Waveland Pr, Waveland Press, 2005.

[212] C. V Nielsen, P.A.F. Martins, Chapter 2 - Formability*, in: C. V Nielsen, P.A.F.B.T.-M.F. Martins (Eds.), Academic Press, 2021: pp. 7–107. https://doi.org/https://doi.org/10.1016/B978-0-323-85255-5.00006-6.

[213] P. Scallan, Material evaluation and process selection, in: P.B.T.-P.P. Scallan (Ed.), Process Plan., Butterworth-Heinemann, Oxford, 2003: pp. 109–170. https://doi.org/10.1016/b978-075065129-5/50005-2.

[214] Y. Ning, Z. Yao, H. Guo, M.W. Fu, H. li, X. Xie, Investigation on hot deformation behavior of P/M Ni-base superalloy FGH96 by using processing maps, Mater. Sci. Eng. A. 527 (2010) 6794–6799. https://doi.org/10.1016/j.msea.2010.07.040.

[215] Y. Kong, P. Chang, Q. Li, L. Xie, S. Zhu, Hot deformation characteristics and processing map of nickel-based C276 superalloy, J. Alloys Compd. 622 (2015) 738–744. https://doi.org/10.1016/j.jallcom.2014.10.118.

[216] G. He, F. Liu, J. Si, C. Yang, L. Jiang, Characterization of hot compression behavior of a new HIPed nickel-based P/M superalloy using processing maps, Mater. Des. 87 (2015) 256–265. https://doi.org/10.1016/j.matdes.2015.08.035.

[217] Z. Wan, L. Hu, Y. Sun, T. Wang, Z. Li, Hot deformation behavior and processing workability of a Ni-based alloy, J. Alloys Compd. (2018). https://doi.org/10.1016/j.jallcom.2018.08.010.

[218] J.C. Malas, V. Seetharaman, Using material behavior models to develop process control strategies, JOM. 44 (1992) 8–13.

https://doi.org/10.1007/BF03222246.

[219] Y.V.R.K. Prasad, H.L. Gegel, S.M. Doraivelu, J.C. Malas, J.T. Morgan, K.A. Lark, D.R. Barker, Modeling of dynamic material behavior in hot deformation: Forging of Ti-6242, Metall. Trans. A. 15 (1984) 1883–1892. https://doi.org/10.1007/BF02664902.

[220] Y.V.R.K. Prasad, Processing maps: A status report, J. Mater. Eng. Perform. 22 (2013) 2867–2874. https://doi.org/10.1007/s11665-013-0732-7.

[221] K. Pitcheswara Rao, C. Dharmendra, Y. Venkata Rama Krishna Prasad, N. Hort, H. Dieringa, Optimization of thermo-mechanical processing for forging of newly developed creep-resistant magnesium alloy ABAX633, Metals (Basel). 7 (2017). https://doi.org/10.3390/met7110513.

[222] S.V.S. Narayana Murty, B. Nageswara Rao, B.P. Kashyap, Instability criteria for hot deformation of materials, Int. Mater. Rev. 45 (2000) 15–26. https://doi.org/10.1179/095066000771048782.

[223] H. Zhang, K. Zhang, Z. Lu, C. Zhao, X. Yang, Hot deformation behavior and processing map of a γ'-hardened nickel-based superalloy, Mater. Sci. Eng. A. 604 (2014) 1–8. https://doi.org/10.1016/j.msea.2014.03.015.

[224] Z. Jia, Z.X. Gao, J.J. Ji, D.X. Liu, T.B. Guo, Y.T. Ding, High-temperature deformation behavior and processing map of the as-cast Inconel 625 alloy, Rare Met. 40 (2021) 2083–2091. https://doi.org/10.1007/s12598-020-01474-6.

[225] S.L. Semiatin, D.W. Mahaffey, N.C. Levkulich, O.N. Senkov, J.S. Tiley, The Effect of Cooling Rate on High-Temperature Precipitation in a Powder-Metallurgy, Gamma/Gamma-Prime Nickel-Base Superalloy, Metall. Mater. Trans. A Phys. Metall. Mater. Sci. (2018). https://doi.org/10.1007/s11661-018-4896-5.

[226] D.J. Cha, D.K. Kim, J.R. Cho, W.B. Bae, Hot shape forging of gas turbine disk using microstructure prediction and finite element analysis, Int. J. Precis. Eng. Manuf. 12 (2011) 331–336. https://doi.org/10.1007/s12541-011-0043-6.

[227] J. Chen, P. Zhang, J. Dong, M. Zhang, Z. Yao, Relevance of Primary γ' dissolution and abnormal grain growth in UDIMET 720Li, Mater. Trans. 56 (2015) 1968–1976.

[228] I.M.D. Parr, T.J. Jackson, M.C. Hardy, D.J. Child, C. Argyrakis, K. Severs, V. Saraf, J.M. Stumpf, Inhomogeneous grain coarsening behavior in supersolvus heat treated nickel-based superalloy RR1000, Proc. 13th Int. Symp. Superalloys (Superalloys 2016). 2016-Janua (2016) 447–456.

https://doi.org/10.1002/9781119075646.ch48.

[229] W. Hermann, M. Fahrmann, H.G. Sockel, Determination of the γ'-solvus temperature of two commercial wrought Ni-base superalloys by thermal expansion measurements, in: Proc. 10th Int. Symp. Superalloys (Superalloys 2004), TMS (The Minerals, Metals & Materials Society), 2004: pp. 517–522. https://doi.org/10.7449/2004/superalloys_2004_517_522.

[230] T. Fedorova, J. Rösler, J. Klöwer, B. Gehrmann, Development of a new 718-type Ni-Co superalloy family for high temperature applications at 750 °C, MATEC Web Conf. 14 (2014). https://doi.org/10.1051/matecconf/20141401003.

[231] T. Ohno, R. Watanabe, T. Fukui, K. Tanaka, Isothermal forging of Waspaloy in air with a new die material, Trans. Iron Steel Inst. Japan. (1988). https://doi.org/10.2355/isijinternational1966.28.958.

[232] S. Lee Raymond,Edward; Krishna Srivatsa, Isothermal forging of nickel-base superalloys in air, US6,908,519B2, 2005.

[233] M. Higashi, N. Kanno, Evaluation of Hot Workability of Powder Metallurgy Ni-Based Superalloy with Different Initial Microstructures, Mater. Des. 52 (2020) 108926. https://doi.org/10.1007/s11661-020-06085-5.

[234] M.C. Somani, K. Muraleedharan, Y.V.R.K. Prasad, V. Singh, Mechanical processing and microstructural control in hot working of hot isostatically pressed P/M IN-100 superalloy, Mater. Sci. Eng. A. 245 (1998) 88–99. https://doi.org/10.1016/S0921-5093(97)00698-9.

[235] M. Shirgaokar, G. Shen, Isothermal and Hot-Die Forging, Mater. Park. OH ASM Int. 2004. (2004) 257–275.

[236] M. Mohamdein, J. Schwar, 2-1/2D Computer Modeling and Verification of Forged Pyromet 718® Alloy, in: Superalloys 718, 625, 706, Deriv., TMS (The Minerals, Metals &Materials Society), Pittsburgh, 2001.

[237] J.M. Hyzak, R.P. Singh, J.E. Morra, T.E. Howson, The Microstructural Response of As-HIP P/M U-720 to Thermomechanical Processing, in: S. Antolovich, R.. Stusrud, R.. MacKay, D.. Anton, T. Khan, R.. Kissinger, D.L. Klarstrom (Eds.), Proc. 7th Int. Symp. Superalloys (Superalloys 1992), TMS (The Minerals, Metals &Materials Society), 1992: pp. 93–101. https://doi.org/10.7449/1992/superalloys_1992_93_101.

[238] F. Liu, J. Chen, J. Dong, M. Zhang, Z. Yao, The hot deformation behaviors of coarse, fine and mixed grain for Udimet 720Li superalloy,

Mater. Sci. Eng. A. 651 (2016) 102–115. https://doi.org/10.1016/j.msea.2015.10.099.

[239] Q.Y. Yu, Z.H. Yao, J.X. Dong, Deformation and recrystallization behavior of a coarse-grain, nickel-base superalloy Udimet720Li ingot material, Mater. Charact. 107 (2015) 398–410. https://doi.org/10.1016/j.matchar.2015.07.035.

[240] K.A. Green, J.A. Lemsky, R.M. Gasior, Development of Isothermally Forged P/M Udimet 720 for Turbine Disk Applications, in: Proc. 8th Int. Symp. Superalloys (Superalloys 1996), TMS (The Minerals, Metals &Materials Society), 1996: pp. 697–703. https://doi.org/10.7449/1996/superalloys_1996_697_703.

[241] J. long Qu, Z. nan Bi, J. hui Du, M. qing Wang, Q. zeng Wang, J. Zhang, Hot Deformation Behavior of Nickel-Based Superalloy GH4720Li, J. Iron Steel Res. Int. 18 (2011) 59–65. https://doi.org/10.1016/S1006-706X(12)60023-5.

[242] Y. Zhao, S. Fu, S. Zhang, X. Tang, N. Liu, G. Zhang, An advanced cast/wrought technology for GH720Li alloy disk from fine grain ingot, in: 7th Int. Symp. Superalloy 718 Deriv. 2010, TMS (The Minerals, Metals & Materials Society), 2010: pp. 271–280. https://doi.org/10.1002/9781118495223.ch20.

[243] P.W. Lee, H.A. Kuhn, Fracture in cold upset forging -a criterion and model, Metall. Trans. 4 (1973) 969–974. https://doi.org/10.1007/BF02645597.

[244] H. Kakimoto, T. Arikawa, Prediction of surface crack in hot forging by numerical simulation, Procedia Eng. 81 (2014) 474–479. https://doi.org/10.1016/j.proeng.2014.10.025.

[245] A.S.M. Handbook, Materials Selection and Design, Vol. 20, ASM Int. Ohio. (1997).

[246] B.J. Griffin, A comparison of conventional Everhart-Thornley style and in-lens secondary electron detectors: a further variable in scanning electron microscopy., Scanning. 33 (2011) 162–173. https://doi.org/10.1002/sca.20255.

[247] D.G. Brandon, The structure of high-angle grain boundaries, Acta Metall. 14 (1966) 1479–1484.

[248] K.R. Bain, M.L. Gambone, J.M. Hyzak, M.C. Thomas, Development of damage tolerant microstructures in Udimet 720, Proc. 6th Int. Symp. Superalloys (Superalloys 1988). (1988) 13–22.

[249] M. Soucail, Y. Bienvenu, Dissolution of the γ' phase in a nickel base superalloy at equilibrium and under rapid heating, Mater. Sci. Eng. A. (1996). https://doi.org/10.1016/S0921-5093(97)80011-1.

[250] P.M. Mignanelli, N.G. Jones, M.C. Hardy, H.J. Stone, The influence of Al: Nb ratio on the microstructure and mechanical response of quaternary Ni-Cr-Al-Nb alloys, Mater. Sci. Eng. A. 612 (2014) 179–186. https://doi.org/10.1016/j.msea.2014.06.021.

[251] C.H. Zenk, S. Neumeier, H.J. Stone, M. Göken, Mechanical properties and lattice misfit of γ/γ' strengthened Co-base superalloys in the Co-W-Al-Ti quaternary system, Intermetallics. 55 (2014) 28–39. https://doi.org/10.1016/j.intermet.2014.07.006.

[252] J.C. Russ, The image processing handbook, CRC press, 2006.

[253] K. Gopinath, A.K. Gogia, S. V. Kamat, R. Balamuralikrishnan, U. Ramamurty, Tensile properties of Ni-based superalloy 720Li: Temperature and strain rate effects, Metall. Mater. Trans. A Phys. Metall. Mater. Sci. 39 (2008) 2340–2350. https://doi.org/10.1007/s11661-008-9585-3.

[254] H. Bian, X. Xu, Y. Li, Y. Koizumi, Z. Wang, M. Chen, K. Yamanaka, A. Chiba, Regulating the coarsening of the γ' phase in superalloys, NPG Asia Mater. 7 (2015) 212. https://doi.org/10.1038/am.2015.96.

[255] A. Baldan, Progress in Ostwald ripening theories and their applications to the γ'-precipitates in nickel-base superalloys Part II: Nickel-base superalloys, J. Mater. Sci. 37 (2002) 2379–2405. https://doi.org/10.1023/A:1015408116016.

[256] N. D'Souza, W. Li, C. Argyrakis, G.D. West, C.D. Slater, On the Evolution of Primary Gamma Prime Precipitates During High Temperature and High Strain Rate Deformation and Subsequent Heat Treatment in the Ni-Based Superalloy, RR1000, Metall. Mater. Trans. A Phys. Metall. Mater. Sci. 50 (2019) 4205–4222. https://doi.org/10.1007/s11661-019-05330-w.

[257] E. Alabort, R.C. Reed, D. Barba, Combined modelling and miniaturised characterisation of high-temperature forging in a nickel-based superalloy, Mater. Des. 160 (2018) 683–697. https://doi.org/10.1016/J.MATDES.2018.09.048.

[258] M. Panzenbock, Scanning Electron Microscope, an Essential Equipment for Failure Analysis, Microsc. Microanal. 24 (2018) 702–703. https://doi.org/10.1017/s1431927618004002.

[259] E.R. Weishaupt, Intergranular Fracture, Fail. Anal. Prev. 11 (2021) 356–

365. https://doi.org/10.31399/asm.hb.v11.a0006777.

[260] P.J. Noell, R.B. Sills, A.A. Benzerga, B.L. Boyce, Void Nucleation During Ductile Rupture of Metals: A Review, Prog. Mater. Sci. 135 (2023) 101085.

[261] Y. Yuan, Y. Gu, C. Cui, T. Osada, T. Yokokawa, H. Harada, A novel strategy for the design of advanced engineering alloys—strengthening turbine disk superalloys via twinning structures, Adv. Eng. Mater. 13 (2011) 296–300.

[262] J. Wang, X. Zhang, Twinning effects on strength and plasticity of metallic materials, MRS Bull. 41 (2016) 274–281.

[263] S. Liu, D. Kent, N. Doan, M. Dargusch, G. Wang, Effects of deformation twinning on the mechanical properties of biodegradable Zn-Mg alloys, Bioact. Mater. 4 (2019) 8–16.

[264] F. Masoumi, M. Jahazi, D. Shahriari, J. Cormier, Coarsening and dissolution of γ' precipitates during solution treatment of AD730™ Ni-based superalloy: Mechanisms and kinetics models, J. Alloys Compd. 658 (2016) 981–995. https://doi.org/10.1016/j.jallcom.2015.11.002.

[265] V.V. Lifshitz, I.M.; Slyozov, The kinetics of precipitation from supersaturated solid solutions, J. Phys. Chem. Solids. 19 (1961) 35–50.

[266] V.C. Wagner, Theorie der Alterung von Niederschlägen durch Umlösen (Ostwald-Reifung), Zeitschrift Für Elektrochemie, Berichte Der Bunsengesellschaft Für Phys. Chemie. 65 (1961) 581–591.